Resonant Cavity Light Emitting Diodes: Device Characterisation and Spectroscopy

by

Konstanze S. Hild

A thesis submitted to the University of Surrey for the degree of Doctor of Philosophy

Department of Physics, School of Electronics and Physical Sciences, University of Surrey, Guildford, Surrey, GU2 7XH, United Kingdom

June 2003

Abstract

The operation of a new type of light emitting diode (LED) developed in the last decade is investigated. In the so called "resonant cavity" LEDs (RCLEDs) the active region is embedded into a resonator formed by distributed Bragg reflectors. The devices considered here are for emission at 650nm to coincide with one attenuation loss of a particular plastic optical fibre (POF) to be used in local area networks.

In this thesis room temperature photo-modulated reflectance and edge electroluminescence measurements have shown to give valuable results in determining the quantum well (QW) emission wavelength of these structures, where photoluminescence cannot be applied. The cavity mode (CM) (resonator) wavelength is determined with reflectivity (R) measurements on wafers and devices. R spectra are also fitted with theoretical calculations and reveal differences in the layer structure.

It has been found that the de-tuning between the QW emission and the CM has a stronger influence on the light output compared with the reflectivity of the top mirror. It also improves the temperature stability. Larger devices show higher maximum efficiencies and are also less temperature sensitive than smaller devices. All devices are influenced by the carrier leakage into the indirect X-minima of the cladding, which has been shown to play a major role in the devices at high temperatures (above 40°C) and for carrier densities higher than $\sim 200A/cm^2$. The Ohmic self-heating adds to this, causing the high temperature sensitivity of these devices. The self-heating increases with decreasing device size and a value of $(0.15 \pm 0.02)W/cm°C$ for the thermal conductivity of these devices was found.

The coupling into POF shows that strongly de-tuned devices only have an advantage over tuned ones in terms of temperature stability but are much worse if the total amount of coupled light is compared. For a given operation current smaller devices could be modulated faster due to the higher current densities but no intrinsic size dependence was found. From the modulation measurements the carrier density and values for the different recombination processes, defect related and radiative current were found showing that at low current densities the overall current was dominated by non-radiative defect recombination.

Glossary

LED Light emitting diode

RCLED Resonant cavity LED

VCSEL Vertical cavity surface emitting laser

DBR distributed bragg reflector

QW quantum well

λ_{QW} quantum well wavelength

CM cavity mode

λ_{CM} cavity mode wavelength

POF plastic optical fibre

SI-POF step index POF

GI-POF graded index POF

PMMA polymethylmethacrylate

c.w. continuous wave

DC direct current

PR photomodulated reflectance

R reflectance

EL electroluminescence

LI light-current characteristics

OSA optical spectral analyzer

OPM optical power meter

DDM drift diffusion model

η_{in} internal efficiency

η_{extr} extraction efficiency

η_{eqe} external quantum efficiency

RT room temperature (20-28°C)

Communications

Conference presentations:

Condensed Matter and Materials Physics Conference (CMMP), University of Bristol, December 19th-21th 2000: Characterisation of visible (~650nm) RCLED wafers and device performance K. HILD, T.E. SALE, T.J.C. HOSEA, M. HIROTANI, Y. MIZUNO AND T. KATO

International Workshop on Microcavity Light Sources, University of Paderborn, April 7th 2001: Temperature dependence and spectral properties of Resonant Cavity LEDs emitting at 650nm, K. HILD, T.E. SALE, T.J.C. HOSEA, M. HIROTANI, Y. MIZUNO AND T. KATO

Semiconductor and integrated optoelectronics (SIOE), Cardiff, April 9th-11th 2001: Spectral and thermal properties of red AlGAInP RCLEDs for polymer fibre applications, K. HILD, T.E. SALE, T.J.C. HOSEA, M. HIROTANI, Y. MIZUNO AND T. KATO

Semiconductor and integrated optoelectronics (SIOE), Cardiff, March 25th-27th 2002: Influence of the top DBR Reflectivity, quantum well-cavity de-tuning and aperture size on the current and temperature dependence of red RCLEDs K. HILD, T.E. SALE, T.J.C. HOSEA, M. HIROTANI, Y. MIZUNO AND T. KATO

International Quantum Electronics Conference/Conference on Lasers, Applications and Technologies (IQEC/LAT), Moscow, June 22th-27th 2002: Effect of de-tuning on the temperature dependence of 650nm Resonant Cavity LEDs, K. HILD, T.E. SALE, T.J.C. HOSEA, M. HIROTANI, Y. MIZUNO AND T. KATO

Semiconductor and integrated optoelectronics (SIOE), Cardiff, April 14th-16th 2003: Modulation speed and leakage current in 650nm resonant-cavity LEDs K. HILD, T.E. SALE, S.J. SWEENEY, M. HIROTANI, Y. MIZUNO AND T. KATO

ACCEPTED:

European Conference on Lasers and Electro-Optics/European Quantum Electronics Conference CLEO/Europe-EQEC, Munich, June 23th-27th 2003: Leakage current and self-heating in 650nm resonant-cavity LEDs, K. HILD, T.E. SALE, M. HIROTANI, Y. MIZUNO AND T. KATO

Publications:

Influence of Quantum Well and Cavity Features on the Spectral, Angle- and Temperature-Dependent Emission of 650 nm Resonant Cavity LEDs, K. HILD, T.E. SALE, T.J.C. HOSEA, M. HIROTANI, Y. MIZUNO AND T. KATO, *phys. stat. sol. (a),* **188**, No. 3 (2001)

Spectral and thermal properties of red AlGAInP RCLEDs for polymer fibre applications, K. HILD, T.E. SALE, T.J.C. HOSEA, M. HIROTANI, Y. MIZUNO AND T. KATO, *IEE Proc. Optoelectron.,* **148**, No. 6 (2001)

IN PREPARATION:

Modulation speed and leakage current in 650nm resonant-cavity LEDs K. HILD, T.E. SALE, S.J. SWEENEY, M. HIROTANI, Y. MIZUNO AND T. KATO, for invited publication in *IEE Proc. Optoelectron.,* April (2004)

Acknowledgements

I would like to thank all the people that helped me on the way to this PhD thesis. First of all I would like to thank Professor Eoin O'Reilly and Professor Alf Adams for putting the idea of doing a PhD in optoelectronics here in Surrey into my head some 6 years ago. Dr Terry Sale and Dr Jeff Hosea for taking me on as a PhD student and for their helpful discussions throughout. I want to thank all the students/ postdocs around me in particular the now Drs Stephanie Constant and Gareth Knowles for giving me insight into photomodulated reflectance and device measurements and the gold wire bonder, respectively. I would like to thank Dr Sweeney for his interest in my work, his suggestions and also for reading my thesis. I want to thank Daido Ltd. and in particular Dr Masumi Hirotani for the samples, their financial and technical support and their interest in my work.

I would like to thank Professor Markus Pessa and Dr Pekka Pöyhönen for giving me the opportunity to work at the ORC in Tampere, Finland as a Marie Curie Research Fellow. I want to thank all the people at ORC and in Tampere and in particular Antti Isomäki who lent me some equipment, Nico Leine and Tomi Leinonen for letting me into the secrets of device processing and MBE growth, respectively and Anne Viherkoski for the help to find the washing maschine and other things. Kitos!

In Surrey I also want to thank the technical support staff: Roger Warren, Willie Scherrer, Marion Wiley, John-William Brown for the help with the device pictures, Gary Strudwick, Gill Gibbs from MSSU for the help with the SEM picture and Liz Griffith. I would like to thank my science teachers, professors, collegues and office mates for teaching and encouragement on the way. From my colleagues in Surrey I would like to particular thank Damien Clarke for all our useful discussions and for teaching me the word of the day and some php. Others including Gary Pearson, Andrew Hollingworth, Daren Lock, Robin Fehse, Stuart Ellaway, Gunnar Blume who will hopefully carry on some of my work, Carl O'Rourke and Dr Igor Marko.

I also want to thank my family for all their support through my life. I would also like to thank my in-laws, my university cell group and all the other people that supported me here in Guildford.

Vor allem möchte ich mich aber bei meinem Mann Stephen für all seine Unterstützung, Liebe und Geduld bedanken und ihm zusammen mit meinem Grossvater Kurt diese Arbeit widmen.

Ylistä Herraa, minun sieluni, ja kaikki mitä minussa on, ylistä hänen pyhää nimeään.

Quote

Ideen, wie absolute Gewissheit, absolute Genauigkeit, endgültige Wahrheit und so fort sind Einbildungen und haben in der Wissenschaft nichts zu suchen.

MAX BORN

Contents

Abstract i

Glossary ii

Communications iii

Acknowledgements v

Quote vi

1 Introduction 1

1.1 History of Optical Communication 1

1.1.1 Applications of plastic fibres 7

1.2 Light Sources 8

1.2.1 Light emitting diodes 8

1.2.2 Vertical Cavity Surface Emitting Lasers 8

1.2.3 Resonant Cavity Light Emitting Diodes 10

1.3 Thesis aim and outline 15

2 Resonant cavity light-emitting diodes: Background 17

2.1 Theory of Light Emitting Diodes 17

2.2 Resonant Cavity LEDs 21

2.3 De-tuning 25

2.4 Structures, growth and fabrication 25

2.5 Experimental device characterisation 28

3 Photo-modulated Reflectance and Edge Electroluminescence 31

3.1 Introduction 31

3.2 Edge Electroluminescence 32

3.3 Modulation Reflectance (MR) 34

3.3.1 Theory of MR for vertical-cavity structures 34

3.3.2 Photo-modulated Reflectance (PR) 37

3.4 PR Analysis techniques 39

3.4.1 QW PR-feature 40

3.4.2 PR Resonance technique 40

3.4.3 PR Symmetry technique 41

3.4.4 Fitting of PR spectra 42

3.4.5 $\Delta\varepsilon_2$-analysis 42

3.5 PR and edge-EL Results for RCLED wafers 44

3.5.1 Comparison of PR results of RCLED wafers with one and two QW transitions 44

3.5.2 Results for RCLED wafers with different numbers of top DBRs and different doping 51

3.5.3 Results on RCLED wafers with varying cavity modes 56

3.6 Conclusion 59

4 Reflectivity 61

4.1 Introduction 61

4.2 Theory 62

4.2.1 Reflectivity calculations 64

4.2.2 Reflectivity fitting . . . 66
4.3 Reflectivity directly on the device . . . 71
4.3.1 Temperature dependence . . . 74
4.4 Conclusions . . . 76

5 Effect of cavity mode - quantum well de-tuning 77
5.1 Introduction . . . 77
5.2 Angular dependence - far field pattern . . . 79
5.3 Angular dependence - EL spectra . . . 81
5.4 Normal incidence EL spectra . . . 86
5.4.1 Temperature dependence . . . 92
5.5 Light current characteristics . . . 96
5.6 Influence of carrier leakage and self-heating . . . 98
5.6.1 Self-heating . . . 99
5.6.2 Leakage . . . 104
5.7 Conclusions . . . 110

6 Influence of top DBRs and aperture size 112
6.1 Introduction . . . 112
6.2 Dependence on number of top DBRs . . . 113
6.2.1 Electroluminescence spectra . . . 114
6.2.2 Light-current characteristics . . . 115
6.2.3 Temperature dependence . . . 117
6.3 Size dependence . . . 119
6.3.1 Electroluminescence spectra . . . 120
6.3.2 Light-current characteristics . . . 122

6.3.3 Temperature dependence 126
6.3.4 Self-heating 129
6.4 Conclusions 132

7 Fibre coupling and modulation bandwidth 134

7.1 Introduction 134
7.2 Fibre coupling 135
7.2.1 Influence of de-tuning 136
7.2.2 Temperature dependence 138
7.3 Modulation bandwidth 141
7.3.1 Effect of de-tuning 142
7.3.2 Influence of aperture size 143
7.3.3 Calculation of the carrier density 147
7.3.4 Temperature dependence 153
7.4 Conclusions 155

8 Thesis conclusions 157

8.1 Summary 157
8.2 Outlook 161

References 163

Appendix 175

Chapter 1

Introduction

Since the first "Let there be light" all kinds of light sources, beginning with the sun, have played a crucial role in people's lives. From pure survival to art and technology, light has always been important and a source of fascination. In the following a brief overview about one modern application of light, optical communication, will be given. This is followed by a short description of some of the most topical light-emitting optoelectronic devices.

1.1 History of Optical Communication

The history of the transmission of information using *optical* techniques is much older than the history of electrical communication. Optical communication through means like fire (via smoke) date back to the early days of mankind [1]. In later days, the transmission of messages by flag-signals became a very common form of optical communication. By replacing the human flag-signallers with a set of semaphores mounted on top of towers at the end of the 18th century a French engineer called Claude Chappe created the first optical telegraphs [2] and so the "far-writer" was invented. In his system the message was still relayed by humans but the speed com-

pared to a purely human messenger was vastly improved. The transmission over the 425km distance from Paris to Strasbourg took only 6 minutes [2]. This optical technique was soon to be replaced by electrical telegraphy that allowed faster signal transmission. A century later the inventor of the telephone, Alexander Graham Bell, took optical communication a step further by patenting his photo-phone in 1880 [3]. However, this device in which speech was transmitted by light did not prove very successful and the technology of optical communication was forgotten for a while.

At the beginning of the 20th century the development of a new technology involving optical fibres took place. The idea of an optical fibre is to transmit light by total internal reflection. Total internal reflection occurs at the interface between a material with high optical density and a material with lower optical density for example from water or glass to air if the angle of incidence exceeds a certain critical angle depending on the two material refractive indices involved. The idea of total internal reflection is much older and this principle was first demonstrated by light being guided by jets of water in the 1850s [4].

In the first optical fibres, a silica core with high refractive index (i.e. high optical density) is surrounded by a cladding material with a lower refractive index. The numerical aperture (NA) for optical fibre can be calculated from the refractive indices of the core n_c and cladding n_{cl} of the fibre (assuming that the outside refractive index $n_0 = 1$).

$$NA = sin\alpha_0 = \sqrt{n_c^2 - n_{cl}^2} \tag{1.1}$$

as illustrated in figure 1.1.

All the light that gets accepted in the small fibre NA is then totally internally reflected and travels along the fibre allowing it to even be bent around corners (providing a minimum bend radius of ~15mm, depending on n_c, n_{cl} and the fibre thickness). The applications in the 1940s were fairly limited and included things such as dental illuminators and special light effects. In 1954 [6] the main application for fibres was to transport light and images over short distances as for example needed for an endoscope.

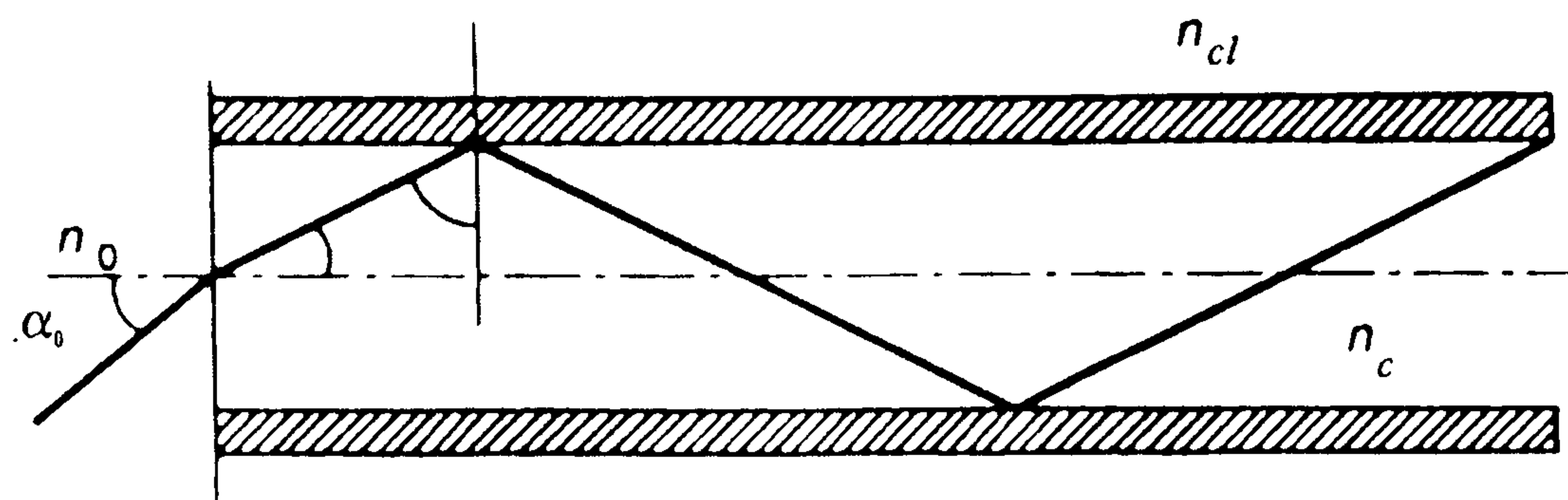

Figure 1.1: Definition of numerical aperture (after [5])

The development of the laser in the 1960s [7] and in particular the achievements in semiconductor technology that led to light emitting diodes (LEDs) and semiconductor lasers focused research back onto optical communication. Atmospheric disturbances in the air limit the range of free space communications and had a century earlier hindered the further development of Bell's photophone. The solution to this problem was the introduction of optical waveguides [8]. The ultimate solution however came by using lasers together with optical fibres [9]. As soon as the loss in silica fibre could be reduced drastically, the advantages of fibres over rigid waveguides became clear, as fibres can be bent and fed around things easily.

The development of the semiconductor laser made it possible to engineer the wavelength of the laser towards the minimum loss of the optical fibre. This minimum loss of the silica ("glass") fibre lies at $1.55\mu m$ as can be seen in figure 1.2. There is another local minimum at $1.31\mu m$ which coincides with the point of zero dispersion in the fibre. These two wavelengths are generally referred to as the telecommunication windows and a great deal of research has been focused on these two wavelengths exploring new semiconductor material systems. There are now new silica fibres available that exhibit low attenuation over a wavelength range from 1.2-1.6μm. However, since many of the original silica fibres remain in place, $1.55\mu m$ and $1.31\mu m$ are still the mainly investigated wavelengths.

In the same way as laser technology successfully investigated new semiconductor materials, new materials for optical fibres have also been developed in the last decade. One of these new materials is PMMA (Polymethylmethacrylate) as used for one type of plastic optical fibre (POF). A comparison of the wavelength dependence of the attenuation of different optical fibres can be seen in figure 1.2.

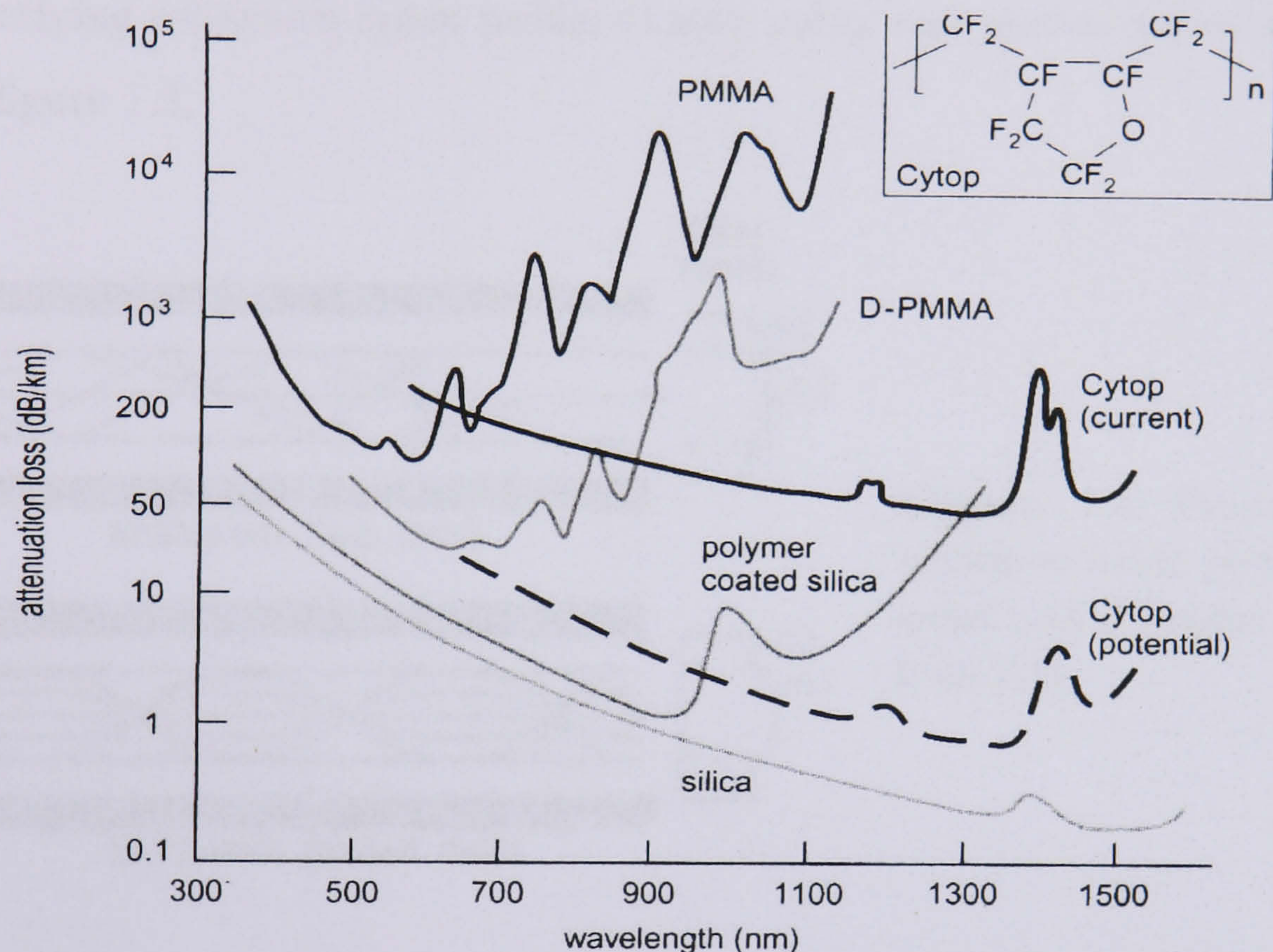

Figure 1.2: Attenuation of different optical fibres vs. wavelength

The advantages of POF over silica fibre are cheaper production, the easier alignment due to the large (1mm) core diameter compared to $\sim 6\mu$m for single mode or 60μm for multimode silica fibre, the greater ease of terminating and connecting single fibres and also its robustness. However the (glass) transition temperature T_g of currently available PMMA-POF is only $\sim 100°$C and so may prove problematic if placed in a harsh thermal environment such as near a car engine. They also cannot withstand normal soldering temperatures [10]. A more significant disadvantage is the much higher attenuation at all wavelengths which is about 100dB/km at the 570nm minimum. This compares with only 0.2dB/km at $1.55\mu m$ in silica fibre.

Nevertheless plastic fibres prove useful in short range data links where the attenuation is less critical.

The plastic optical fibres used in this work are PMMA-based step index fibres. In recent years, newer plastic fibres such as per-fluorinated fibres (for example Cytop in figure 1.2) exhibit a much larger region of low attenuation. These fibres are usually fabricated as graded index fibres. The different modes of propagation and the underlying refractive index profile of step index and graded index fibres can be seen in figure 1.3.

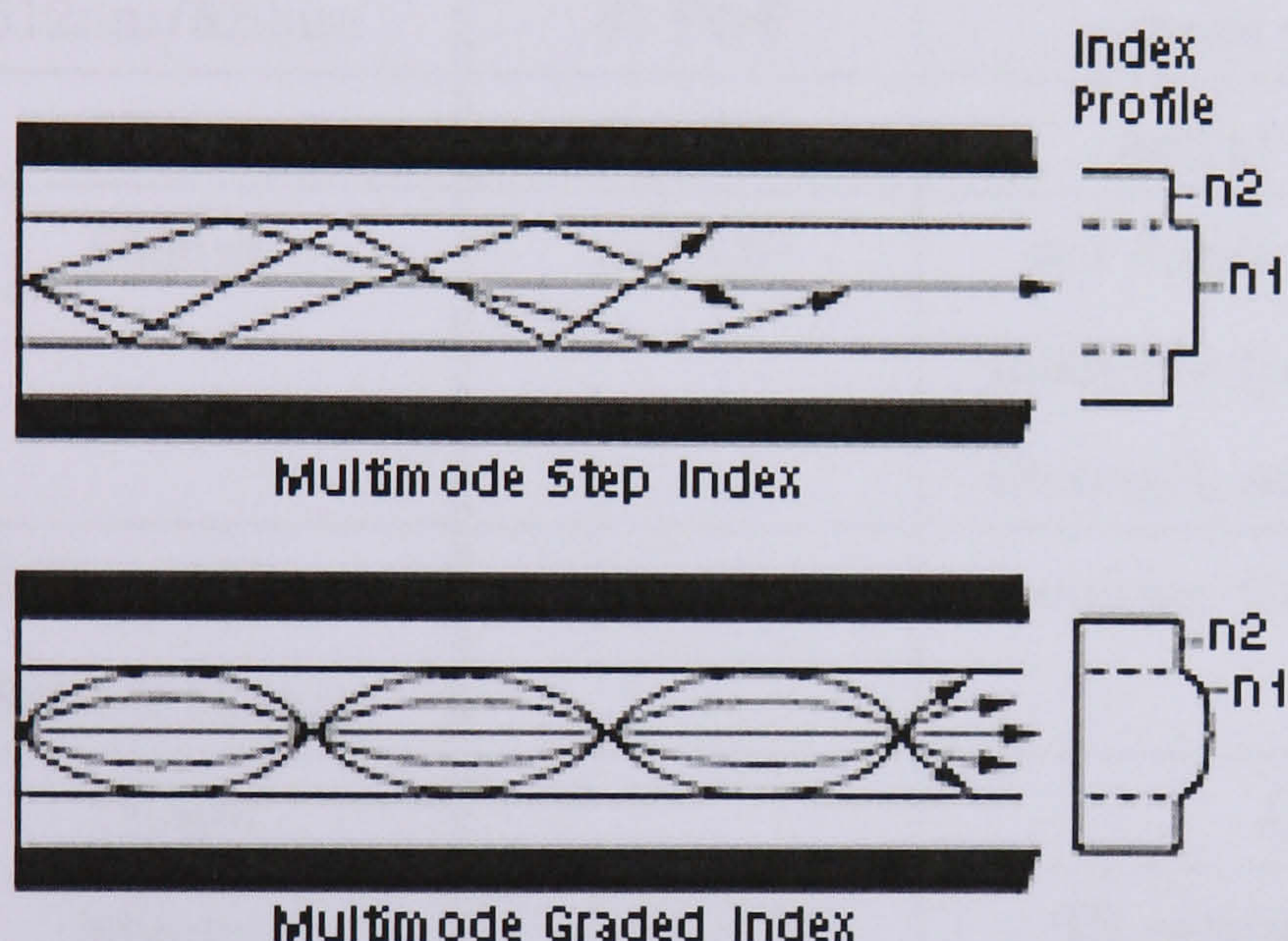

Figure 1.3: Propagation and refractive index profile in a step index and a graded index fibre from [11].

Graded index fibres usually have a smaller numerical aperture and their modal dispersion is less than in step index fibres. However step-index fibres do in turn have the advantage of being easier to fabricate.

The sources used for the first generation of semiconductor based optical communication system were AlGaAs LEDs (in 1977) which emitted at 850nm where the silica fibre loss is, even today, about 2dB/km. The wavelength was therefore increased to reach the ideal wavelength for optical communication through silica fibre. For use in the new plastic fibres the emission wavelength for lasers and LEDs is instead decreased into the visible to coincide with the low attenuation minima of plastic fibre. One minimum of the POF attenuation lies at 650nm as can be seen from figure 1.2. The absolute attenuation minimum lies at 570nm, a wavelength at which detectors are less sensitive. Hence devices at 650nm are a good compromise

between current detector sensitivity and fibre absorption. It still proves difficult to achieve efficient 570nm devices, but there is a great deal of research in the area of green and amber emitting devices based mainly on GaN so good devices could be expected in the next few years. In table 1.1 applications for light sources emitting at various wavelength are shown, focussing on the different fibres available for optical communication.

λ(nm)	fibre	other applications	active region
450nm/470nm		blue displays, medicine [12]	In(GaN)
512nm/520nm	Si-POF	green displays	In(GaN)
570nm	Si-POF	amber displays	GaP, GaN, InGaN
650nm	Si-POF	red displays, printing, medicine (photodynamic therapy), storage (DVD)	GaInP/AlGaInP
660nm-760nm 880nm-940nm		medicine (oximetry [12]) "	AlGaAs GaAs
780nm		CD	AlGaAs
850nm- -1300nm	pf GI-POF pf GI-POF	IR remote controls	various various
980nm	EDFA	laser surgery	InGaAs/GaAs
~1310nm	silica fibre	gas sensing (1321nm)	InGaAsP, AlGaInAs GaInNAs
~1480nm, 1460nm	EDFA, Raman		InGaAs(P)/InP
~1550nm	silica fibre	gas sensing (1578nm)	InGaAs(P)/InP

Table 1.1: Applications for various light sources at different emission wavelengths. Key to fibre notation: SI: step-index, GI: graded index, pf Gi-POF: perfluorinated POF [13] e.g. Cytop ^{TM}, EDFA: Erbium doped fibre amplifier. See figure 1.2 for fibre attenuation details

It is worth noting here that most of the sources currently available for commercial datacommunication based on silica fibre are 850nm devices. This is despite the fact that they are away from the minimum of attenuation of silica but rather due to the use of the more mature AlGaAs/GaAs material system as used for 850nm devices.

From table 1.1 it becomes clear that 650nm devices are not only interesting for communications but have a variety of other applications.

1.1.1 Applications of plastic fibres

The main use for plastic fibres and therefore for 650nm devices lies in local area networks (LAN) for automotive and avionic applications. As can be seen in figure 1.4, plastic optical fibres will replace slower and heavier copper cables due to the increasing demands of in-car navigation systems and other on-board computer functions. Another advantage is that plastic fibres do not suffer from interference with other electronic equipment as do the conventional copper leads.

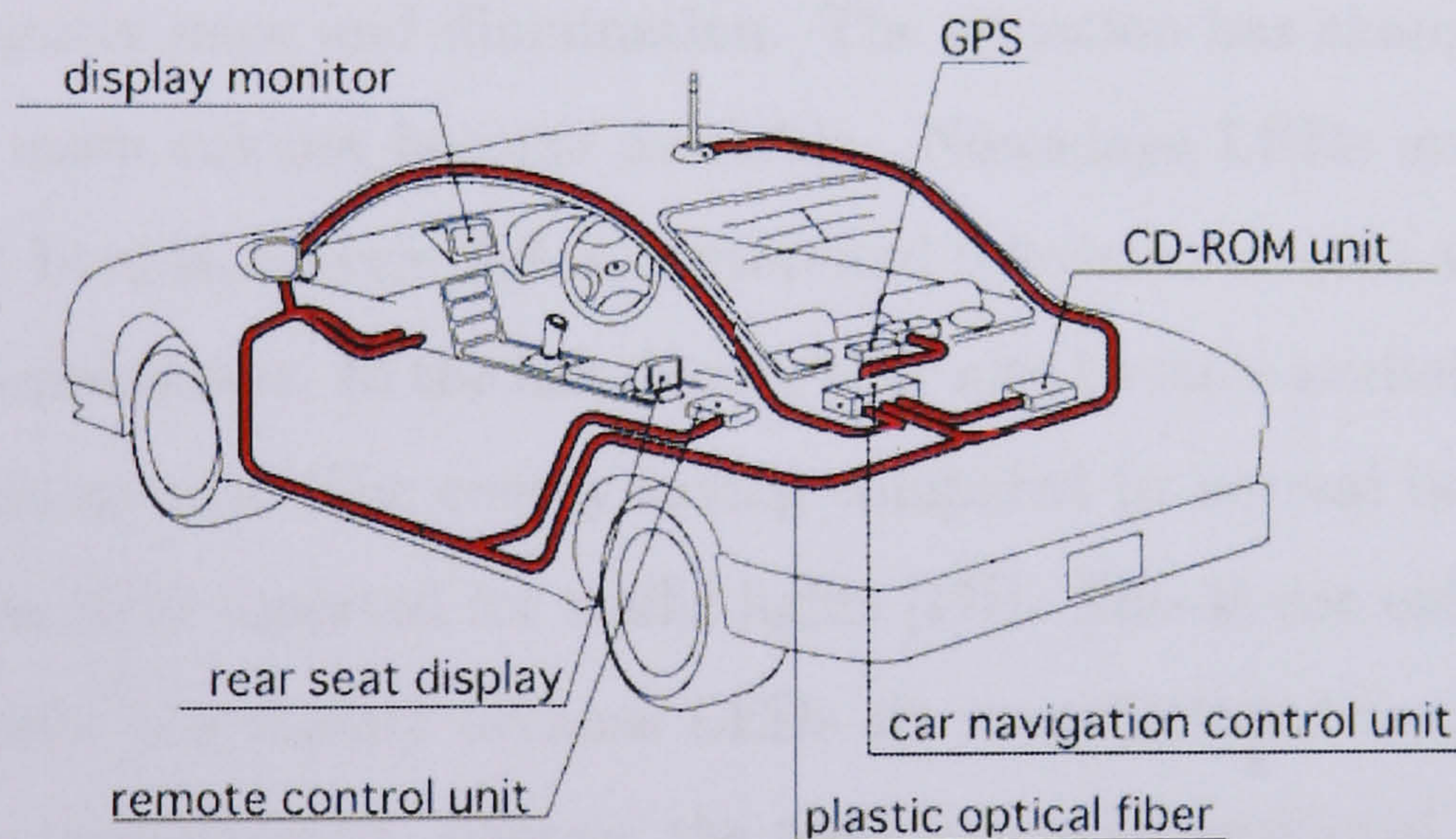

Figure 1.4: Automotive applications for plastic optical fibre. [14]

Plastic fibres are also already used in CD players, PCs and industrial electronics [15]. In Japan where both the centre of plastic fibre research and the market lies, plastic fibres have replaced some copper cables and local area networks in hospitals. The standard connector that is used is the IEEE1394b (Firewire) standard. With this connector and POF it would be possible to connect televisions, digital cameras and other electronic devices to the PC without switching the computer off ("hot-plugging"). POF together with 650nm RCLEDs have been suggested as a

standard with the IEEE1394 interface [16]. The key advantage of IEEE1394b over USB ports, aside from the much higher volume/speed of data transmission, is that an IEEE1394b connector does not have to be used in conjunction with a computer but can be used to connect any two digital devices.

1.2 Light Sources

1.2.1 Light emitting diodes

Light emitting Diodes (LEDs) have tended to be used mainly as indicators on computers and other electronic devices. Other uses include opto-switches, IR remote controls, computer mice and illumination. The situation has changed as LEDs get brighter and more colours become available. Nowadays LEDs are used in traffic lights, display boards, bicycle lights, laptop and television screens and also for various medical applications. In the last decade they also became available for brake and indicator lights in cars. The energy saving compared to normal bulbs is enormous (up to 85% has been reported for traffic lights [17]). This is not only because LEDs are more efficient but mainly because LEDs are manufactured to produce only the wanted colour (wavelength), whereas the need to use conventional colour filters for bulbs means most of the light produced by a bulb is not harnessed [18]. One of the newer challenges for bright LEDs is to produce white light as direct replacements for bulbs (for example in car headlights), some of which are already available [19].

1.2.2 Vertical Cavity Surface Emitting Lasers

Light sources for coupling into optical fibre require high directionality (low beam divergence) of the light output and can therefore not be fulfilled with conventional LEDs. First proposed in the late 1970s and first produced in 1979 [20], vertical cavity surface emitting lasers (VCSELs) are an ideal source for coupling into any

optical fibre because of their relatively symmetrical beam when compared with edge emitting lasers. Therefore it is not surprising that the first VCSELs were produced for emission at 1.3μm. An additional requirement for VCSELs is to find appropriate materials for the Bragg reflectors. These have to have a sufficient difference in their refractive indices to obtain high reflectivity but must also be transparent for the emission. GaAs-based VCSELs, emitting at 780nm, 850nm and 980nm were developed more quickly and are now commercially available, whereas research into the optimisation of 1.31μm VCSELs is still ongoing [21].

The main difference between a vertical and a conventional edge-emitter is that for the vertical emitters the direction of the current (I) is the same as of the photons, perpendicular to the mirrors (m), as can be seen in figure 1.5.

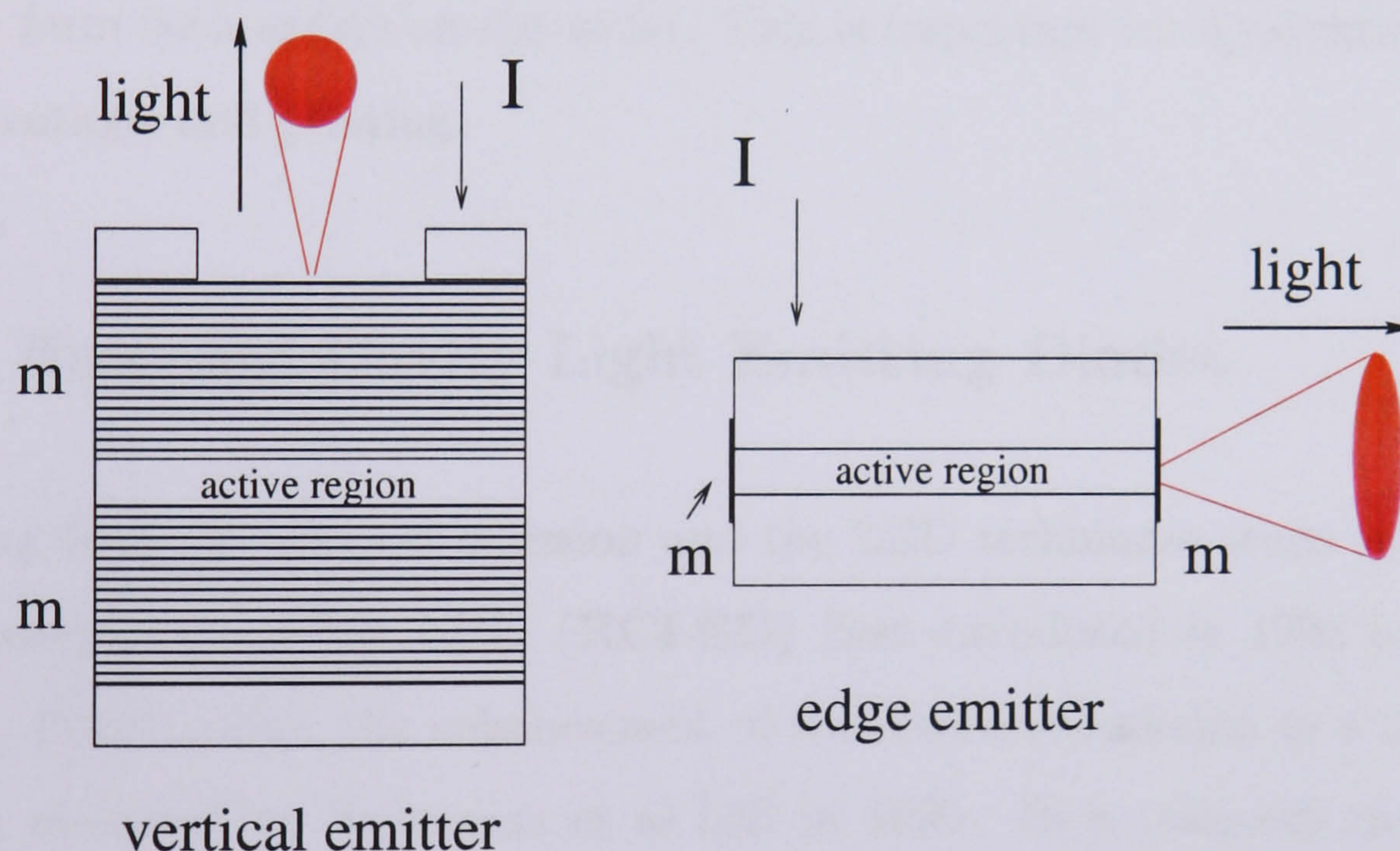

Figure 1.5: Comparison between a vertical- and an edge-emitting laser.

In a conventional edge-emitting laser the photons travel a distance equivalent to 1000s of wavelengths through the active gain medium. In contrast, for a vertical emitter the active region as seen by the photons is only very thin. Hence the reflectivity of the mirrors has to be at least 99.9% to enable multiple passes of the photons through the active region. The number of distributed Bragg reflector (DBR) pairs depends on the difference between the high and low refractive index. As this is low for 650nm devices, around 50 pairs of DBR pairs are needed to achieve a sufficiently high reflectivity. The growth of VCSELs though requires high precision.

It has been suggested that whilst a 1% error in the layer thickness would only lead to a shift of 0.5nm in the wavelength for an edge emitter, this could shift the wavelength up to 8.5nm for a VCSEL [22]. Due to much research in this field, the quality of growth and fabrication is being further developed and this disadvantage of VCSELs compared to edge emitters could soon be resolved.

Apart from the higher directional beam and higher (radial) output symmetry (as shown in figure 1.5) the main advantage over edge emitters is that VCSELs can be tested on the wafer before being cleaved and packaged. This is very cost efficient as poor quality wafers do not have to be fully processed. Hence time and money is saved. Consequently another advantage of VCSELs with respect to edge emitters is that VCSELs can easily be arranged in two dimensional arrays as they naturally form such arrays on the wafer. This is important for applications such as communications and printing.

1.2.3 Resonant Cavity Light Emitting Diodes

Combining both the vertical emission and the LED techniques leads to a new device the **resonant cavity LED (RCLED)** first introduced in 1992 by Schubert et al [23]. Prior to this, the enhancement of spontaneous emission in a microcavity had been observed by Yokoyama et al [24] in 1990. In a resonant cavity device the spontaneous emission is enhanced by putting the active region into a resonator. The advantages of RCLEDs over conventional LEDs include a more directional light output, higher brightness and a narrower output spectrum in the normal direction. The resonant cavity also reduces the radiative lifetime [25] and so RCLEDs can have higher modulation speeds than conventional LEDs. Moreover due to the higher spectral purity coupled into a fibre, the modal dispersion in an RCLED-fibre system will be lower than in an LED based one.

One of the disadvantages of VCSELs is that they have very temperature sensitive threshold currents. The absence of a threshold in an RCLED gives rise to a higher temperature stability compared with VCSELs. Thus, in the visible regime

(650nm, 570nm) RCLEDs become of most technological interest. Carrier leakage is particularly important in 650nm devices where a temperature dependent leakage current plays a larger role than in longer wavelength (for example 850nm) devices [26]. The light output of a GaInP-based 650nm devices for a fixed current not only decreases due to the broadening of the QW emission but also due to the increased amount of leakage. This effect is particularly pronounced in VCSELs where, for example, a 650nm VCSEL may not lase continuous wave (c.w.) at temperatures above 80°C, as the gain will not be high enough at the cavity wavelength. However, such a temperature induced de-tuning of λ_{CM} and λ_{QW} has less of an effect on the light output of an RCLED due to the absence of a threshold and a larger CM-QW-emission alignment tolerance. This is due to the wider cavity dip in RCLEDs compared to VCSELs and also their lower finesse that lets light leave the device at higher angles away from the main cavity mode. As the light output decreases with increasing temperature, great emphasis was put on the improvement of the temperature sensitivity of the devices. For even longer wavelengths ($> 1\mu$m), devices are also very temperature sensitive due to Auger recombination. Since new graded index POFs have become available RCLEDs are also becoming interesting in this wavelength range [13]. The speed at which RCLEDs can be modulated is much lower than for VCSELs. Nevertheless 622Mbps data transmission of 650nm RCLEDs have been demonstrated [27]. However, in a POF based communication system using step index (SI) guided plastic fibre, the modulation speed is actually limited by the modal dispersion of the fibre rather than by the source [28] due to the high modal dispersion of the fibre. By using SI-(step index) POF the higher speed that can be obtained by VCSELs is of no advantage. This is illustrated in figure 1.6 which shows typical modulation bandwidths of normal LEDs, RCLEDs and VCSELs together with the bandwidth of SI-POF as a function of distance.
As there is also a certain limit for the length of the fibre(approximately 50m) due to the high attenuation it can be seen from figure 1.6 that the RCLEDs seem the ideal partner for POF to achieve the best possible modulation bandwidth.

This therefore makes RCLEDs an attractive alternative to VCSELs. Other

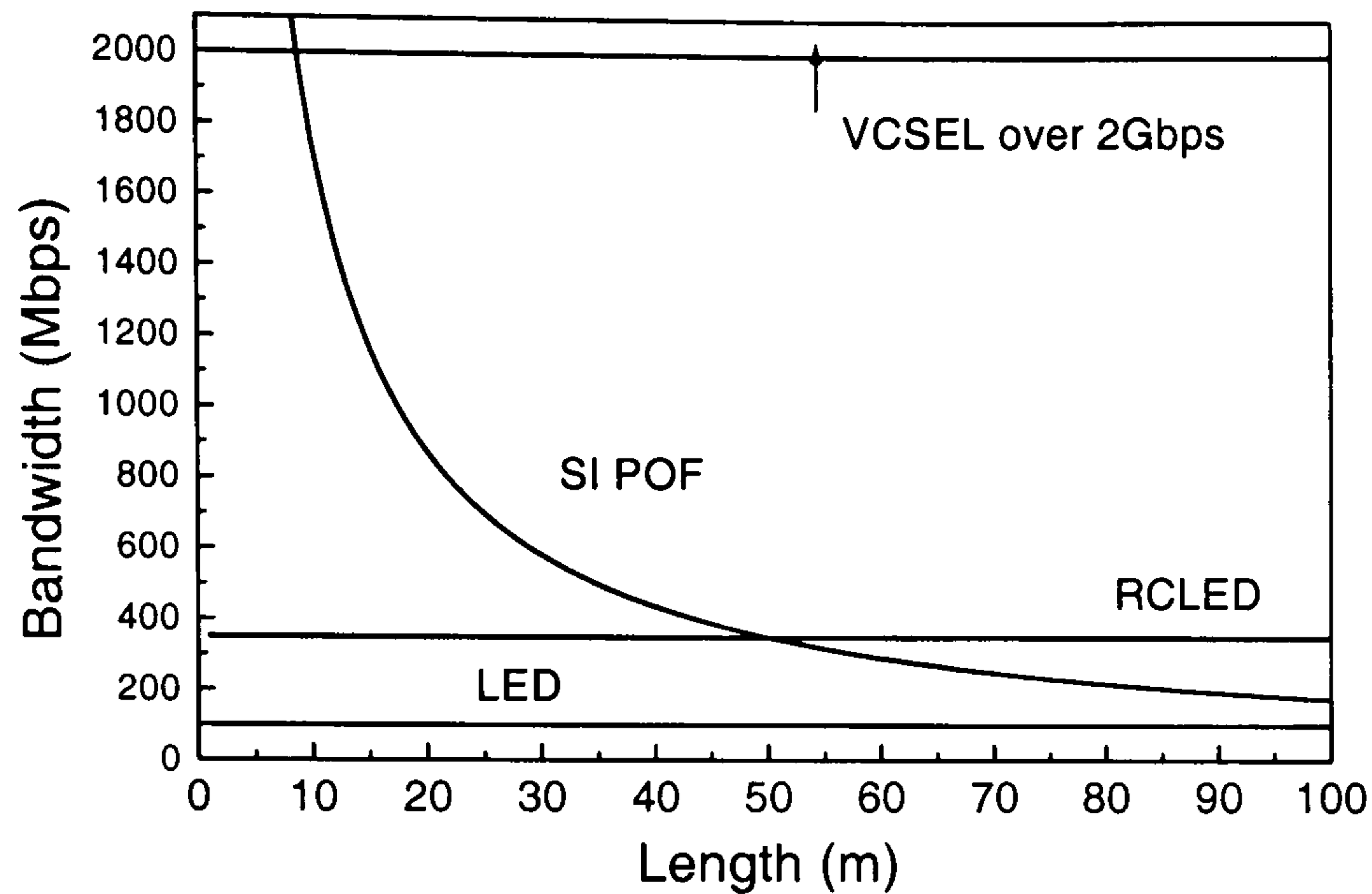

Figure 1.6: Comparison of modulation bandwidth of SI plastic fibre and three devices after [29].

advantage of RCLEDs over VCSELS are that they are also easier and cheaper to fabricate. As fewer layers have to be grown it takes less time and also leads to higher uniformity. RCLEDs are aslo much more eye safe.

1.2.3.1 Recent Achievements

Since RCLEDs were first proposed in 1992 the concept has aroused much interest. This is primarily as alternatives to lasers and conventional LEDs for various applications, especially at visible wavelengths, but also for resonant detectors [30]. The first RCLEDs developed [23] emitted around 850nm with a GaAs active region. In the last 10 years various wavelengths, mainly near-infrared and visible, have been achieved for RCLEDs. This was mainly triggered by the search for optical sources for use with different optical fibres.

The first red RCLED was reported as early as 1993 by Lott et al [31]. It had a peak emission wavelength of 670nm and a device diameter of 35μm. Its light output was somewhat low at 93μW. In 1997 Jalonen et al [32] increased the light output for a 660nm (80μm diameter) device to 1.1mW reporting a maximum external efficiency of 2%.

For infrared materials higher efficiencies had been reported earlier. In 1995

Blondelle et al [33] reported a maximum quantum efficiency, η_{eqe}^{max}, of 16% for a 940nm RCLED. For a 980nm device in 1999 Wierer et al [34] obtained an efficiency of 27%. The advances in device performance in the 900nm-1000nm region are due mainly to the very suitable material system as opposed to any specific application in this wavelength range. These advantages include the use of highly reflective gold mirrors, the transparent GaAs substrate and thus the use of high contrast $AlAs/GaAs$ or $GaAs/Al0_x$ DBRs. Benisty et al [35] showed that a larger difference between the refractive indices, Δn, of the DBR layer leads to a higher extraction efficiency. In addition since Δn is higher, fewer layer pairs are required to achieve the high reflectivity necessary. In 1999 Bockstaele et al [36] achieved a maximum external quantum efficiency, η_{eqe}^{max}, of 14.6% for 850nm RCLEDs and in 2000 Vilokkinen et al [37] showed $\eta_{eqe}^{max} = 14\%$ for 880nm devices. In the same year Depreter et al measured $\eta_{eqe}^{max} = 9\%$ for InP based 1.3μm RCLEDs [38].

Due to the fact that $GaAs$, and even $Al_xGa_{1-x}As$ with low aluminium content (low x) absorb visible light, the DBRs for 650nm devices are made using $AlAs/Al_{0.5}Ga_{0.5}As$ pairs. However their Δn is considerably lower than for longer wavelength devices where $AlAs/GaAs$ pairs can be used in the DBRs. Thus, relatively high efficiencies, albeit not as high as infrared devices have been achieved in the visible region only in the past three years due largely to the improvements in the growth quality.

In 1998 Streubel et al [39] achieved a maximum external quantum efficiency of 4.8% for a 660nm device (84μm diameter) and also showed that the devices could be modulated at speeds of up to 512Mbps after being coupled into 1m of POF [40]. Two years later in 2000, Gray et al [41] showed similar efficiencies of up to 6% for the more important wavelength of 650nm albeit for relatively large devices (400μm diameter). The high efficiencies of almost 10% obtained by two groups in 2001 [28] and [42], were due to the use of a coating of transparent epoxy over the devices to enhance the extraction efficiency. Wirth et al [42] achieved this high efficiency for both large area $(300 \times 300)\mu m^2$ and small aperture 80μm devices. Dumitrescu et al [28] achieved a bandwidth of 350MHz for a 40μm aperture device, which decreased

for bigger devices and for an 84μm device modulation speeds of up to 622Mbps were observed. Modak et al [43] showed in 2001 that efficiencies of 5% could also be achieved with a germanium substrate allowing the possibility of replacing the commonly used GaAs substrate by a possible cheaper alternative [44]. The latest achievements for red RCLEDs are summarised in table 1.2.

group, year and wavelength(nm)	η_{eqe}^{max} and max. light output	bandwidth/speed temp. coefficient (0-70°C)
Streubel [39], [40] (1998), 660nm	4.8% (84μm), 8.4mW (120mA)	250Mbps (30m Pof), 512Mbps (1m POF) 1.3%/°C (tuned) 0.7%/°C (de-tuned)
Gray [41] (2000), 650nm	6% (400μm) 1mW (13mA)	- -
Dumitrescu [28] (2001), 650nm	9.5% epoxy (84μm), 15mW (50mA, 500μm)	200MHz (84μm), 622Mbps 350MHz (40μm) 0.5-0.89%/°C for POF coupling [45]
Wirth [42] (2001), 650nm	9.6% epoxy (300×300)μm 12mW (100mA) 9.2% (80μm), 2.9mW (20mA)	- -
Modak [43] (2001), 640nm	5.2%, 8mW (100mA)	- -
Zarlink [46] (2002), 650nm	3.5% 2mW (30mA)	> 120MHz 0.7%/°C (fibre coupled)

Table 1.2: Recent Progress in red RCLEDs. **key:** η_{eqe}^{max}: maximum external quantum efficiency. temp. coefficient is a measure of the decrease of the light output with increasing temperature.

In order to achieve the high efficiencies mentioned in table 1.2, high currents had to be used. For commercial applications this is not desirable as the power consumption needs to be sufficiently low. Since 1999 red RCLEDs have become

commercially available. An example of the performance of devices from Zarlink Semiconductor (formerly Mitel) is also included in table 1.2 [46]. From the table it can be seen that, in order to achieve both high light output and also a high bandwidth, a compromise for the device size has to be found. Bigger devices have higher efficiencies but smaller devices show higher modulations bandwidths.

Part of the work for this thesis has been to find if this size dependence can be explained entirely through the difference in current density, or if any intrinsic size dependence plays a role. Another focus of this thesis as perhaps apparent from table 1.2 is the difference in the temperature sensitivity for devices with a de-tuning between the emission of the active region (often quantum well emission) and the cavity mode wavelength. The main aim and outline of this thesis shall be discussed in the next section.

1.3 Thesis aim and outline

The aim of this thesis is to understand how 650nm RCLEDs work, what their problems are and how they might be improved. The main points are to identify how certain parameters influence the device performance and how these can be optimised. This is not only to achieve higher light output but also higher coupling efficiencies into optical fibres, higher modulation bandwidths and a lower temperature sensitivity. These improvements for the devices will be discussed in particular with respect to their applications. In the following, the outline of the thesis shall briefly be discussed.

In **chapter 2** the basic theory of LEDs and in particular of resonant cavity LEDs is discussed. The structural details of RCLEDs and the experimental techniques to characterise the devices are also introduced.

As one important feature of RCLEDs is the peak of the QW emission (λ_{QW}), the techniques for determining it are introduced in **chapter 3**. Here the theory of edge electroluminescence and photo-modulated reflectance (PR) and associated

analysing techniques of these measurements are discussed together with the results.

The other important feature of an RCLED is the cavity mode wavelength (λ_{CM}). This can be extracted from measurements or simulations of the device reflectivity. The theory of the reflectivity of a multilayer structure, results from reflectivity measurements and simulations will be shown in **chapter 4**. The possibility of fitting R spectra with theoretical calculations is also introduced and results of these fits are discussed. A newly developed technique of measuring R directly on a device will also be described in that chapter followed by the results of these measurements. Measuring λ_{QW} with PR and the λ_{CM} on individual devices helps to determine the critical CM-QW de-tuning.

This is followed by three chapters of results of device measurements. In **chapter 5**, the effect of CM-QW de-tuning on the device performance is discussed. Electroluminescence spectra and light-current characteristics particularly for different temperatures are shown. The reasons for the temperature sensitivity, namely carrier leakage and self-heating are discussed. It shall be shown that the de-tuning of the devices actually helps to make the devices less temperature sensitive if a 30° collection angle is assumed (as in POF).

In **chapter 6** the influence of top reflectivity and aperture size on the device performance are discussed. It will be shown that de-tuning has a stronger influence on the temperature sensitivity than the top DBR reflectivity. The size dependence of the self-heating leads to a simple model of the heating effects present in these devices.

In the final results chapter (**chapter 7**) device characteristics important for their applications are investigated. This consists of describing the coupling into and the transmission along plastic optical fibre and also measurements of the modulation bandwidth. With a simple model the carrier density and the ratio of the radiative current with respect to the total current is extracted from modulation bandwidth measurements.

The thesis concludes with **chapter 8** which is a summary of what has been achieved and an outlook towards the future.

Chapter 2

Resonant cavity light-emitting diodes: Background

This chapter deals with the general principles of RCLEDs and gives a brief introduction into their fabrication and the experimental details for their characterisation.

2.1 Theory of Light Emitting Diodes

A conventional light emitting diode (LED) is a direct bandgap semiconductor p-n junction operated under forward bias as illustrated in figure 2.1.

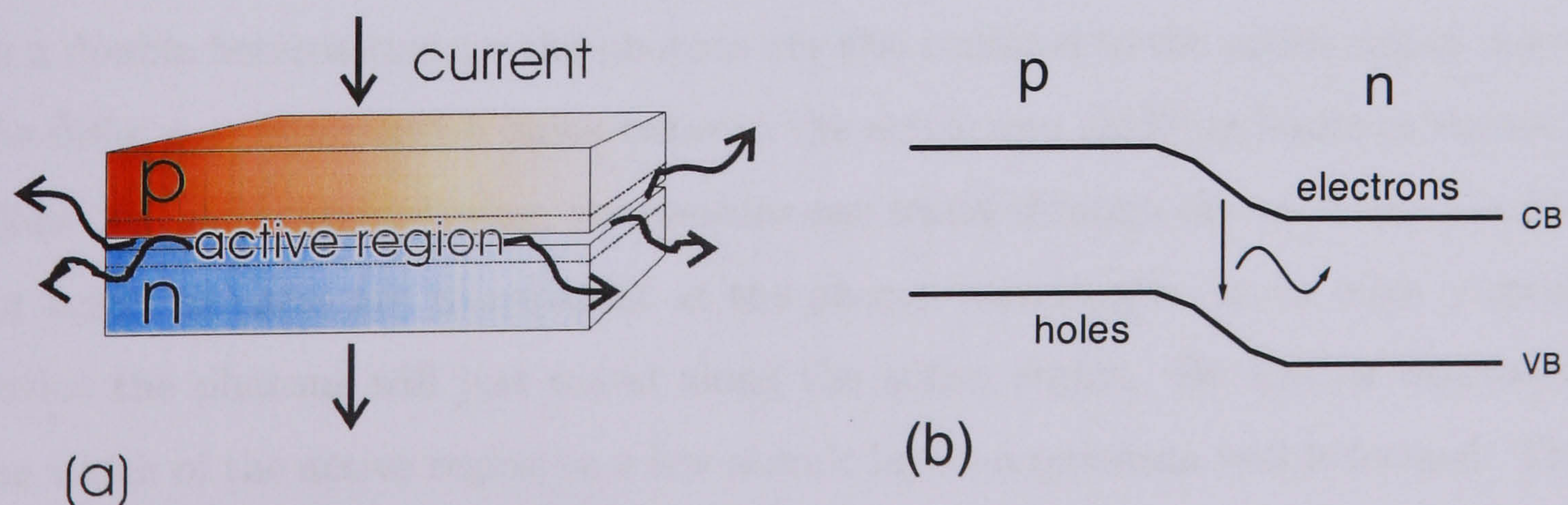

Figure 2.1: (a) Light emitting diode. (b) Band alignment for an LED (pn-junction) under forward bias.

The wavelength of the light emitted is largely determined by the bandgap of the active semiconductor material. For example, in the case of the much used GaAs, this is around 870nm which lies in the near infrared.

One of the major problems with these first "homojunction" LEDs was the high probability of the generated photons being reabsorbed and the difficulty to confine the electrons and holes to the same region. This was overcome by reducing the width of the active region and sandwiching it between two layers of another semiconductor material with a wider bandgap. This invention of the double heterostructure [47] for which its inventors were finally awarded the Nobel prize in the year 2000 was also very important in the development of semiconductor lasers. By placing the active region between layers of a higher band gap material the injected carriers are confined to the active region as it contains the lowest energy states. The principle of a double heterostructure under forward bias is shown in figure 2.2.

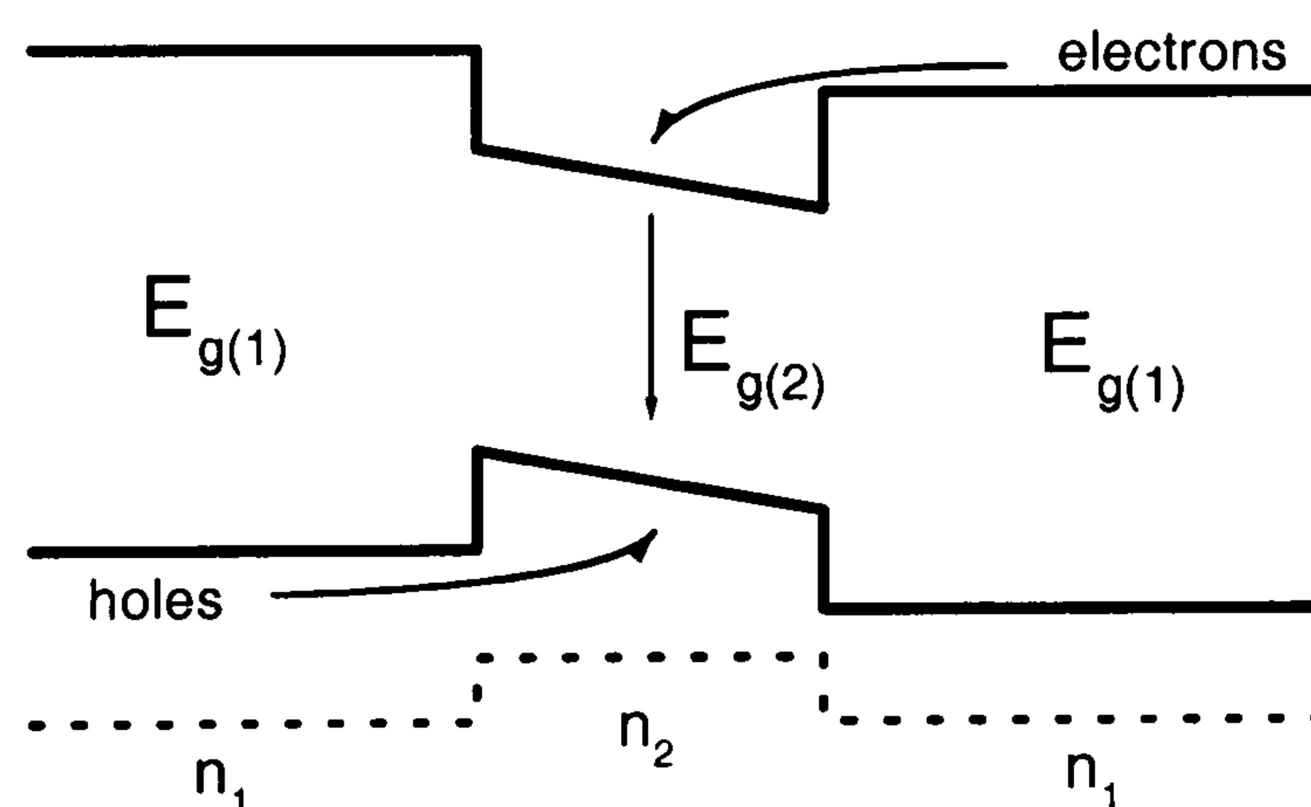

Figure 2.2: Double heterojunction under forward bias together with the refractive index (n) profile.

In a double heterostructure the photons are also confined to the active region due to the difference in refractive index between the active and cladding layers as shown in figure 2.2. After recombining, the photons can travel through the outer semiconductor layers as these are transparent at the photon wavelength. In an edge emitting device the photons will just travel along the active region. By further decreasing the width of the active region to a few atomic layers a quantum well is formed. This concept is far more important for lasers than for LEDs. It has the effect of reducing the volume that is electrically pumped and hence the threshold current density (the

current density at which the lasing action will start) will also be reduced. A final advantage of QWs is that a variety of wavelengths can be engineered with one active material. This can be achieved by changing the composition/ strain of the QWs, and/or the QW width since decreasing the width increases the confinement energy, and thus decreases the ground state transition wavelength.

In general, the main problem of an LED is not so much the *internal* quantum efficiency η_{in} (how many photons are produced per electron injected), as this can be close to unity due to the aformentioned confinement plus excellent growth that minimises defects. It is, rather, the *external* quantum efficiency η_{eqe} which is important. This is basically a measure of how much optical power is produced compared with the electrical power input. Apart from the problem of reabsorption, there are other reasons which prevent a photon produced in the active region from leaving the device. η_{eqe} is thus the product of the internal efficiency and the extraction efficiency, η_{extr}:

$$\eta_{eqe} = \eta_{in}\eta_{extr}. \tag{2.1}$$

η_{extr} is defined as the ratio of the light emitted into a cone of an angle smaller than or equal to the critical angle (of total internal reflection) to the total light produced, i.e. the ratio of the light that leaves the device to the total light produced. The extraction efficiency depends on the critical angle

$$\theta_c = arcsin\frac{n_0}{n}, \tag{2.2}$$

and thus also on n_0 and n, which are the outside and device refractive indices respectively. An illustration of the principal of total internal reflection showing the critical angle θ_c can be seen in figure 2.3.

Assuming the outside material to be air and therefore n_0=1, the extraction efficiency of an LED can be evaluated by calculating the fraction of light that is emitted within a cone restricted by the critical angle, compared with the total (in the whole solid angle) emitted light. This leads to an extraction efficiency of $\propto \frac{1}{4n^2}$. For example for n=3.4 [1], (and thus a critical angle of 17°) η_{extr} would only be $\sim 2\%$ [35].

[1] 3.4 is the refractive index of AlGaInP at 650nm as used here

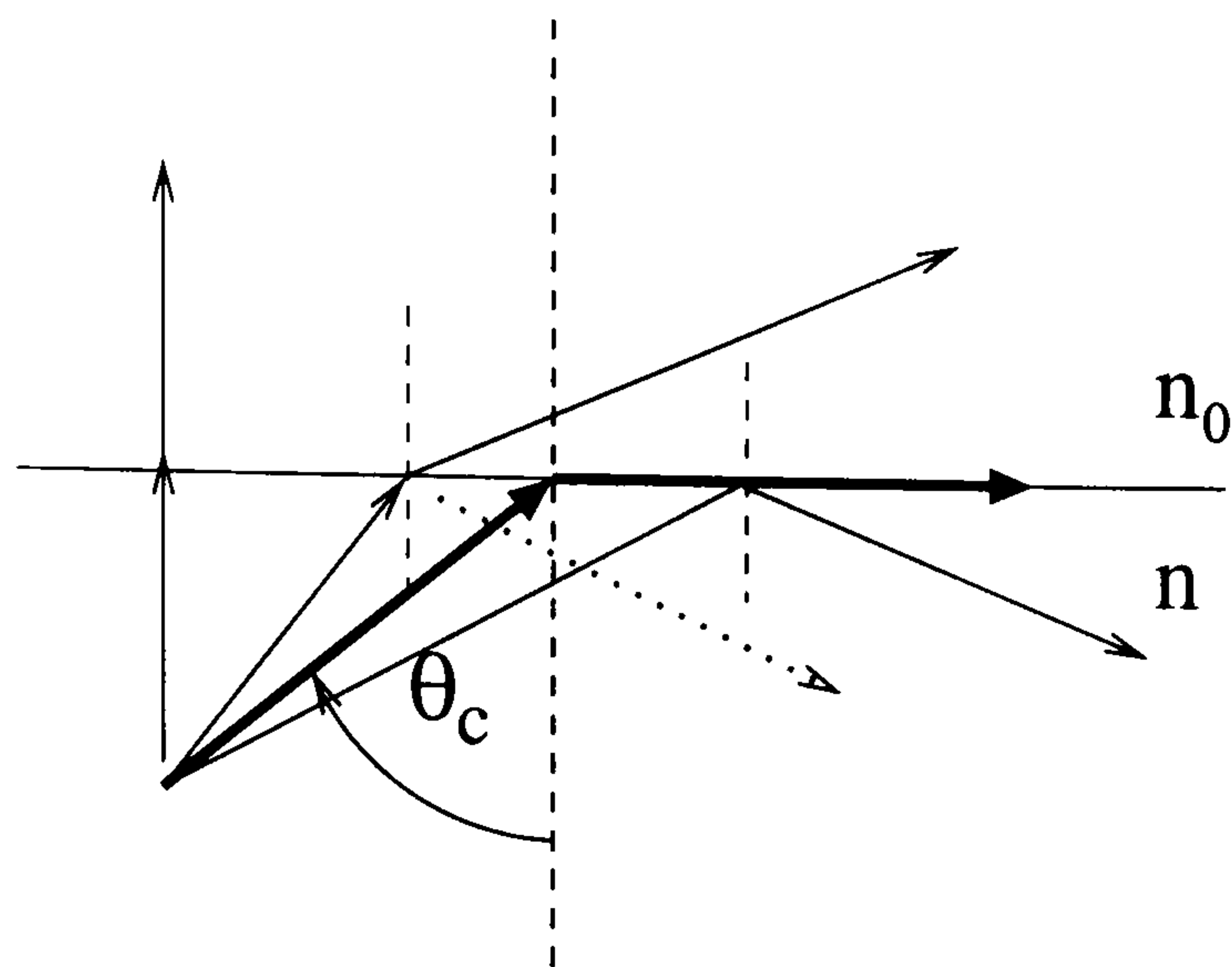

Figure 2.3: Illustration of the critical angle for total internal reflection where $n > n_0$.

The principle of total internal reflection is just a special case of the reflection at a boundary that can be derived from Fresnel's equations. For a single interface and s-polarisation (perpendicular), the exact value of R for any angle can be calculated:

$$R = \left(\frac{n_0 \; cos\theta_0 - n \; cos\theta}{n_0 \; cos\theta_0 + n \; cos\theta} \right)^2 , \tag{2.3}$$

where n and θ are the refractive index and the angle in the incident layer and n_0 and θ_0 the properties of the second layer corresponding to air for one device air interface. Thus, in addition to the fact that a fraction of that light reaching the device-outside interface at a particular angle gets reflected, a certain percentage of light will always get reflected at an internal interface. For normal incidence ($\theta = 0$) and assuming again n_0=1 and n=3.4 this leads to 30% internal reflection. For a more accurate description equation 2.3 would have to be integrated over all possible angles. How can the extraction efficiency of an LED be increased ?

One way, often used in conventional LEDs, is to surround the LED by a dielectric. As this has a higher refractive index ($\sim$ 1.6) than air, more light will emerge from the device due to the fact that less light will get reflected at the device-dielectric and the dielectric-air interfaces. In spite of the introduction of another interface that leads to further possible reflection, the overall internal reflection will be reduced as can be calculated using equation 2.3. More importantly the critical angle will be increased and thus the extraction efficiency correspondingly increases.

Another possibility is to make use of the reabsorption of photons, a process called photon recycling. High efficiencies of up to 22% for devices featuring photon recycling have only been reported for cryogenic (77K) temperatures [48].

The concept of a non-resonant LED introduces a mirror on the bottom of the device which reflects back all the photons that did not leave the device when they first got to the top interface [49]. With the device surface being textured and so achieving strong surface scattering external efficiencies of 30% are achieved [49]. By introducing a second mirror on the top it is possible to create a resonant LED as will be discussed in the next section.

2.2 Resonant Cavity LEDs

By surrounding the active region of an LED with top and bottom mirrors a cavity is produced. If the cavity optical path length L is a half-integer multiple of the wavelength of the emission peak we have a resonant cavity (RC). Here $L = l\bar{n}$, where l is the actual cavity length and $\bar{n}$ is the average reflective index of the structure comprising the cavity. In most of the studied cases L was approximately equal to the QW emission wavelength (1λ) as shown in figure 2.4.

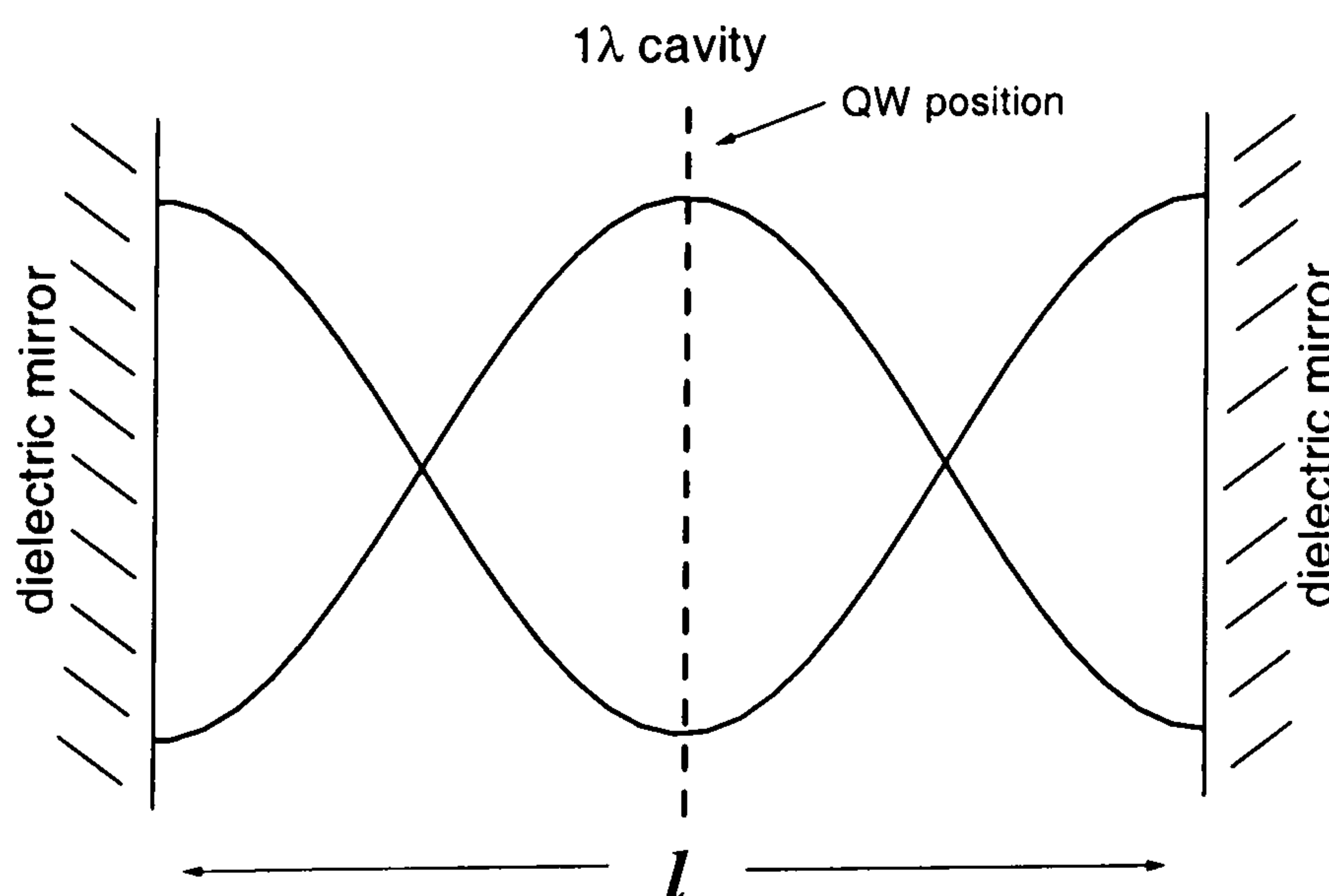

Figure 2.4: Illustration of the optical field in a 1λ cavity. The QW is placed at the antinode of the field.

For example, for emission at 650nm and a refractive index for the AlGaInP as used here of n=3.4, the actual cavity length (thickness), l, is about 190nm. Due to this

small dimension, RCLEDs are often also referred to as microcavity LEDs (MCLED).

If the RCLED is a top emitting device the reflectance of the bottom mirror is usually chosen to be as high as possible (about 99%) to ensure that few of the photons produced are wasted by leaking into the substrate. The top mirror reflectivity then has to be optimised to achieve the highest light output [50] i.e. it has to be large enough in order for the cavity to play an important role in the light output but should not be too large as otherwise little light will leave the device from the top. The cavity also strongly modifies the light output of the LED. If the QW (or QWs) are placed at an anti-node of the cavity optical field (see figure 2.4), the amount of spontaneous emission that is coupled into the CM (and thus at the cavity wavelength) and into the forward (normal incidence) direction is greatly enhanced [51]. The external quantum efficiency can be enhanced for a RCLED by a factor of two to four compared with a normal LED, depending on the position of the emitter in the cavity [35]. It has been shown that this position within the cavity is crucial as the spontaneous emission can also be inhibited by the presence of the cavity [52].

Purcell was first to study the particular influence of a cavity on the spontaneous emission in 1946 [53] for nuclear magnetic moment transitions at radio frequencies. According to Purcell the spontaneous emission is enhanced by a factor $f = 3Q\lambda^3/4\pi^2 V$ where $Q = \lambda/\Delta\lambda$ is the quality factor of the circuit or resonator, V its volume and λ the resonating wavelength. For a microcavity $Q \propto F$, where the finesse, F, is given by

$$F = \frac{\pi \sqrt[4]{R_1 R_2}}{1 - R_1 R_2}, \tag{2.4}$$

where R_1 and R_2 are the reflectivities of the mirrors confining the cavity. For infrared emission in semiconductors this enhancement was demonstrated in 1990 [54]. The change in the spontaneous emission of a dipole within a cavity becomes clearer when it is considered that this is not an intrinsic property of the dipole itself but is always a result of the dipole coupling with the surrounding modes of the electromagnetic field [55]. The total spontaneous emission rate (W_{spont}) is given by

$$W_{spont} = \int_0^\infty W^l_{spont}\, \rho(\nu_l)\, d\nu_l, \tag{2.5}$$

where W^l_{spont} is the spontaneous emission rate into the optical mode l and $\rho(\nu_l)$ the optical mode density of that mode and ν_l the mode frequency [56]. If there is no mode (i.e. the mode density equals zero) into which a dipole can emit then it clearly cannot do so and thus the dipole would stay in its excited state. Hence, by changing the optical mode density, the spontaneous emission can be controlled. If, for example, by creating a very small cavity only one mode was available for the emission it should be possible, in theory, to achieve a thresholdless laser as all the power is coupled into the only allowed mode [57].

One way of illustrating the possible modes in a cavity is by showing the modes in k-space as seen in figure 2.5 [58]. In k-space the QW emission is represented as a sphere with the radius $k_{QW} = 2\pi/\lambda_{QW}$ if the QW emission is isotropic. The modes allowed by the cavity of length l_z are planes in the **r** direction (as the cavity is unbound in that direction) intersecting the k_z-axis at $k_z = n\pi/l_z$ for $n = \pm1, \pm2, \pm3, ..$ corresponding to the order of the cavity i.e. $\lambda/2$, λ or $3\lambda/2$-cavities. As most of the structures investigated here were λ-cavities only the planes corresponding to the second order are drawn in figure 2.5.

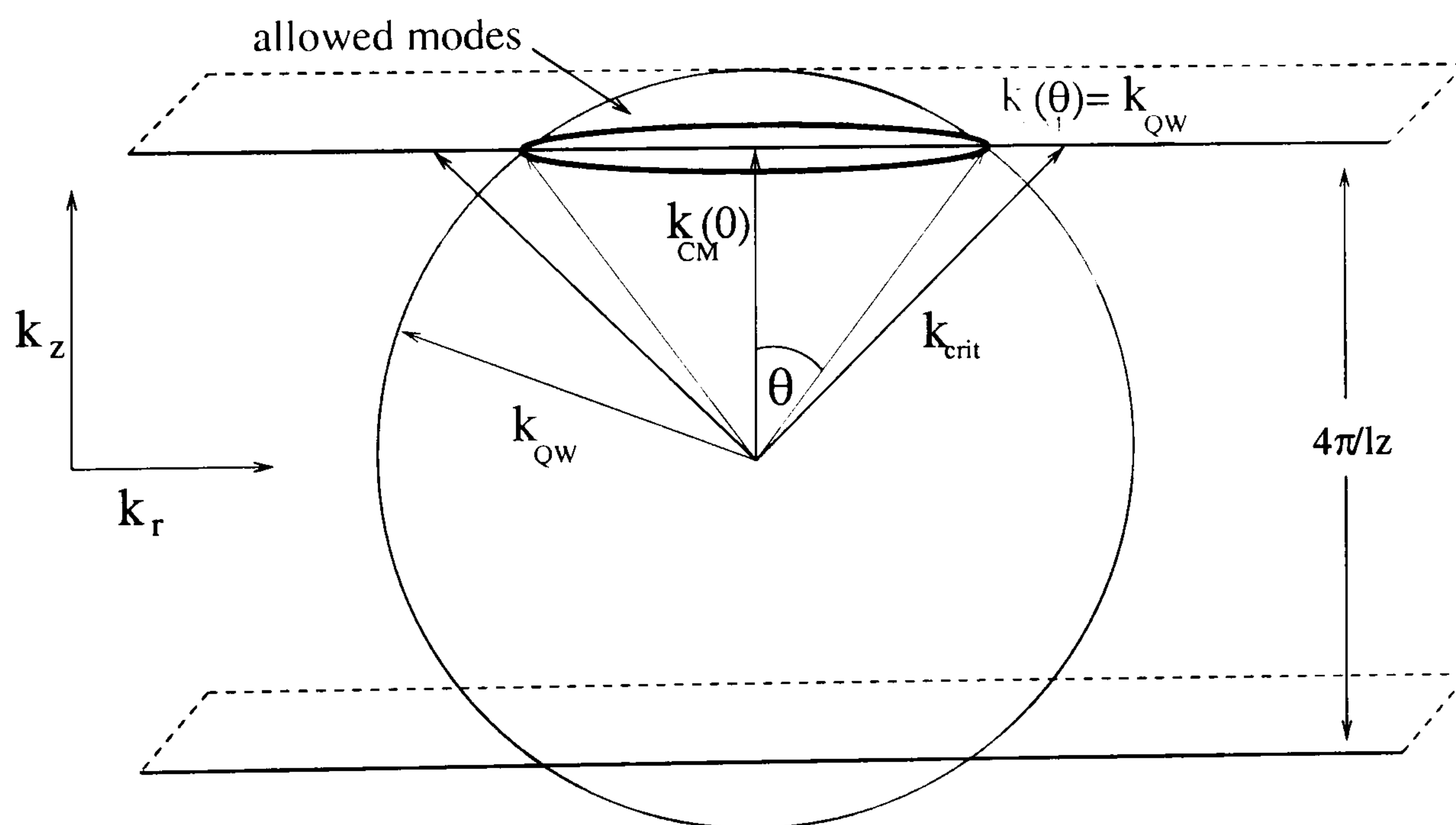

Figure 2.5: Modes in k-space: The surface of the sphere with radius k_{QW} represents the unperturbed QW peak emission. k_{crit} is the critical angle that defines the light output cone for any LED device.

The allowed cavity modes are represented by the k-vectors that start within the centre of the cavity where the QW is situated and end at the intersection with the

plane defining the cavity mode. The actual output will also be restricted by the critical angle. The mode density is now defined as the ring that marks the crossing of the QW emission sphere with the cavity planes, marked as allowed modes in figure 2.5. If the QW emission was very narrow, consisting of only one wavelength, the light output would consist of only this ring. Since the QW emission is fairly broad it can be represented by many spheres with different radii corresponding to the range of wavelengths (for clarity only one sphere is shown in figure 2.5). Hence different wavelengths can leave the device at different angles. For higher k values the intersection with the cavity will be at higher angles. As a higher k corresponds to a shorter wavelength it can be seen that light at shorter wavelengths can leave the device at higher angles as seen from the representation in k-space in figure 2.5. This is an important point for understanding the light output of these devices. Another important fact that can be derived from figure 2.5 is that light of wavelengths longer than λ_{CM} cannot leave the device, as there would be no intersection of a circle of radius $2\pi/\lambda$ for $\lambda > \lambda_{CM}$ with the cavity plane. As the cavity mode has a finite width the actual "cut-off" frequency lies at λ_{CM} + half the width of the CM dip. The overall light output will depend on the relative positions of the QW emission and the cavity mode.

The two important features of an RCLED are therefore the QW transition wavelength (λ_{QW}) in the active region and the length of the cavity l, which results in a certain cavity mode wavelength (λ_{CM}). The aim is for both of these wavelengths to be approximately the same at the device operating temperature, and that;

$$\lambda_{QW} \sim \lambda_{CM} \sim \lambda_{Bragg}, \tag{2.6}$$

where λ_{Bragg} is defined as the centre wavelength of the reflectance stopband (which will be discussed in more detail in chapter 4) or the wavelength of the Bragg reflector. It marks the centre of the region of the high reflectivity within the device and thus the QW emission is aimed to coincide with it. It is therefore important to find techniques by which both λ_{QW} and λ_{CM} (and also λ_{Bragg}) can be found to monitor the quality of the growth.

2.3 De-tuning

One of the major challenges for optoelectronic devices, and in particular for vertical emitters is to achieve stable operation over a wide temperature range. It has been shown [59] that a slight mismatch in other words a de-tuning between the two crucial wavelengths, λ_{QW} and λ_{CM} actually improves the temperature sensitivity [60],[61] and also may increase the total light output of RCLEDs [41],[62]. The sign of the de-tuning ($\Delta\lambda$) is defined here as,

$$\Delta\lambda = \lambda_{CM} - \lambda_{QW}, \tag{2.7}$$

so that a positive de-tuning refers to a device where the QW emission peak is blue shifted with respect to the CM at normal incidence. As both wavelengths move with temperature at different rates (the QW emission moves faster), the amount and possibly the sign of the de-tuning will change with increasing/decreasing temperature. However, for a device that is negatively de-tuned ($\lambda_{CM} < \lambda_{CM}$ at normal incidence), or becomes negatively de-tuned with increasing temperature, the light output is drastically decreased. This is because only light at shorter wavelengths than the cavity mode can leave the device at higher angles (as can be seen in figure 2.5) as will be discussed in more detail in chapters 3 and 5.

2.4 Structures, growth and fabrication

The active region of the RCLEDs investigated in this thesis consists of two $In_{0.51}Ga_{0.49}P$ QWs between AlInGaP barriers. Different structures with different QW specifications (width, composition, strain) have been investigated. Full details of the nominal structures can be found in the appendix. To provide the required enhancement of the spontaneous emission, the active region is surrounded by distributed Bragg reflectors (DBRs). The DBRs are made of alternate layers of low-index (n_l) and high-index materials (n_h), which can be semiconductors or

dielectrics. In the present case the DBRs consist of AlAs/$Al_{0.5}Ga_{0.5}As$ pairs. The total maximum reflectivity depends on the difference between the low (n_{lo}) and high (n_{hi}) refractive indices of the DBRs and is given by

$$R = \left(\frac{1 - \frac{n_s}{n_0}\left(\frac{n_{lo}}{n_{hi}}\right)^{2p}}{1 + \frac{n_s}{n_0}\left(\frac{n_{lo}}{n_{hi}}\right)^{2p}} \right)^2, \qquad (2.8)$$

where n_0 and n_s are the refractive indices of the incident medium and the substrate, respectively and p is the number of the layer pairs [63], [35]. From this equation it can be seen that the smaller the difference between n_{lo} and n_{hi}, the more pairs have to be added to achieve the same maximum reflectivity compared with layers with a greater refractive index contrast.

Due to the relatively small difference in the refractive indices (Δn) between AlAs and $Al_{0.5}Ga_{0.5}As$, a large number of DBR pairs is needed to achieve the required high reflectivity. The red RCLEDs investigated here have 8, 11 or 14 pairs for the top and 32 or 34 pairs for the bottom mirrors, compared with typically 34 and 54 periods for top and bottom mirrors respectively in a red VCSEL. To confine the current, apertures can be created by ion implantation or oxide confinement. The devices discussed here utilise H^+ implantation to form the current aperture. A schematic structure of an RCLED device can be seen in figure 2.6.

Parameters that can be varied in the structure are the de-tuning between the QW emission and the cavity mode wavelength, the number of top DBRs and thus the reflectivity, the size of the aperture and the number and emission wavelengths of the QWs. In this work the de-tuning was altered by only varying the cavity mode between devices while keeping the QW emission wavelength constant. The results for these devices will be discussed in chapter 5. The top reflectivity was changed by varying the number of top DBRs between 8, 11 and 14 and the results for these devices will be the subject of chapter 6. Six different aperture sizes (25μm, 50μm, 70μm, 100μm, 150μm and 200μm) were available to investigate the size dependence. The aim of all these variations was to find less temperature sensitive and more efficient devices.

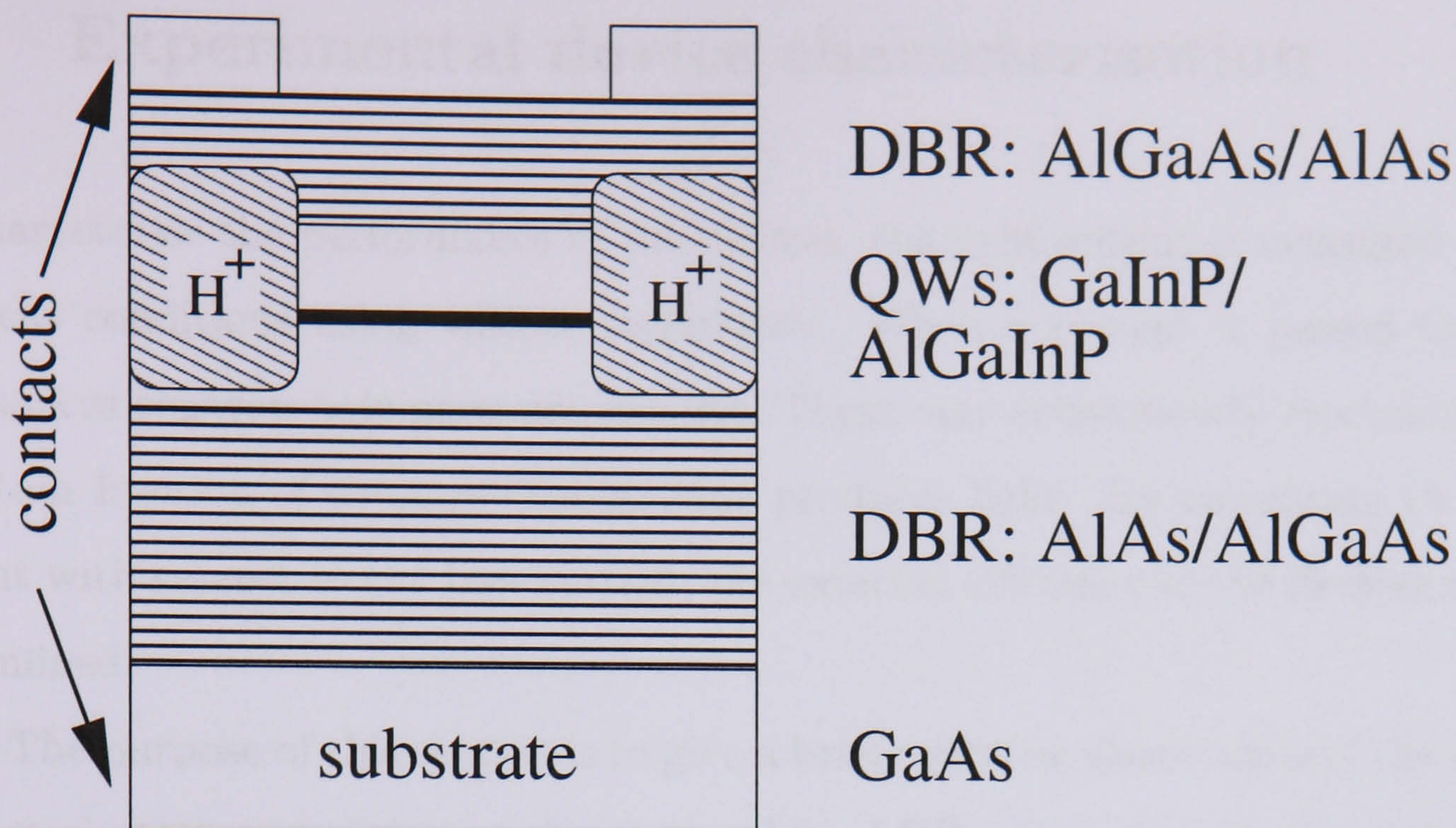

Figure 2.6: Schematic structure of an RCLED device consisting of substrate, top and bottom mirrors (DBRs), active region with a QW and two sets of contacts. The proton implanted regions and the top contacts confine the current to certain areas and leave different size apertures for the light output.

The successful growth of RCLED wafers has been reported using both MBE (molecular beam epitaxy) and MOVPE (metal organic vapour phase epitaxy) techniques [32],[42]. To define the current and light output aperture different masks were used. The diameter of the masks for the implant (for current confinement) were 10μm bigger than the aforementioned (light output) aperture sizes. After the metallisation of the top and bottom of the device to create the contacts the device can be tested on a probe station (details in chapter 4). The last step in the fabrication process is bonding the device onto a TO-header as shown in figure 2.7 .

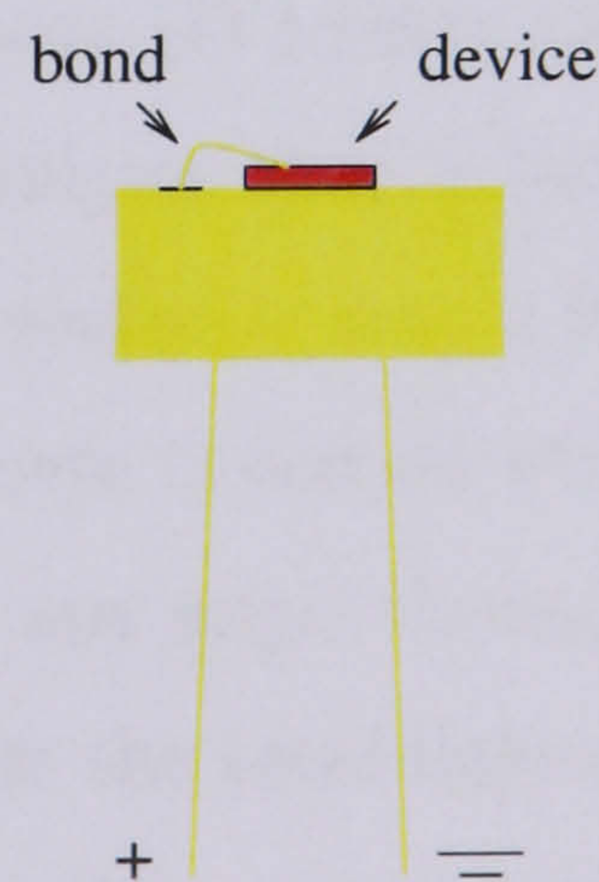

Figure 2.7: Device mounted and bonded onto a TO-header

2.5 Experimental device characterisation

To characterise the performance of the devices, the light output is measured under different conditions using various techniques. When a current is passed through the devices electron-hole pairs are created. These may subsequently recombine and a certain fraction of these recombinations produces light. By measuring the light output with respect to the bias current, the external efficiency of the devices can be determined.

The purpose of this section is to give a brief overview about some of the device characterisation techniques used in general for LEDs, focussing on the techniques used in this thesis. Details of the set-ups will be discussed together with the device results in chapters 5, 6 and 7. A generalised sketch of possible experiments for the device measurements is shown in figure 2.8.

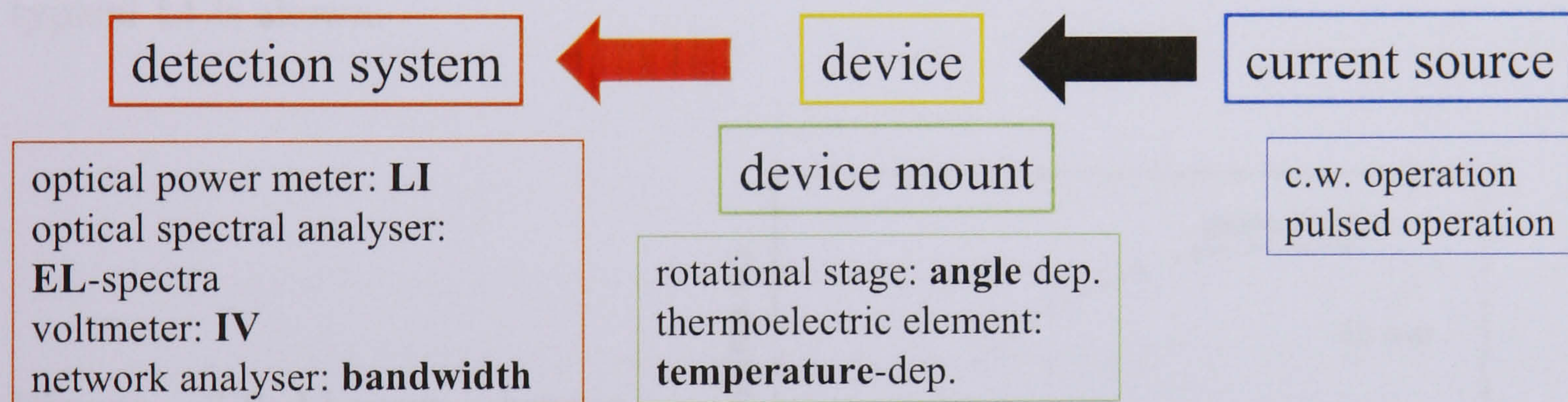

Figure 2.8: General set-ups for device measurements.

The device under investigation is placed on a mount connected to a current source. By connecting a voltmeter to the circuit a current voltage (IV) curve can be measured. For all other device characteristics, the light output that is generated by the bias current is either focussed onto a broad area detector or into a fibre or one port of an integrating sphere. The inside of such a sphere is coated with a highly reflective coating so that light that enters the sphere at any angle through one port is reflected to reach the second port of the sphere so that the total light output can be measured. The light can be analysed spectrally using either an optical spectrum analyser (OSA) or other spectrometer.

The first test of a fully processed device is to measure the voltage across the device as a function of bias current. These are the so called current voltage characteristics or IVs. From these the relative series resistance of different devices can be compared. If it is very high this can indicate problems that may have occurred during fabrication for example at the bonding stage, but can also indicate poor contacts due to contamination or inadequate doping.

To characterise the light output two main measurement principles were used: light-current characteristics, LI, and electroluminescence (EL) spectra. Various setups have been used to measure LIs and spectra under variable conditions that will be explained together with the results in chapters 5, 6 and 7. In the following only the basic principles of these two measurements are discussed. In the LI characteristics two main features are observed, the maximum light output and at which current this occurs i.e. at which current the device thermally rolls over. In figure 2.9 a typical LI is shown.

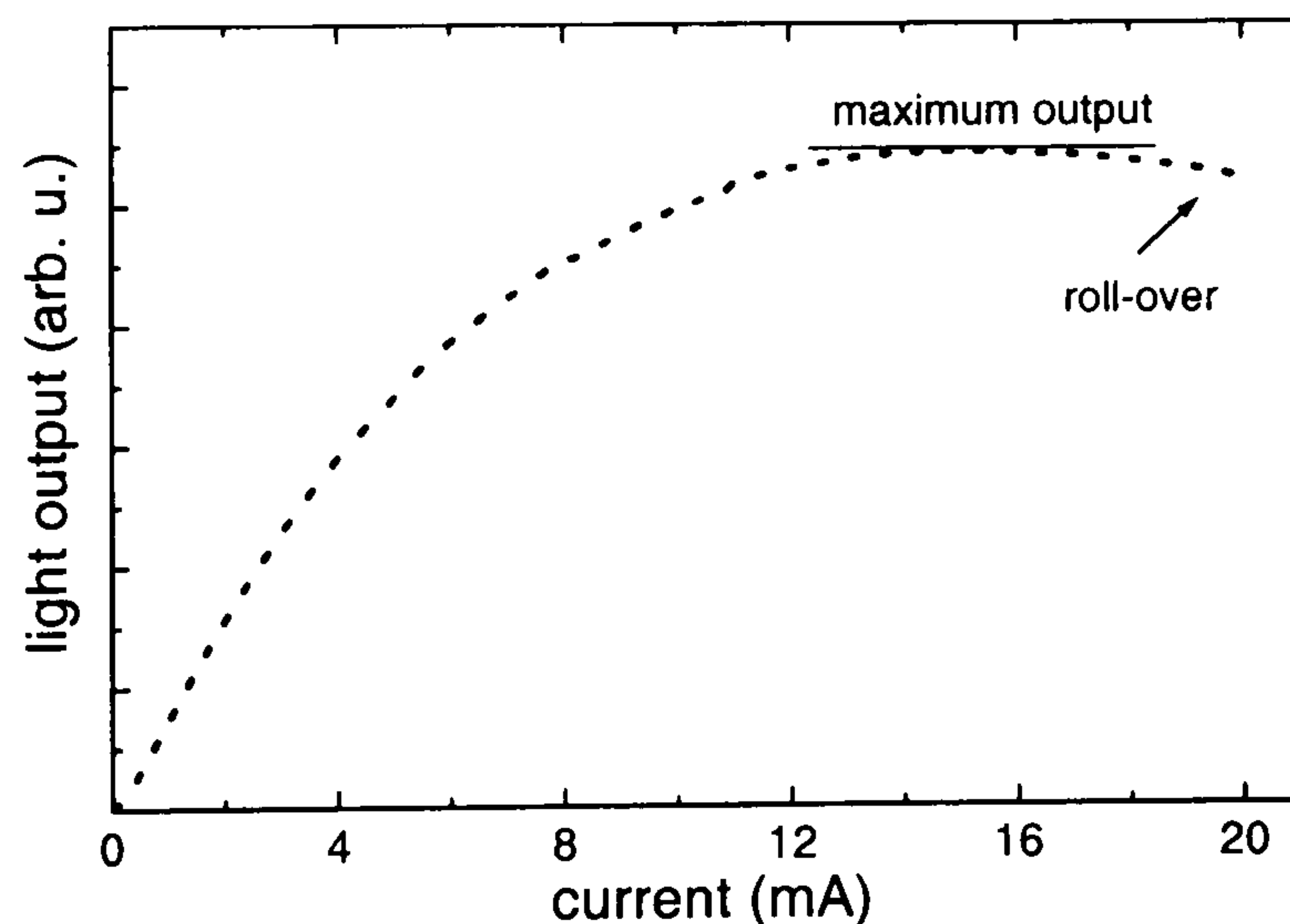

Figure 2.9: LI-curve showing thermal roll-over.

The measurements can be performed either under continuous wave (c.w.) or pulsed operation to investigate the self-heating of the devices. With the light-current characteristics the spectrally integrated light output is measured. Measuring the light output under electrical bias is called electroluminescence (EL). This can also be spectrally resolved to create an EL spectrum. Here the output of the electrically pumped device (or sometimes even the wafer) is analysed in a spectrometer or optical spectral analyser (OSA). A typical spectrum can be seen in figure 2.10.

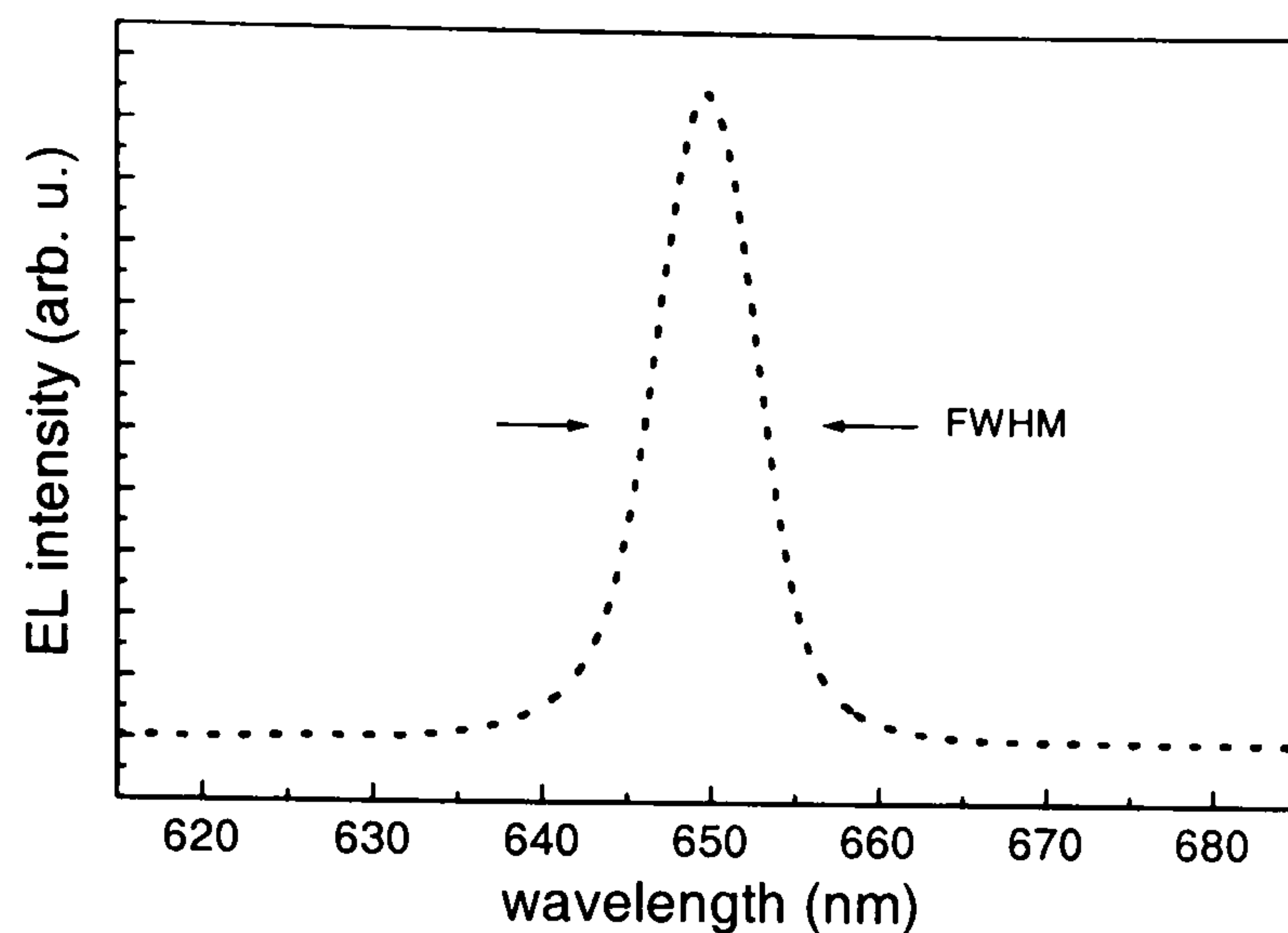

Figure 2.10: EL spectra for a 650nm RCLED. The peak occurs at 649.6nm and the FWHM is 7.2nm.

Measuring the spectra not only yields information about the exact wavelength position of the light output but also about the spectral width (full width at half maximum: FWHM) and a possible shift with increasing temperature. Both the spectrally resolved and the spectrally integrated light output can be measured as a function of the emission angle to create a far field pattern. This can be performed by mounting the device on a rotation stage.

Since 650nm RCLEDs will be used in short distance plastic optical fibre links more than just the intrinsic properties of the devices should be investigated. Thus coupling into these fibres and transmission along them shall be considered. Again both LIs and EL spectra are measured before and after the light is passed through POF to find the coupling efficiency and the spectral dependence of the coupling. The modulation bandwidth that determines how fast the devices can be modulated is also of great importance. This is measured using a network analyser. These experiments will be explained in more detail in chapter 7.

Chapter 3

Photo-modulated Reflectance and Edge Electroluminescence

3.1 Introduction

The wavelength of the light emitted by the RCLED is determined by the quantum well (QW) transition energies and the cavity mode (CM) wavelength. It is therefore important to know the QW transition wavelength to determine the quality of the wafer or to select an optimum area of the wafer to process into devices. As the actual device fabrication takes considerable time money, it is very important to know the wavelength of both the QW (λ_{QW}) and the CM wavelength (λ_{CM}) before starting the processing of devices to check if they meet the specifications (see equation 2.6 in the previous chapter). This chapter will deal with the experimental methods used to find λ_{QW}.

Due to the modulation by the Bragg mirror reflectivity the peak of the QW emission cannot be measured with conventional, top emission room temperature photoluminescence (PL) or electroluminescence experiments. Any emission from the top of the wafer will yield spectra distorted by the Bragg mirror reflectivity and will generally show a peak in the spectrum at the CM wavelength. To overcome

this, the PL is often measured before the top DBR pairs are grown. This leads to two problems. Firstly, if the sample has bottom DBRs, the PL can still be influenced by reflections from these and will not show the accurate QW emission peak. Secondly, if the sample is only a PL test sample (without DBRs) the growers cannot be sure that a subsequently grown full device structure will have exactly the same QW emission. It is therefore essential to find techniques that can measure the QW emission of a full RCLED wafer structure.

This chapter will introduce two of these techniques, namely edge electroluminescence and photo-modulated reflectance. After describing the background theory and the experimental set-ups of these methods the results for various sets of wafers are presented and compared.

3.2 Edge Electroluminescence

One method to determine λ_{QW} is the measurement of the edge electroluminescence (EL). The EL that comes out at the side is relatively unaffected by the mirrors and thus shows the QW emission without the influence of the mirrors. To clarify the terms of "front" and "edge" emission a diagram is shown in figure 3.1.

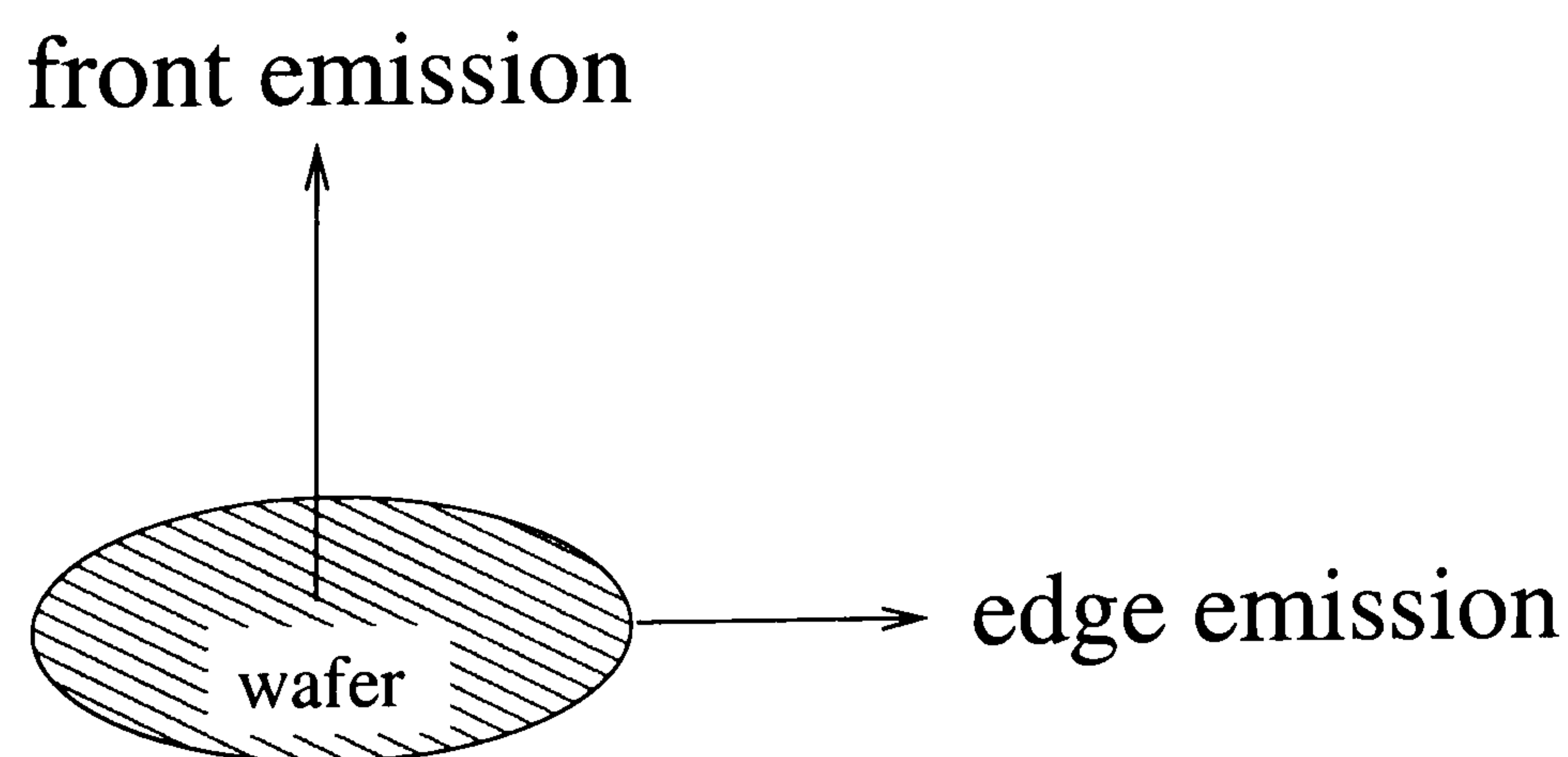

Figure 3.1: Diagram explaining front and edge emission of a wafer.

To measure the edge-EL, a piece of the wafer is held in a special mount between a grounded copper plate and a transparent conducting indium tin oxide (ITO) coated glass slide. The top ITO contact is tilted so that carriers are only injected into a small strip near the edge. The mount is then placed in front of the spectrometer so that only the EL coming from the edge of the sample is collected, as shown in figure

3.2.

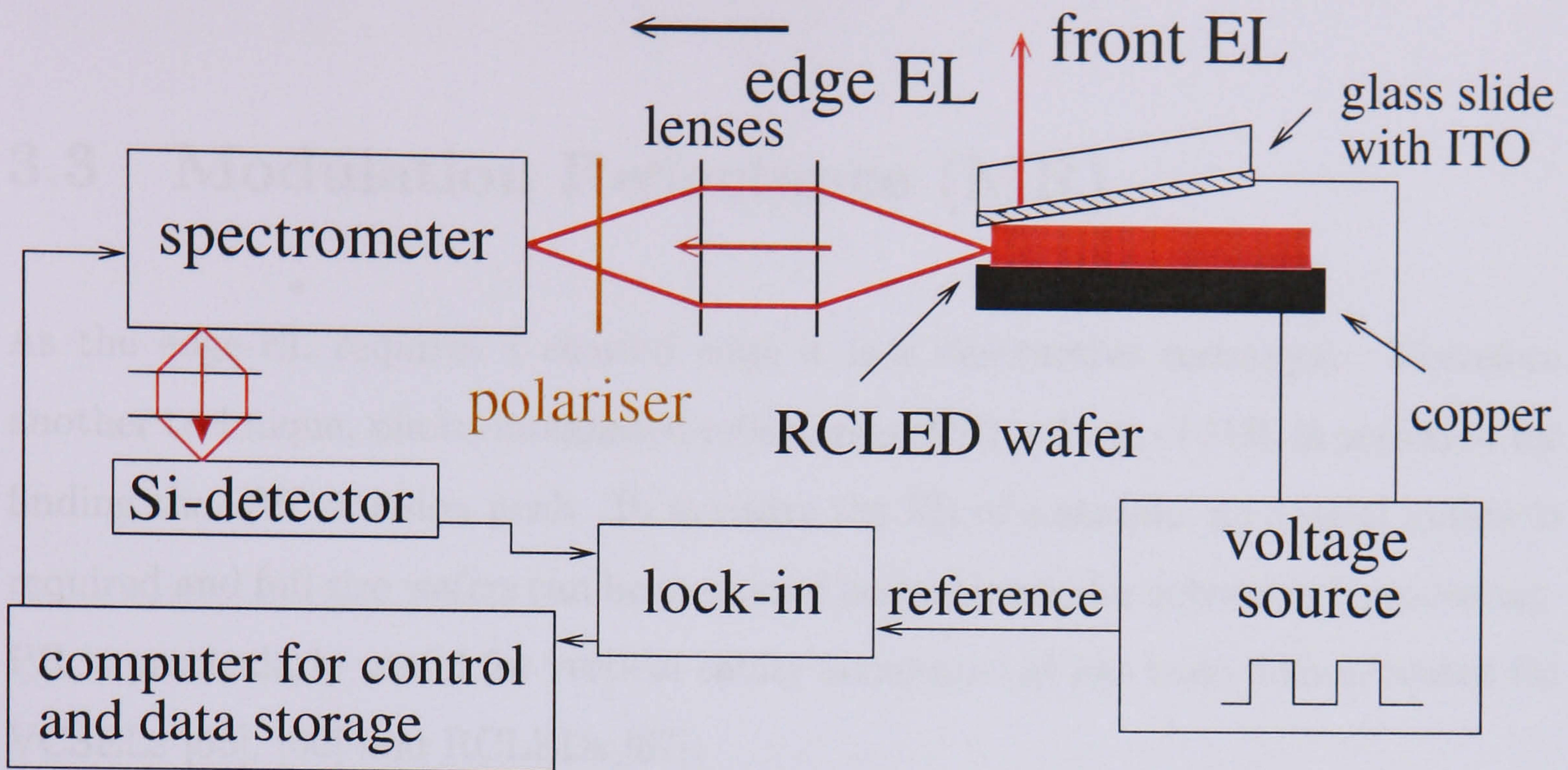

Figure 3.2: Sketch of the set-up to measure the edge electroluminescence of a RCLED wafer.

By simply rotating the sample holder through 90° the front (top) emission can also be measured. As relatively small amounts of light are collected, a lock-in amplifier is used. The reference frequency is provided by the voltage source, that supplies a square wave. Edge-EL is a destructive technique since it requires a small piece of the wafer, in general approximately $5mm \times 5mm$, with a cleaved edge. Details of the edge EL method can be found in [64]. This method must be used with caution however, as the edge-EL can be red-shifted with respect to the true QW emission, depending on how much of the wafer is pumped (i.e. how wide the excitation stripe is) due to self absorption [64]. As the light that is emitted in the plane of the device may consist of a mixture of transverse electric (TE) and transverse magnetic (TM) polarised light, a polariser is placed in front of the spectrometer, to only allow TE-polarised light to be measured. This is the polarisation at which the device emits in the front direction. Nevertheless the technique is very good to get an approximate idea for where the QW peak position lies and also about how wide the QW emission spectrum is. It can also provide a first hint if there are two different QW transitions in the device. Not only do measurements of the TE- and TM-polarised light reveal the heavy-hole and light-hole contributions but also, if the wafer has two dissimilar

λ_{QW} that are far enough apart to be resolved, both these transitions can be detected.

3.3 Modulation Reflectance (MR)

As the edge-EL requires a cleaved edge it is a destructive technique. Therefore another technique, photo-modulated reflectance (PR), a form of MR, is preferred for finding the QW emission peak. To measure the PR of a sample, no special mount is required and full size wafers can be measured and returned for subsequent processing. PR is particularly useful for vertical cavity structures as has been demonstrated for VCSELs [65], [66] and RCLEDs [67].

3.3.1 Theory of MR for vertical-cavity structures

PR is a particular form of modulation reflectance spectroscopy [68] that came first into use in the mid 1960s [69]. In such techniques, the reflectivity of the investigated sample is modulated by various methods. These methods include the modulation of the wavelength of the incoming light, the sample temperature (thermo-reflectance) [70], the sample stress (piezo-reflectance) [71], an intrinsic, built-in electric field via a chopped laser (photo-reflectance) [72] or an applied field (electro-reflectance ER). The reflectivity of a multilayer structure depends on the dielectric functions of the various materials forming the structure. The dielectric functions are changed by these modulations. Thus, in addition to the normal reflectivity a change in reflectivity, ΔR (the difference between the reflectivity R with and without the perturbation) can be measured. In this way a derivative-like signal ($\Delta R/R$) of the reflectivity can be obtained. As R is a function of the real and imaginary dielectric functions ε_1 and ε_2 respectively a change in these, $\Delta\varepsilon_i$ can be translated into a change in R and the signal can be approximated by

$$\frac{\Delta R}{R} = \frac{1}{R}\left(\frac{\partial R}{\partial \varepsilon_1}\Delta\varepsilon_1 + \frac{\partial R}{\partial \varepsilon_2}\Delta\varepsilon_2\right). \tag{3.1}$$

With the substitution of $\alpha = \frac{1}{R}\frac{\partial R}{\partial \varepsilon_1}$ and $\beta = \frac{1}{R}\frac{\partial R}{\partial \varepsilon_2}$, where α and β are the Seraphin coefficients (after Seraphin and Bottka [73]), this leads to

$$\frac{\Delta R}{R} = \alpha \Delta \varepsilon_1 + \beta \Delta \varepsilon_2. \tag{3.2}$$

As α is proportional to the change of R with respect to ε_1 it effectively relates to the change in the refractive index. Similarly β relates to the change in the absorption. For bulk materials the dependence of α and β on the energy (wavelength) is slow and virtually featureless but near a critical point, one of them always dominates [73]. In a QW structure it is more complicated and both contributions of α and β have to be considered.

A full theoretical description for a multilayer structure like an RCLED is rather more complicated as the $\Delta R/R$ in equation 3.2 becomes a sum over all layers and therefore certain approximations are made. In the following, different approaches for the theoretical description of the PR signal are discussed.

It has been shown for a vertical cavity structure that in the vicinity of the CM, the Seraphin coefficients are rapidly varying and can be empirically described by the real and imaginary parts of a complex Lorentzian:

$$\alpha(E) = \alpha_0 \frac{\Gamma_{CM}\,(E - E_{CM})}{(E - E_{CM})^2 + \Gamma_{CM}^2}, \quad \beta(E) = \beta_0 \frac{\Gamma_{CM}^2}{(E - E_{CM})^2 + \Gamma_{CM}^2}, \tag{3.3}$$

where E_{CM} and Γ_{CM} are the energy position and the half width of the CM and α_0 and β_0 are amplitudes [74]. α is thus described by an anti-symmetric lineshape and β by a symmetric lineshape. Furthermore it is assumed that the modulation of the dielectric function of the QW dominates over the contributions of the other layers in the structure and hence only $\Delta\varepsilon_{QW}$ is taken into account. The dielectric function for the QW, $\varepsilon(E) = \varepsilon_1(E) + i\varepsilon_2(E)$ can also be approximated with a complex Lorentzian [75]:

$$\varepsilon(E) = \frac{I_{QW}}{(E - E_{QW}) + i\Gamma_{QW}}, \tag{3.4}$$

where I_{QW}, E_{QW} and Γ_{QW} are the intensity, energy position and the linewidth of the QW respectively. For room temperature the use of a Gaussian lineshape has also been suggested [76]. To work out the values for $\Delta\varepsilon_1$ and $\Delta\varepsilon_2$ a linear combination

of the derivatives of ε_i with respect to Γ_{QW} and E_{QW} are used

$$\Delta\varepsilon_i = \frac{\partial\varepsilon_i}{\partial E_{QW}}\Delta E_{QW}\, cos\phi - \frac{\partial\varepsilon_i}{\partial\Gamma_{QW}}\Delta\Gamma_{QW}\, sin\phi, \tag{3.5}$$

where ϕ accounts for the degree of mixing of these two derivatives i.e. $\phi = 0$ ($\phi = 90°$) corresponding to a derivative purely with respect to E_{QW} (Γ_{QW}). For the $\Delta\varepsilon_i$ values this results in the following:

$$\Delta\varepsilon_1 = I_{QW}\left(\frac{(E-E_{QW})^2-\Gamma_{QW}^2}{[(E-E_{QW})^2+\Gamma_{QW}^2]^2}cos\phi + \frac{2\Gamma_{QW}(E-E_{QW})}{[(E-E_{QW})^2+\Gamma_{QW}^2]^2}sin\phi\right) \tag{3.6}$$

and

$$\Delta\varepsilon_2 = I_{QW}\left(\frac{-2\Gamma_{QW}(E-E_{QW})}{[(E-E_{QW})^2+\Gamma_{QW}^2]^2}cos\phi + \frac{(E-E_{QW})^2-\Gamma_{QW}^2}{[(E-E_{QW})^2+\Gamma_{QW}^2]^2}sin\phi\right) \tag{3.7}$$

Putting equations 3.6, 3.7 and 3.3 back into equation 3.2 results in a very lengthy expression and will therefore not be stated here.

Another approach comes from the description of the PR lineshape of bulk materials. The various different methods of modulation spectroscopy can be classified into those that conserve the translational symmetry and those that do not. As piezoreflectance conserves the lattice periodicity it can be described with a first derivative expression [71]. In the case of PR and ER the electric field destroys this periodicity and a third derivative expression has been very successful in describing the lineshape. This has been introduced by Aspnes [77]. Equation 3.2 can be represented as $\Delta R/R = Re\{(\alpha - i\beta)(\Delta\varepsilon_1 + i\Delta\varepsilon_2)\}$. In bulk materials the Seraphin coefficients are not strongly energy dependent and thus can be substituted by $\alpha - i\beta = Ce^{i\theta}$. Thus, according to Aspnes the PR signal near a critical point energy E_{CP} can be described as the real part of the following complex function

$$\frac{\Delta R}{R} = Re\left[\frac{Ce^{i\theta}}{(E - E_{CP} + i\Gamma)^n}\right], \tag{3.8}$$

where n=3 corresponds to two dimensional (QW) and n=2.5 to a three dimensional (bulk) critical points. After substituting $E - E_{CP} + i\Gamma = Be^{i\zeta}$ and thus $B^2 = (E - E_{CP})^2 + \Gamma^2$ and $\zeta = arccos(\Gamma/(E - E_{CP}))$ the real part of the function can be calculated [78]:

$$\frac{\Delta R}{R} = \left[\frac{C\, cos(\theta - \zeta)}{(E - E_{CP} + i\Gamma)^{n/2}}\right]. \tag{3.9}$$

3.3.2 Photo-modulated Reflectance (PR)

In ***photo***-modulated reflectance the internal field (therefore the sample in question must be appropriately doped) is modulated by a chopped laser beam that is incident onto the same spot as the unmodulated beam. Such a built-in electric field will be modulated as the chopped laser periodically creates electron-hole pairs. The reflected light is then collected with a detector. Care has to be taken to avoid collecting any of the scattered laser light. The small changes in the field alter the QW dielectric function and thus the refractive index of the structure.

For the vertical cavity structures both important features, λ_{QW} and λ_{CM}, can generally be seen in the PR spectra. However as they interact with each other, it is useful to vary this interaction in order to study the features. This is of particular interest if it becomes necessary to deduce λ_{QW} indirectly through λ_{CM} as is sometimes necessary when QW is not visible. In order to do this a technique has to be found that varies the position of one of the features with respect to the other. The possibilities for this are to vary the angle of incidence, the temperature or use a combination of both.

The QW transition energy E_{QW} decreases with increasing temperature (T) according to the Varshni [79] equation

$$E_{QW}(T) = E_{QW}(0\text{K}) - \left(\frac{aT^2}{T+b}\right), \tag{3.10}$$

where a and b are the material dependent Varshni coefficients. Thus, the wavelength increases with increasing temperature. Due to thermal expansion of the cavity and the increase of the refractive index with increasing temperature [80] λ_{CM} also increases, albeit not as fast as λ_{QW}. Indeed the rate of increase of λ_{QW} is about four times higher than of λ_{CM} for the samples studied here [81]. By recording PR spectra as a function of temperature the relative position of the two features can be changed and at a certain temperature it may be possible to make them overlap. A disadvantage of this technique is that an accurate measure of λ_{QW} will not be made at room temperature but at whatever temperature both features overlap.

3.3.2.1 Angular dependent PR

Angular dependent PR measurements are more straightforward as only one of the two features is changed. The QW ground-state transition wavelength is (as expected) unaffected by varying the incident angle, θ. However, due to interference effects occurring between the DBR layers, which can be approximated as a Fabry Perot cavity, the CM wavelength λ_{CM} decreases with increasing incident angle θ as:

$$\lambda_{CM}(\theta) = \lambda_{CM}(0°)\left(1 - \frac{n_0^2\, sin^2\theta}{n^2}\right)^{\frac{1}{2}}, \tag{3.11}$$

where n is the effective value of the refractive index in the layers comprising the cavity and n_0 is the refractive index of the outside medium, which is assumed to be air and therefore equals 1. If, as normally required for a working device, the QW emission wavelength is at a shorter wavelength than the CM at normal incidence at room temperature, but in the range

$$\lambda_{CM}(90°) = \lambda_{CM}(0°)\sqrt{(1 - 1/n^2)} < \lambda_{QW} \leq \lambda_{CM}(0°), \tag{3.12}$$

the CM can be made to cross λ_{QW} and be brought into resonance with the QW by increasing the angle θ away from the normal. In figure 3.3 a schematic diagram of the angular dependent PR set-up is shown.

The sample is mounted on a rotation stage to measure the angular dependence. The sample holder may also be equipped with a heater, or placed in a cryostat, to measure the temperature dependence. In order to be able to measure the normal incidence reflectivity, a beam splitter is inserted between the two incident lenses. The photon energy of the modulation laser used has to lie above the bandgap of the investigated material so that the material can absorb the laser radiation. In the present study an argon-ion laser emitting at 514nm was used for the modulation. The power of the laser was approximately 1mW but could be reduced with neutral density filters. This is sometimes necessary as the laser-induced PL will also be detected by the lock-in amplifier, creating a high PL background proportional to the laser power. For most cases in this study the unattenuated laser yielded the best

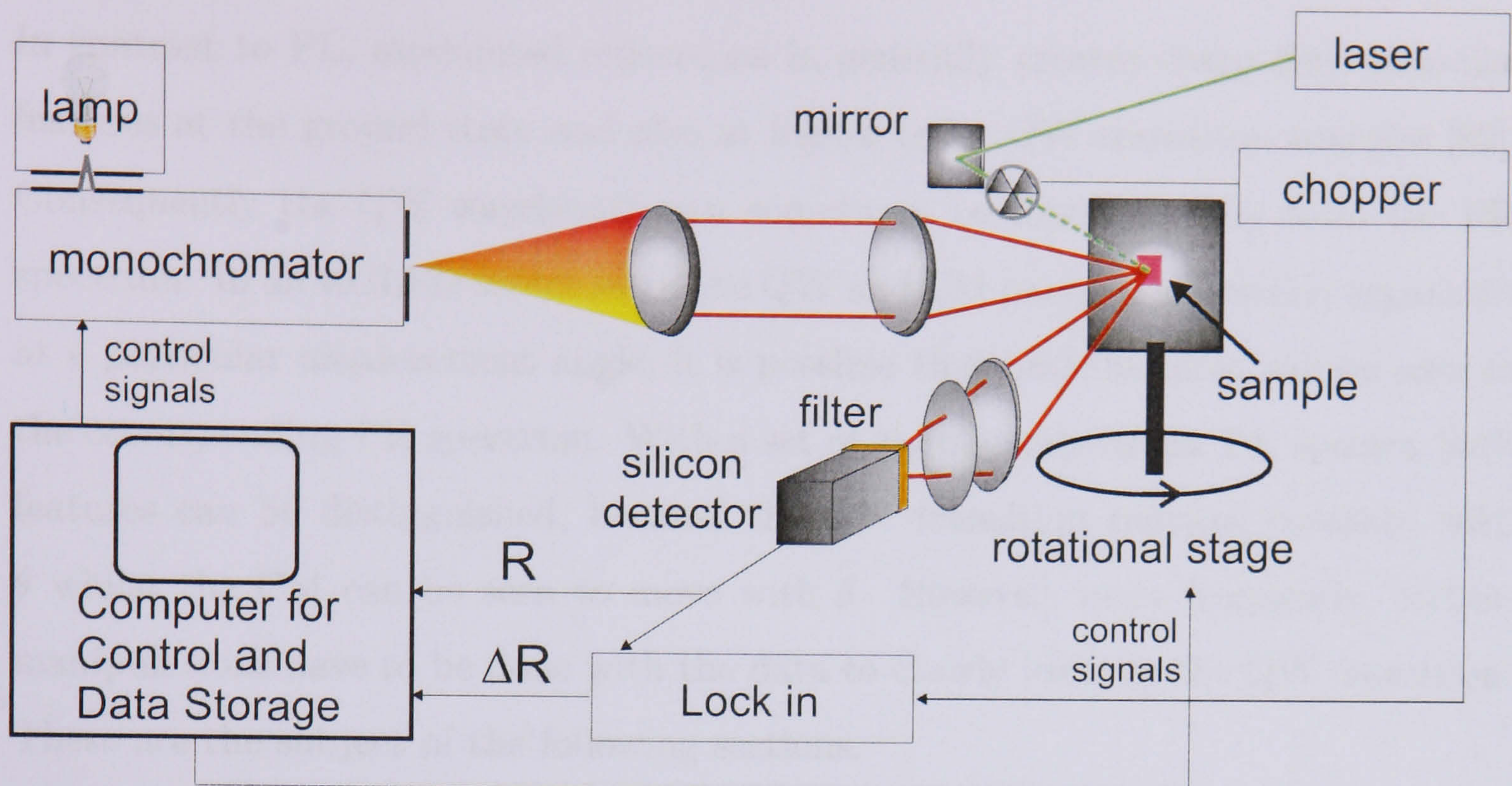

Figure 3.3: A schematic diagram of the set-up used to measure the angular dependent PR.

results. The chopper is driven at a frequency of approximately 330Hz and a 570nm high pass filter is used in front of the detector to avoid measuring the scattered laser beam (at 514nm). The filter also suppresses second order light coming from the spectrometer, which becomes more important at longer wavelengths ($> 700nm$).

3.4 PR Analysis techniques

There are various ways to analyse the experimental data obtained from PR measurements. These have to be exploited to find the QW transition as accurately as possible. In the following these shall briefly be described.

3.4.1 QW PR-feature

In contrast to PL, modulated reflectance in generally creates sharp derivative-like features at the ground state and also at higher order QW transition energies [82]. Consequently the QW wavelength can sometimes be found directly from the PR spectrum. In an RCLED structure, if the QW and CM position are clearly separated at a particular measurement angle, it is possible that both features will be seen in the corresponding PR spectrum. With a set of angular dependent PR spectra both features can be distinguished, because the QW transition remains constant with θ whilst the CM can be seen to move with θ. However, more frequently, certain manipulations have to be done with the data to clearly identify the QW transition. These are the subject of the following sections.

3.4.2 PR Resonance technique

If the CM and QW move closer together they start to interact and thus can be seen in the PR spectra [67]. This can lead to an enhancement of the PR intensity allowing the "resonance technique" to be used to identify the QW position [83]. Theoretically, the interaction can be described as a multiplication of both features, as can be seen in equation 3.2, where α and β describe the CM feature and $\Delta\varepsilon_1$ and $\Delta\varepsilon_2$ the QW feature. When they are far apart they will not influence each other and may be seen individually, as mentioned above. If they are made to overlap then the amplitude of the PR signal can be enhanced, depending on the shape and the broadening of the features. By changing the angle and thereby altering the overlap, the peak-to-peak PR intensity will correspondingly increase and decrease. By plotting this PR signal intensity versus angle, or versus the corresponding $\lambda_{CM}(\theta)$, the position of λ_{QW} can be found at the maximum where $\lambda_{QW} = \lambda_{CM}(\theta)$.

This resonance effect may be seen more clearly in the PR spectra by plotting their moduli. The modulated reflectivity can effectively be described as the real part of a complex function that depends on the wavelength. Thus the modulus of

the function can be found by performing a Kramers-Kronig transformation which relates the real and imaginary parts of the complex function, if they are related by a linear response function [84]. Further details of this technique will be discussed in section 3.5 and its particular application to PR spectra can be found in [85].

3.4.3 PR Symmetry technique

It has been suggested by Ghosh et al [86], that in certain cases, for example when the broadening of the QW and CM features are different, the resonance technique may not work. An assumption that has been made here is that the derivative of the dielectric function with respect to energy will be dominant in equation 3.5, equivalent to $\phi = 0$. Thus, leading to a symmetric lineshape for $\Delta\varepsilon_1$ and an anti-symmetric one for $\Delta\varepsilon_2$ as can be seen from equations 3.6 and 3.7. If $\Gamma_{QW} \gg \Gamma_{CM}$ the intensity will not be enhanced when λ_{QW} and λ_{CM} are in alignment. In some cases the interaction of both features can lead to an anti-resonance effect. Then the intensity of the PR signal goes down when λ_{CM} and λ_{QW} are aligned. In these cases a symmetry argument can help to find λ_{QW}. If the broadening of the QW exceeds the broadening of the CM, α and β will be much sharper features than the $\Delta\varepsilon_i$. As $\Delta\varepsilon_2$ is a broad and therefore slowly varying anti-symmetric feature, which is zero at λ_{QW}, $\beta\Delta\varepsilon_2 \sim 0$ near λ_{CM} and so $\alpha\Delta\varepsilon_1$ dominates. Therefore the lineshape of the PR-signal for the angle at which $\lambda_{QW} = \lambda_{CM}$ is, like α, anti-symmetric. For lower and higher angles the PR spectra will again be mixtures of both contributions and therefore will be asymmetric. If the intensity does not increase, the overlap and hence the QW peak position can still be found through the lineshape by identifying the anti-symmetric spectrum. In cases, when there is no resonance effect observed, the opposite will be true, which means that the PR intensity will pass through a local *minimum* where λ_{CM} and λ_{QW} are aligned.

3.4.4 Fitting of PR spectra

As described earlier in this chapter the PR signal can be represented theoretically. Hence, calculated spectra can be used to fit experimental ones with a least-squares fitting algorithm. The QW position can then simply be extracted as one of the fitting parameters.

As has been demonstrated earlier for VCSELs [83] and RCLEDs [67], the lineshape of the PR spectra is mainly determined by the product of β and $\Delta\varepsilon_2$. This is due to the fact that at λ_{CM} (where the largest changes in the signal are expected), α is zero (see equation 3.3). Therefore a simplified fitting function taking only β and $\Delta\varepsilon_2$ into account is used to fit the data. Thus the fittings are performed with a slightly modified equation based on Aspnes' third derivative function and thus referred to as TDFF [78]:

$$\frac{\Delta R}{R} \sim \left(\frac{\Gamma_{CM}^2}{(E-E_{CM})^2+\Gamma_{CM}^2}\right)\left(\frac{\Gamma_{QW}^n}{[(E-E_{QW})^2+\Gamma_{QW}^2]^{\frac{n}{2}}}\right) cos(\Psi), \tag{3.13}$$

where $\Psi = n\ arctan(-\Gamma/(E-E_{QW}))$. The fitting with the above described equation is performed using a Marquard-based least-squares algorithm and the program used was developed by Dr. J. Hosea [87]. In addition to the QW transition energy, E_{CM}, Γ_{CM} and Γ_{QW} are also extracted as fitting parameters. It has been found that the choice of the exponent n does not have a strong influence on the fits.

3.4.5 $\Delta\varepsilon_2$-analysis

In some cases it may only be necessary to measure the PR intensity at the CM energy. At the CM α passes through zero and β is at a maximum (see equation 3.3). Thus, equation 3.1 reduces to

$$\frac{\Delta R}{R}(E_{CM}) = \beta_{max}\Delta\varepsilon_2(E_{CM}). \tag{3.14}$$

By changing the angle of incidence, E_{CM} will be tuned through E_{QW} (if both are not too far apart (see equation 3.12)). Providing that β_{max} does not change significantly

with angle the $\Delta R/R|_{E_{CM}}$ values can be plotted with respect to E_{CM} and a pseudo-PR spectrum may be obtained. The lineshape of the spectrum will be determined by the lineshape of $\Delta\varepsilon_2$ as described in equation 3.7. Substituting E_{CM} for E in equation 3.7 shows that when $E_{CM} = E_{QW}$, the first term goes to zero and the second term is at a maximum. To find out which of the two terms dominates the lineshape of $\Delta\varepsilon_2$, the data is fitted with equation 3.7 where I_{QW} is replaced by a new amplitude $I = I_{QW}\beta_{max}$.

$$\frac{\Delta R}{R}(E_{CM}) = I\left(\frac{-2\Gamma_{QW}(E_{CM}-E_{QW})}{[(E_{CM}-E_{QW})^2+\Gamma_{QW}^2]^2}cos\phi + \frac{(E_{CM}-E_{QW})^2-\Gamma_{QW}^2}{[(E_{CM}-E_{QW})^2+\Gamma_{QW}^2]^2}sin\phi\right) \tag{3.15}$$

The energy and linewidth of the QW together with ϕ and β_{max} can then be extracted as fitting parameters. In figure 3.4 the two extreme possibilities for the lineshape (antisymmetric or symmetric about E_{QW}) corresponding to $\phi = 0°$ and $\phi = 90°$, are shown.

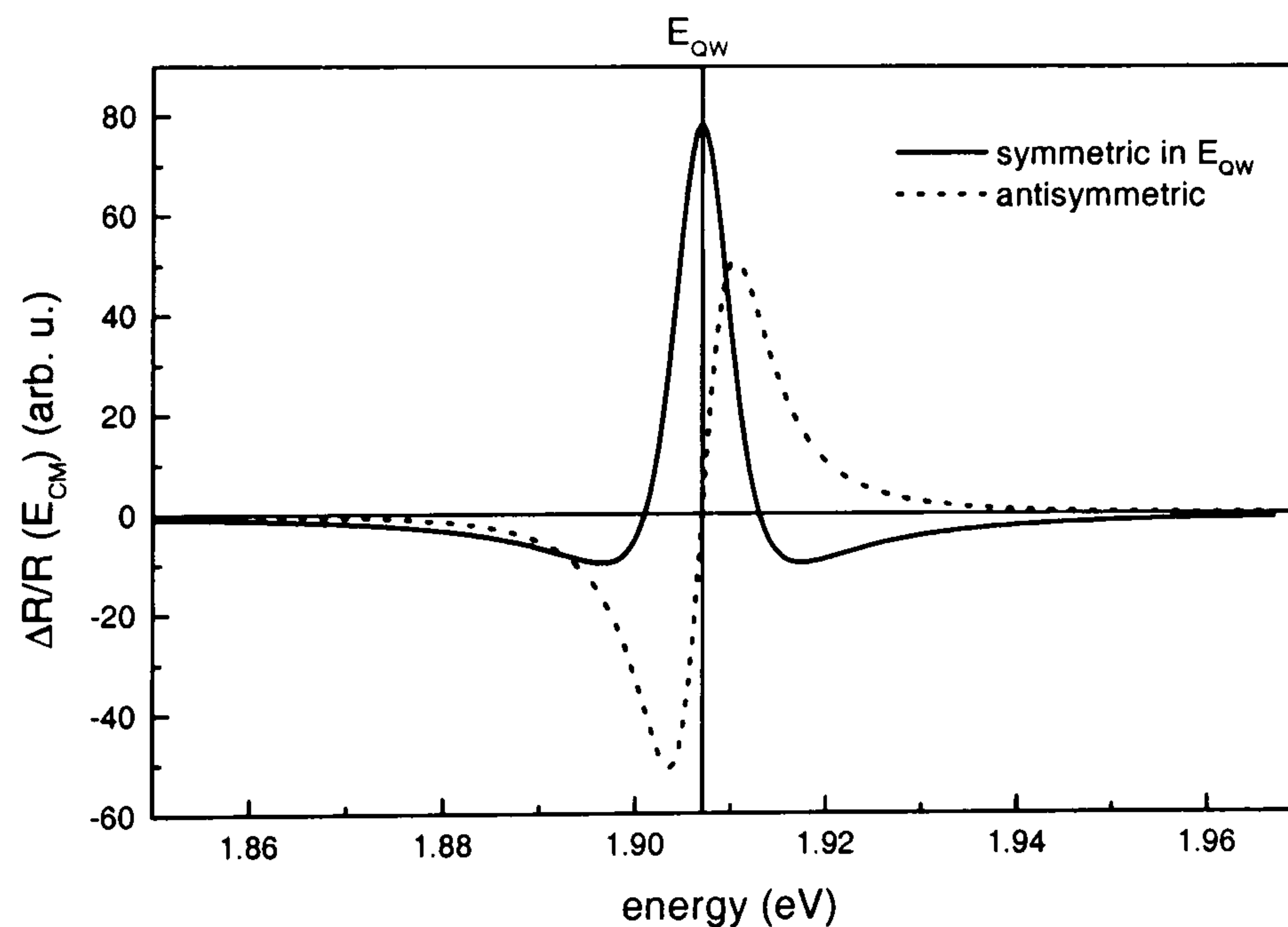

Figure 3.4: Possible symmetric (solid line) and antisymmetric (dashed line) lineshapes of $\Delta\varepsilon_2$ according to equation 3.7.

If the lineshape is symmetric about the QW energy, E_{QW} can be found as the peak position. If the $\Delta\varepsilon_2$-analysis yields an antisymmetric shape, the energy of the QW is found at the point of inflection, where the graph goes through zero. In general there will be a mix of both cases and to extract E_{QW} the data are fitted with equation 3.15.

$\lambda_{CM}(\theta)$ can be taken directly from the reflectivity measurements. To achieve more accurate results the $\lambda_{CM}(\theta)$ are first fitted with equation 3.11 and from this fit the resulting λ_{CM}s are used. If this method obtains reliable results it could promise to save time on the measurement as ideally only one point and not the whole PR spectrum would then have to be measured.

3.5 PR and edge-EL Results for RCLED wafers

In this section the PR and edge-EL results will be discussed. Each of the following sections describes the results on a particular set of wafers and also focuses on one of the analysing techniques.

3.5.1 Comparison of PR results of RCLED wafers with one and two QW transitions

In these sections the first set of two wafers that have nominally identical DBR specifications but differ in the active region are discussed. Wafer 1 (in the following referred to as S1) has two QWs that have the same transition energy (same composition and thickness). Wafer 2 (S2) has two QWs with different thickness and thus different transition energies and also a slightly longer cavity than wafer S1. The structural details of both wafers can be found in the appendix.

3.5.1.1 Results on RCLED wafer S1: One main QW transition

The angular dependent PR results for the wafer S1 at room temperature can be seen in figure 3.5. Here the PR spectra for all the measured angles are plotted. The experimental results are shown as symbols in the graph while the lines correspond to the fitted lineshape model, as described earlier in equation 3.13. It can be seen

that the fits agree very well with the experimental results.

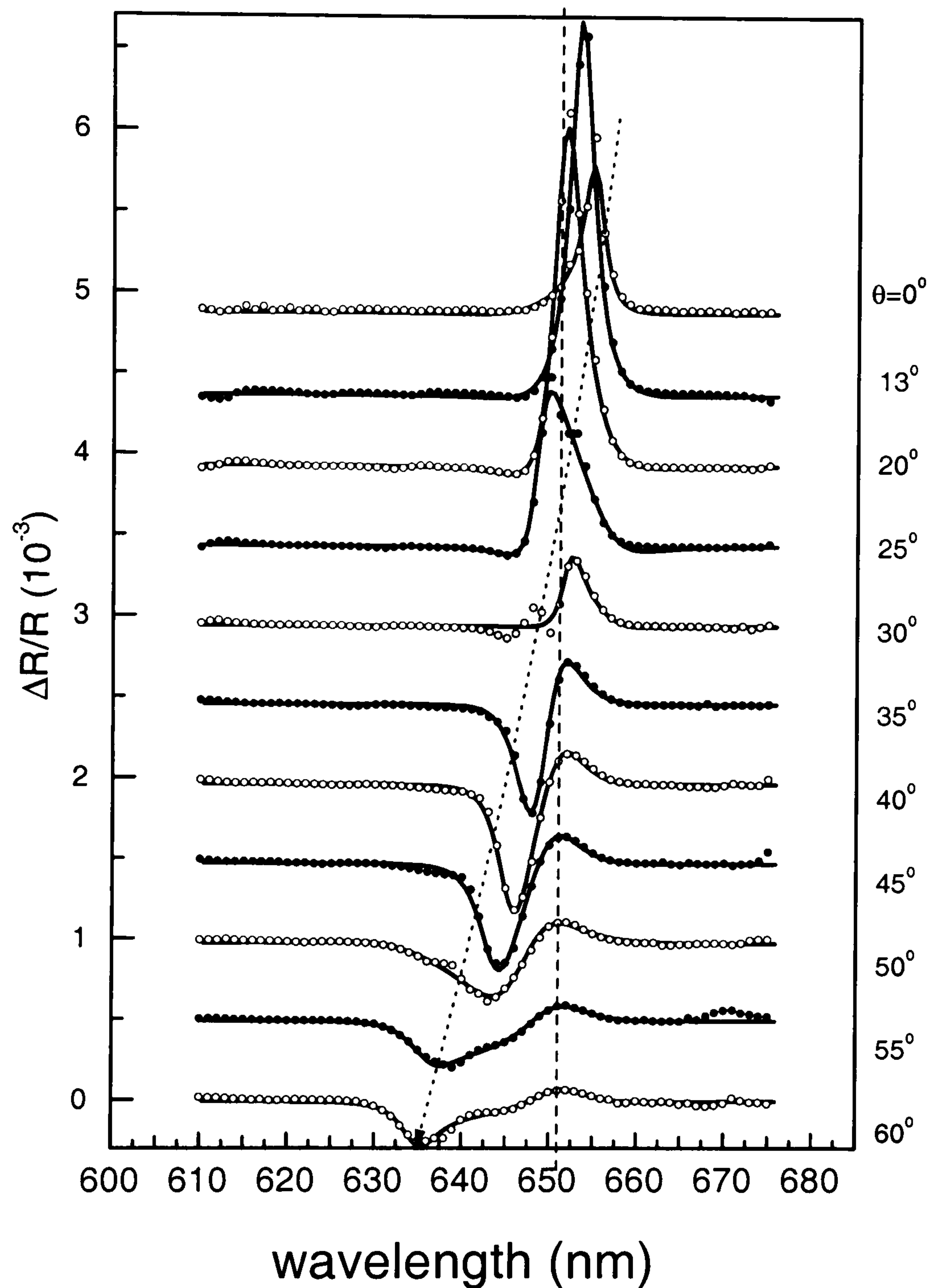

Figure 3.5: PR spectra for different angle of incidence experimentally (symbols) theoretically fitted (solid lines). The dashed vertical line marks the position of the QW according to the later described fit. The dotted line is a guide to eye showing the change in λ_{CM} with angle.

The wafer that was measured here has two nominally identical QWs. In figure 3.5 the position of the ground state transition (the wavelength of the transition as extracted from the fits as described later) is indicated by the vertical dashed line. The shift of the CM with angle is indicated by the dotted line as a guide for the

eye. Where both lines cross, CM and QW will be aligned and a resonance in the intensity is expected to be observed. The resonance can be seen in figure 3.6. This figure shows the overall PR peak to peak amplitude at different angles versus the CM wavelength at that angle as obtained from the spectra in graph 3.5. In figure 3.7 the value of the PR signal exactly at the CM wavelength is plotted and thus a virtual $\Delta\varepsilon_2$-plot is obtained (as described in section 3.4.5).

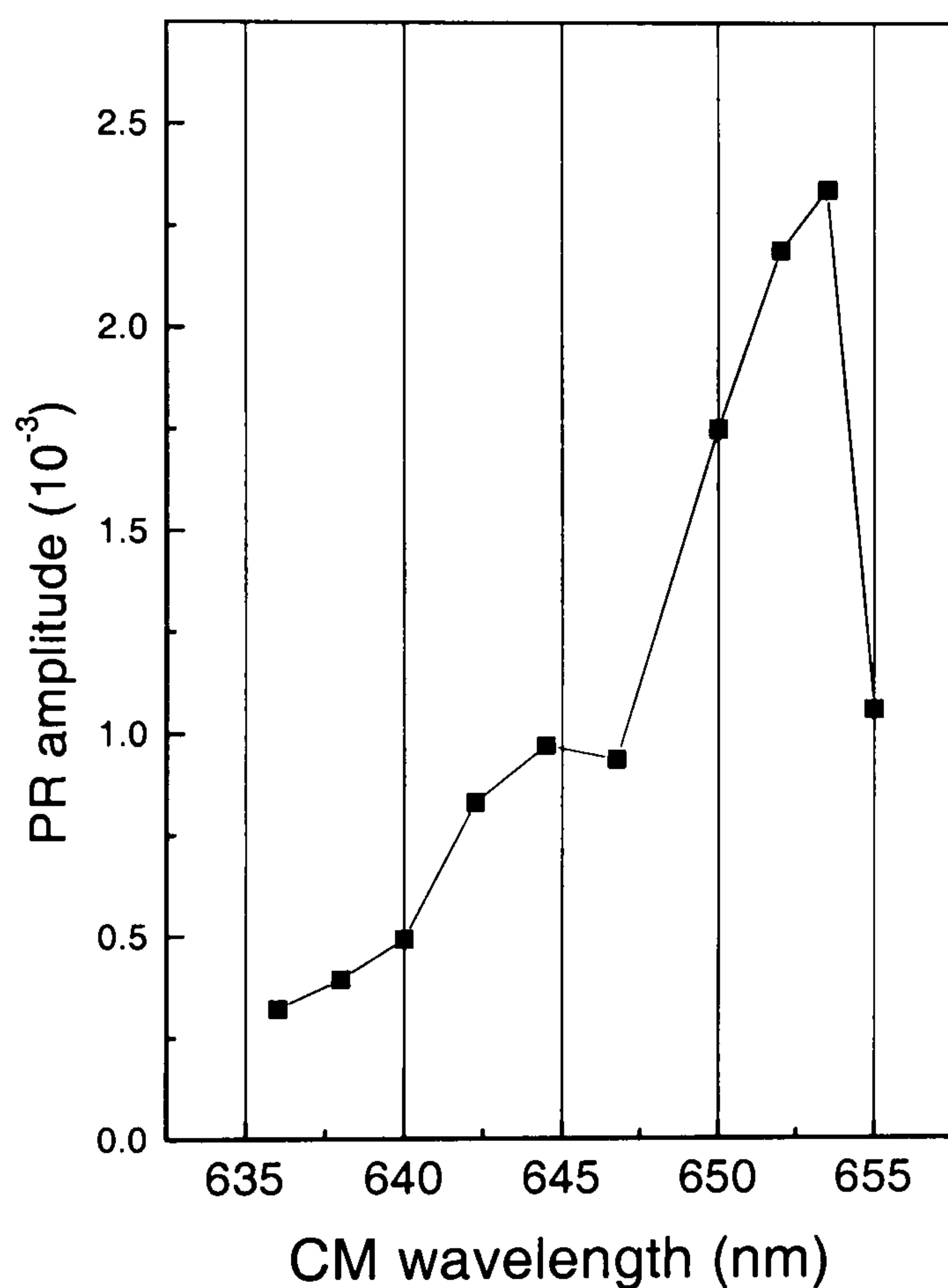

Figure 3.6: PR peak amplitude at the CM wavelength versus CM wavelength. The connecting line is only a guide to the eye.

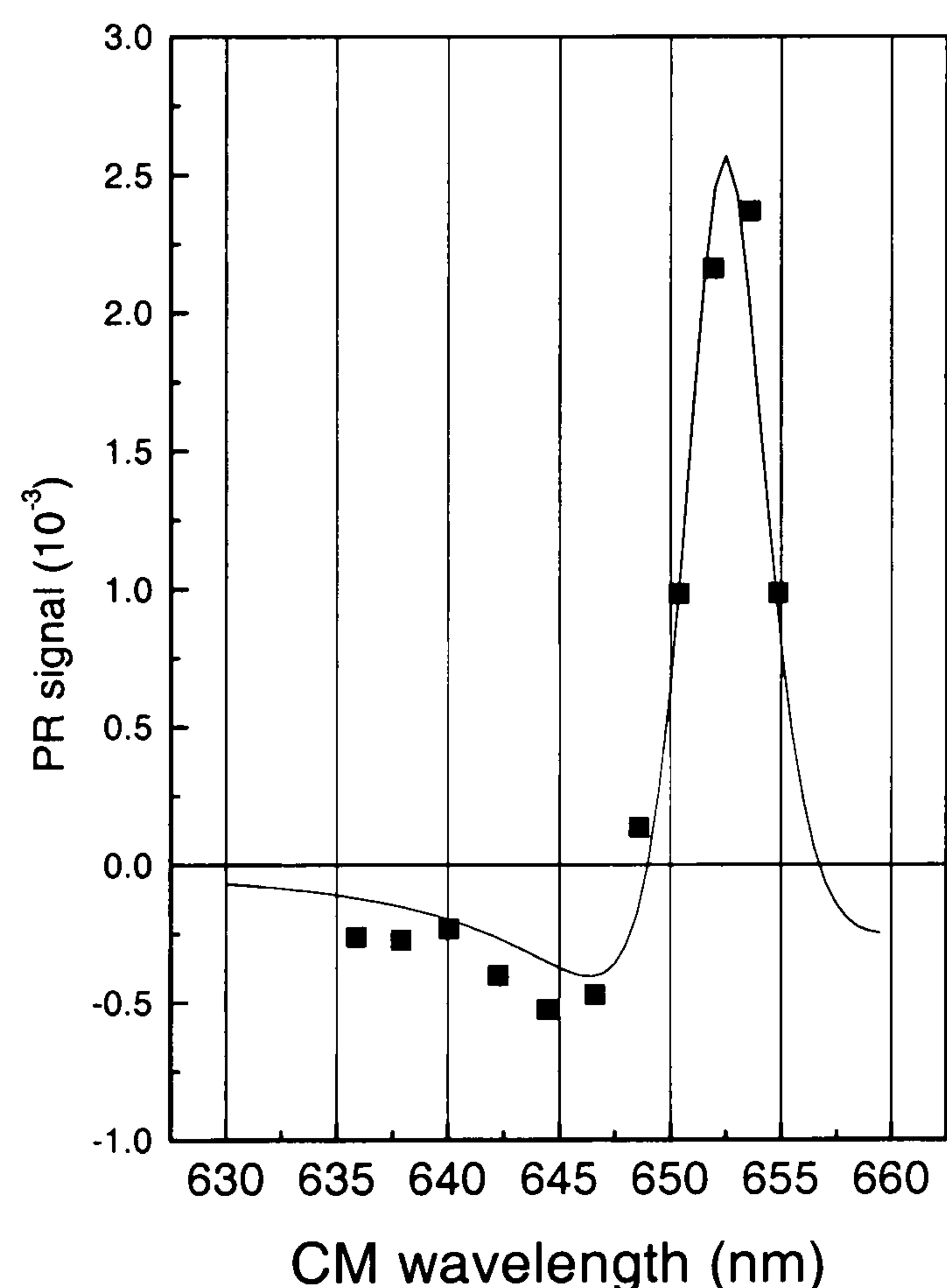

Figure 3.7: PR intensity at the CM wavelength versus CM wavelength ($\Delta\varepsilon_2$-plot). The points have been fitted with equation 3.15.

The highest intensity and thus the resonance occurs at (653.5±1)nm corresponding to an angle of 13°. The data in figure 3.7 has been fitted with equation 3.15. The fit of the $\Delta\varepsilon_2$ data suggests a λ_{QW} of (652.5±0.8)nm.

The actual PR spectra in figure 3.5 were also fitted with equation 3.13 and the result compared with the others. These fits can be seen in figure 3.5. The results

from the fits for λ_{QW} together with the λ_{CM} obtained from the R spectra are shown in figure 3.8.

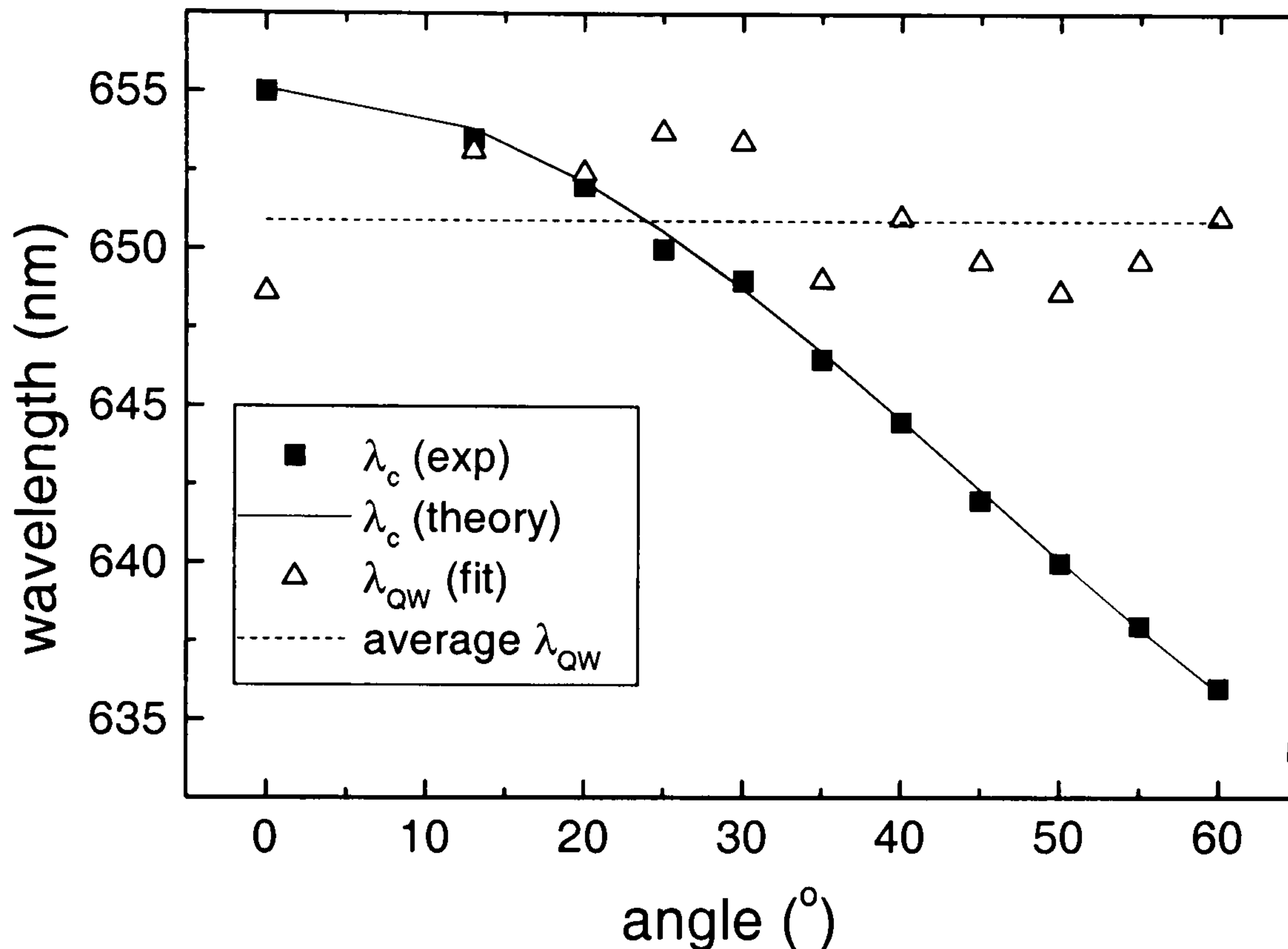

Figure 3.8: Results obtained from the fit of the PR-spectra.

Here the dashed line defines the average of the λ_{QW} values (650.9±2.8)nm extracted from the fits of the spectra for different angles. The experimentally measured λ_{CM} and a fit with equation 3.11 are also shown. These three results together yield (652.3±1.7)nm for λ_{QW}. This has now only to be corrected for any temperature effects. The temperature at which the PR measurements were taken was ∼ 28-30°C. As λ_{QW} shifts 0.147nm per degree C [81], this leads to a QW wavelength at 20°C at (651±2)nm. The uncertainty of the lab temperature adds an uncertainty of approximately ±0.3nm to the result.

To finally confirm the value for λ_{QW}, a destructive edge-EL measurement was performed (with the set-up seen in figure 3.2 on page 33). The result for the device performance important TE-polarised emission is shown in figure 3.9.

Here not only the peak at 649.5nm±1.0nm but also the width of the spectrum can be seen. The FWHM (full width at half maximum) is 22nm. As the increase in the lab temperature was caused by the heat generated by the air-cooled argon ion

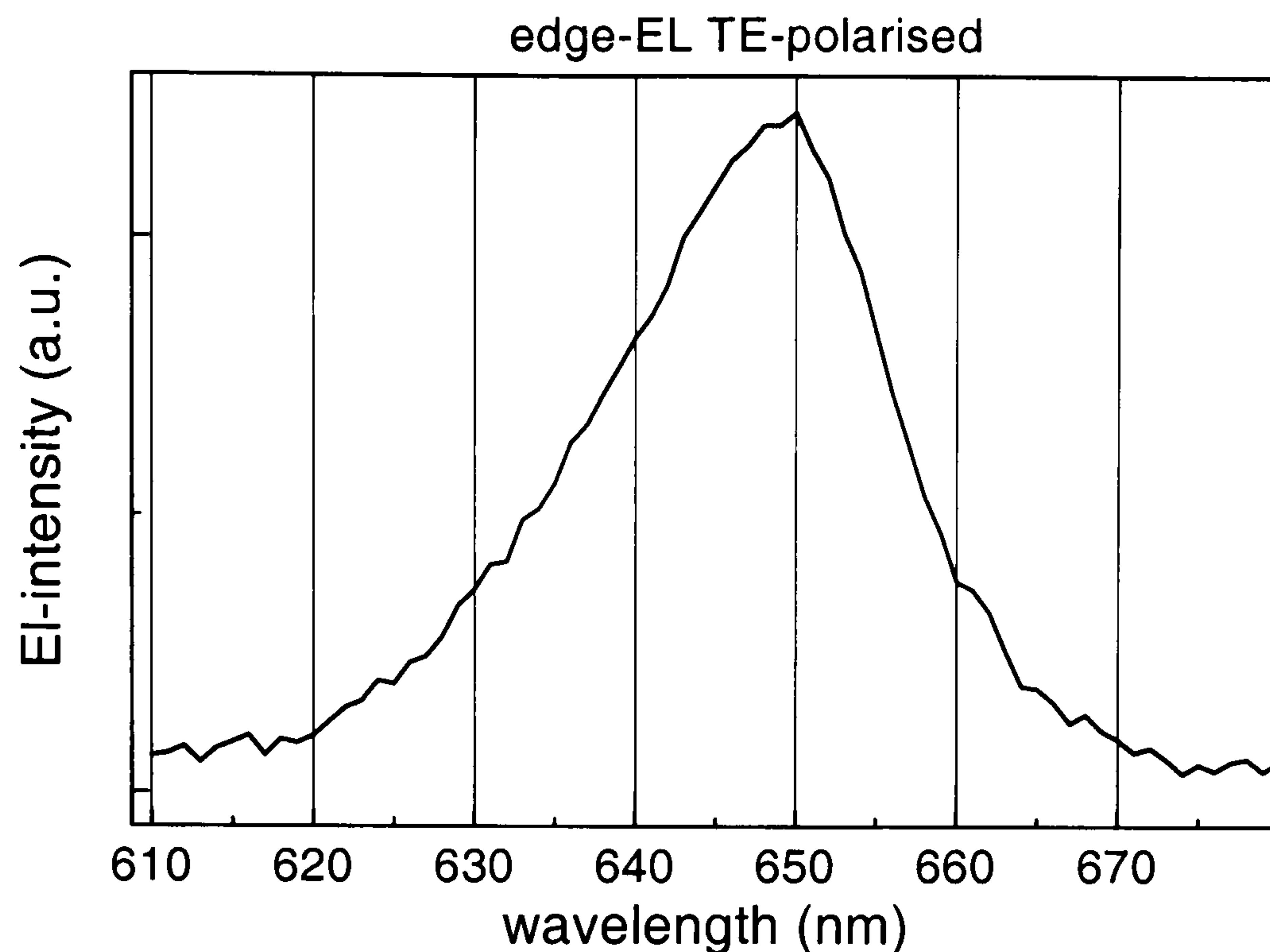

Figure 3.9: TE-polarised edge-EL confirming the QW wavelength and also showing the width.

laser that is used to carry out the PR measurements, for the EL measurements (for which the laser is not used) only a correction of ~0.7nm has to be applied, as the lab temperature for these measurements was ~25°C. This would lead to λ_{QW} ~(648.3±1.0)nm at 20°C from the EL, which is within the uncertainty of the PR result. This result also shows that there cannot be any appreciable redshift (and hence little re-absorption effects) observed in the EL, as the wavelength obtained from this is shorter than obtained from PR.

3.5.1.2 Results for RCLED wafer S2: Two dissimilar quantum wells

The second RCLED wafer (S2) has two QWs with different thicknesses and thus different transition wavelengths. The first choice of measurement is edge EL and the results can be seen in figure 3.10. this spectrum with the one for the wafer with only one QW transition (as seen in figure 3.9) the difference can clearly be seen. Both transitions can be seen as peaks in the spectra and suggests $\lambda_{QW}(1)$=654nm and $\lambda_{QW}(2)$=643nm. The only difference in the structures of wafer S1 and wafer S2

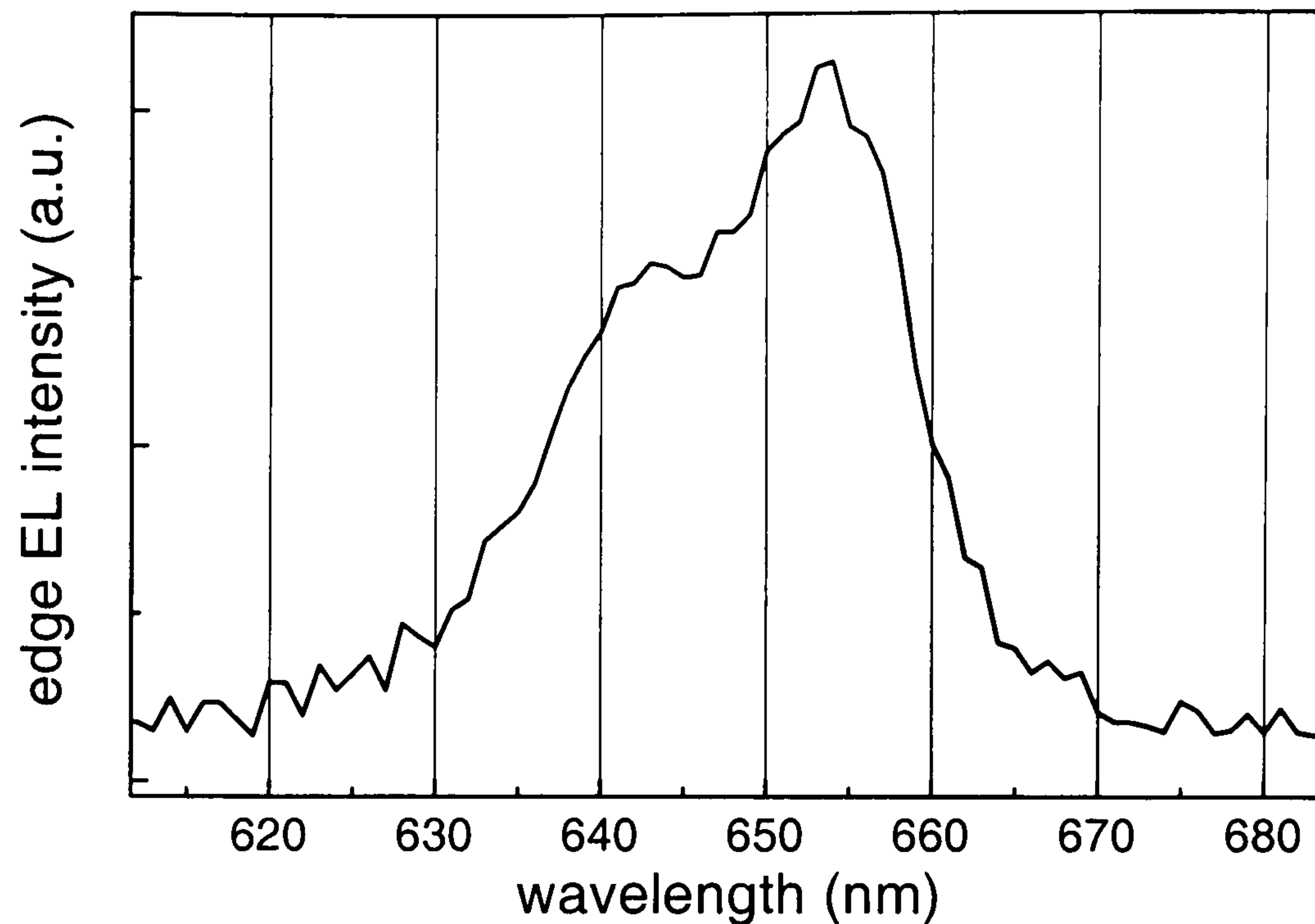

Figure 3.10: Edge-EL that shows two peaks corresponding to the two QW transitions at 654nm and 643nm.

is the number of different QWs. Thus, as there is only one peak in the EL spectra for wafer S1, the two peaks in the EL spectrum for wafer S2 are assigned to the two different QWs and not to two transitions within one QW (the splitting is too large for this to be true). The results for the λ_{QW} at longer wavelength are confirmed by PR measurements as the QW feature occurs at (655.5±0.5)nm, which is also the result that the $\Delta\varepsilon_2$ method yields. In figure 3.11 these results are shown.

Figure 3.11 (a) shows the angular dependent PR spectra and the QW feature can clearly be seen at the indicated line (at 655.7nm). The line at 642nm suggests the position of the second QW transition. In figure 3.11 (b) $\Delta R/R(E_{CM}) = \beta_{max}\Delta\varepsilon_2$ is shown. From the fit the first transition is found at 655.4nm. It was not possible to find the transition at shorter wavelength with PR as no measurements could be performed down to 642nm due to the angular restrictions of the set-up (see equation 3.12). The intensity plot does not show a clear resonance in the amplitude but by applying the symmetry theory an estimate for the QW transition can be found as the PR spectra for 30° is antisymmetric so $\lambda_{QW} = \lambda_{CM}(30°)$=655.5nm. So the results for this wafer at 20°C are, $\lambda_{QW}(1)$=(654±1)nm and $\lambda_{QW}(2)$=(642±2)nm.

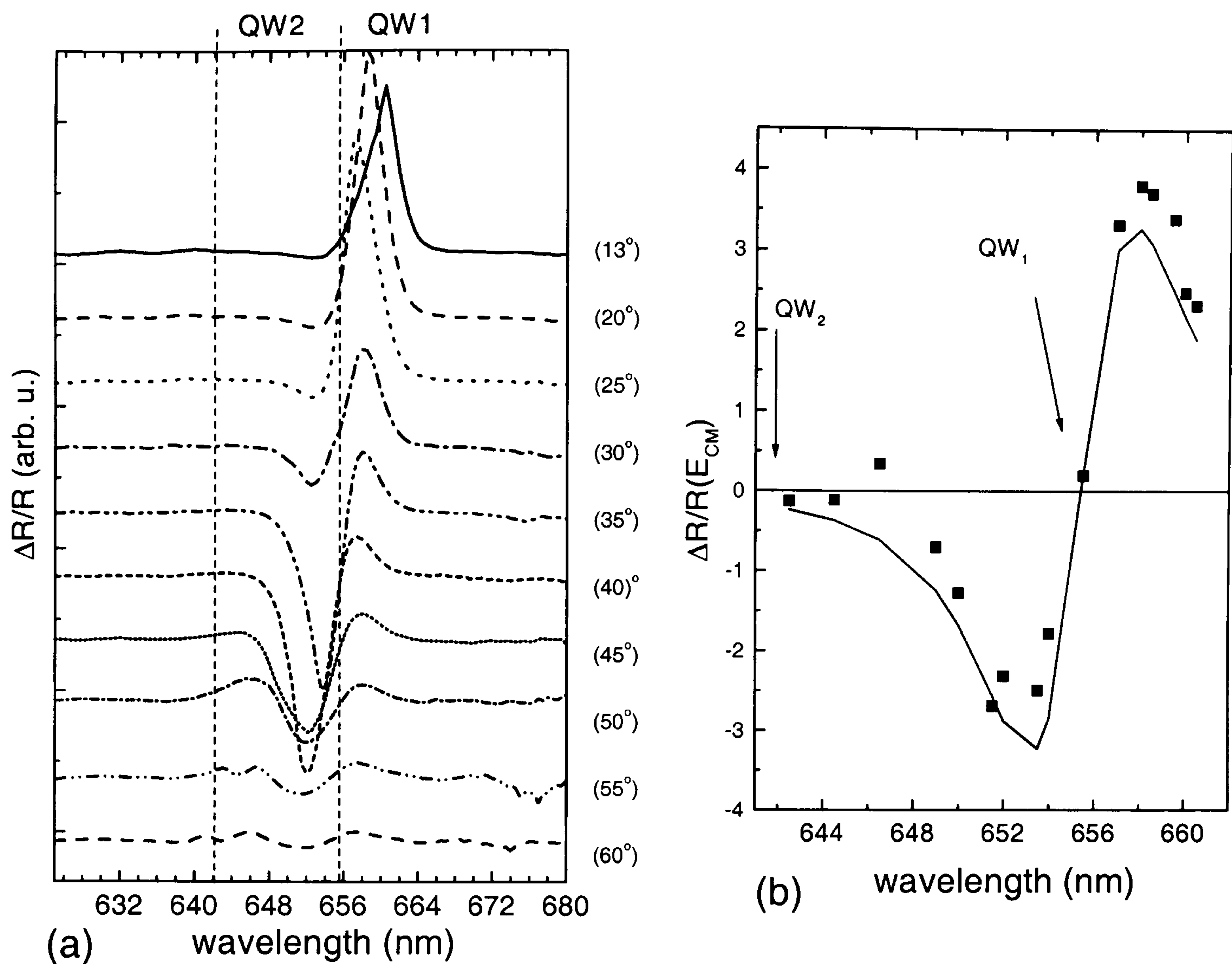

Figure 3.11: $\Delta R/R$ spectra and $\Delta R/R(E_{CM}) = \beta_{max}\Delta\varepsilon_2$ for the wafer with two different QWs. The position of the QW at longer wavelength can be seen as indicated in both graphs. The position of the other QW transition is also marked, even though it cannot be deduced from these graphs.

3.5.1.3 Summary

A summary of the results for the QW transition of wafer S1 and both transitions for wafer S2 (S2a and S2b) can be seen in table 3.1. The final result in the last column is corrected for any temperature differences.

This summary shows that by using many analysing techniques a more accurate value for λ_{QW} can be obtained. The average result of 650nm for λ_{QW} of the wafer S1 will be used in chapter 5 where results for devices processed from a wafer with the same λ_{QW} as S1 but slightly varying λ_{CM} will be compared.

	PR-feature	$\Delta\varepsilon_2$fit	Res./Sym.	fit	edge-EL	λ_{QW} (20°C)
S1	650	652.5nm	653.5nm	650.9nm	649.5nm	**(650±2)nm**
S2a	655.7nm	655.4nm	655.5nm	-	654nm	**(654±1)nm**
S2b	~642nm	-	-	-	643nm	**(642±2)nm**

Table 3.1: Summary of the results for the two wafers showing the results for the different analysing techniques.

Key: **PR-feature:** position of the constant feature in the angle-dependent PR due to the QW transition, $\Delta\varepsilon_2$**fit**: fit of the $\Delta\varepsilon_2$-plot using the PR signal at CM, **Res./Sym**: through the resonance or symmetry technique acquired result, **fit**: TDFF fit of the PR spectra, **edge-EL**: peak of edge-EL spectrum.

3.5.2 Results for RCLED wafers with different numbers of top DBRs and different doping

To investigate the influence of the top reflectivity, this set of RCLED wafers consist of wafers with either 8, 11 or 14 top DBR pairs. Details about the structures can be found in the appendix. All of the wafers had two QWs with different transition wavelengths. The structures varied slightly from the previously discussed ones (S1 and S2) as they had a 3/2-λ and not a 1-λ cavity. Consequently the two QWs of the structure were placed 1/2 λ apart at the two antinodes of the structure. The p-dopant had also been varied but the rest of the structures were nominally identical. Three different p-dopants Zn, C and Mg were studied. In total, seven wafers have been investigated. Results on devices processed from these wafers will be presented in chapter 6. The R-spectra for these wafers can be seen in figure 3.12.
Apart from a shift of λ_{CM}, the decrease of the width of the cavity dip with increasing number of top DBRs can be observed and shall be discussed in more detail in the next chapter. The growth for all wafers was aimed to produce two QWs with transition wavelengths at 652nm and 642nm. As only one of the seven wafers has a CM wavelength higher than 650nm this one shall be used to deduce the results via the resonance and the QW feature techniques.

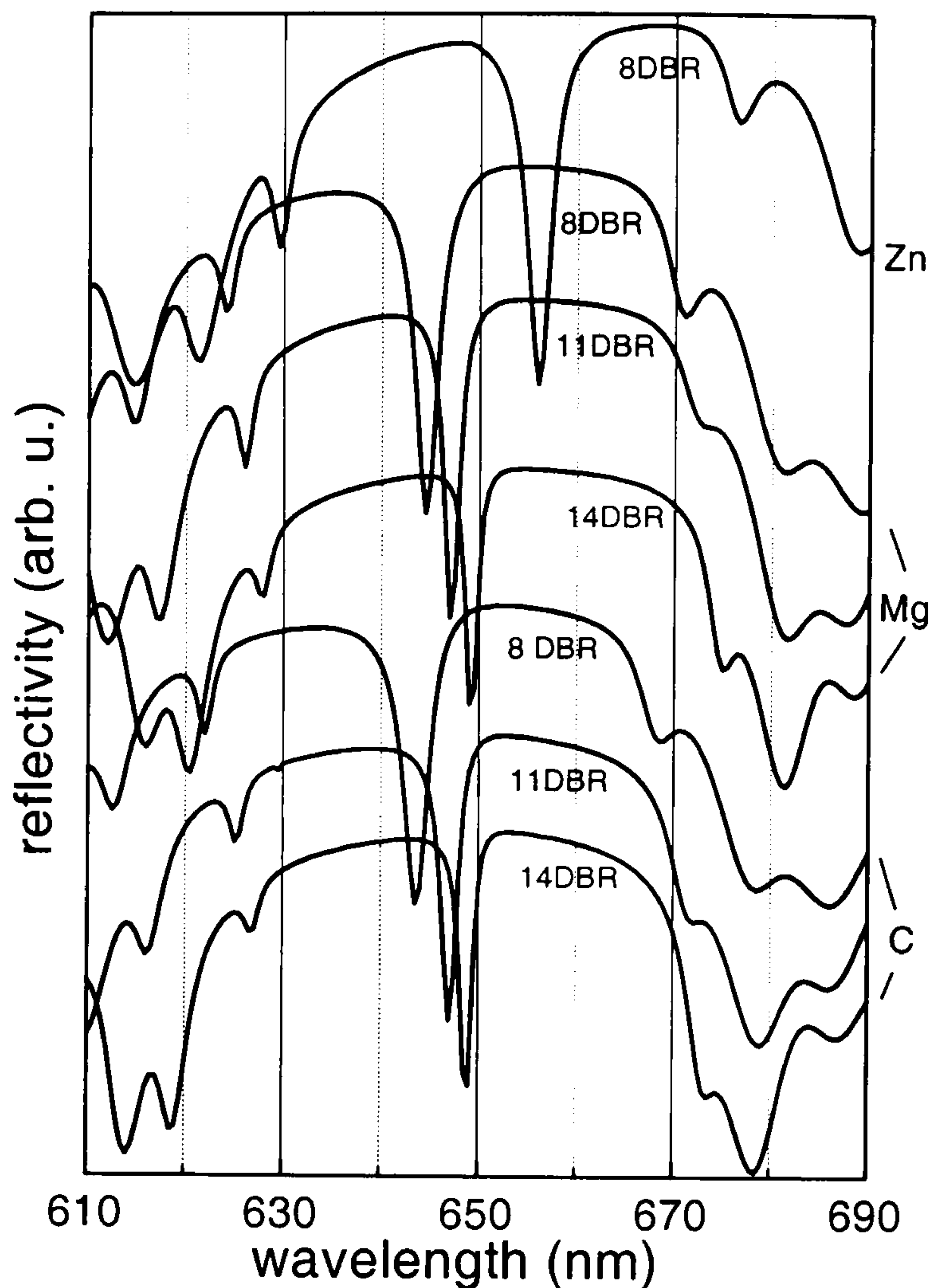

Figure 3.12: Reflectivity at normal incidence for the seven wafers differing in the p-dopant and the number of top DBR pairs as indicated. The spectra are offset vertically for clarity.

Sometimes the PR spectra are not easily interpreted and the position of the QW feature cannot obviously be identified. A way around this is to calculate the modulus of the PR spectra as can be seen in figure 3.13. The modulus can be calculated with the help of a Kramers-Kronig transformation that relates the real σ_1 and imaginary part σ_2 of a complex function, σ (see for example [88]).

$$\sigma(\omega) = \sigma_1(\omega) + i\sigma_2(\omega) = \frac{1}{i\pi}\int_{-\infty}^{+\infty} d\omega\prime \frac{\sigma(\omega\prime)}{\omega\prime - \omega} \tag{3.16}$$

The measured PR signal can be interpreted as the real part of a complex function that depends on the wavelength. In reality only positive values of the energy can be measured and so the limits of the integral have to be changed. With the help of some algebra two equations for the real and imaginary part can be deduced from equation 3.16:

$$\sigma_1(\omega) = \frac{2}{\pi}\int_0^{\infty} d\omega\prime \frac{\sigma_2(\omega\prime)}{\omega\prime^2 - \omega^2}\omega\prime, \quad \sigma_2(\omega) = \frac{2\omega}{\pi}\int_0^{\infty} d\omega\prime \frac{\sigma_1(\omega\prime)}{\omega\prime^2 - \omega^2} \tag{3.17}$$

Using the Kramers-Kronig transformation, the imaginary part of this function can be found and thus the modulus ($|\sigma| = \sqrt{Re(\sigma)^2 + Im(\sigma)^2}$) can be calculated. In

practice the values of ω are not measured from 0 to ∞ therefore care has to be taken that the contribution to the integral outside the measured range is negligible i.e. the function has to go to zero at both sides.

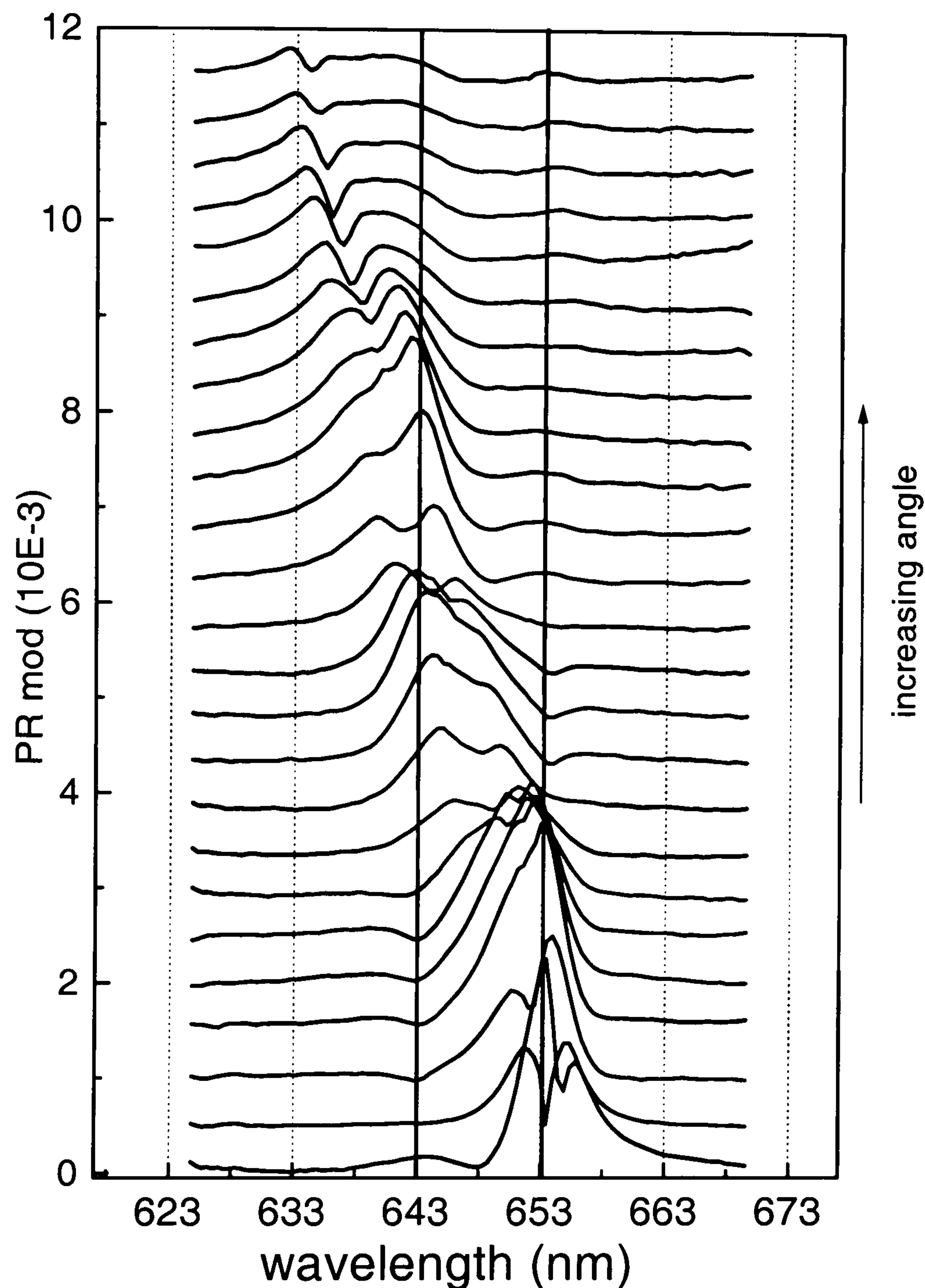

Figure 3.13: PR modulus spectra for different angles between 15° and 75°.

In figure 3.13 the modulus spectra for different angles for one wafer (Zn doped with 8 pairs of top DBRs) can be seen. In the modulus spectra, the QW transition (and the changing position of the CM) can be seen as peaks rather than derivative like functions as in the original PR spectra. The PR signal can be represented by a third derivative function as in equation 3.8. Together with equation 3.9 this leads to the

following for the modulus:

$$\left|\frac{\Delta R}{R}\right| = \frac{C}{((E - E_{CP})^2 + \Gamma^2)^{(\frac{n}{2})}}. \tag{3.18}$$

Thus the modulus is showing a peak when $E = E_{CP}$. Hence, for the two QWs transition wavelengths of 653nm and 643nm can be extracted. These wavelengths are confirmed by the resonance and the $\Delta\varepsilon_2$ technique as can be seen in figure 3.14.

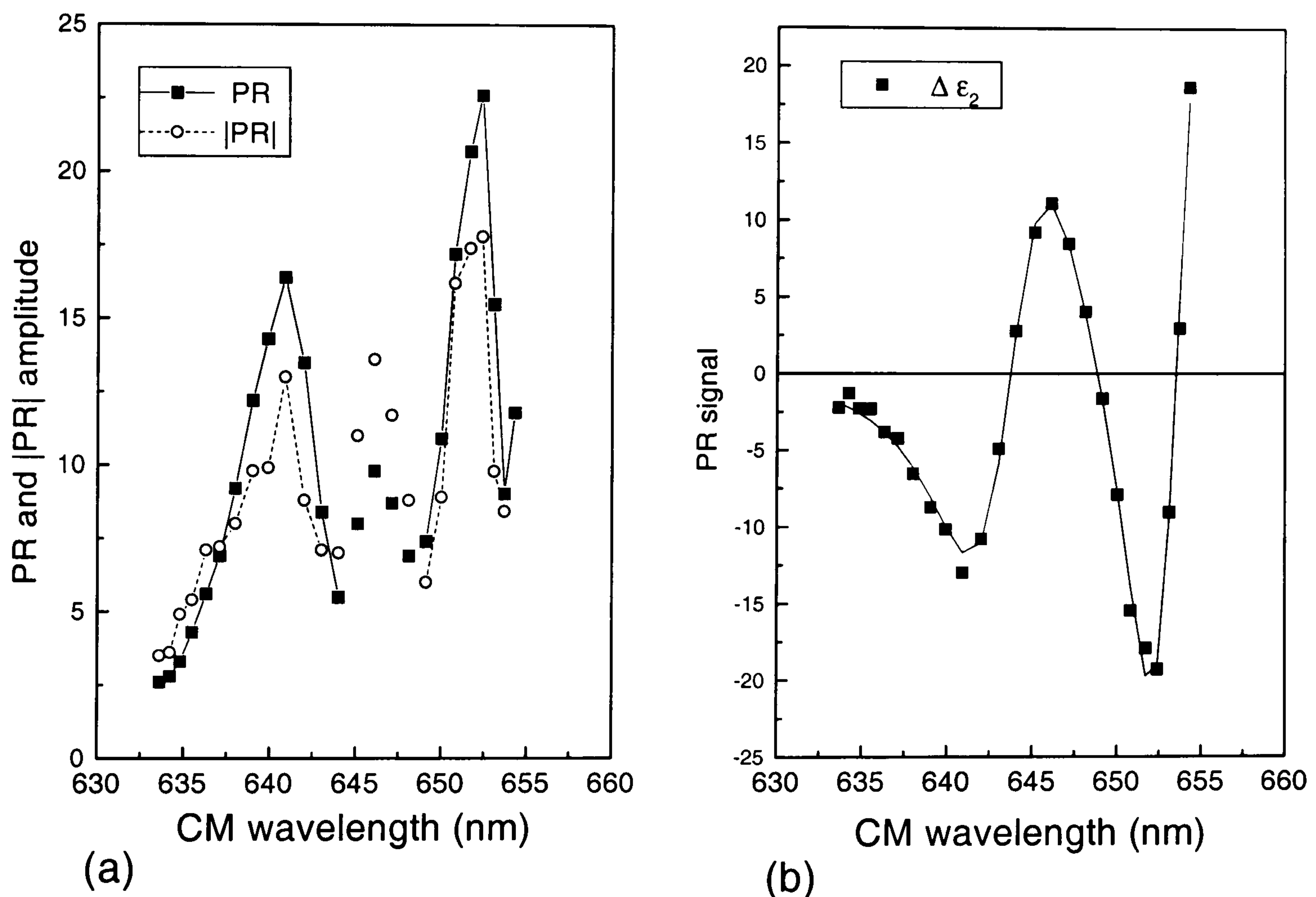

Figure 3.14: *PR* and $|PR|$ (PR modulus) amplitude (a) and the value for the PR signal (b) at the CM all versus CM wavelength. The line in graph (b) is a fit to the data that helped to extract λ_{QW}.

The main peaks in the intensity plot of figure 3.14 suggest QW transition wavelengths of (652.4 ± 0.5)nm and (640.9 ± 0.5)nm. From the $\Delta\varepsilon_2$ technique the values for the QW transitions are (653.4 ± 0.3)nm and (643.9 ± 0.3)nm. This leads to an overall best estimate for the two QWs of (652.9 ± 0.6)nm and (642.6 ± 0.6)nm and

thus of (652±1)nm and (641±1)nm at 20°C. These results, as shown in table 3.2, show that the target values of 652nm and 642nm have been achieved for this wafer.

	PR-feature	$\Delta\varepsilon_2$fit	Res.	result (20°C)
Zn 8DBR λ_{QW1}	653nm	653.4nm	652.4nm	**(652±1)nm**
Zn 8DBR λ_{QW2}	643nm	643.9nm	640.9nm	**(641±1)nm**

Table 3.2: Summary of the results for the two QW transitions of the Zn doped wafer. For explanations of the table headers see table 3.1.

For the other six wafers, transitions around 650.5nm and 641nm are also observed. As the resonance technique could not be used here for the λ_{QW} at 650nm, the transitions for one of the wafers are measured with edge-EL. The results for the edge and front EL for a carbon doped wafer with 8 top DBR pairs can be seen in figure 3.15 together with the front EL (FEL).

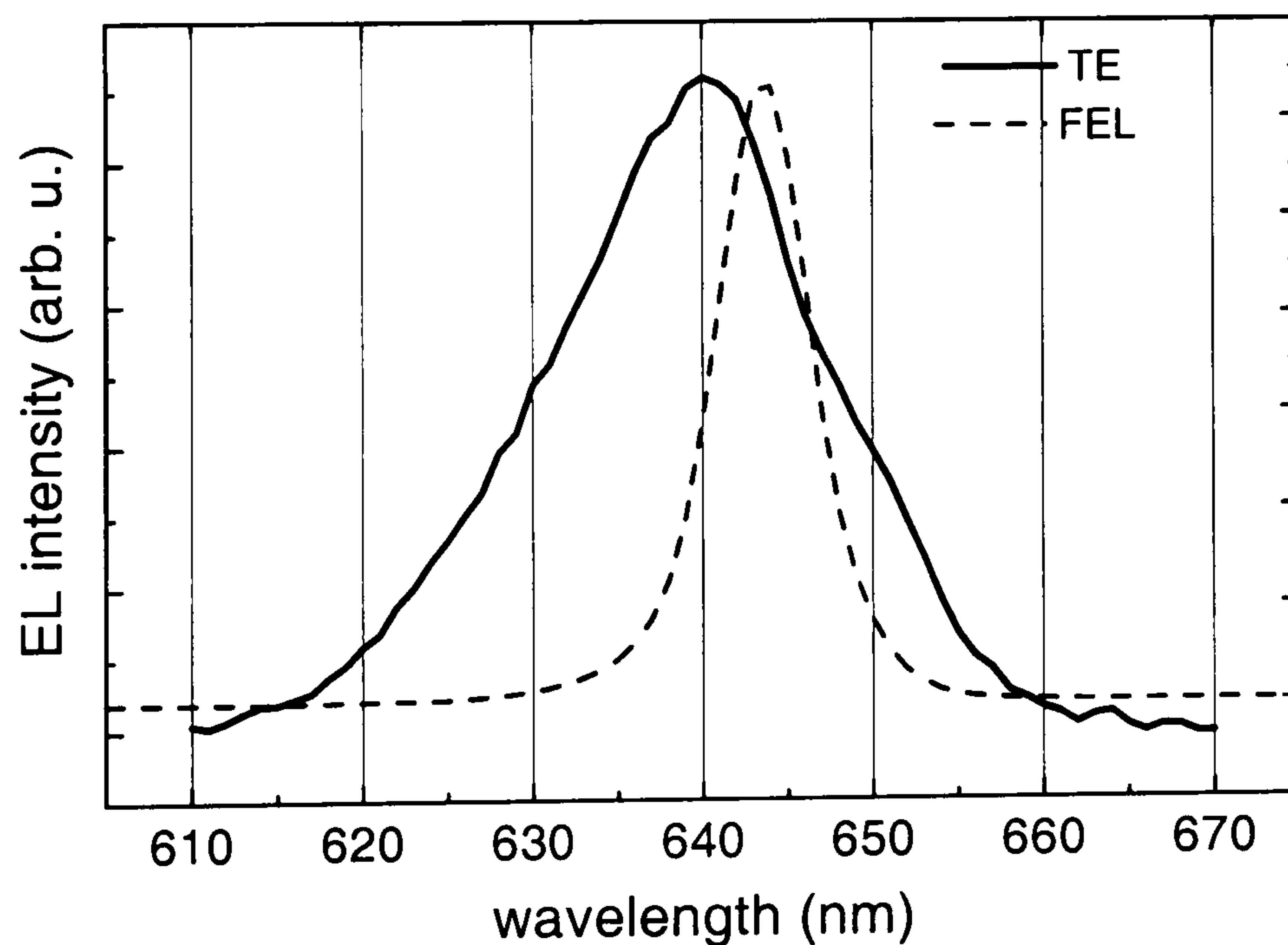

Figure 3.15: Front (FEL) and TE-polarised edge-EL (TE) for a device with 8 DBR pairs. The FEL peaks at the CM, which is at 643.5nm for this wafer. The edge-EL has its main peak at 640nm and a shoulder at ~ 651nm.

The main peak of the edge-EL is at 640nm. The feature of the second QW can only be seen as a shoulder and lies near 651nm. The front EL (FEL), that is also shown

in the graph, confirms that with this method only the λ_{CM} and not the λ_{QW} can be measured as it peaks at 643.5nm which is the λ_{CM} for this wafer. If a device was processed from this part of the wafer, the performance would not be very good. This is because all of the light produced by the first QW (λ_{QW} = 651nm) would not escape from the device, as only light at wavelengths shorter than λ_{CM} can leave the device.

3.5.3 Results on RCLED wafers with varying cavity modes

A set of wafers was grown with deliberately varying CM wavelength over a large range of 100nm. All of the wafers had only one QW and its transition was aimed at 650nm in all wafers. The influence of the varying CM on the reflectivity spectra will be discussed in the next chapter. Here the results on wafer J01-1f with λ_{CM} at 650nm will be presented. In figure 3.16 the PR intensity is plotted versus angle of incidence.

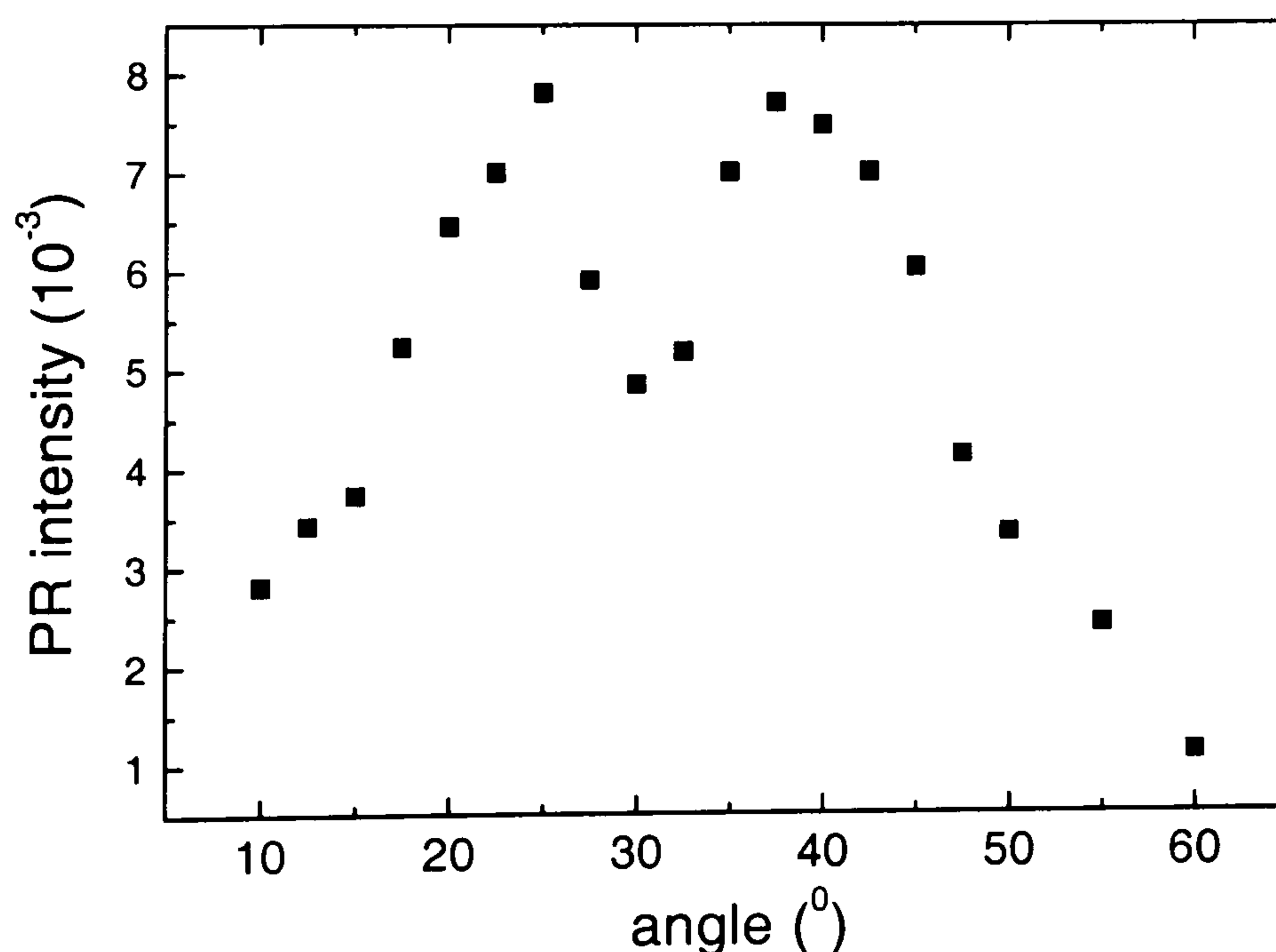

Figure 3.16: PR intensity versus angle of incidence. The drop in the intensity suggests an antiresonance at 30°.

It is not clear from this plot if there are two resonances and thus two QW transitions or if indeed an antiresonance around 30° has occurred. Therefore it cannot be de-

termined from this plot where the QW/CM overlap is. Other methods of analysing the data have to be used. In figure 3.17 the PR intensity at the CM, together with a fit of equation 3.14, is plotted against λ_{CM}. This is a virtual $\Delta\varepsilon_2$-plot and in this case the lineshape is anti-symmetric and the symmetry method can also be applied.

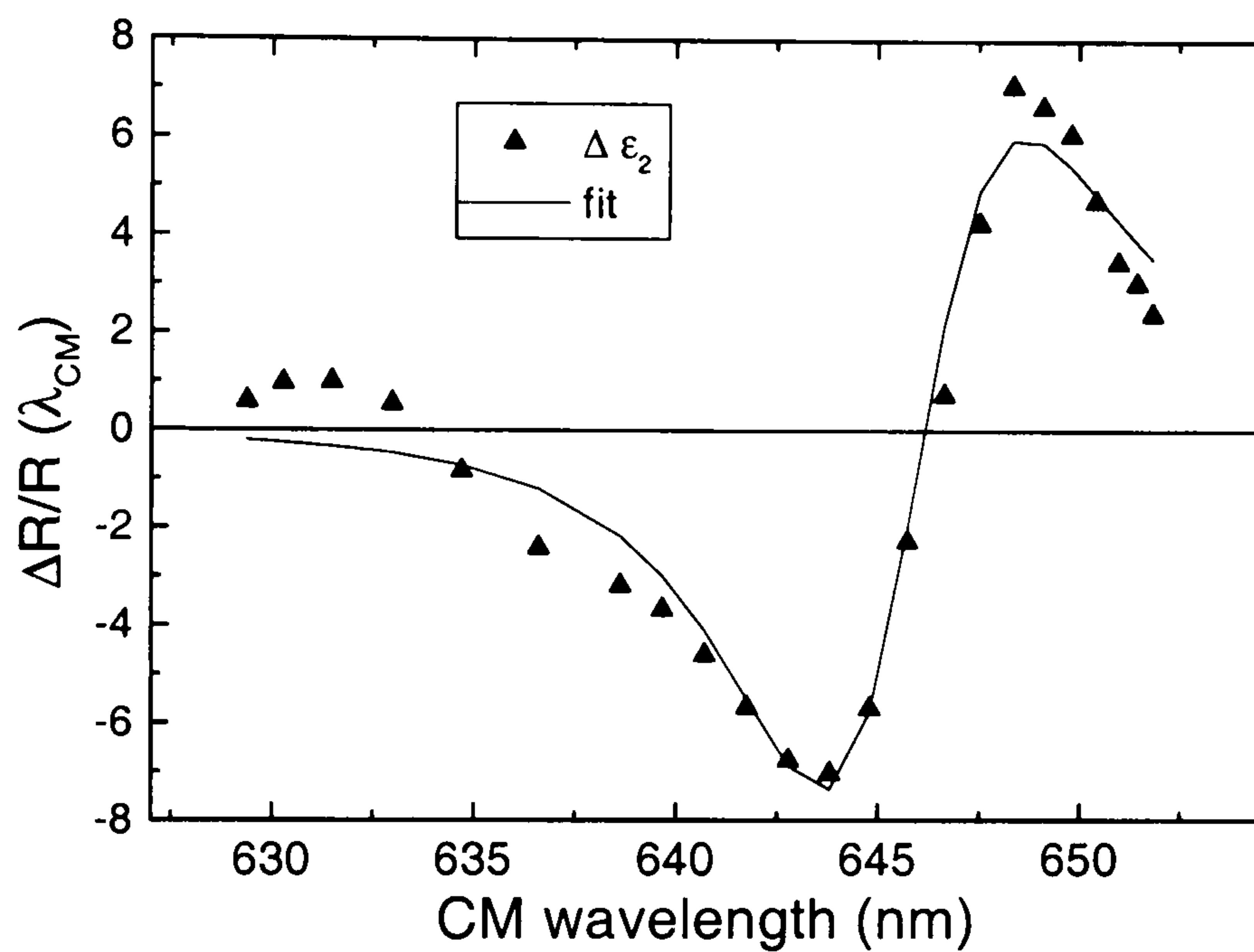

Figure 3.17: $\Delta R/R|\lambda_{CM}$ versus λ_{CM} together with a fit of the data.

The fit suggests $\lambda_{QW} = 645.9nm$, which is approximately where the $\Delta\varepsilon_2$-data goes through zero. The angle associated with $\lambda_{CM} = 645.9$nm is ~30°. This is where in the resonance plot in figure 3.16 the minimum occurs. To verify if it is an antiresonance the lineshape of the PR spectra has to be examined. The PR spectra of 30° and surrounding angles are shown in figure 3.18.

It can be seen in figure 3.18 that the highlighted PR spectra for 30° and 32.5° are anti-symmetric and occur between more symmetric shapes either side (25° and 40°). This suggests that the overlap between λ_{CM} and λ_{QW} occurs between 30° and 32.5° and therefore $\lambda_{QW} = 646.1$nm as this is the corresponding CM between those angles.

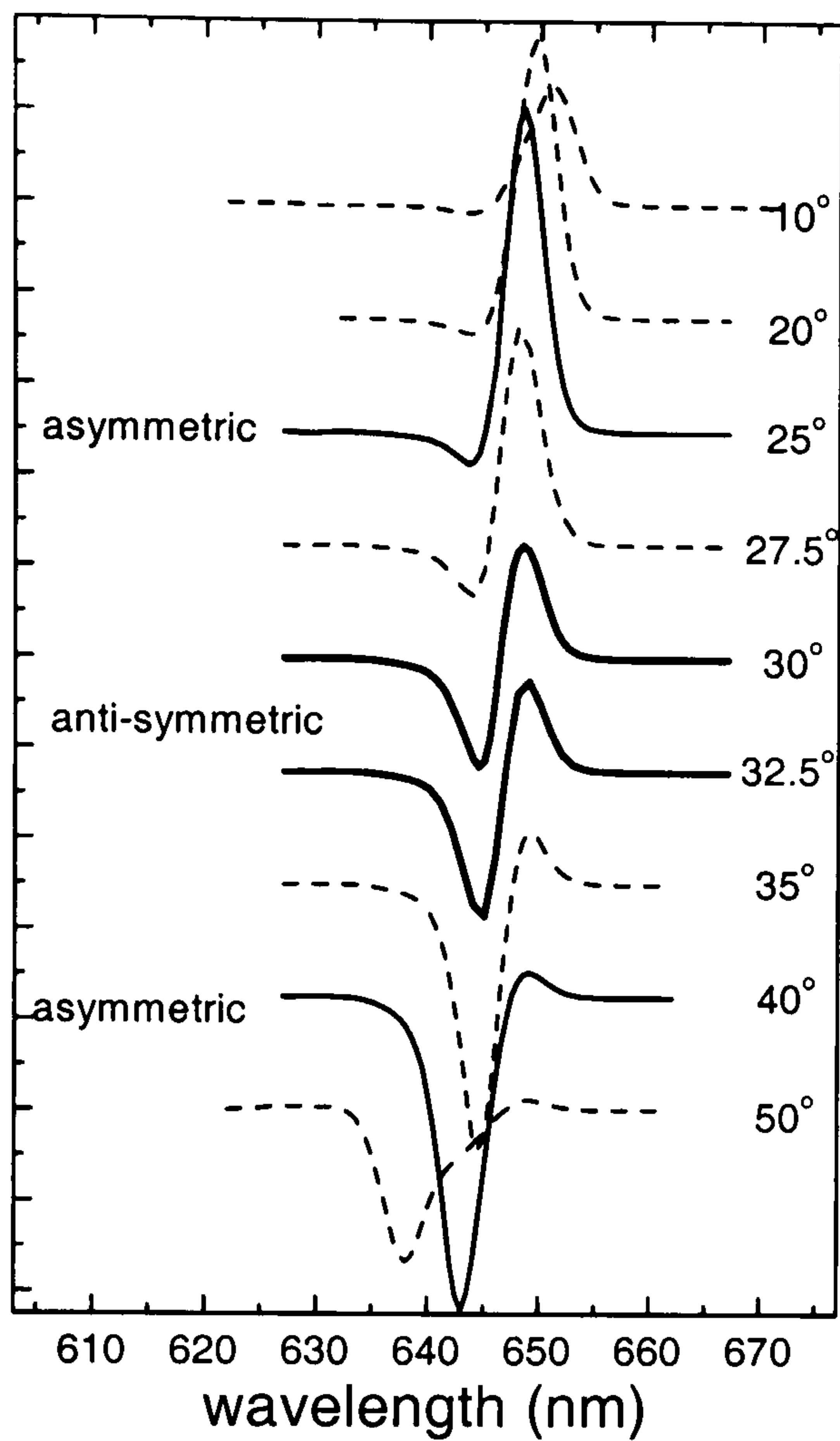

Figure 3.18: PR spectra showing the change from (almost) symmetric to a clear anti-symmetric lineshape.

3.5.3.1 Summary

In table 3.3 a summary of the results for all five wafers is presented.

	PR-feature	$\Delta\varepsilon_2$fit	Res or Sym	λ_{QW} (20°C)	λ_{CM}
J01-1F	646.2nm	645.9nm	646.1nm	**644.7±0.6nm**	650nm
J01-2F	644nm	no main CM	647.6nm	**643.7±2.9nm**	no CM
J01-8F	643.8nm	643.7nm	646.5nm	**643.7±1.4nm**	650nm
J01-8H	643.4nm	643.3nm	644.6nm	**643.8±0.6nm**	663nm
J01-1D	644.5nm	EL: 641.5nm	642.7nm	**641.5±1.9nm**	645nm

Table 3.3: Results for five wafers summarising the different analysing techniques leading to a best estimate for λ_{QW}. Table headers bear the same meaning as in table 3.1.

Wafer 112F did not have a main CM but the overlap could be created with one of

the prominent side dips in the R-spectra. Despite the differences in the proposed and achieved λ_{CM} for the different wafers, which shall be discussed in more detail in the next chapter, λ_{QW} is fairly constant. The value is however closer to (644$\pm$1)nm than to the proposed 650nm. Although this difference is relatively small it is still larger than has been observed for other wafers, suggesting that the nominal QW thickness was too low. The consistency also shows that the great variations in the cavity length did not influence the QW transition energy. It was never intended to process devices from these wafers and with some wafers, as indicated in the last column of table 3.3, which do not have a main CM, device operation would not be possible. For the other wafers, the discrepancy between the intended QW emission of 650nm and the achieved one of 644nm, could lead to quite promising devices processed from these wafers with a small positive CM-QW de-tuning. In chapter 5 the influence of this de-tuning on the device performance and its possible advantages will be investigated.

3.6 Conclusion

In conclusion PR and edge-EL have successfully been applied to determine the QW transition wavelength in RCLEDs. In many cases all of the possible analysing techniques discussed had to be used to obtain a confident result. In this chapter results for various wafers with three different structures have been presented.

The S1 λ_{QW} has been determined to be at the intended 650nm. The result has been obtained with linewidth fitting, the virtual PR-plot method ($\Delta\varepsilon_2$), the resonance technique and edge-EL. The two QWs of the S2 wafer are determined by edge-EL to be 654nm and 642nm. These results were confirmed by PR with the $\Delta\varepsilon_2$-method and an anti-resonance is observed. The Krames-Kronig transformation could successfully be used to determined the QWs for wafers with different numbers of top DBR pairs and different p-dopings to be at 652nm and 641nm. Another example of an anti-resonance is observed in the wafer J01-1F leading to λ_{QW} =

644±1nm. No clear guideline has been found to predict if a resonance or an anti-resonance will be observed as the broadening of the CM and the QW are neither of comparable nor of very different (order of magnitude) size. However, in both cases the results obtained from a resonance or an anti-resonance plot are confirmed with other independent analysing techniques. For both sets of wafers these measurements show that λ_{CM} varies between the structures but λ_{QW} remains reasonably constant.

Chapter 4

Reflectivity

4.1 Introduction

In addition to the quantum well ground state emission wavelength (λ_{QW}), which was the subject of the previous chapter, the cavity mode wavelength (λ_{CM}) is another important parameter that has to be determined in order to understand and predict the light output characteristics of an RCLED. Experimentally this value can be extracted from normal reflectivity measurements, but it can also be calculated. In this chapter the theoretical model for the calculation of reflectivity spectra of multilayer structures shall be described. Results of the calculations will then be compared with measured spectra. In addition the theoretical reflectivity will also be used to directly fit experimental spectra.

In the second part of the chapter a novel experimental technique to measure the reflectivity spectra on individual devices will be introduced. The R spectra measured with this method are then shown and subsequently discussed.

4.2 Theory

The reflectivity spectra of an RCLED is mainly determined by the Bragg stacks. The calculated reflectivity spectrum of a distributed Bragg reflector (DBR) consisting of 40 pairs of alternating $AlAs$ and $Al_{0.5}Ga_{0.5}As$ layers is shown in figure 4.1. The thickness of the layers is $d = \lambda(n)/4$, where $\lambda(n) = \lambda/n$ and n is the refractive index of the particular layer at that wavelength. These thicknesses are optimised to obtain a high reflectivity around $\lambda = \lambda_{Bragg} = 650$nm which is called the stop band. The dips either side of the stop band are due to constructive and destructive interference.

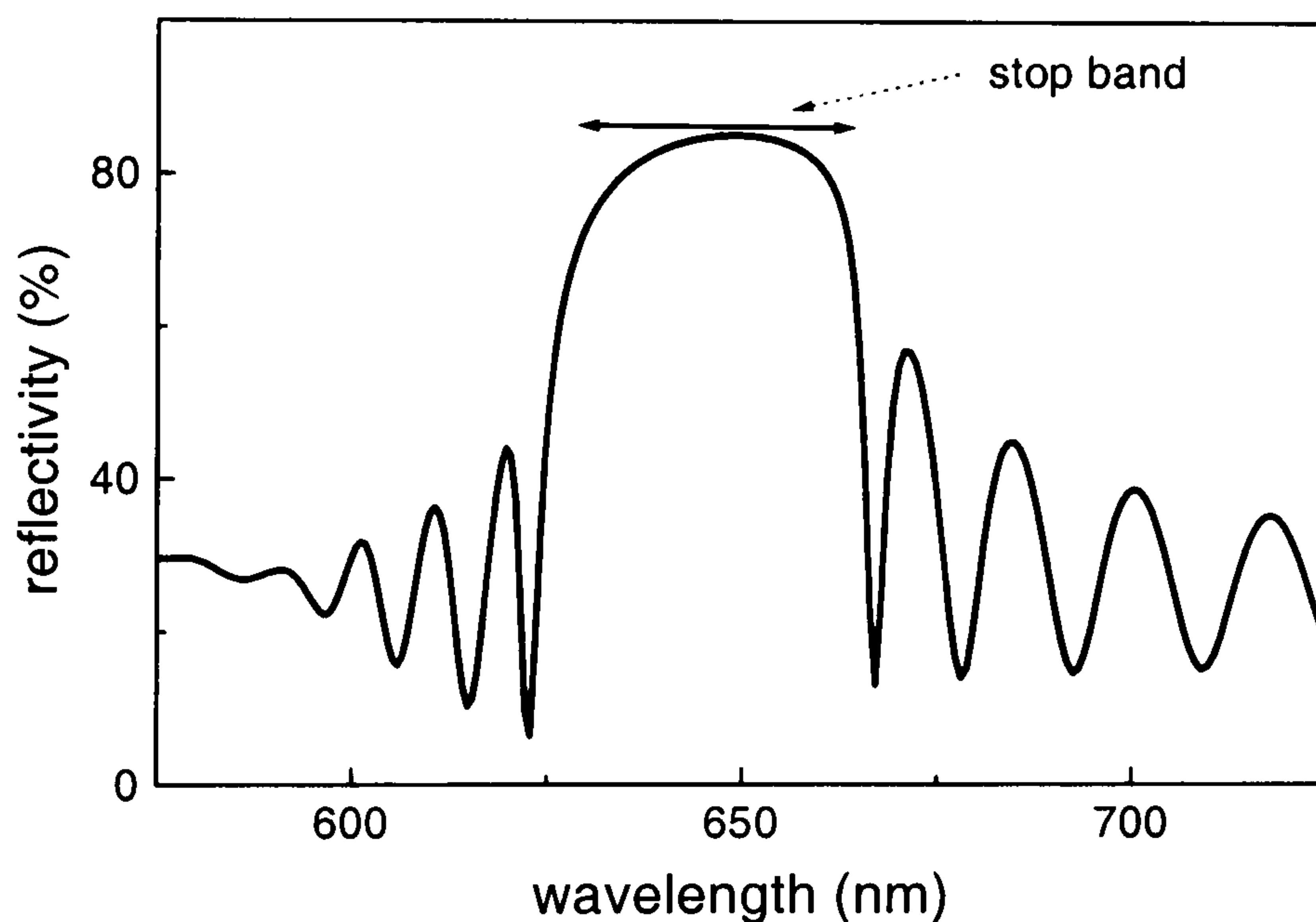

Figure 4.1: Calculated R spectrum of a distributed Bragg reflector indicating the high reflectivity stop band.

If now a cavity is inserted between the DBRs, this is analogous to a defect in a 1D photonic crystal [89] and so produces a localized state. A dip, called the cavity mode, now appears in the high reflectivity stop band. During a measurement of the photo-modulated reflectance, the reflectivity is also simultaneously obtained for all the angles of incidence as the DC component. In figure 4.2 a measured normal incidence reflectivity spectrum of an RCLED wafer with structure S1 can be seen.

Apart from the cavity this RCLED has the same nominal structure as the modelled Bragg stack in figure 4.1. The position of the λ_{CM} at 655.5 nm is marked. The R

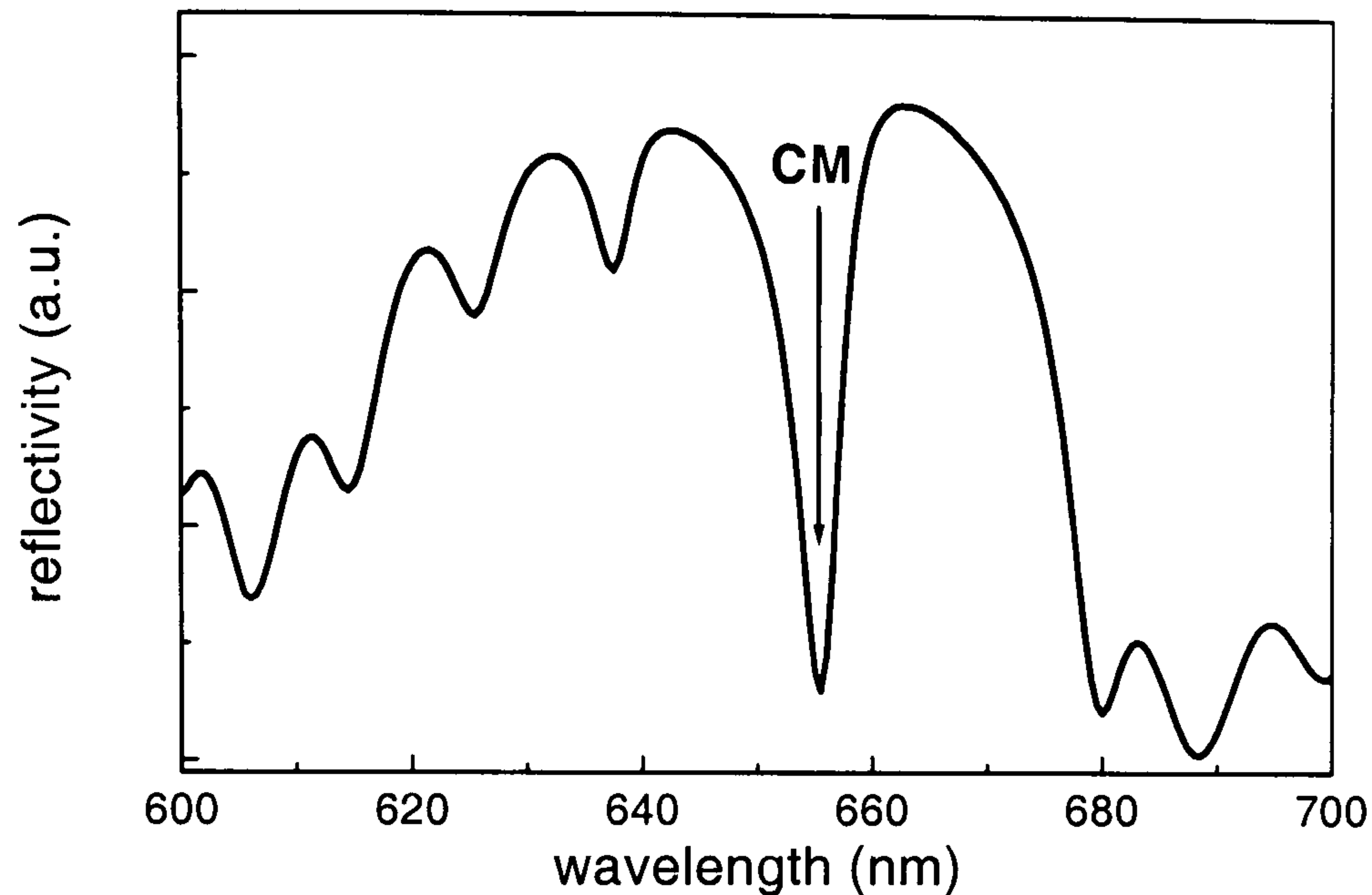

Figure 4.2: The experimental R spectrum of wafer S1 for normal incidence.

spectrum was obtained for normal incidence. λ_{CM} for other angles have also been determined and are plotted in figure 4.3.

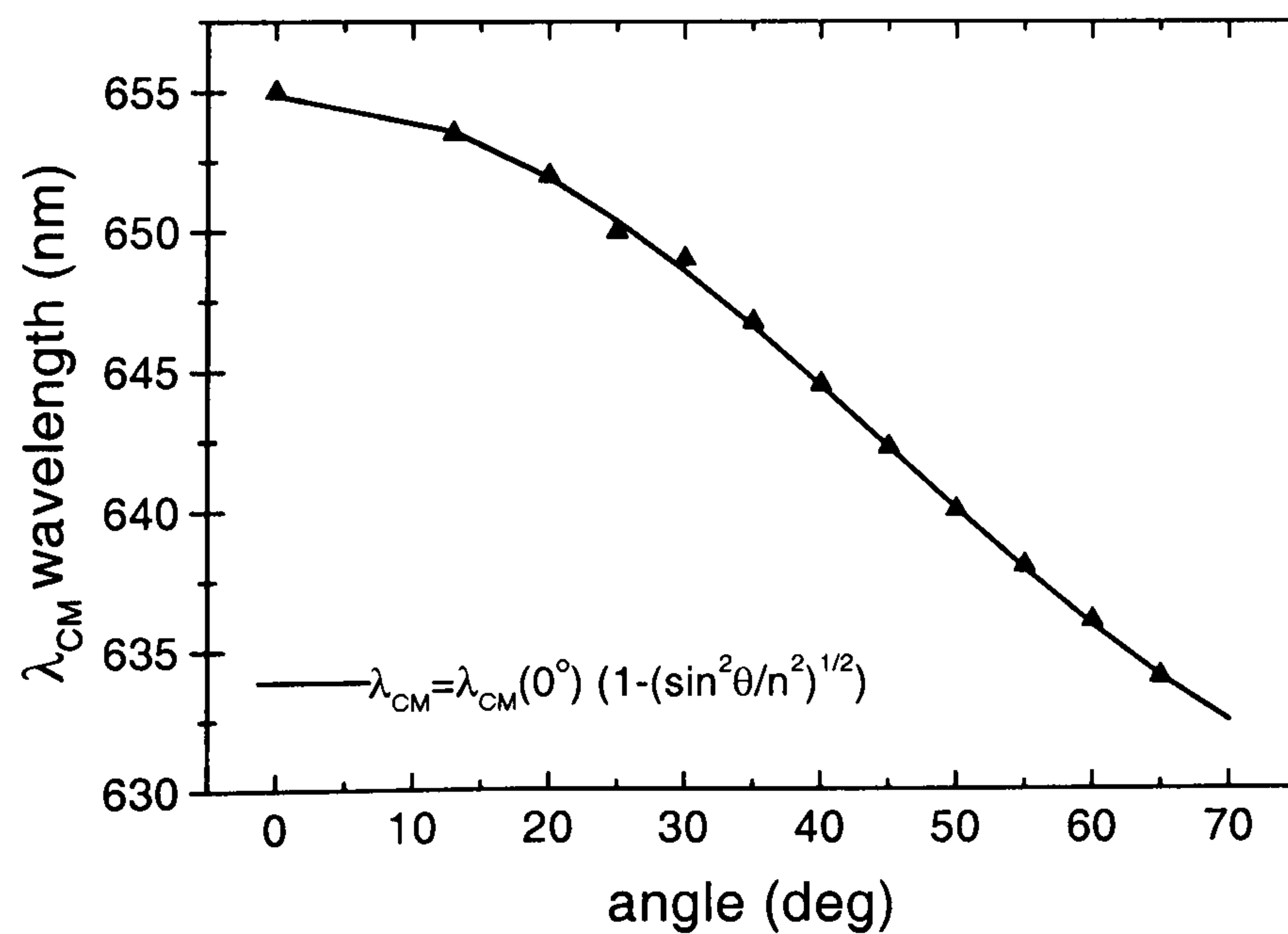

Figure 4.3: λ_{CM} positions for various angles of incidence extracted from R spectra.

The data points are fitted by equation 3.11 as indicated in the graph. The cavity mode at normal incidence ($\lambda_{CM}(0)$) and the effective refractive index (n) can be extracted from the fit. The fit yields a value for $\lambda_{CM}(0) = 655$nm and n=3.6. This agrees well with the measured value of $\lambda_{CM}(0°) = 655.5$nm.

4.2.1 Reflectivity calculations

The reflectivity of a multilayer structure depends on the dielectric functions of all the layers. The total reflectivity spectrum can be calculated by using transfer matrices as has been successfully shown for VCSELs [90]. At each interface, between layers i and j a proportion of the electric field is transmitted into the next layer (j) and a part is reflected into the original layer (i). The total field E_j^+ transmitted from layer i to layer j can be written as

$$E_j^+ = E_i^+ \tau_{ij} + E_j^- \rho_{ji} \tag{4.1}$$

where τ_{ij} is the transmission coefficient at the interface from layer i to layer j and ρ_{ji} the reflection coefficient at the interface from layer j to layer i. Similarly the total field transmitted from layer j to layer i is

$$E_i^- = E_i^+ \rho_{ij} + E_j^- \tau_{ji}. \tag{4.2}$$

The reflection and transmission coefficients (τ, ρ) for each interface can be calculated using Fresnel's equations. In figure 4.4 a schematic layer structure is shown.

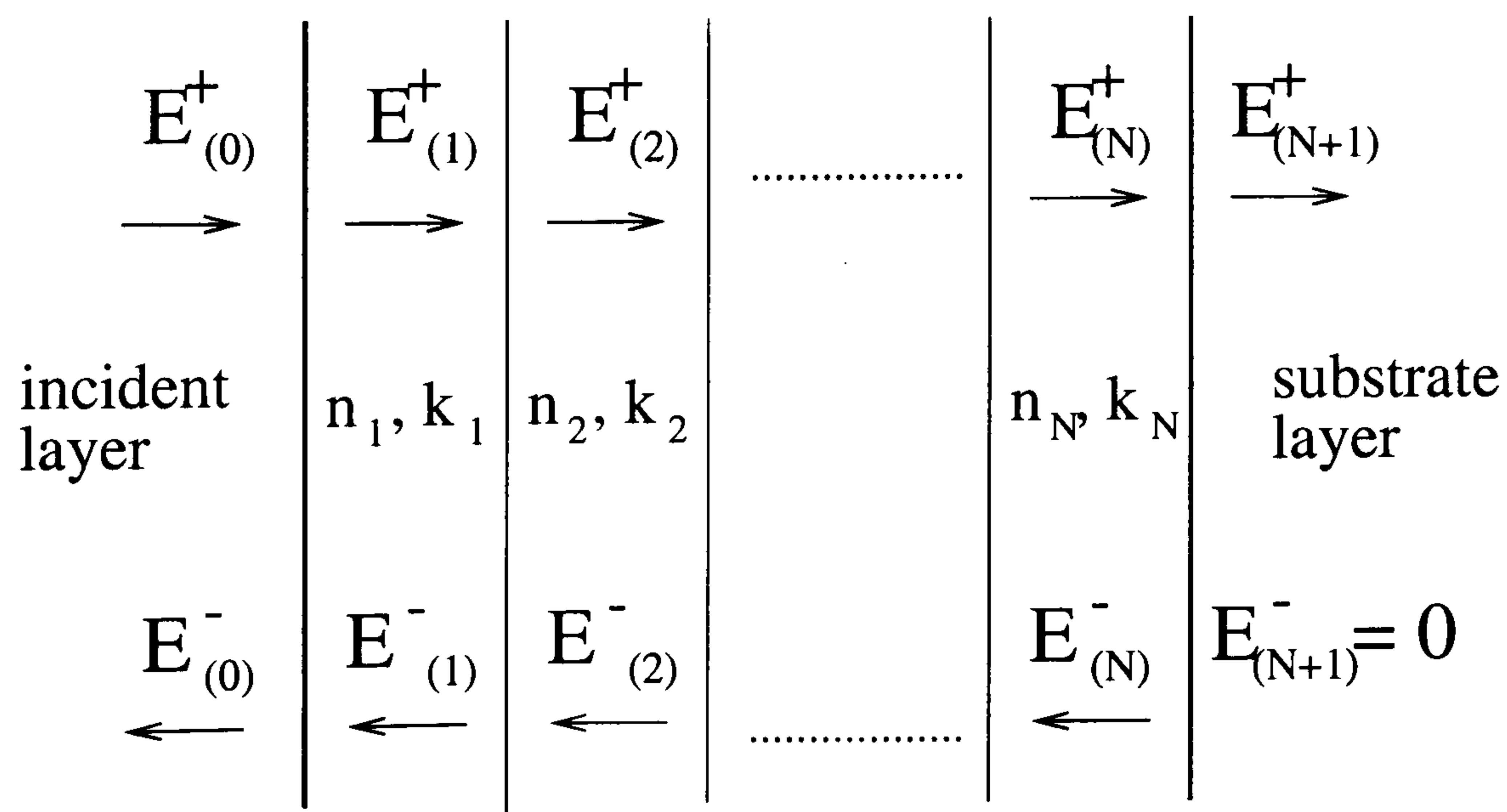

Figure 4.4: Schematic layer structure

If the fields in positive (E_j^+) and in negative (E_j^-) z-direction are now combined to a vector $\mathbf{E_j}$ the transformation from layer i to layer j can be described with a transfer

matrix $\hat{T}$ (details of the matrix formalism can for example be found in [91]):

$$\mathbf{E_j} = \begin{pmatrix} E_j^+ \\ E_j^- \end{pmatrix} = \mathbf{\hat{T}_{ji}} \begin{pmatrix} E_i^+ \\ E_i^- \end{pmatrix} = \frac{\mathbf{1}}{\tau_{\mathbf{ji}}} \begin{pmatrix} 1 & \rho_{ji} \\ \rho_{ji} & 1 \end{pmatrix} \begin{pmatrix} E_i^+ \\ E_i^- \end{pmatrix} \tag{4.3}$$

For the propagation from the left to the right within one layer a phase factor $e^{-i\beta_j}$ has to be added, where $\beta_j = \frac{2\pi}{\lambda_0} n_j d_j cos(\theta_j)$ accounts for the difference in optical path length within layer j and the adjacent layer. Here d_j is the layer thickness and n_j the (complex) refractive index of layer j. The propagation can be represented by another matrix, a propagation matrix

$$\hat{L}_j = \begin{pmatrix} e^{-i\beta_j} & 0 \\ 0 & e^{i\beta_j} \end{pmatrix}. \tag{4.4}$$

If $\hat{T}$ and $\hat{L}$ are determined for all the layers, the field at the left hand side can be calculated with the field from the right side of the layer structure, and all the transfer matrices $\hat{T}$ and propagation matrices $\hat{L}$ are combined into one matrix $\hat{S}$ such that

$$\mathbf{E_0} = \mathbf{\hat{T}_{01}\hat{L}_1\hat{T}_{12}.....\hat{L}_N\hat{T}_{N,N+1}}\ \mathbf{E_{N+1}} = \mathbf{\hat{S}_{0,N+1}}\ \mathbf{E_{N+1}}. \tag{4.5}$$

Finally the boundary conditions $E_{N+1}^- = 0$ stating that the applied field is only incident in the positive z-direction are applied. The matrix $\hat{S}$ of a layer structure can be constructed with the dielectric functions[1] and the layer thicknesses of the materials. The total reflectivity R and the reflectivity coefficient r are related through

$$R = |r^2| = \left|\frac{S_{21}}{S_{11}}\right|^2 \text{ and } r = \sqrt{R}e^{-i\beta_t}, \tag{4.6}$$

where β_t is the total phase change. The calculations are performed using a program developed by Dr J. Hosea based on the theory as described above [92]. An example showing a comparison between calculated and measured spectra for three different wafers with 8, 11 and 14 top DBR pairs can be seen in figure 4.5.

In both the measured and the simulated spectra the decrease in the cavity dip width with increasing number of top DBRs (increasing reflectivity) can be observed. In the simulation the only parameter that was changed between the three structures was the number of top DBR pairs and thus λ_{CM} is constant for all three calculations. The

[1] the wavelength dependent dielectric functions are taken from reference [126]

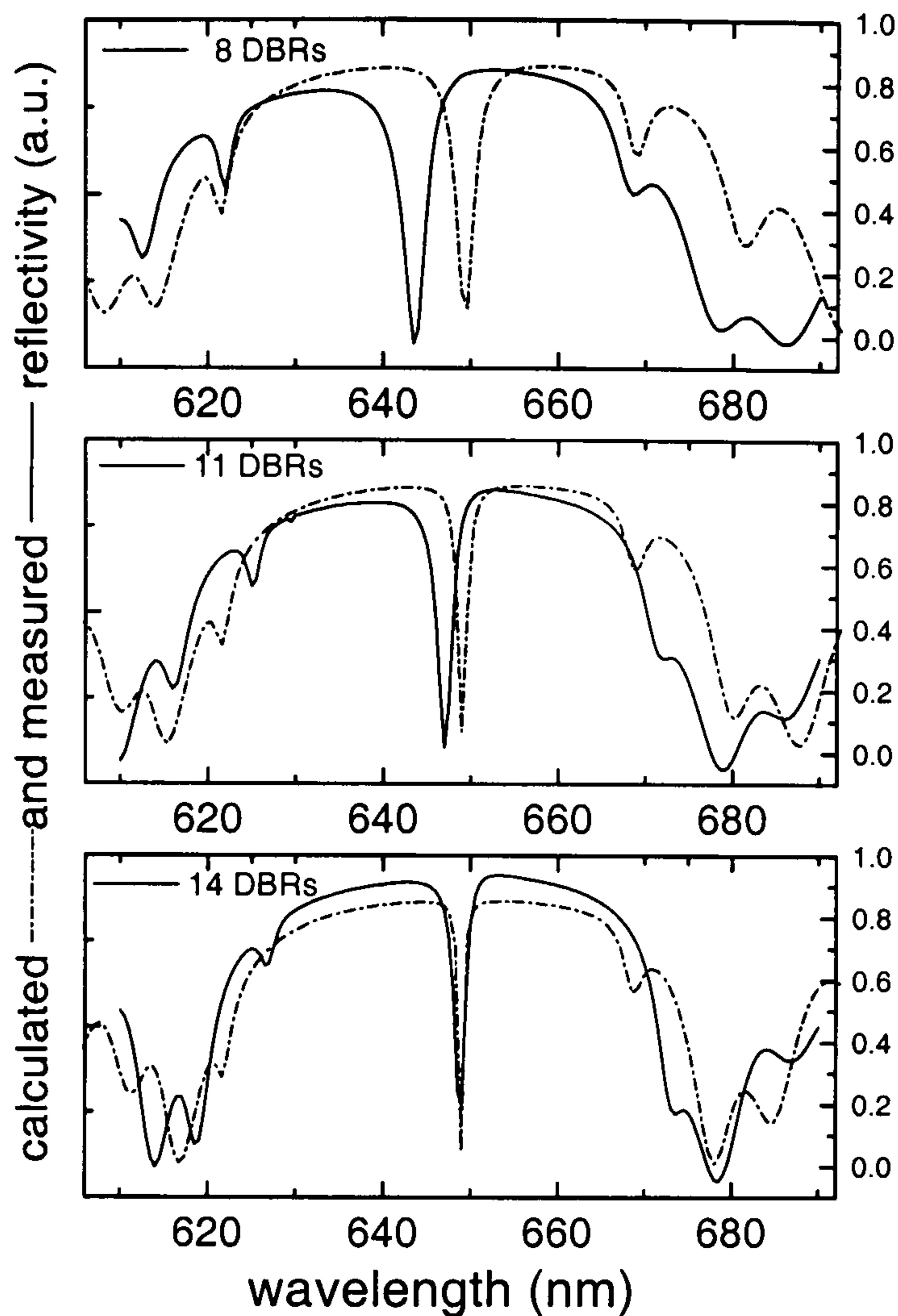

Figure 4.5: Calculated and measured spectra of three RCLED wafers with 8, 11 and 14 pairs of top DBRs. The calculations are performed with the nominal values and the shift between the wafers is due to growth variation.

measured spectra however show a shift towards longer wavelength with increasing number of DBR pairs. This suggests some drift in the growth conditions, resulting in a variation of layer thicknesses between the different wafer growths.

4.2.2 Reflectivity fitting

The calculated reflectivity can also be used to directly fit the measured reflectivity spectra using a least squares fitting procedure [93]. This is a very useful tool as one can use fitting to determine the actual layer thicknesses and to compare them with the nominal values. This very important piece of information can then be fed back to adjust the crystal growth parameters, should there be deviations in the layer thicknesses. If done within the growth facility the feedback could be provided within hours so that a repeat structure can be attempted before the machine conditions have drifted significantly. Figure 4.6 shows both the measured and the calculated

reflectivity spectra using the nominal values for one wafer.

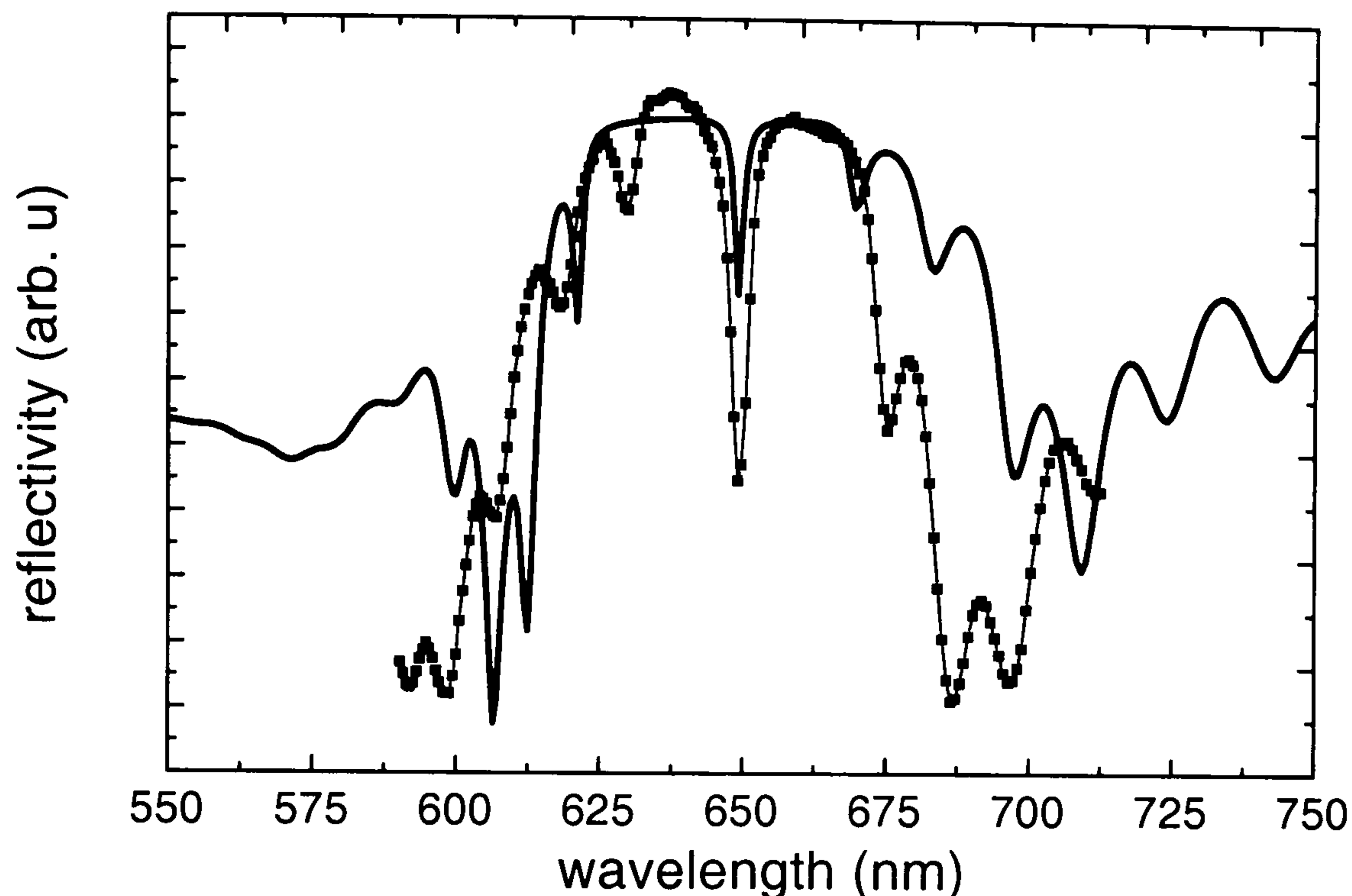

Figure 4.6: Calculated and measured spectra of wafer J01d. In order to compare both graphs the experimental data have been scaled-up.

It becomes clear that, whilst the position of the cavity dip agrees, there are significant differences between the calculated and the measured reflectivity spectra indicating deviations from the nominal structure. By fitting the experimental data, the reasons for this can be found. The fitting routine uses the nominal layer structure but the Al concentration of the $Al_xGa_{1-x}As$ layer, and the thicknesses of the DBRs layers and the cavity, as fitting parameters. To obtain stable fits, several are obtained for a range of fixed Al concentration in which only the DBR thicknesses are varied automatically to give a least squares fit to the measured data. One assumption of the fitting process is that the DBR pairs within the top and bottom DBRs are uniform. A scanning electron microscope (SEM) picture obtained from this wafer confirms that this assumption is reasonable. It was also assumed that the Al concentration was the same throughout the DBRs. Furthermore, to reduce the number of fitting parameters the whole cavity is assumed to consist only of the barrier material (*AlGaInP*) (i.e. the QWs are assumed to have negligible effect on the spectra which is a reasonable assumption). This means that only five layer

thicknesses for the structure are varied, two for the top DBR pairs and two for the bottom pairs. The overall intensity is adjusted by an additional fitting paramter. The left graph of figure 4.7 shows the experimental spectra (squares) together with a set of best fits (lines) for the Al concentration varying between 48% and 64%. It is difficult to visually determine which of the aluminium concentrations gives the best fit, hence the mean squared error, χ^2, a measure of the quality of the fit to the data, is plotted on the right of figure 4.7 as function of the Aluminium concentration.

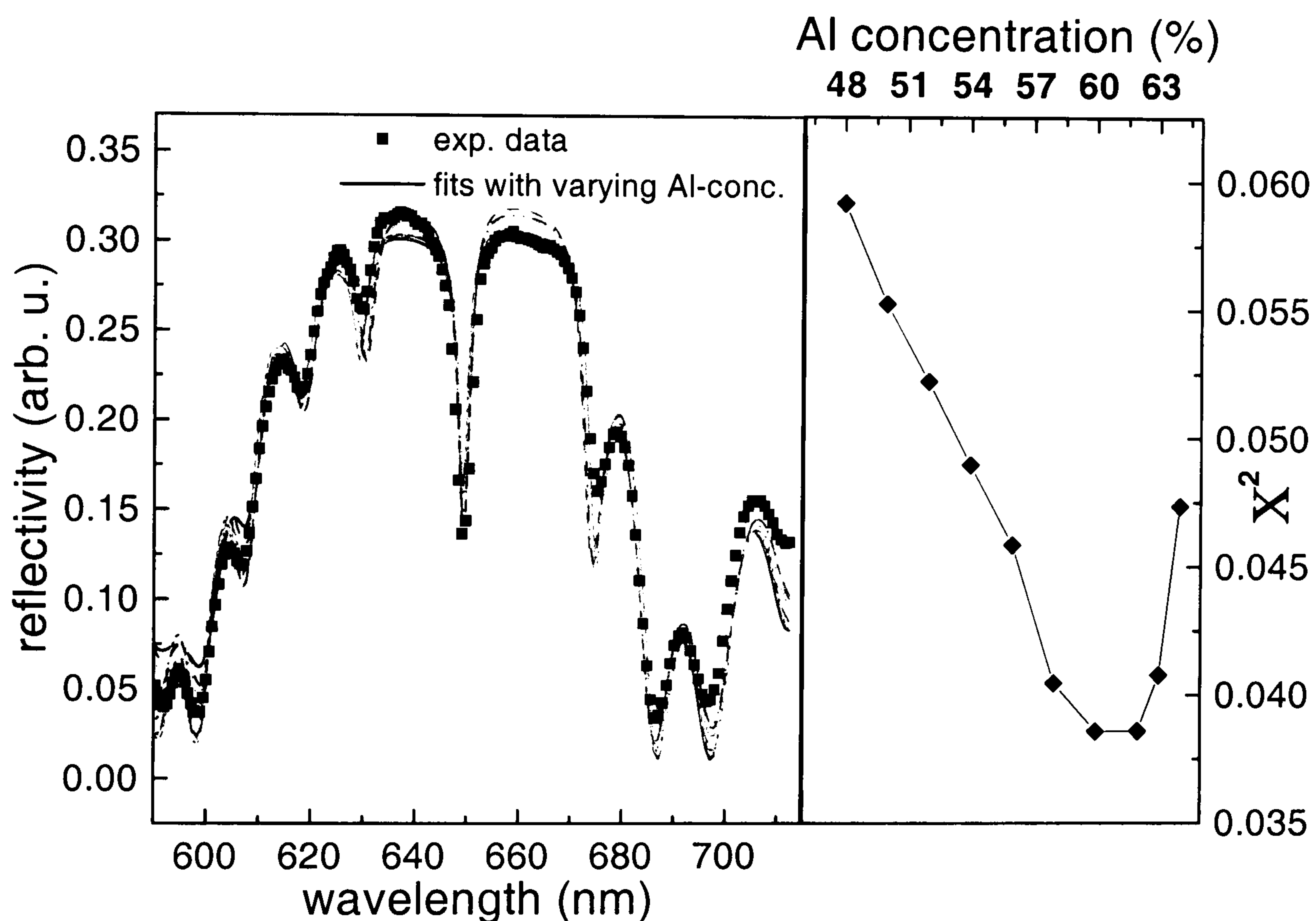

Figure 4.7: Left: Experimental R spectra together with a set of fits for varying aluminium concentration. Right: χ^2 parameter of the fits as a function of Al concentration.

From this it becomes apparent that the best fits are obtained with an aluminium concentration between 60% and 62% and not for the nominal concentration of 50%. Thus the better fits are the ones between 58% and 63%, where χ is minimized. Figure 4.8 shows the layer thicknesses from the fits versus the aluminium concentration. The thicknesses from the fit are shown in the upper graph of figure 4.8. For comparison the nominal values for this structure are plotted in graph 4.8 as lines. The layer thicknesses from the fits assuming Al-concentrations in the range 58%

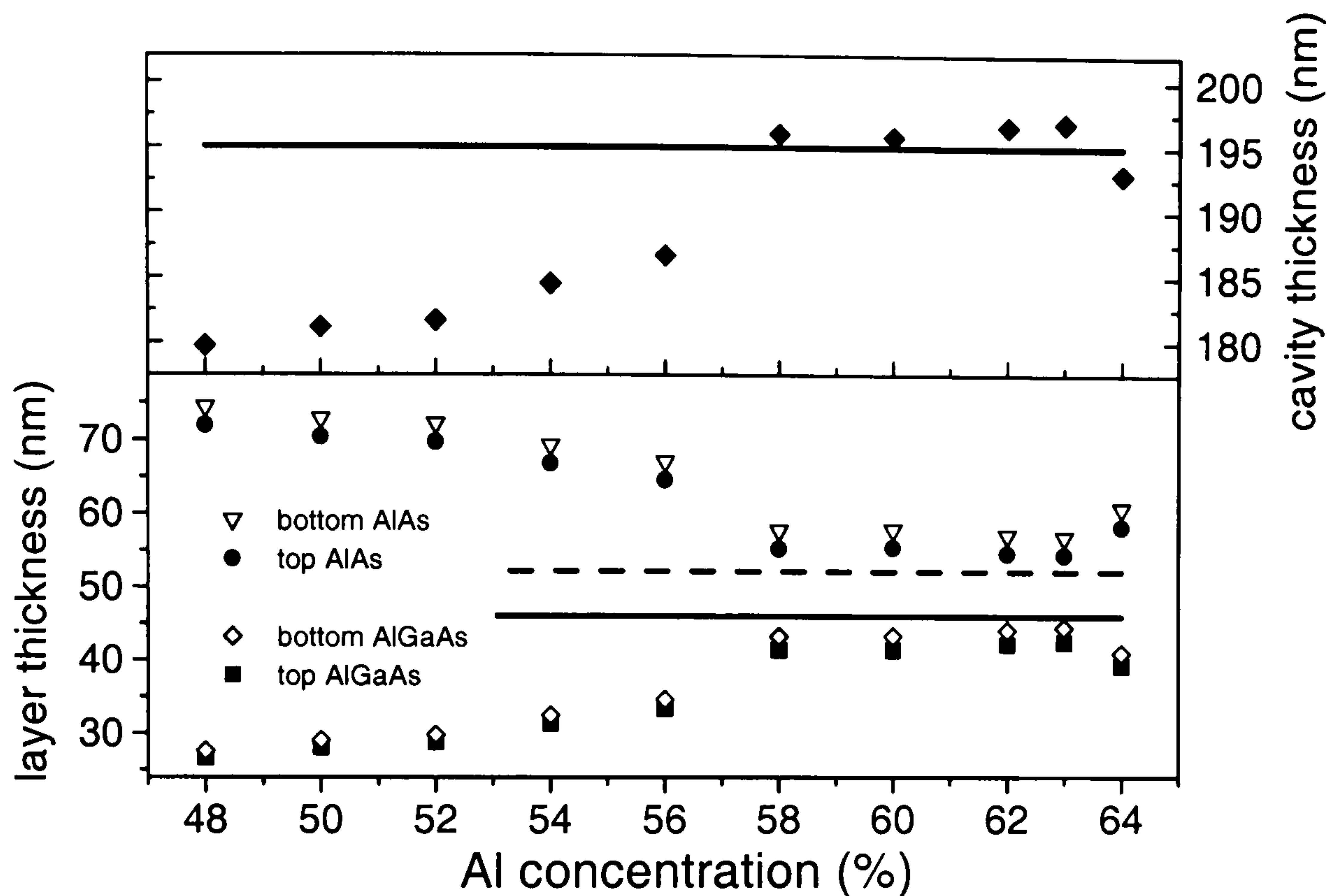

Figure 4.8: Layer thicknesses obtained from the fits versus Aluminium concentration.

to 63% are closer to the nominal ones than for the other Al contents . The fitted DBR thicknesses are within 6% and 10% of the nominal values whereas the cavity thickness agrees to 1%. At the same time the bottom layers appear to be $\sim$ 4% thicker than the top layers. This is also observed in the SEM images. Figure 4.9 shows an SEM image together with an averaged linescan (over 20 lines) plot showing the brightness profile of the SEM image. The linescan is obtained from a program that extracts the brightness values from the SEM image (in this case these values were averaged over 20 pixel-lines). The brighter regions refer to a lower Al content (in this case the *AlGaAs* layers) whilst the *AlAs* layers appear darker.

The linescan shown in figure 4.9 shows that, on average, the bottom pairs are $\sim$ 5% thicker than the top pairs. This is in good agreement with the result obtained from the fitting of the R spectra. Hence with fitting it is possible predict the difference in the layer thicknesses by making reasonable assumptions about the structure.

Furthermore it can be seen from the fits that it is possible to obtain essentially the same R spectra without necessarily having $\lambda/4$-thick layers. Indeed for the fitted wafer the period of the optical thickness of the $AlAs - AlGaAs$ for the bottom

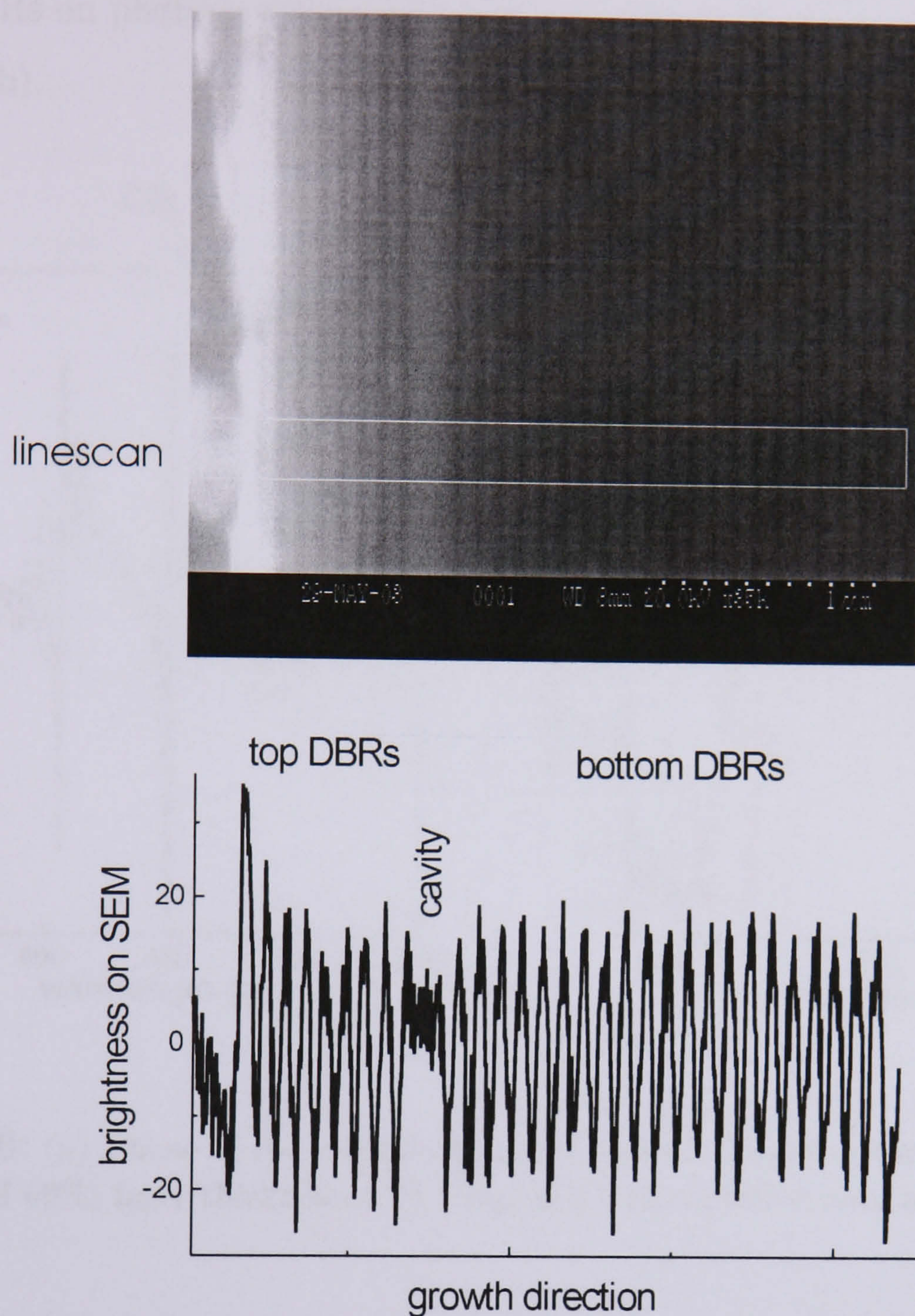

Figure 4.9: SEM picture together with a linescan representing the brightness profile of the SEM. The SEM and the linescan do not show all the bottom layers.

DBRs adds up to $\lambda/2$. The fitting shows that in order to get the appropriate phase change, β_t, as defined in equation 4.6 at the cavity mode wavelength, the actual cavity length had to be changed by 8% if the deviation from quarter wavelength was very high as for the 50% Al concentration. The calculated reflectivity phases for the nominal and the values obtained from the fits with 52% and 60% Al respectively are shown in figure 4.10(a). It shows for all different layer thicknesses the expected phase change at the cavity mode. Finally the individual effect of the top and the

bottom DBRs on photons within the cavity is calculated. The results are shown in figure 4.10(b).

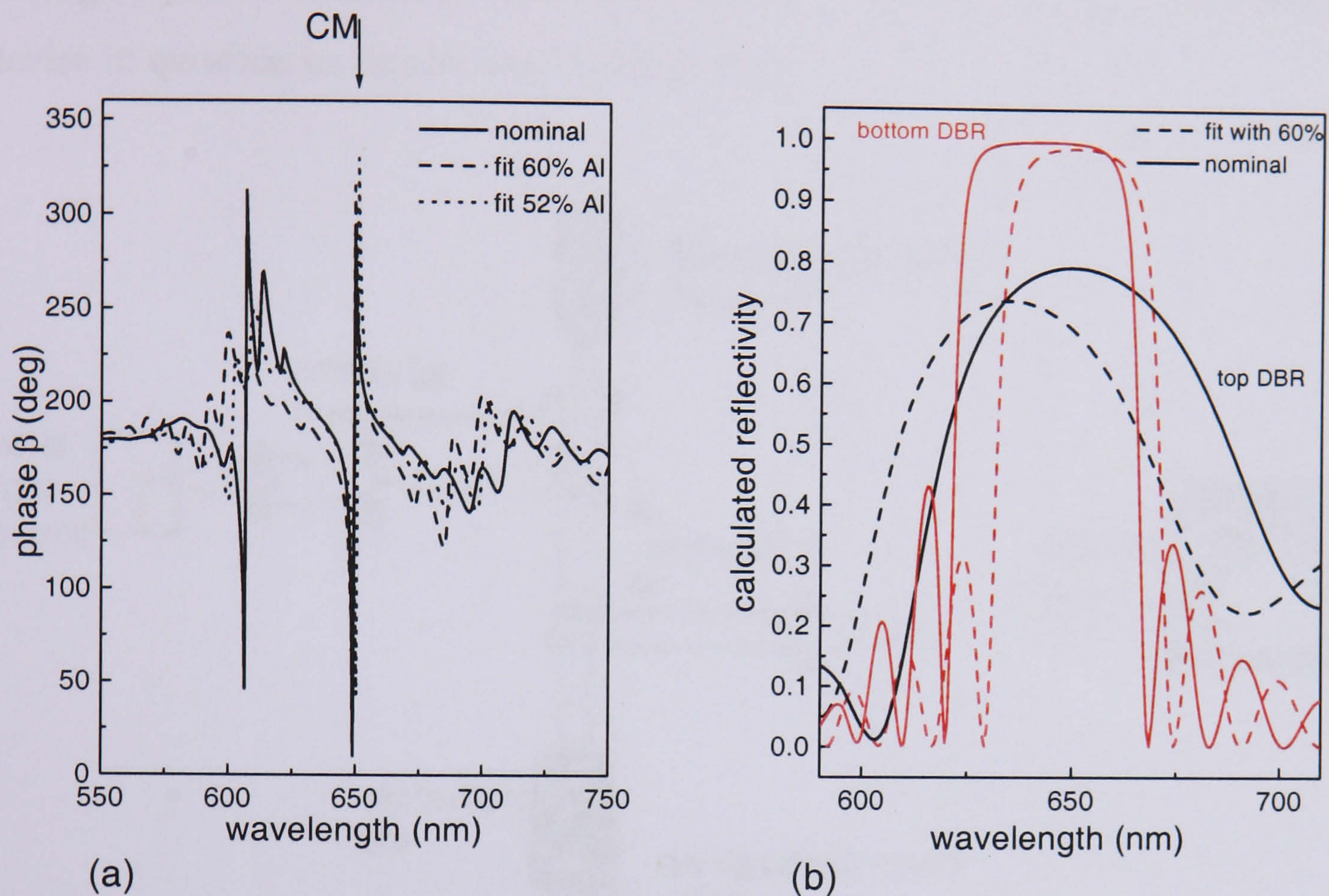

Figure 4.10: (a) Phase of the reflectivity calculated according to the nominal and the fitted (52 and 60%) layer thicknesses. (b) Top and bottom reflectivity as seen from inside the cavity.

From figure 4.10(b) it becomes clear that due to its rapidly varying features the bottom mirror has the stronger influence in determining the total reflectivity. The assymmetry seen for the top mirror is caused by the influence of the air - wafer interface.

4.3 Reflectivity directly on the device

Generally, the cavity mode wavelength varies slightly across each wafer, and between wafers grown in the same growth run, due to non-uniformities of the growth reactor. In order to accurately correlate the features in the emission spectrum of a device, the cavity mode wavelength is determined by measuring the reflectivity directly on

the device itself. This is particularly useful for devices processed from a wafer deliberately grown non-uniformally. To measure the reflectivity, white light passing through a pinhole is focused via a microscope lens onto the emitting aperture of the device in question as can be seen in figure 4.11.

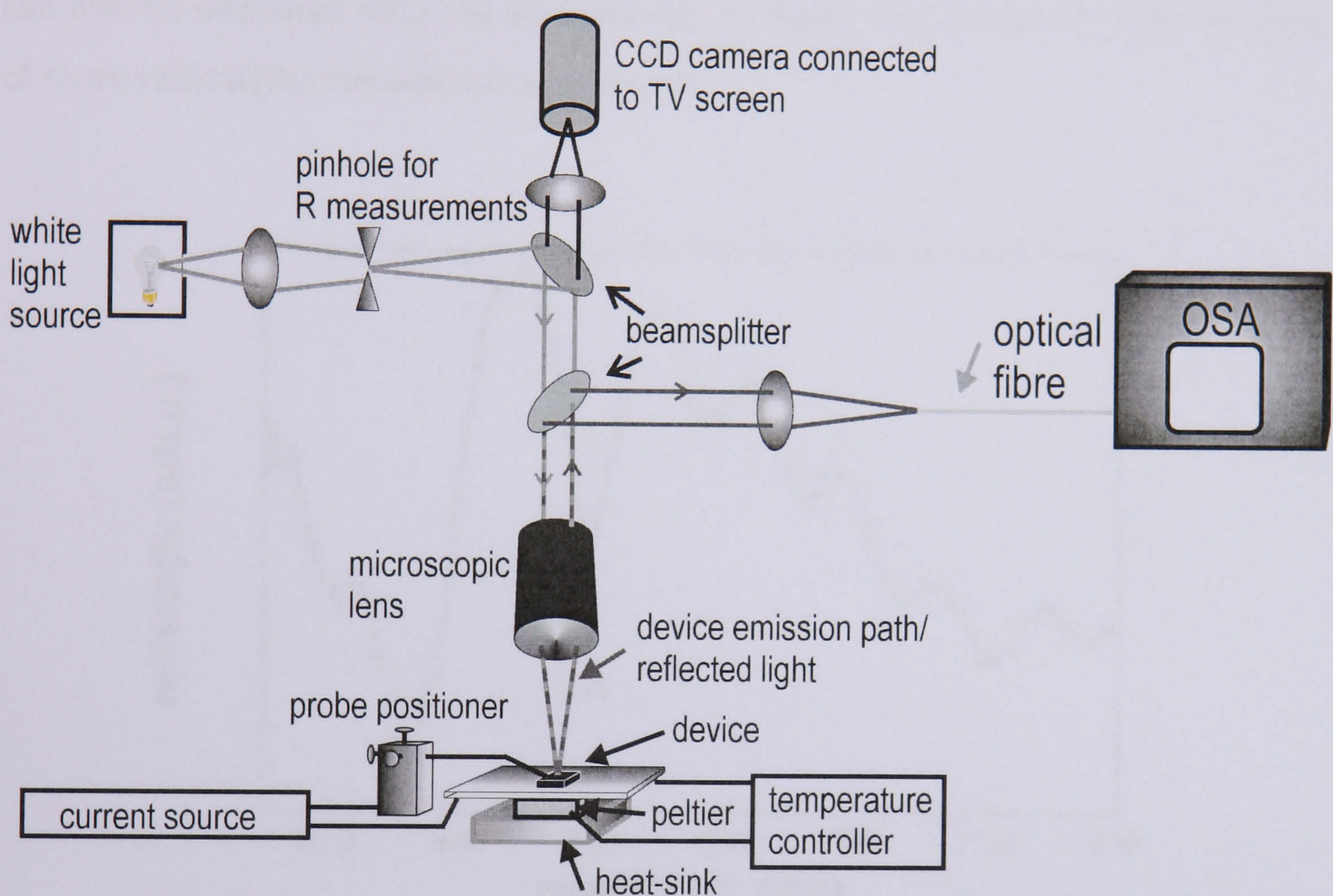

Figure 4.11: Probe station set-up used to do reflectivity measurements directly on a working RCLED device explained in more detail in the text.

In order to place the pinhole so that all of the aperture but not the contacts are illuminated, an image of the device is obtained using a CCD camera and is displayed on a TV screen. The reflected light is collected through the microscope lens and focused by means of another lens into an optical fibre to be analysed using an optical spectrum analyser (OSA). The light level that is finally collected into the OSA is very low and so the obtained reflectivity spectra are noisy. The collection angle is reduced to approximately 5°. Together with the possible variation of CM across the wafer this leads to a broadening of the CM feature. However, as λ_{CM} only changes by $\sim$0.2nm for this angular variation it can be assumed that the measured dip wave-

length corresponds to the normal incidence λ_{CM}. Hence this technique provides a reasonable measure of where the CM is for a certain device. The set-up is also equipped with electrical connections so that bare devices can be probed (electrically contacted). The image on the camera also helps to accurately locate and probe the devices. Therefore, in addition to the R spectra, the electroluminescence spectra can also be measured with the same set-up. In figure 4.12 a typical result from one of these reflectivity measurements is shown.

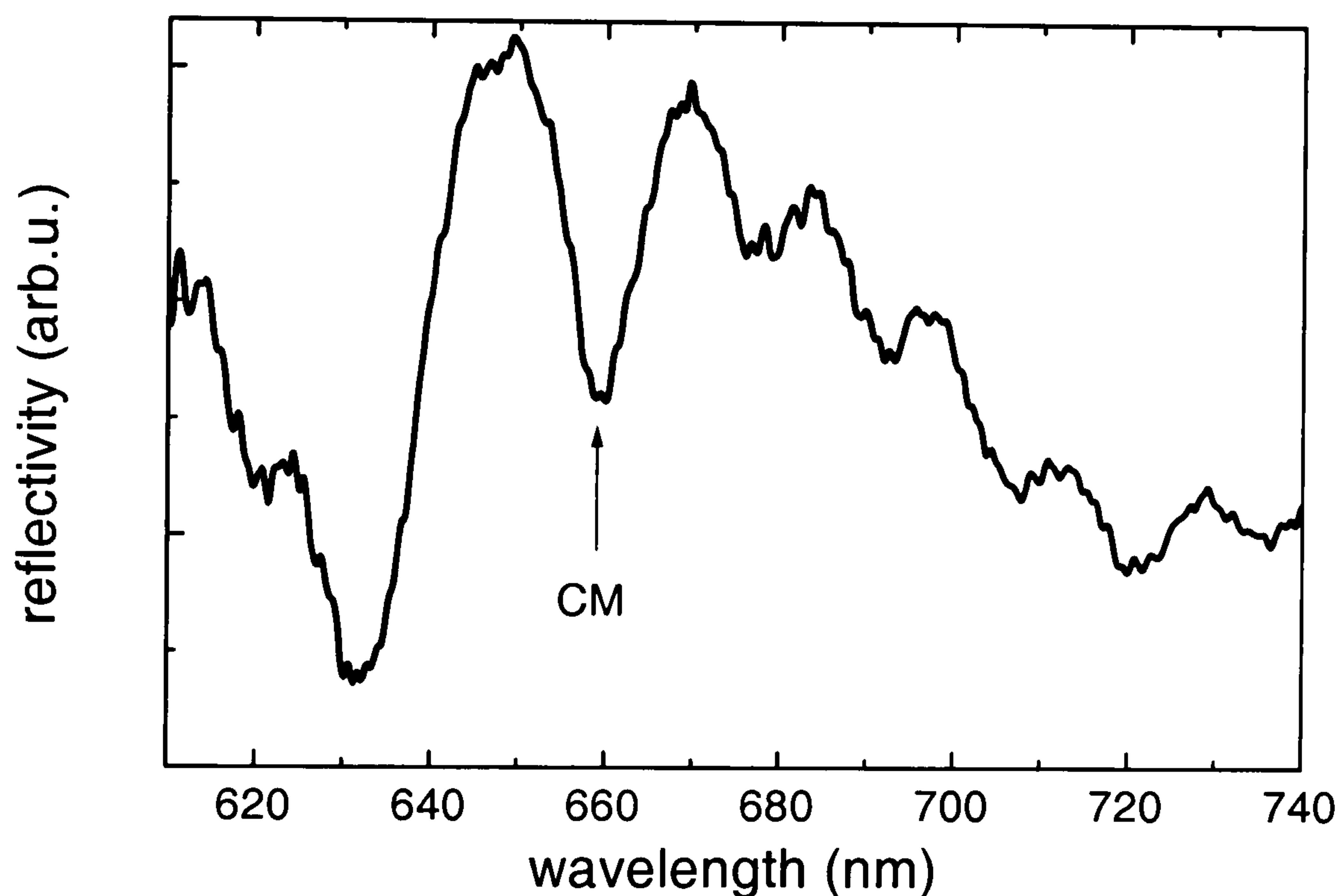

Figure 4.12: Normal incidence reflectivity spectrum of a $75\mu m$ (S1) device measured on the set-up in figure 4.11. The cavity mode $\lambda_{CM} = 659$nm.

As expected the cavity dip is not as sharp as in the earlier presented results of reflectivity spectra from wafers (see for example figure 4.2). However, λ_{CM} can still be clearly identified and in this case is at 659 nm. This measured device was processed from a wafer from the same growth run as the one for which the R spectrum was previously shown in figure 4.2. This indicates a shift of 4.5nm between the two CM measurements. One would expect a slight difference due to the presence of the GaAs cap layer on the wafer (etched away for the device). However, reflectivity calculations of structures with and without the cap layer, give a shift of between only 0.5nm and 1nm. The reason for the experimentally observed shift seems to

lie in the variation of λ_{CM} between different wafers due to the non-uniformity of the growth reactor. In the previous chapter λ_{QW} for this device was determined to be 650nm. Hence a QW-CM de-tuning for all the devices made from this wafer is expected to be about 9nm.

In a similar way the de-tuning can be determined for the devices processed from the wafer with two dissimilar QWs (S2 structure). The R spectrum for a 75μm device is shown in figure 4.13.

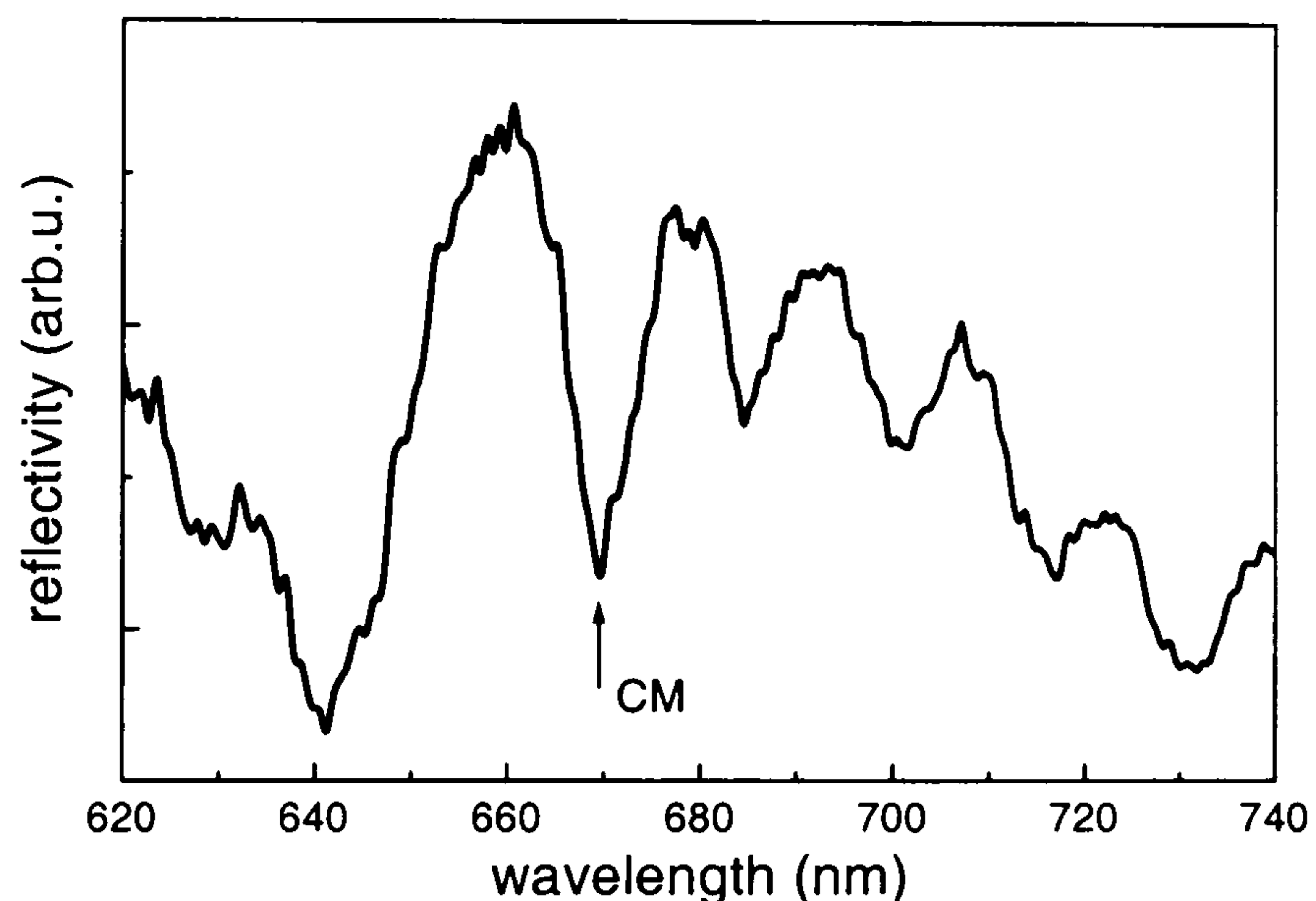

Figure 4.13: Normal incidence reflectivity of an S2 device (with two dissimilar QWs) indicating λ_{CM} at 669.5nm.

Here the CM wavelength is indicated at 669.5nm. The transition wavelengths for the two QWs have been determined in the previous chapter; $\lambda_{QWa} = 654$nm and $\lambda_{QWb} = 642$nm. Thus the de-tuning of the devices is 15.5nm with respect to the first QW and 27.5nm with the respect to the second QW. Therefore both sets of devices differ not only in the number of QW transitions but also in the de-tuning with respect to the QWs and the emission wavelength.

4.3.1 Temperature dependence

To observe the temperature shift of the cavity mode, the set-up in figure 4.11 is also equipped with a Peltier thermoelectric cooler (TEC) and a temperature controller to vary the temperature in the range of 15°C to 75°C . Due to the thermal expansion of the layers, the CM wavelength increases slightly with temperature. The more

prominent effect is the increase of the refractive indices of the layers with temperature which increases the optical cavity length [80], [94]. In figure 4.14 the R spectra of one device at two temperatures can be seen.

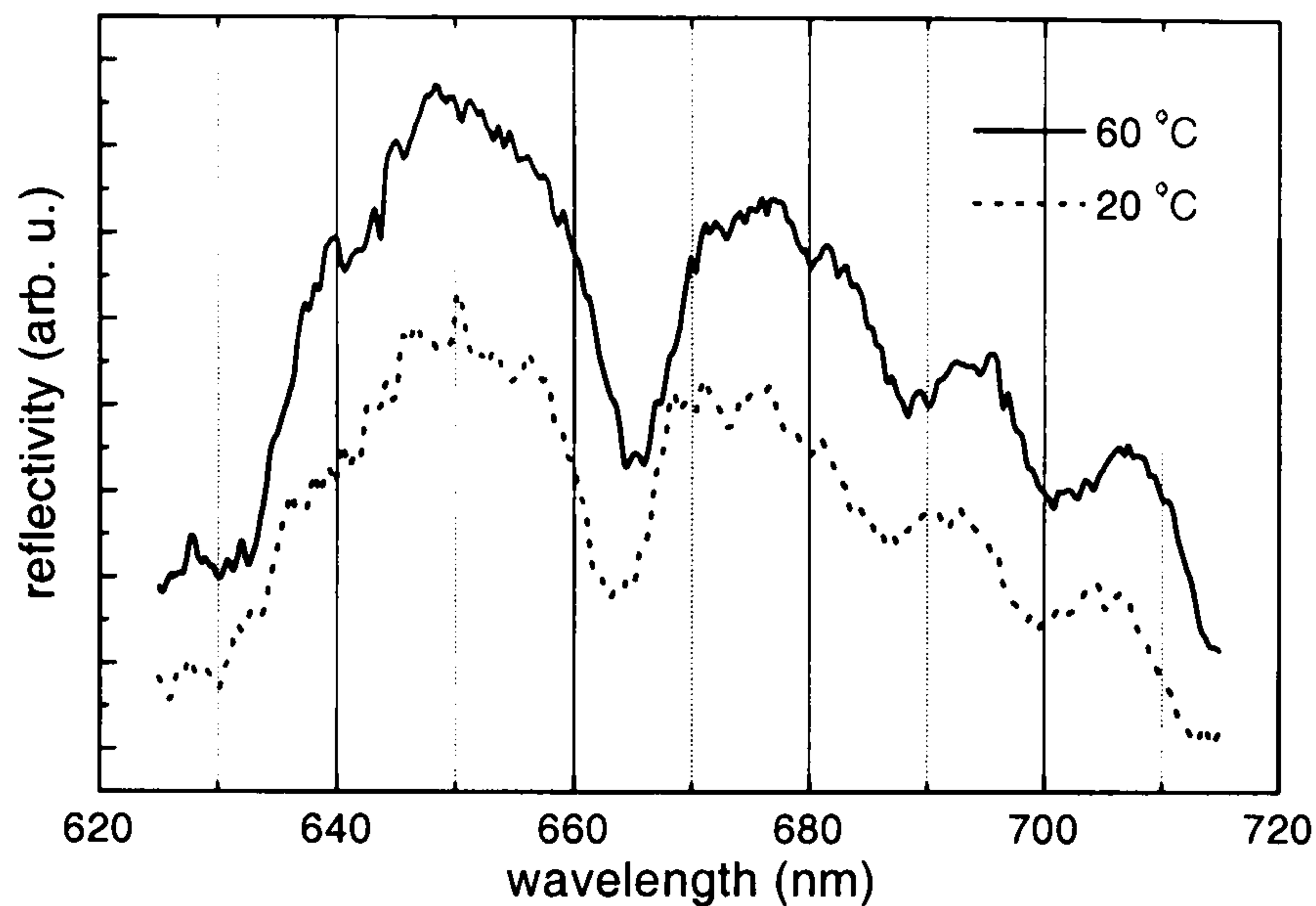

Figure 4.14: Reflectivity spectra from a device at 20°C and 60°C. The shift of λ_{CM} is 1.5nm.

The λ_{CM} at 20°C is determined to be (643.5±0.7)nm and (665±0.7)nm at 60°C. The 1.5nm shift, which corresponds to a shift of 0.0375nm/degree, is the same as has been found in red VCSELs [81]. For a range of wafers, λ_{CM} shifts between 1.3nm and 1.8nm have been observed between 20°C and 60°C .

In additon to the cavity mode shift, the QW emission is also temperature dependent. It not only broadens with increasing temperature but the peak wavelength also increases (as the bandgap decreases). To estimate the shift for GaInP a linear extrapolation of the shifts of GaP and InP is performed. Using the Varshni equation (equation 3.10) and the values for the Varshni coefficients a and b of GaP and InP from [95] [1] leads to a temperature shift of $\sim$ 0.14nm/degree which is about 3 to 4 times larger than the shift of the cavity mode. This has strong consequences for the temperature sensitivity of the devices. This will be discussed in the next chapter, in particular for devices with a difference in the initial (at room temperature) QW-CM de-tuning.

[1] $a_{InP} = 0.363meV/K$, $b_{InP} = 162K$, $a_{GaP} = 0.5771meV/K$, $b_{GaP} = 372K$

4.4 Conclusions

In this chapter theoretical and experimental approaches for finding λ_{CM} have been discussed. λ_{CM} can be extracted as the main dip in calculated and measured reflectivity spectra. The reflectivity of the multilayer structures investigated here can be calculated using transfer matrices. The spectra are calculated assuming nominal layer thicknesses and are compared with experimentally determined reflectivity spectra. To find the reasons for any discrepancies between theory and experiment, the measured spectra are fitted with a least squares fitting algorithm in which layer thicknesses and compositions can be varied. Fitting has been shown to be a valuable tool for predicting differences in the layer thicknesses.

The variation of λ_{CM} within a wafer and between wafers grown during the same growth run, led to the need to develop a technique of measuring λ_{CM} directly on working devices. With this technique the reflectivity, and thus λ_{CM}, can be measured for different devices and, with the knowledge of λ_{QW}, the de-tuning for each of the devices can be obtained. Finally, the temperature dependence of λ_{CM} has been measured. Compared with calculations of the shift of λ_{QW} with increasing temperature it has been found that the shift of λ_{CM} is about 3 - 4 times smaller. This leads to a strong temperature-induced tuning/ de-tuning effect. The consequences of this for the device temperature sensitivity will be discussed in the next chapter.

Chapter 5

Effect of cavity mode - quantum well de-tuning

5.1 Introduction

In contrast to a VCSEL where the wavelength of the light output is entirely determined by the CM wavelength, in a RCLED the QW peak position also influences the spectral position of the light output due to the lower finesse of the cavity. As λ_{CM} and λ_{QW} vary differently with temperature and λ_{CM} varies with the angle, it is useful to compare the light output of devices with different relative positions of λ_{QW} and λ_{CM} as a function of angle and temperature. In this chapter the influence of this λ_{CM} -λ_{QW} de-tuning on the performance of the RCLED devices will be discussed. One of the important characteristics of device performance is their temperature sensitivity. λ_{QW} and λ_{CM} both increase with temperature but λ_{QW} moves much faster. The different rates have been stated in chapter 4 and [81]. In this chapter a rate of change for λ_{CM} of 0.0375nm/°C and for λ_{QW} of 0.147nm/°C are used in accordance with Knowles et al [81]. A positive de-tuning ($\Delta\lambda = \lambda_{CM} - \lambda_{QW} > 0$) should help to make the devices less temperature sensitive. The maximum efficiency should occur when the QW emission peak is centred in the middle of the spectral escape window

[96] as then the highest proportion of light produced should be able to leave the device. The range of wavelengths (the spectral escape window) that can leave the devices lies between $\lambda_{CM}(0°)$ and $\lambda_{CM}(90°)$ and hence is approximately 30nm for the devices investigated here. To allow all wavelengths of an underlying spectrum that stretches over 30nm to exit the device it is best if this emission is centred in the escape window. This would lead to an optimum de-tuning of 45°, which corresponds to ~15nm for the devices investigated here. This assumes that all of the total light output is collected. The FWHM of the QW emission of the devices investigated here is ~22nm, so more than ~ 60% of the emission could already exit the device if the QW emission was only 11nm de-tuned.

In this chapter, the influence of the QW-CM de-tuning on the device performance will be described. Firstly the angular dependence of the light output and thus the far field pattern is investigated. For different emission angles λ_{CM} changes but λ_{QW} remains constant. The maximum light output (for a particular cross-section and not per unit solid angle) occurs at the angle where both features are aligned. This angle indicates the degree of positive de-tuning. Electroluminescence spectra for different emission angles help to confirm the expected de-tuning from PR and far field measurements. Spectra obtained at normal incidence but with a greater collection angle (similar to the collection angle of plastic optical fibre) show the influence of the de-tuning on the lineshape, the maximum light output and also the difference in the spectral shift with temperature. The effect of different amounts of de-tuning on the temperature dependence can be seen on the spectra and also on the total light output for temperatures up to 80°C. The main contributions to the temperature sensitivity of 650nm RCLEDs, namely carrier leakage and self-heating are introduced. The chapter concludes by stating the advantages and disadvantages of λ_{CM} -λ_{QW} de-tuning.

In order to provide samples that are identical apart from the amount of the de-tuning, the devices compared here were processed from a wafer which was deliberately not rotated during the growth. Wafers are normally constantly rotated during the deposition of epitaxial layers to achieve uniformity. By not rotating them

the thickness of all the layers varies across these wafers. The λ_{QW} is not appreciably influenced by such small variations but the λ_{CM} varies gradually across this wafer. Apart from a few exceptions the results presented here are all from devices either made from the S1 (structural details in the appendix) or the equivalent non-rotated wafer. The λ_{QW} (assumed to be constant) for the wafer was determined by PR and edge-EL as described in chapter 3 to be 650nm at 20°C. The λ_{CM}s were then measured on the individual devices as discussed in chapter 4. The R spectra will be shown together with the EL spectra measured on the same devices in section 5.4. The λ_{CM}s that were measured at 20°C, varied from 647.3nm and 666.7nm and in this and the following chapters the devices will be labelled according to their λ_{CM} at 20°C. To avoid further complications only devices of one aperture size (70μm) were used to compare the temperature dependent light output.

5.2 Angular dependence - far field pattern

A measure of the de-tuning can be obtained from the angular dependence of the light output. The far field pattern shows the light intensity far from the device. One way of measuring the angular response is to mount the device on a turntable which can be rotated over 180 degrees and set a small detector that is connected to an optical power meter (OPM) ~90cm away. A schematic of the set-up can be seen in figure 5.1.

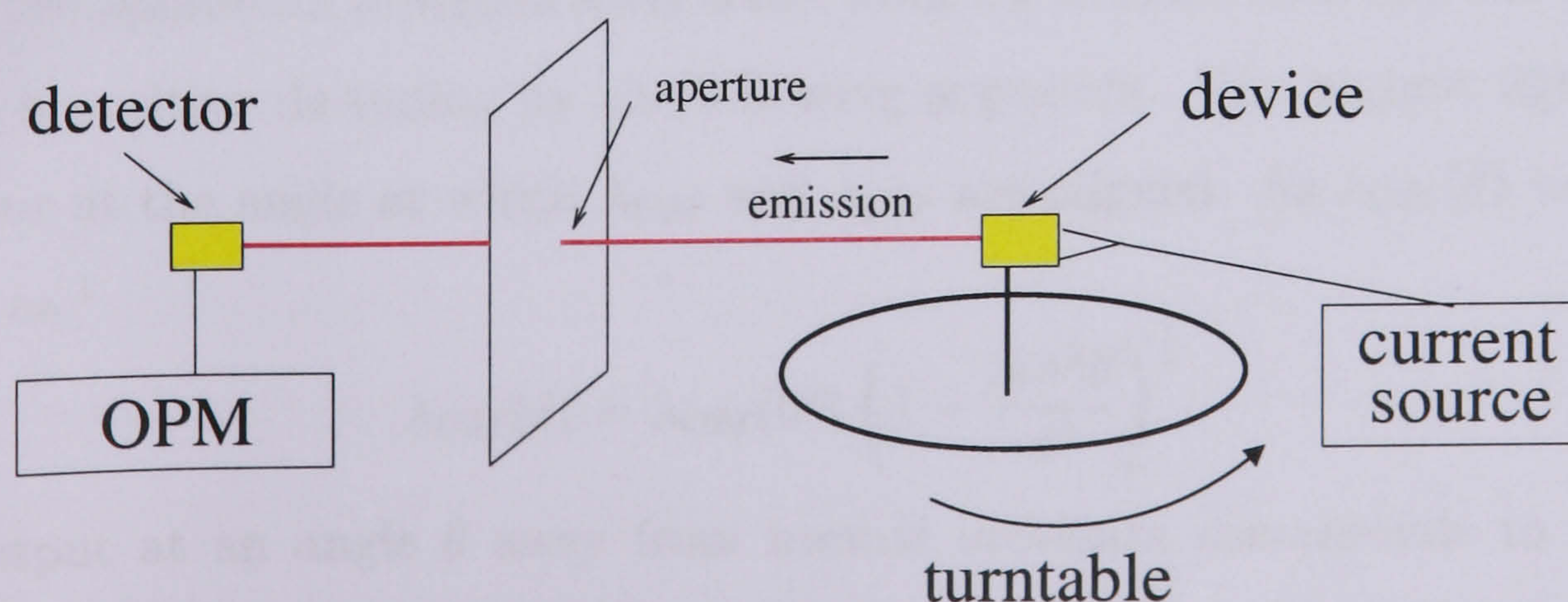

Figure 5.1: Se-tup to measure the far field.

The numerical aperture (NA), a measure of the maximum acceptance angle, ϕ, for the set-up in figure 5.1 can be calculated as $NA = sin\phi = \frac{r}{\sqrt{d^2+r^2}}$, where r is the radius of the detector and d the distance between the device and this detector. The detector used has a 4mm diameter and was placed 90cm from the device giving an NA=0.002, and an acceptance cone of 0.3° and thus a very tight angular resolution. Hence with this set-up measurements can be made in small steps $\sim$ 1°. The light output as a function of angle can be recorded and plotted on a polar graph as seen in figure 5.2. The resulting graph then shows at which emission angle the highest intensity occurs.

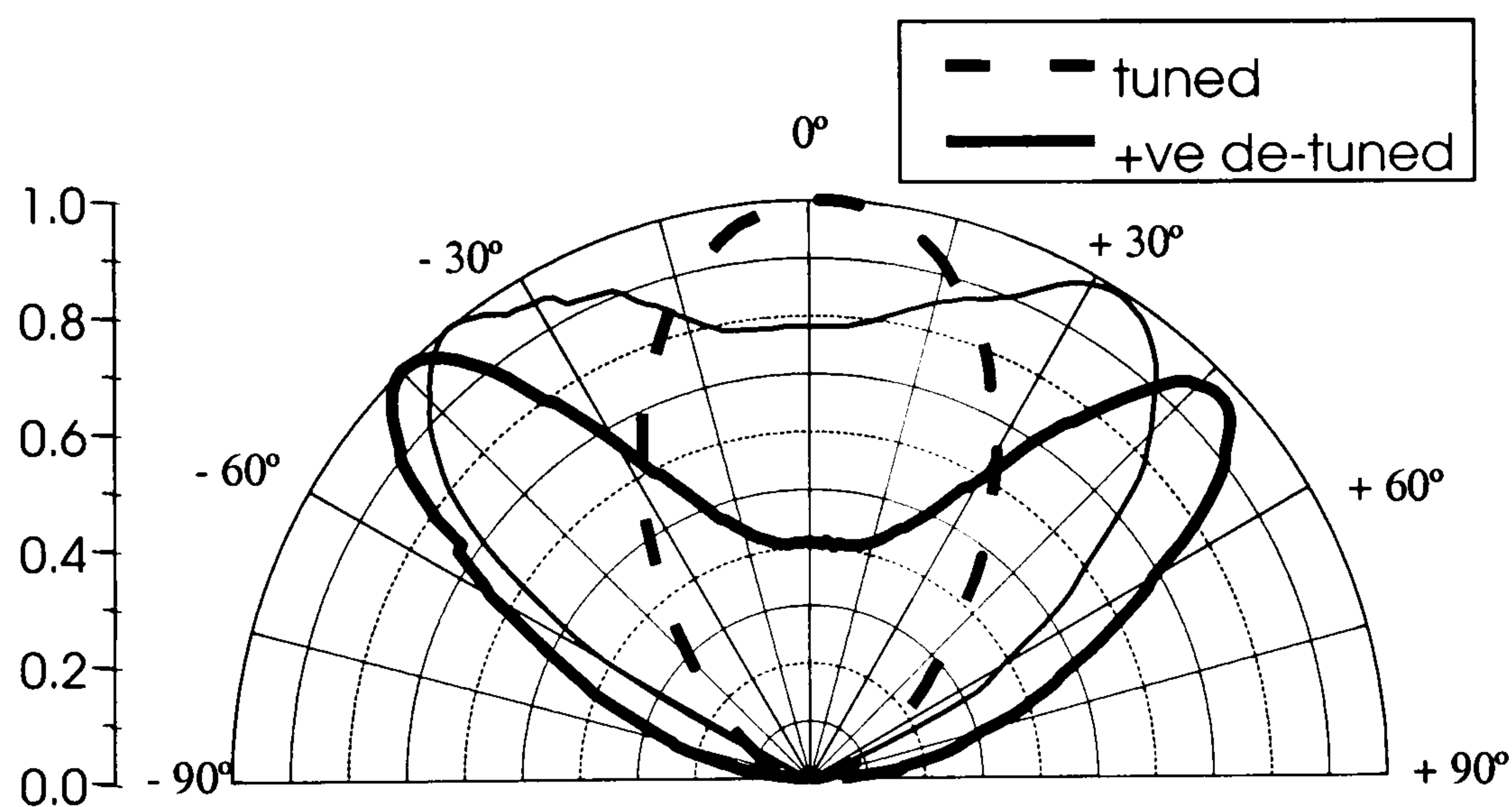

Figure 5.2: Far Field pattern for three different devices from different wafers (O1 (thick dashed line), O2 (thick solid line) and S1 (thin solid line)) measured at 20mA and 20°C.

If the maximum is significantly away from the normal then one can infer that there is a positive de-tuning by the following argument. The highest light output will occur at the angle at which λ_{CM} and λ_{QW} are aligned. As $\lambda_{CM}(\theta)$ varies with angle θ as [1]

$$\lambda_{CM}(\theta) = \lambda_{CM}(0°)\left(1 - \frac{sin^2\theta}{n^2}\right)^{\frac{1}{2}}, \tag{5.1}$$

light output at an angle θ away from normal incidence corresponds to a shorter wavelength of $\lambda_{CM}(\theta)$. If now the peak in the far field spectrum occurs at an

[1] This has already been shown as equation 3.11 in chapter 3 but is repeated here for convenience.

angle away from the normal it means that λ_{QW} and λ_{CM} are aligned at this angle. Therefore the peak wavelength of the QW transition will be at $\lambda_{CM}(\theta)$, a shorter wavelength than the CM at normal incidence (as can be seen from equation 5.1) and hence the device will be positively de-tuned. In figure 5.2 three far field patterns measured at 20°C with the set-up described in figure 5.1 are shown. The intensity is normalised to the peak intensity for each curve and the 0° direction corresponds to normal incidence. Together with the far field of one of the S1 devices two more devices are shown, illustrating the effect of de-tuning on the far field pattern. The device that has its highest intensity at normal incidence is a tuned device (at 20°C) and the two with their highest intensity at 45° (device O2) and ~35° (device S1) either side away from the normal are highly (positively) de-tuned. The exact amount of de-tuning for the O1 and O2 devices could not be confirmed independently, as no wafers were available to perform PR measurements. However for the S1 device a de-tuning of 9nm has been found in chapters 3 and 4 corresponding to a peak in the far field between 34 and 36°. This is consistent with the far field pattern.

These far fields give a first insight into the nature and the amount of the de-tuning of the devices. They also help to visualise the effect of de-tuning. To learn more about the underlying de-tuning of a device the wavelength dependence of the far field shall be considered next. With this method it is possible to more precisely quantify the degree of de-tuning for the S1 devices.

5.3 Angular dependence - EL spectra

Since the CM wavelength varies with angle as described in equation 5.1, the peak wavelength of the light output will also depend on the emission angle [97]. To measure the spectral, angular dependency, the devices were mounted on a rotation stage. A current of 1mA was passed through the devices and the resulting light output was collected from a small solid angle only, using a fixed optical fibre, as seen in figure 5.3. The light output was then analysed by an optical spectrum analyser (OSA),

which provided a spectral resolution of 0.2nm. Here the $NA \sim 0.02$ as the core diameter of the fibre is 67μm and the device was ~2-2.5mm away from it.

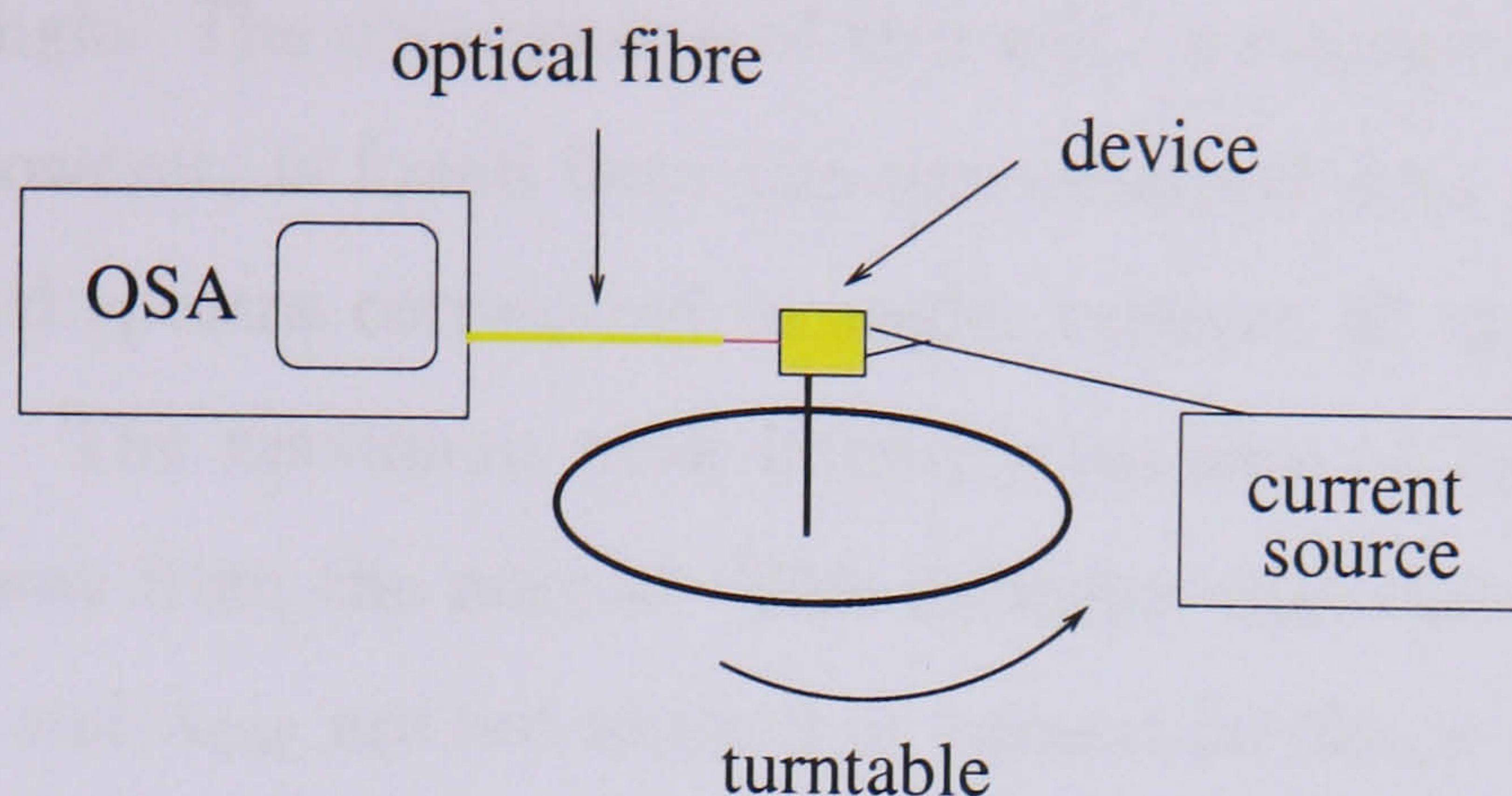

Figure 5.3: Set-up to measure angle dependent EL spectra.

A spectrum for each emission angle was recorded. The optical fibre used was a standard multimode silica fibre and the spectra were internally corrected for the fibre and OSA response. The angular dependent EL spectra for one device with a 50μm aperture diameter are shown in figure 5.4.

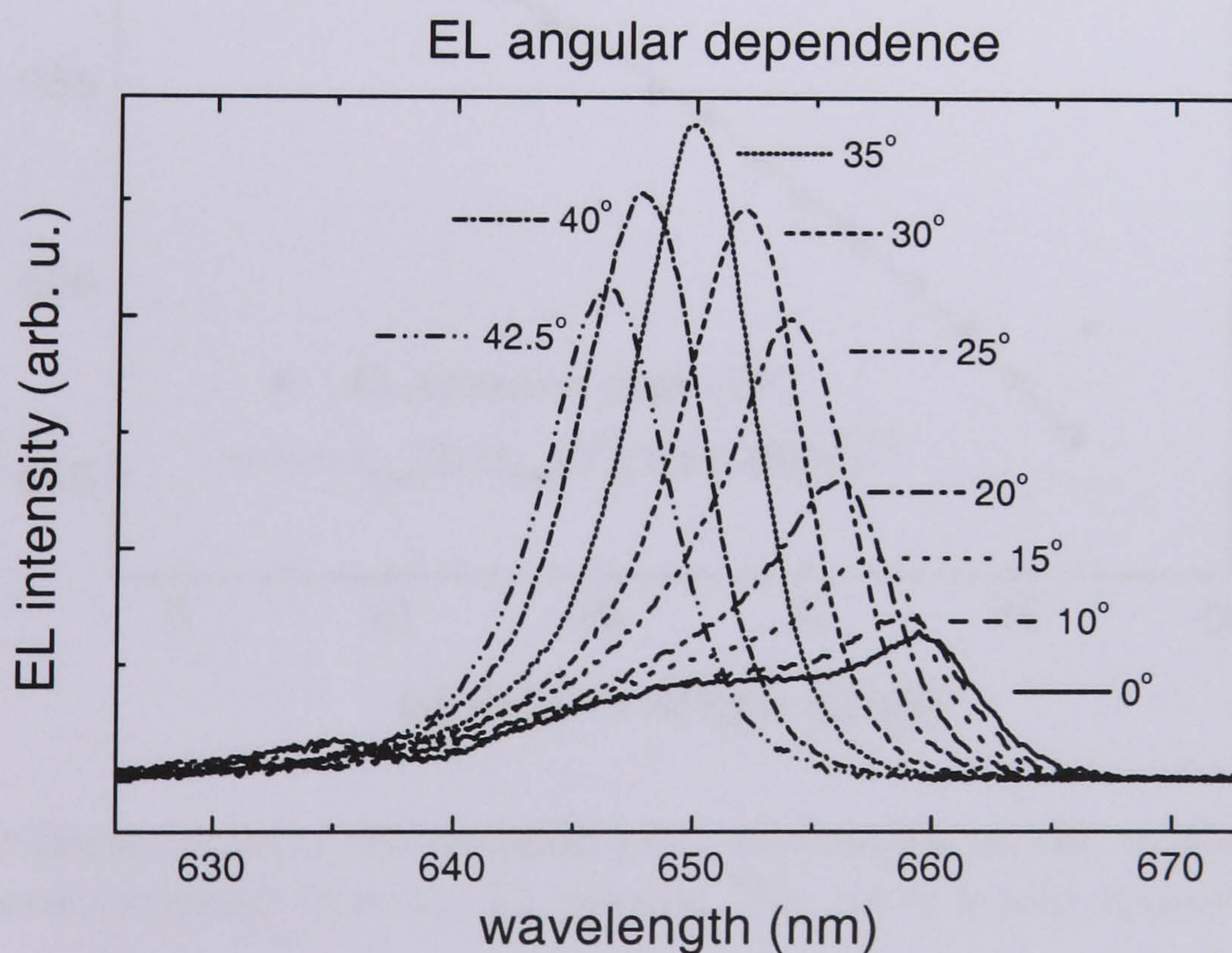

Figure 5.4: EL spectra as measured through a section of the emission cone for different angles of extraction for a 50μm S1 device from 0° (normal incidence) to 42.5° away from the normal. The maximum light output occurs at 35°. The smaller peak at 635nm (in the 0° curve) is due to light coming out at a cavity side-dip at this position, as confirmed by the R spectrum.

It should be noted that the results do not show the total light output at the measured angle as only a cross-section was measured with the set-up rather than the whole solid angle. The consequence of this will be discussed later. The λ_{CM} - λ_{QW} alignment however, is found from the unnormalised data presented in figure 5.4. The measured spectra correspond to angles between 0° and 42.5° away from normal incidence. The maximum peak intensity (as seen in figure 5.4) occurs at an angle of 35° away from the normal. This indicates that the device is positively de-tuned as λ_{QW} and λ_{CM} are not aligned at normal incidence but 35° away from the normal.

In figure 5.5 the EL peak position for all emission angles, as extracted from the spectra shown in figure 5.4, together with a fit with equation 5.1, can be seen.

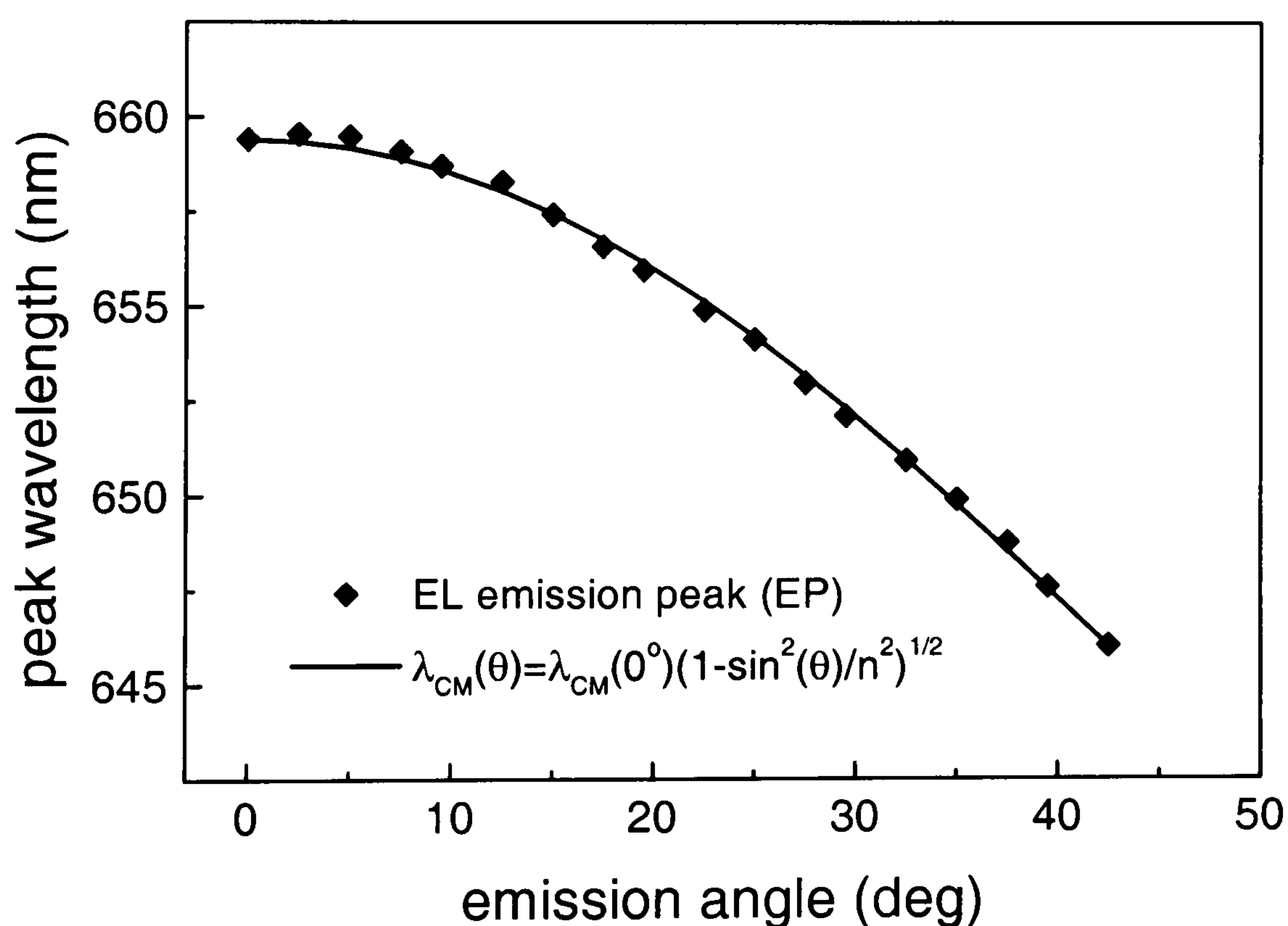

Figure 5.5: Dependence of the emission peak wavelength on the emission angle. The data points were extracted from the EL spectra. The curve is a fit according to equation 5.1.

Clearly the angular dependence of the EL peak wavelength follows the angular dependence of the cavity mode, as described in equation 5.1. This confirms the strong influence of the cavity mode on the emission. The fit to the experimental data

shown in figure 5.5 with equation 5.1 yields n=3.37. The peak emission wavelength at normal incidence is at 659.5nm, very close to the cavity mode wavelength. The peak wavelength at 35° is (649.9±0.3)nm. This closely relates to the wavelength of the peak QW emission of 650nm±2nm as determined by PR (chapter 3). Hence the results from the angular dependence confirm the positive de-tuning of the first set of devices.

In figure 5.6 the angular dependence of the spectrally resolved light output for two wavelengths 652nm and 659nm, as extracted from the angular dependent spectra, can be seen in a polar plot.

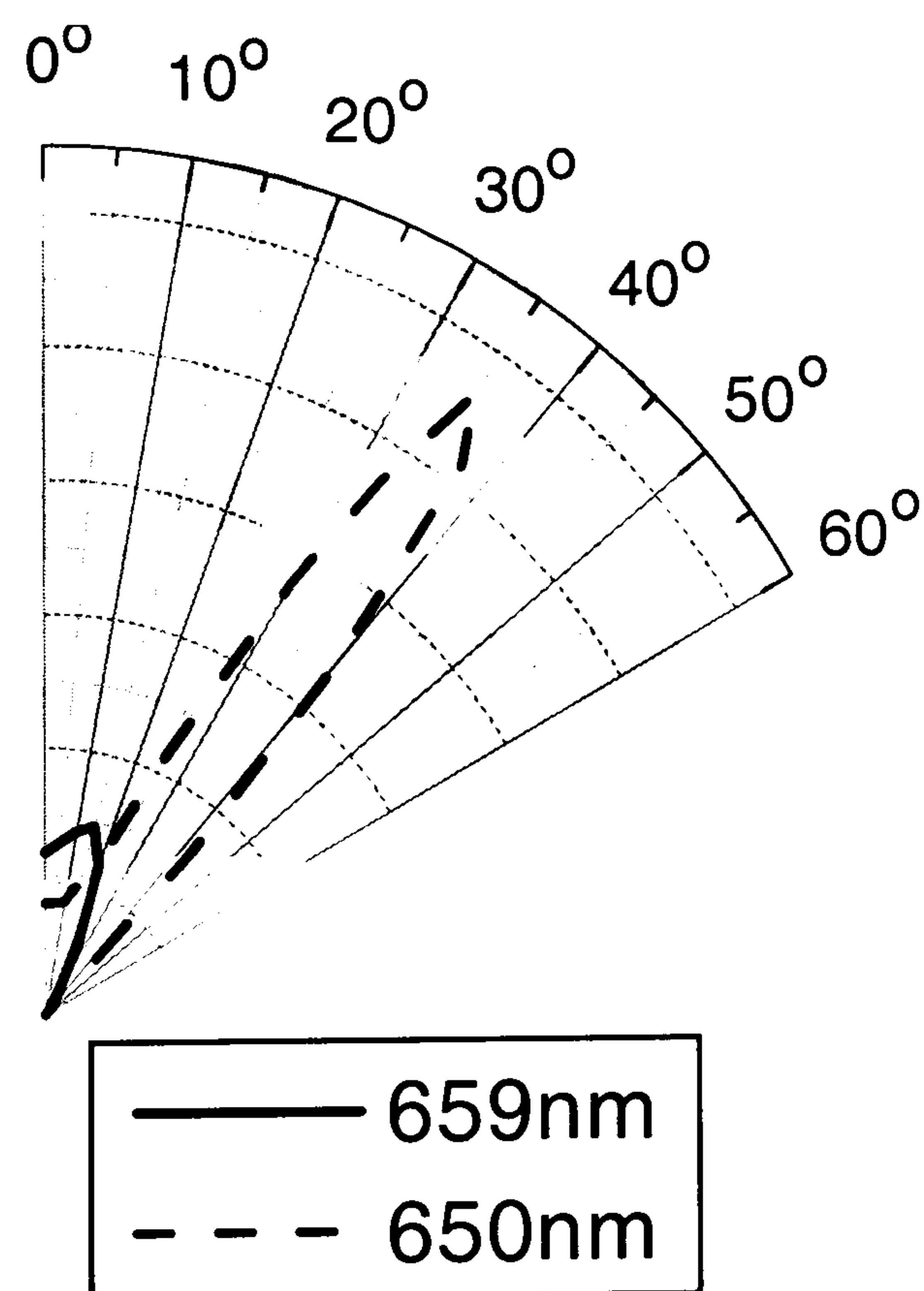

Figure 5.6: Polar plot of the light output for two different wavelengths. Here 0° is the direction of normal incidence and the increasing angle away from it.

These wavelengths have been chosen as they correspond to the $\lambda_{CM}(0°)$ and λ_{QW}. The curve for 650nm reaches a maximum, as expected, at 35° which further confirms the de-tuning and the relation between the angle and the wavelength. The peak for the 659nm curve does reach a maximum at 0°. The reason for this is clear from figure 5.4. Although the curve at 0° peaks at 659nm the maximum for 659nm occurs for the 15° curve as the total intensity for the curves up to the maximum at 35° increases.

The angular dependent EL could be used to identify the underlying QW emission [98]. The spectra shown in figure 5.4 do not show the total light output into the whole solid angle. In figure 5.7 a sketch of the fraction of the measured light output compared to the total light output is shown.

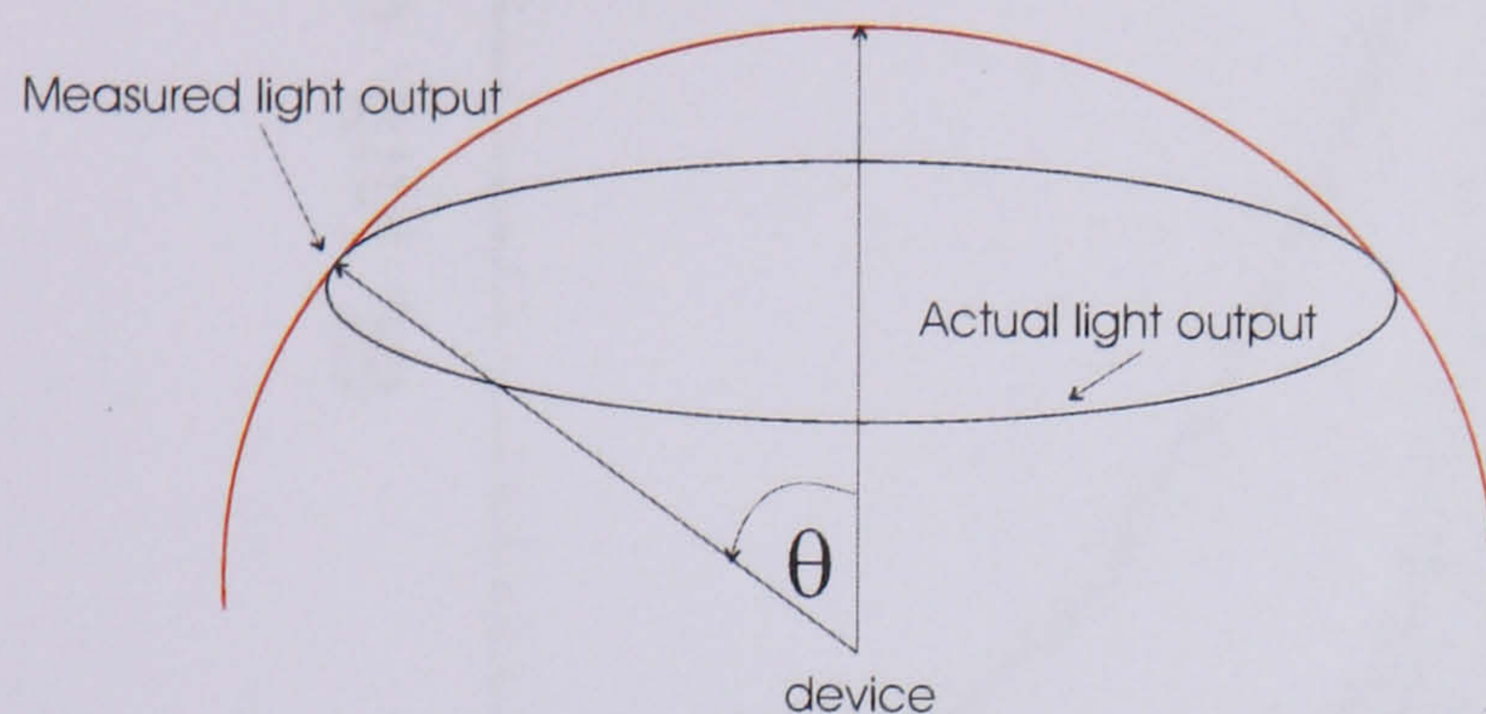

Figure 5.7: Geometry of the angular dependent EL measurements.

The light output is symmetrical in the azimuthal angle and so the measured light output only has to be multiplied by a function proportional to $sin\theta$ (as for example derived in [99]). This then takes into account the larger area corresponding to the higher angles. Figure 5.8 shows the spectra normalised in this way together with the QW emission as measured with edge-EL (see chapter 3).

In contrast to the angular dependent emission spectra, the edge-EL is measured on the wafer and the light collected with a spectrometer. Therefore the total light output for both measurements is not the same. To compare them in figure 5.8 they are normalised to their peak values. It can be seen that the peak position agrees very well with the maximum of the angular dependence. There is no significant amount of emission for the angular dependent EL above 659nm as that is the longest CM. Hence all the QW emission above 659nm cannot leave the device. As there were no measurements performed above 45°, there is a deviation between the two measurements at shorter wavelength, corresponding to larger angles. These effects account for the difference in the width of the two sets of data.

To summarize, measurements of the far field and the angular dependence of the EL spectra have confirmed the relationship between the emission angle and the wavelength (as shown in equation 5.1), and have also shown how de-tuning affects the far field spectra. Far field measurements can be used to confirm if and to what

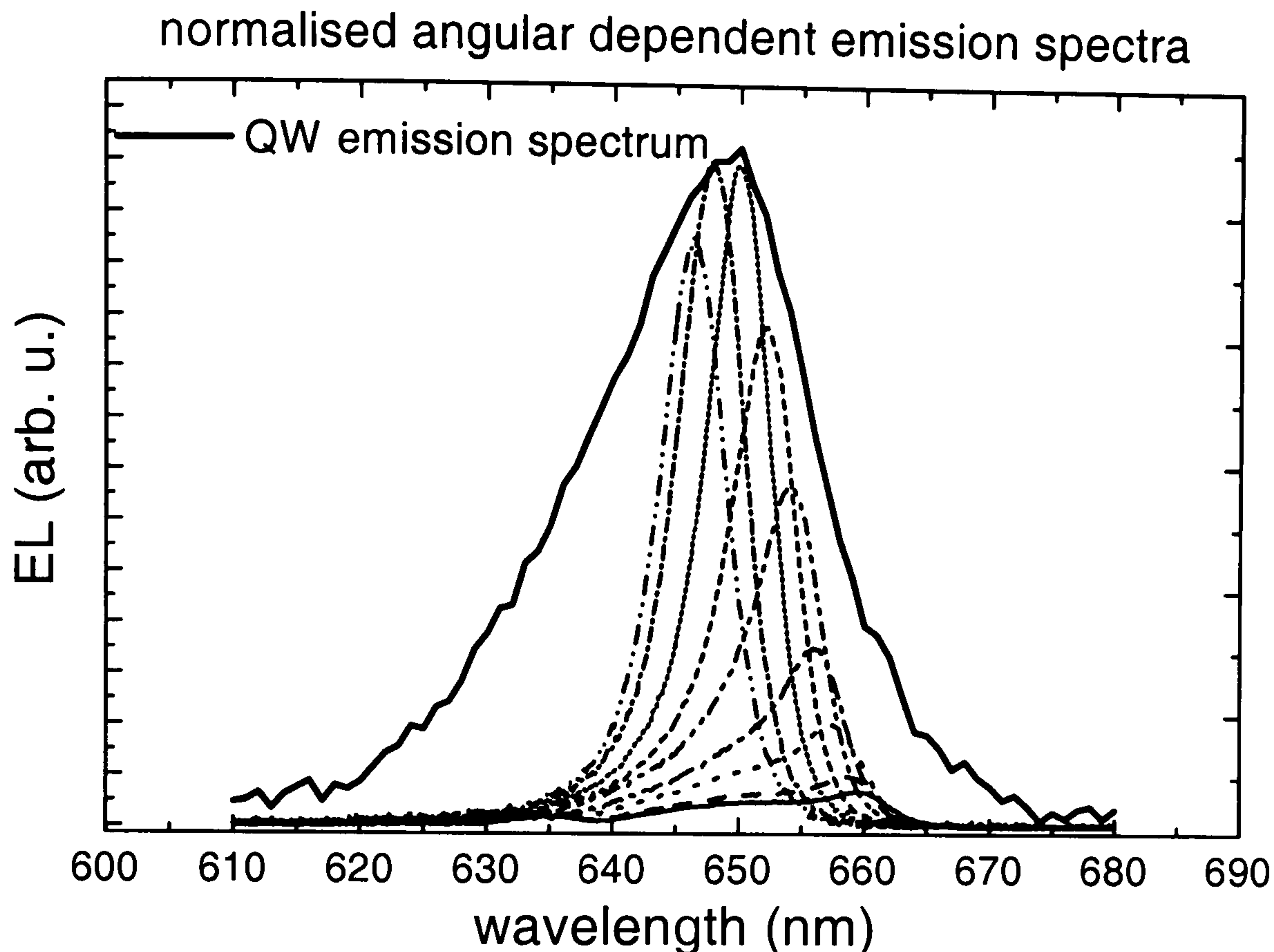

Figure 5.8: Normalised angular dependent spectra together with the measured QW emission.

degree devices are positively de-tuned. With the additional information of the peak wavelength at different angles, the QW emission peak wavelength can be confirmed. For a device processed from the S1 wafer, the maximum light intensity occurs at 35° with a peak wavelength of 649.9nm which confirmed the findings for $\lambda_{QW} = 650$nm obtained by PR in chapter 3.

5.4 Normal incidence EL spectra

To investigate the influence of the QW-CM de-tuning on the device performance, EL spectra for the devices with different amounts of de-tuning were measured at 20mA for different temperatures ranging from 15°C to 70°C. The device aperture for all the devices studied here was 70μm. The size dependence of the devices will be discussed in chapter 6.

The measured devices were bare chips that had not been bonded into a pack-

age. This allowed the reflectivity to be measured on the devices. As the contacts were already formed the EL could also be measured on the same probe station set-up as described earlier in chapter 4. A schematic of the set-up used to measure the light output is shown in figure 5.9.

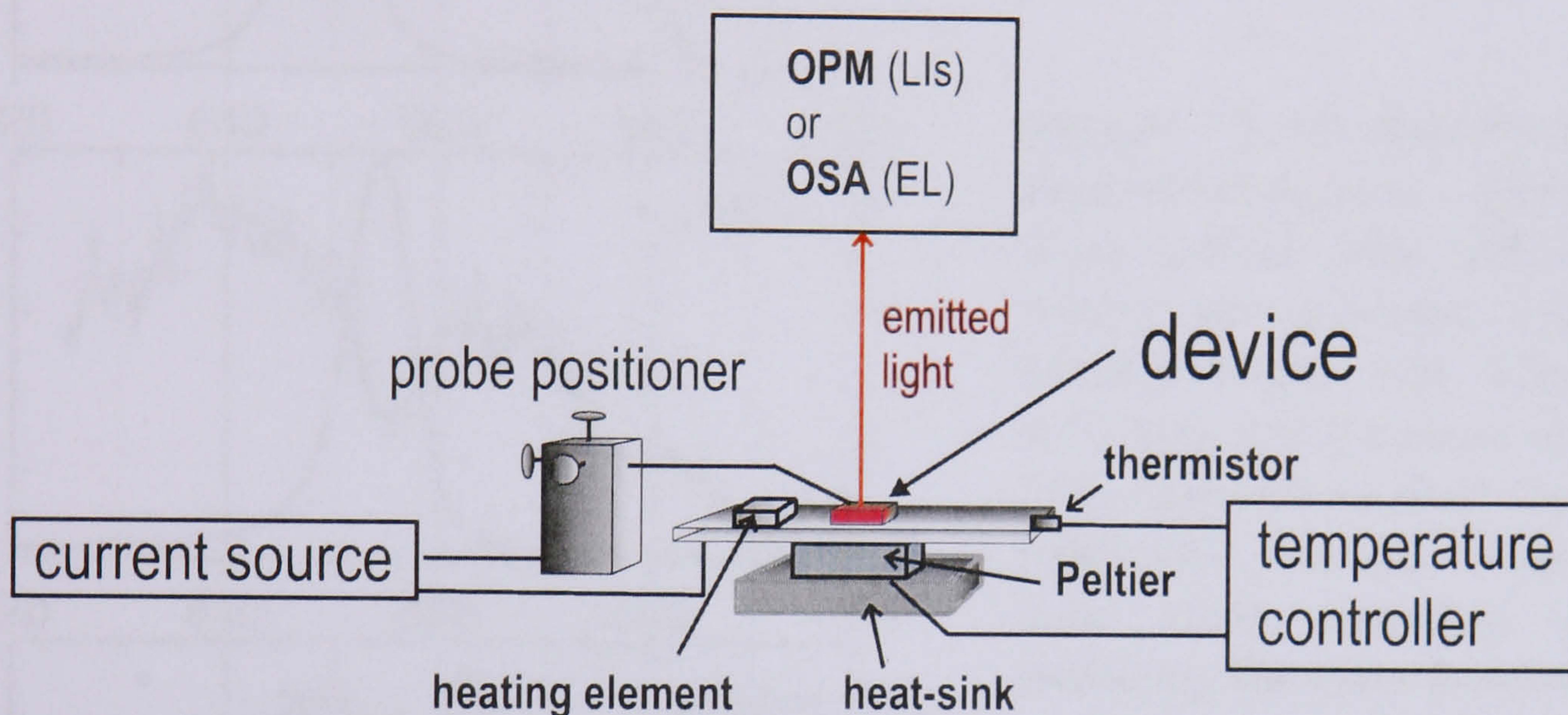

Figure 5.9: Detail of the Probe station set-up showing the possibilities of measuring EL spectra and LI curves of bare devices. The exact light path is omitted here but can be found in figure 4.11 in chapter 4.

The detail of the set-up shows how the device is contacted. It can also be seen that this set-up could be used to measure the EL spectra (with an OSA) or the total light output (L) with an OPM. The Peltier cooler, connected to a temperature controller, allowed the device temperature to be varied between 15 and 75°C. To be able to measure even higher temperatures a heating element connected to a variable 15V 4A power supply was mounted on the same copper plate as the device. The heating element enabled measurements up to 85°C to be made.

The output spectra depend on the relative position and width of the QW emission and cavity mode. The QW emission, determined previously by PR, is centred at 650nm and has a FWHM of 20nm, as seen in the edge-EL. Three of the R spectra, as measured with the probe station for devices with different de-tuning can be seen in figure 5.10. In the same figure the corresponding EL spectra for 20 mA all at

20°C are plotted.

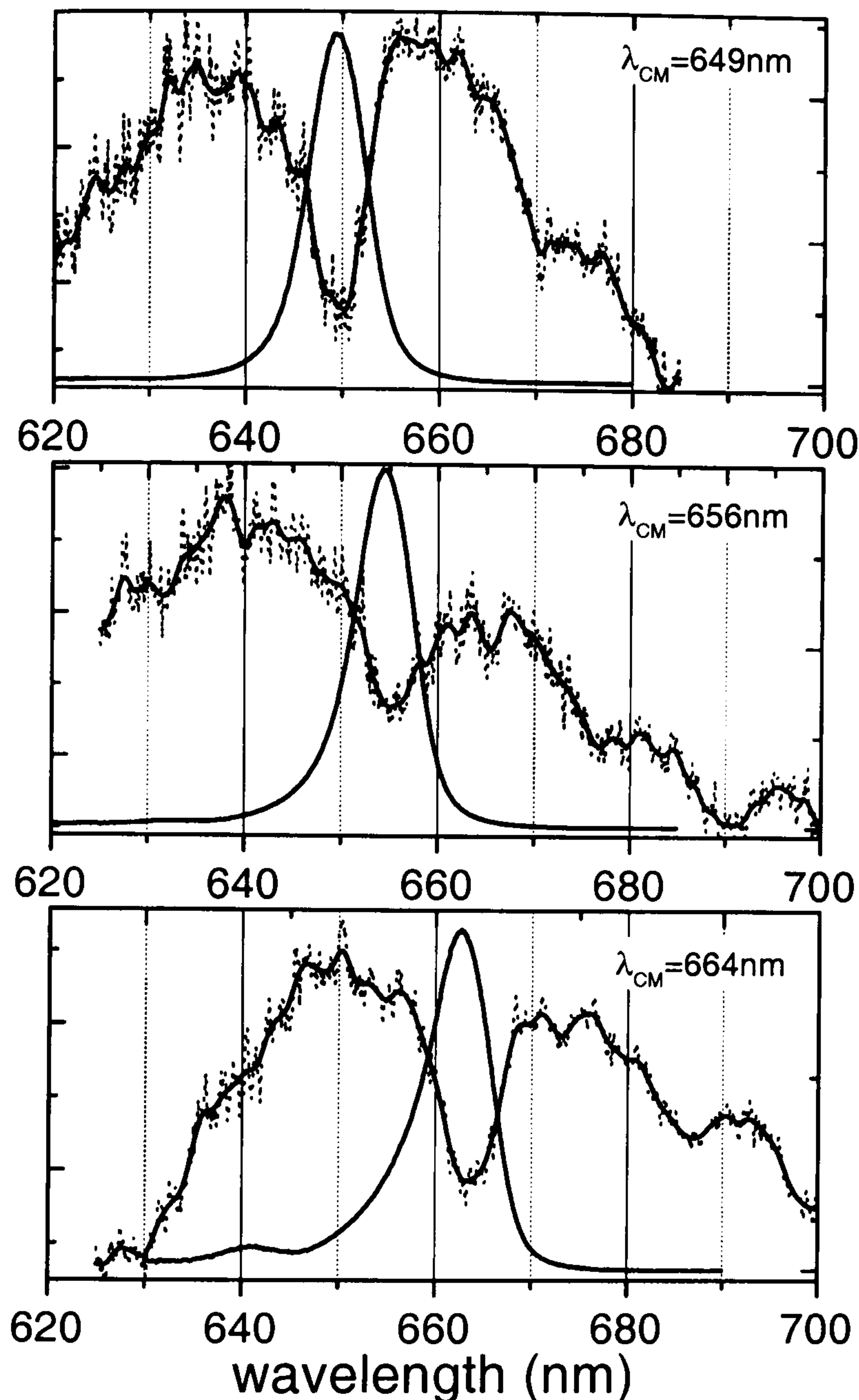

Figure 5.10: Reflectivity and electroluminescence spectra of three devices with different detuning as indicated (λ_{CM} = 649nm, 656nm and 664nm) at 20°C with a bias current of 20mA. (The dashed lines show the actual reflectivity spectra, whereas the lines show smoothed spectra indicating the main features.)

The angle of collection was about 27° for the EL measurements and approximately 5° for the R measurements. Hence not only the front emission is measured (corresponding to $\lambda_{CM}(0°)$ and thus the light influenced by the normal incidence cavity mode), but also any light that leaves the device at any higher angles up to 27°. The λ_{CM}s of the shown devices are determined from their R spectra to be 649nm, 656nm and 664nm respectively. The influence of the cavity mode as seen in the R spectra on the EL can be seen quite clearly, as both the width and the peak position of the EL are approximately the same as the width and position of the cavity dip.

The influence of the QW emission on the spectra is more subtle and can be understood by comparing the three spectra. The peak position of the EL, in par-

ticular for the de-tuned devices, is not exactly at the cavity mode. This can be understood by considering that the QW emission peak is blue-shifted with respect to λ_{CM} for those devices. Due to the high collection angle of the measurements, light produced by the QW at a shorter wavelength than λ_{CM} that leaves the device away from normal incidence will still be measured. The effect of the collection angle can be simulated. To simulate the EL spectra the transmission spectra, T, of the devices were calculated from the experimentally obtained reflectivity spectra, R as $T = 1 - R$. The calculations were done for each angle of 0°, 13°, 20° and 30°as shown in figure 5.11 (a). The experimenally obtained reflectivity was normalised to a maximum reflectivity of 85%, which has been obtained from reflectivity calculations.

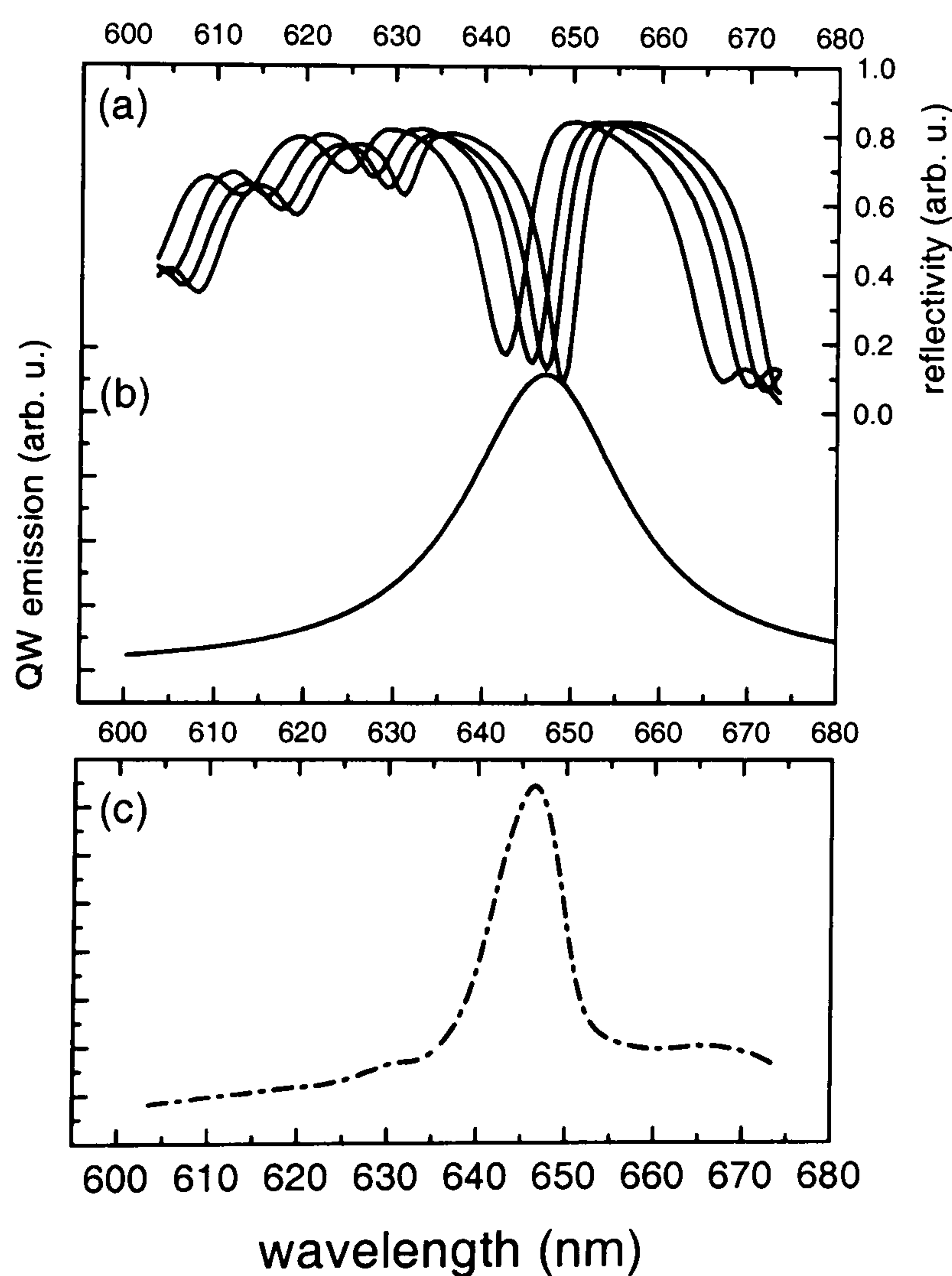

Figure 5.11: (a) Measured reflectivity for 0°, 13°, 20°and 30°, (b) QW emission obtained from a Lorentzian fit of the edge-EL of the wafer, (c) resulting simulated EL spectrum (c).

The simulated EL graph in figure 5.11 (c) was obtained by multiplying the transmission for all four angles with the QW emission as shown in figure 5.11 (b) and adding the results together. The QW emission was obtained as a Lorentzian fit to

the edge-EL spectrum measured for the wafer in chapter 3. The relatively strong emission at longer wavelengths than λ_{CM} i.e. the spurious peak at ~667nm does not agree with the measurements. At these wavelengths this relatively simple model fails as it gives strong emission if the transmission is high (corresponding to a low reflectivity). However, for very low reflectivity values no emission is expected as light produced at these wavelengths will not be reflected by the bottom mirror and thus will not subsequently emerge from the top of the device. In figure 5.12 the spectrum shown in figure 5.11 (c) together with a spectrum for a de-tuned device are shown together with spectra where only the reflectivities up to 20° were taken into account. In reality the spectra would need to be sampled continously over all the angles and so by taking only discrete steps a difference to the real spectra is expected. However to illustrate the trend for these measurements this method is sufficient.

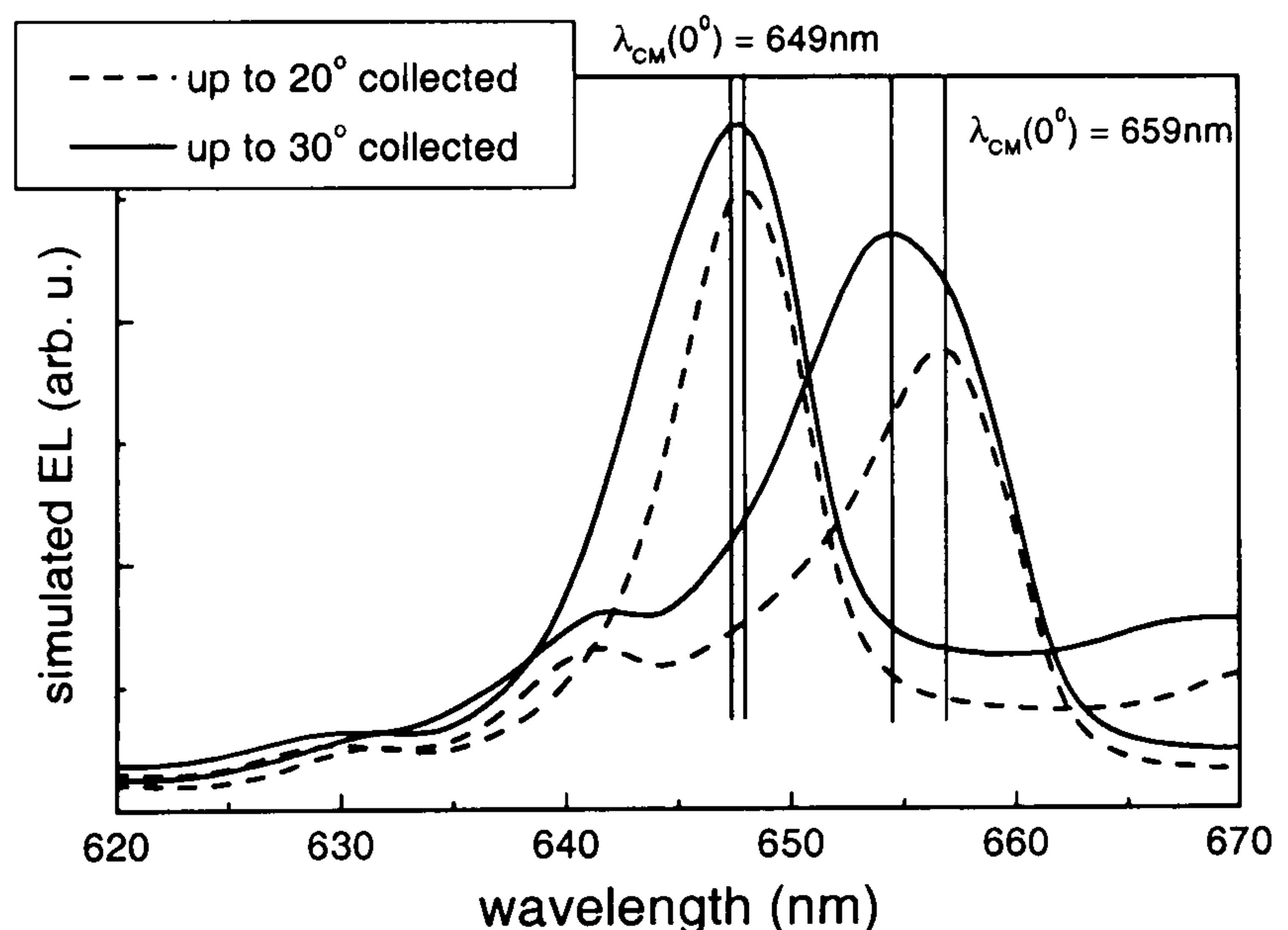

Figure 5.12: Simulated EL spectra for two devices with different de-tuning at two different collection angles. The vertical lines indicate the peak position and show the difference in the shift between the devices.

The shift between the different collection angles, indicated by the vertical lines in figure 5.12 is indeed greater for the de-tuned device (λ_{CM} = 659nm) as more light is produced off axis. The light produced at higher angles represents also a greater fraction of the solid angle as the light produced at normal incidence, which has not been taken into account for the simulation. This enhances the effect that a de-tuned QW emission peak has on the EL spectrum. For the strongly de-tuned device (λ_{CM} = 664nm) almost all the light produced by the QW lies below λ_{CM}. Therefore, as

can be seen in the angular dependence, the peak of the light output will be away from normal incidence and therefore also determined by the CM of the angle at which the highest light output occurs. The same argument applies for the FWHM of the EL spectra, as for the de-tuned devices most of the light is produced below λ_{CM} and the spectra will be asymmetric. The de-tuning not only has an influence on the line-shape and peak position of the EL spectra but also on the peak intensity. Without the influence of the larger solid angle at higher emission angles figure 5.12 suggests that the intensity for the stronger de-tuned devices will be less for both collection angles. However as can be seen from figure 5.12 the light output for the de-tuned device increases more for the higher acceptance angle than the tuned device. The experimental EL spectra measured with a collection angle of ~27° for six devices with different de-tuning at 20°C and 20mA are compared in figure 5.13.

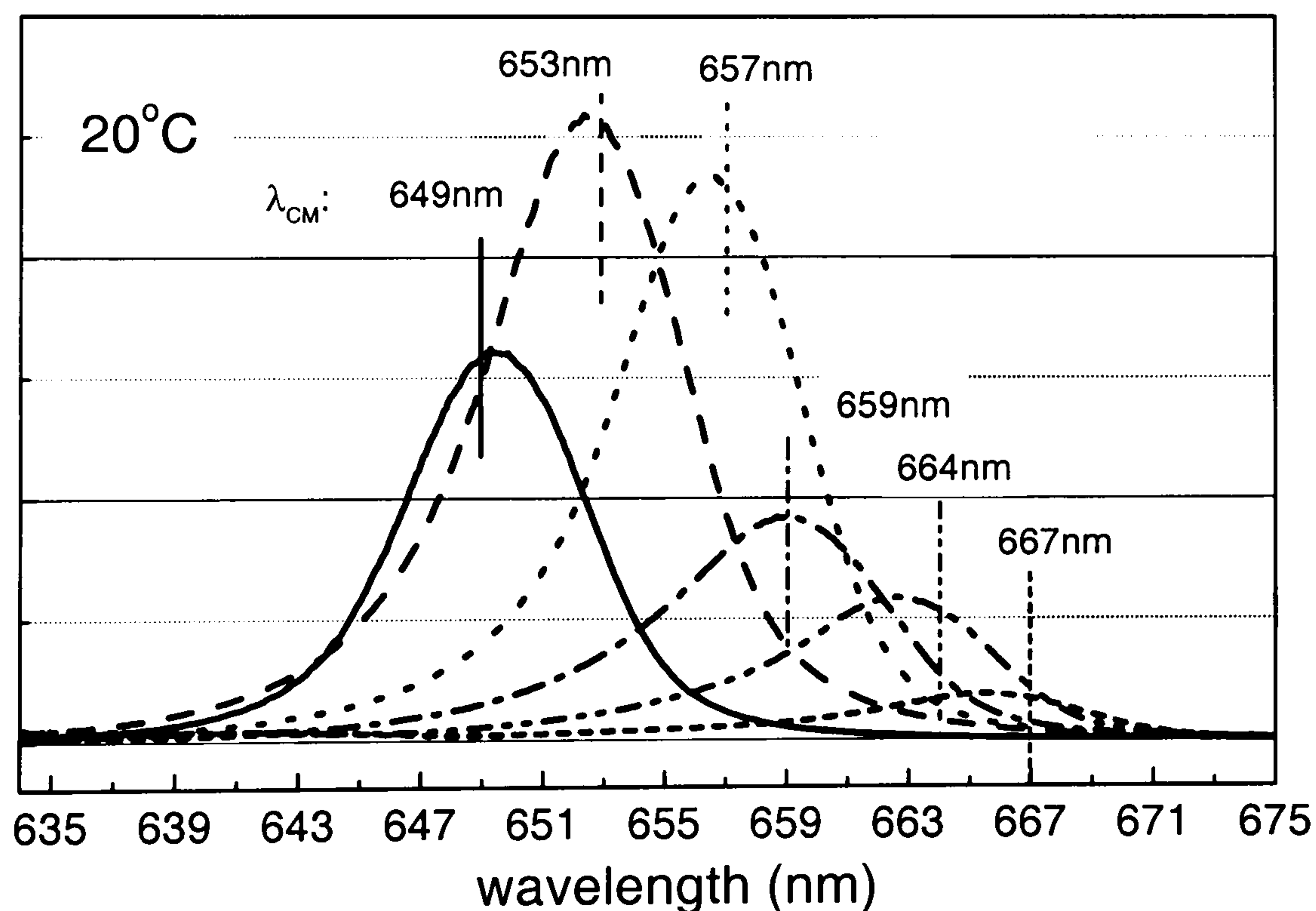

Figure 5.13: EL spectra at 20mA and 20°C for six devices with λ_{CM} (20°C) as indicated.

The λ_{CM}s measured at 20°C are indicated. It can be seen that the maximum peak at this temperature does occur for the device that is slightly de-tuned (as no device with λ_{CM} exactly at 650nm could be found). The EL intensity drops off for the stronger de-tuned devices. Hence, the maximum light output at a given temperature occurs for the device which is only slightly de-tuned *at that temperature.*

This confirms the prediction that the maximum light output should occur, when the de-tuning corresponds to an emission that is centered in the middle of the escape window [96]. In this case the acceptance angle was only about 27° and so the maximum should occur for a device de-tuned to 13.5°. 13.5°corresponds to a wavelength shift of ~1.6nm (from equation 5.1). The closest available device to this is the one with λ_{CM} = 652.7nm, having its emission centred at 18.6°. This device has the highest light output at 20°C. However the advantage of the stronger de-tuning even for small acceptance angles can be seen in the temperature dependence of the devices as will be discussed in the next section.

5.4.1 Temperature dependence

Figure 5.14 shows the temperature dependence of the EL spectra in the three graphs. Here the EL spectra for the same 6 devices at 20mA for three temperatures (20°C, 40°C and 60°C, all on the same scale) are shown.

With increasing temperature, the drop in the EL intensity for the initially de-tuned devices (whose emission peaks lie at longer wavelength) is not as significant as for the tuned ones. The reason for the decrease in the amplitude and in the integrated area of the emission, with increasing temperature can be partly attributed to the thermal broadening of the QW emission. As mentioned earlier, the width of the EL is determined by the width of the cavity mode. As this does not change with temperature (whereas the QW emission width increases linearly with increasing T) a smaller fraction of the light produced by the QW leaves the device with increasing temperature. Thus not only the amplitude but also the integrated light output decreases. The maximum light output at 40°C and 60°C occurs for the device with λ_{CM}(20°C) = 656.7nm. If the de-tuning and thus the angle of maximum emission for each device at each temperature is calculated using the values for the shift of λ_{QW} and λ_{CM} with temperature, it becomes clearer for which devices the maximum peak in figure 5.14 occurs. It is the device that at a given temperature is positively de-tuned and whose angle of maximum emission is at half the collection angle (13.5°)

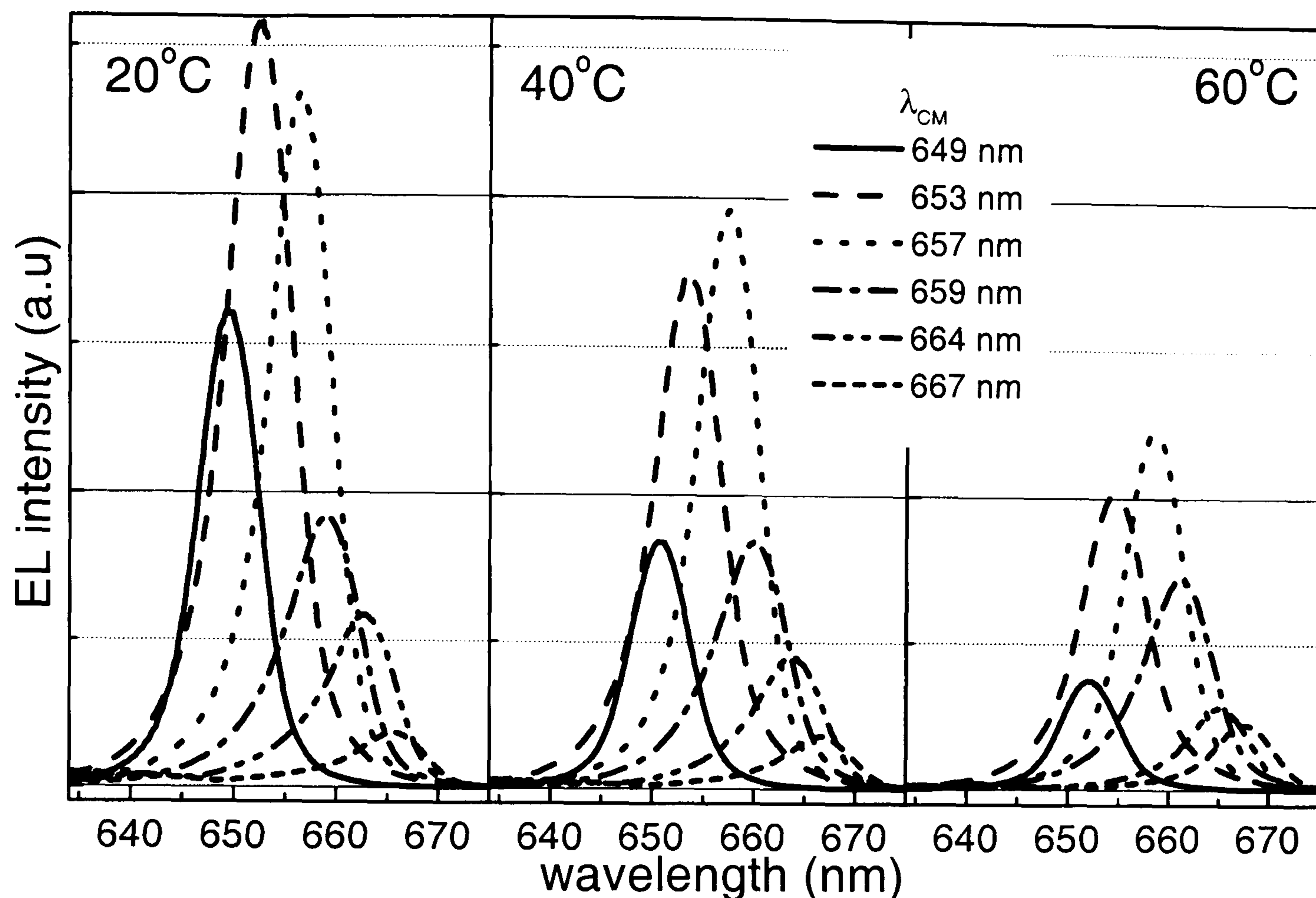

Figure 5.14: EL spectra for the same devices as in figure 5.13 at 20°C, 40°C and 60°C for a collection angle of 30°.

but not less. In other words the maximum light output occurs for a device for which $\lambda_{CM}(\theta = 13.5°,T) \geq \lambda_{QW}(T)$. For less de-tuning i.e. when the maximum output occurs at an angle below 13.5° a large fraction of that light cannot exit the device. For much higher de-tuning a large fraction of the light will be at angles higher than 27° and therefore can not be collected.

In the case of a large difference between λ_{CM} of two devices the efficiency for the device de-tuned at 20°C, will be even higher than that for the tuned device at higher temperatures. Compare, for example, the EL spectra for the device with $\lambda_{CM} = 649$nm with the one with $\lambda_{CM} = 659$nm as shown in figure 5.15.
Here the EL spectra for the two devices at three temperatures are shown. It can be seen that compared to the 649nm device the light output for the 659nm devices at 20°C is lower, then approximately equal at 40°C and higher at 60°C. This, and the smaller temperature sensitivity, can be explained by considering that light at longer wavelengths than the cavity mode (plus a window equal to the half width of

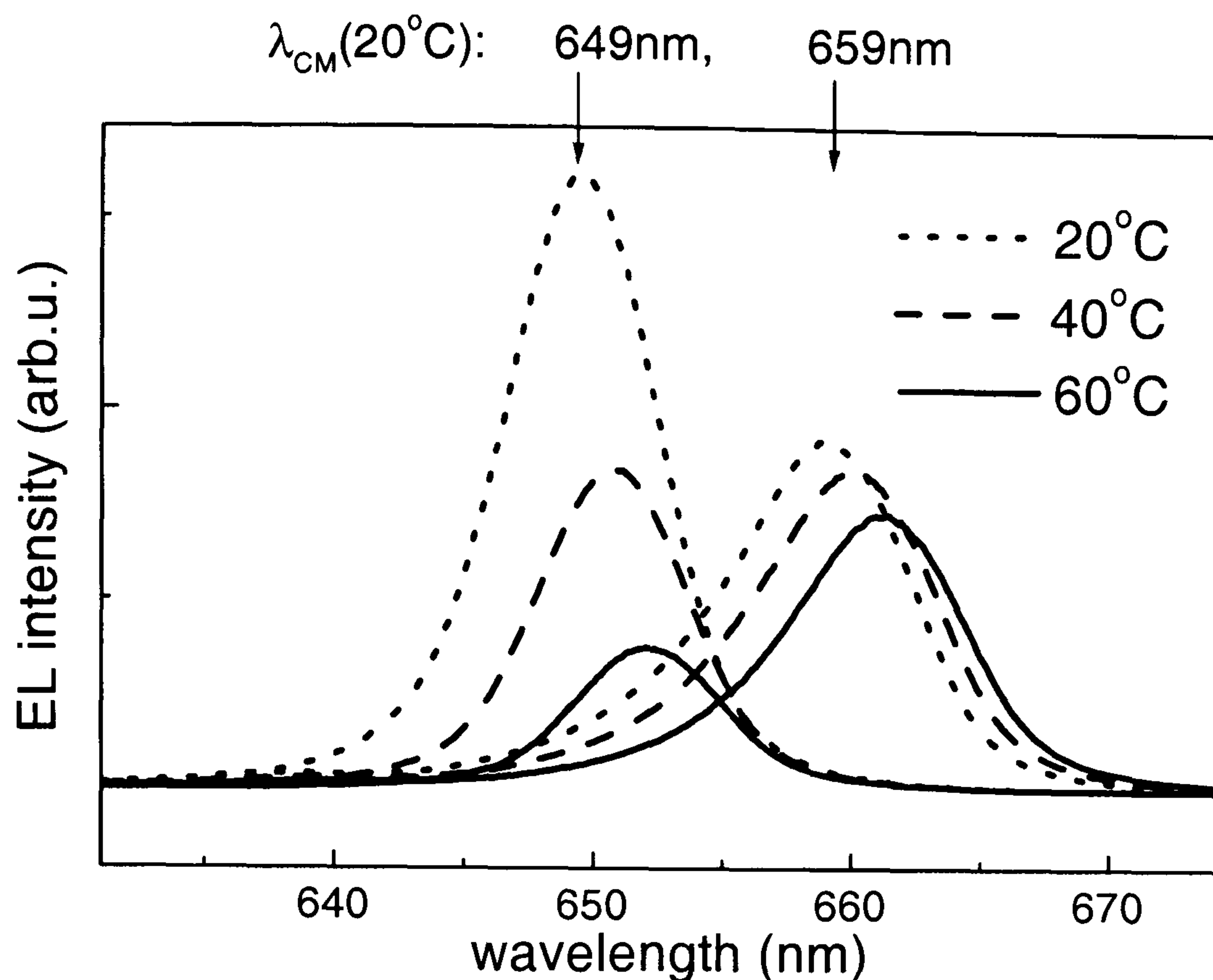

Figure 5.15: Temperature dependence of the EL spectra for two devices, one initially tuned that becomes negatively de-tuned with higher temperature and one initially positively de-tuned.

the dip on either side) cannot escape the device, it is "cut-off". As can be seen from figure 2.5 and equation 5.1 there are no modes at wavelengths longer than the CM. Firstly the light at these longer wavelengths does not get enhanced by the cavity (a small amount of emission at these wavelengths is expected as the top DBR reflectivity is only $\sim$ 85%). Secondly, as can again be seen by equation 5.1, the longest wavelength (λ_{CM}) leaves the device at normal incidence. Shorter wavelengths can leave the device at higher angles but wavelengths longer than λ_{CM} cannot exit the device. For the initially tuned device more and more of the QW emission will lie at wavelengths longer than the cavity mode as the temperature increases. In contrast, for the device de-tuned at 20°C, most of the QW emission is at shorter wavelengths than the CM and can therefore escape from the device at higher angles. With increasing temperature the peak of the QW emission moves towards the CM dip. Only after the temperature is increased beyond a temperature at which λ_{CM} and λ_{QW} are tuned does the same temperature sensitivity (as for the initially tuned devices) apply since most of the light that is produced by the QW cannot leave the device.

The temperature dependence can also be simulated in the same way as shown in figure 5.11 and the results are shown in figure 5.16. To simulate the temperature dependence a shift of 0.0375nm/°C for λ_{CM} and a shift of 0.147nm/°C for the QW was assumed. The QW emission, approximated by a Lorentzian, is calculated to broaden linearly with T.

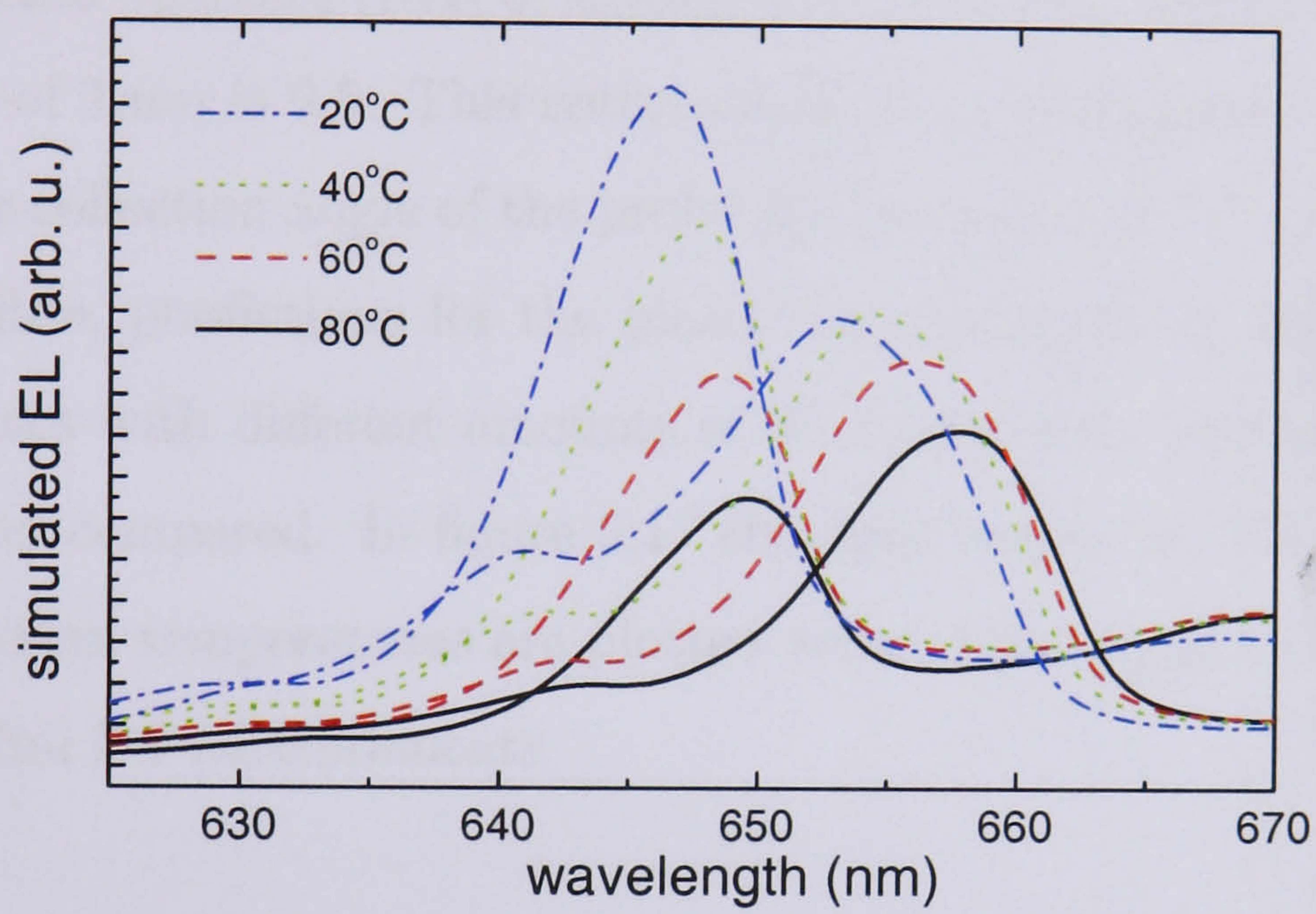

Figure 5.16: Simulated EL spectra for the devices shown in figure 5.15

The figure shows clearly the difference in the temperature dependence between the two devices which can therefore be attributed to the de-tuning. Nevertheless the light output decreases much less for the simulation. This indicates that there must be other loss mechanisms that contribute to the temperature sensitivity.

In conclusion, measuring the EL spectra at different temperatures (for a fixed fibre-like collection angle) provides valuable information about the effect of de-tuning on the light output. The maximum light output depends on the de-tuning, the collection angle and the temperature. It was confirmed in this section that the maximum light output occurs if, for a given temperature, the maximum emission (observed in the far field spectra) occurs at half the collection angle. For the collection angle used here it was also observed that the stronger positive de-tuning leads to less temperature sensitivity as devices tune-in with increasing temperature.

5.5 Light current characteristics

For light-current measurements on the probe station set-up the only change to the previous set-up (in figure 5.9) was to replace the OSA by a calibrated 7mm silicon detector connected to an optical power meter (OPM) in order to measure the integrated light output.

The numerical aperture (NA) of standard PMMA step index plastic fibre with a core diameter of 1mm is 0.5. This corresponds to an acceptance/collection angle of 30°. Since the collection angle of the probe station set-up is 27° (NA=0.45), close to that of the fibre, predictions for the plastic fibre application can be made. LIs for a set of devices with different amounts of de-tuning were measured at different temperatures and compared. In figure 5.17 the light output at 20mA for eight devices at five different temperatures are plotted versus their λ_{CM}(T). These data are extracted from full L-I measurements.

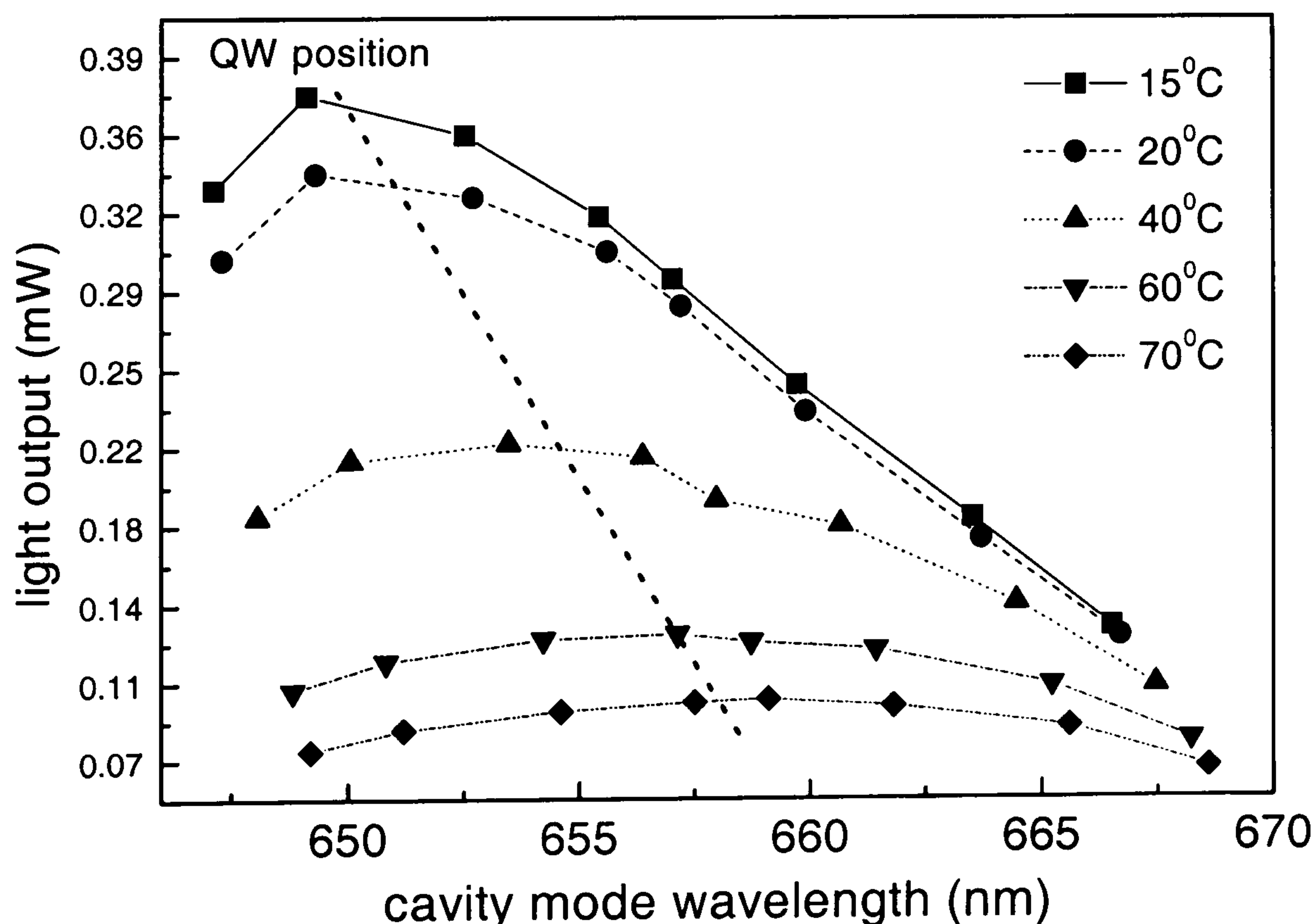

Figure 5.17: Total light output at 20mA for 8 devices with different CM-QW de-tuning measured at 5 different temperatures. The shifts of λ_{CM} and λ_{QW} with temperature are also indicated.

The light output is plotted versus the cavity mode wavelength at normal incidence and the appropriate calculated shift in λ_{CM} with temperature is indicated. The position of the QW emission peak for all devices was determined to be 650nm±2nm at 20°C. The quantum well position, and its calculated shift with temperature, is indicated by the dashed line. From this figure it is apparent that the de-tuning of devices changes with increasing temperature as the λ_{QW} moves more rapidly to longer wavelengths than λ_{CM} with increasing T. The decrease of the light output with temperature varies between 0.9%/°C and 1.6%/°C for the different devices. This confirms the lower temperature stability compared to VCSELs for which values between 1.6%/°C and 2.27%/°C are reported [100]. Figure 5.18 shows the actual total light output at 20mA and RT (~20°C) of three of the devices shown in figure 5.17. The measurements were performed after the devices were bonded onto a header and all the light was collected into the same broad area detector.

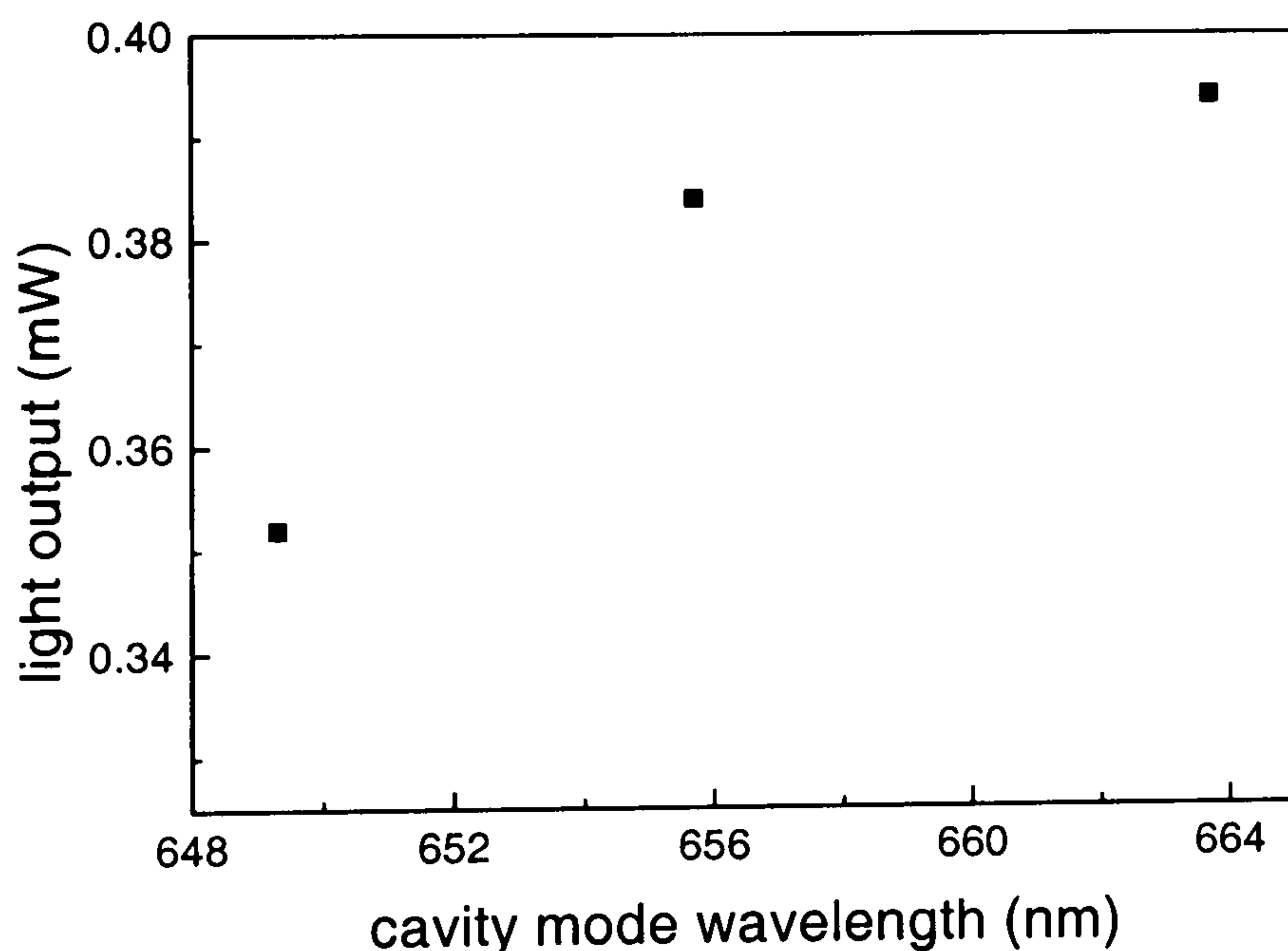

Figure 5.18: Total light output at 20mA for three of the devices shown in 5.17 (after being bonded onto a header). The data points are extracted from full L-I curves measured with a broad area detector.

From these measurements it can be observed that the light output is higher with increasing de-tuning, up to the maximum of ~14nm corresponding to a cavity mode wavelength of 664nm confirming earlier predictions. It is now apparent that the effect of de-tuning on coupled power depends on the NA of the collection. This was also observed by Oulton et al [99]. Therefore to predict the best de-tuning the application and its NA have to be considered. If the total light output is measured, the de-tuned devices (up to a de-tuning of 14nm) show the highest light output for a

given current. If a smaller collection angle is considered, the maximum light output occurs for only slightly de-tuned devices ($\sim$ 2nm). However, the higher de-tuning leads to a lower temperature sensitivity. As for the temperature dependence, the light output for all devices decreases with temperature. The decrease in the spontaneous emission factor with increasing temperature cannot alone account for the drop in intensity, as the comparison between simulated and measured EL spectra in figures 5.15 and 5.16 showed. In the next section the main reasons for the temperature sensitivity are considered.

5.6 Influence of carrier leakage and self-heating

At higher temperatures the QW emission broadens and therefore the peak intensity of the QW decreases for the same current density. More importantly, since the width of the CM, which does not change significantly with temperature, determines the spectral width of the light able to exit the RCLED device, it will select a smaller fraction of light with increasing temperature making the device less efficient. As seen in the previous section the λ_{CM} -λ_{QW} de-tuning does weaken the effect this has on the light output, as positively de-tuned devices tune-in with increasing temperature, but cannot fully compensate for it. The reason for this is that there is another temperature dependent loss mechanism in devices at these wavelengths. These devices suffer, as all 650nm InGaP-based devices from carrier leakage into indirect X-minima [101], [102]. Another problem arising from the compact nature of the devices is the problem of self-heating. Both of these effects influence each other. Therefore in order to de-couple the way in which these processes individually influence the device performance they will be considered separately. Self-heating will be described first.

5.6.1 Self-heating

The current passed through a device heats it up due to resistive (Joule) heating. This is a particular problem for vertical emitters as the active region is very compact compared to edge emitters and so any Ohmically generated heat cannot easily be dissipated [103]. To minimise self-heating, the device can be driven in pulsed mode. The duty-cycle (the ratio of the pulse width to the period between the pulses) for the pulsed measurements is chosen so that the pulse width is small enough to avoid too much heating but also not too short in case the device cannot respond fast enough. The repetition rate also has to be high enough to measure a reasonable average output signal. For these measurements a pulse width of 0.1μs at a frequency of 10kHz, resulting in a 0.1% duty-cycle, was chosen. In figure 5.19 the LIs measured under pulsed and c.w. operation are compared at 20°C and 50°C. In the inset of figure 5.19 a comparison of two different duty-cycles with c.w. operation is plotted, showing that at a duty-cycle of 0.5% heating still plays a role.

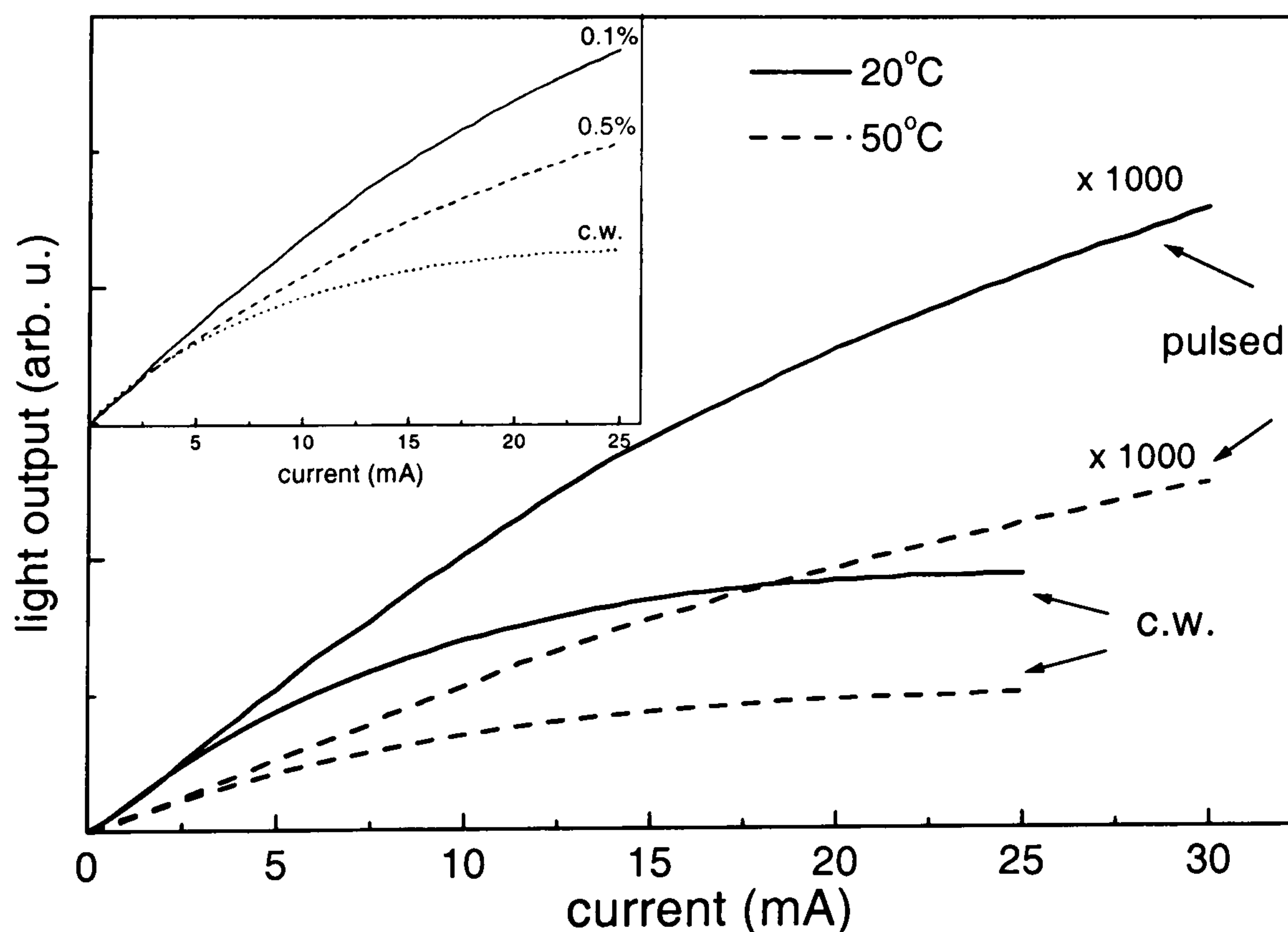

Figure 5.19: Comparison of LIs measured in pulsed and c.w. mode for two temperatures. The inset shows a comparison of the c.w. with pulsed operation for different duty cycles.

To measure the effect of self-heating the pulsed LIs (for which no heating of the de-

vice is assumed) were then compared with the c.w. ones. Pulsed operation with such a small duty-cycle will not be used for RCLEDs in any real application, as the light output would be too low. However this is a very useful method as it removes the influence of self-heating in the device. The light output for the pulsed measurements was multiplied by 1000 (as a 0.1% duty-cycle was used) to be comparable with the c.w. measurements. For very low currents both curves (at each temperature) are similar showing a linear rise of the light output with current. However by 5mA the c.w. curves deviate from the linear behaviour. With increasing c.w. current the light output increases less and finally saturates. At very high currents the output would decrease, once the rate of decrease in η with I becomes larger than the additional number of electrons this current can supply (not shown in figure 5.19). This point is called the thermal roll-over. At higher currents the pulsed curve also deviates from the linear behaviour, suggesting that even in pulsed mode the increasing current may lead to some self-heating. The main reason however for the reduction is attributed to carrier leakage which increases with current and leads to a sub-linear LI. Figure 5.20 compares the current that is needed to achieve a constant light output for one device under pulsed and c.w. operation. For lasers, measuring the variation of threshold current with temperature gives insight into the temperature variation of the underlying recombination mechanism. In the absence of a threshold in an LED, a similar analysis may be performed by measuring the variation of current required for a constant light output as a function of temperature.

The higher current required for the c.w. operation is due to self-heating whereby the active region becomes considerably hotter than the heatsink. The percentage of current required to compensate for the heating can be estimated from figure 5.20. At 20°C $\sim$ 10% extra current is required to maintain the same constant light output. At 70°C the percentage of the current due to self-heating has reached $\sim$ 50%. Nevertheless as there is no threshold to achieve in RCLEDs the devices continue to operate at high temperatures. This is a considerable advantage over visible VCSELs for which there are a few reports of c.w. operation at high temperatures: 642nm-678nm RT [104], 690nm 45°C [105], 657nm 60°C [106] and 667nm 80°C [100]

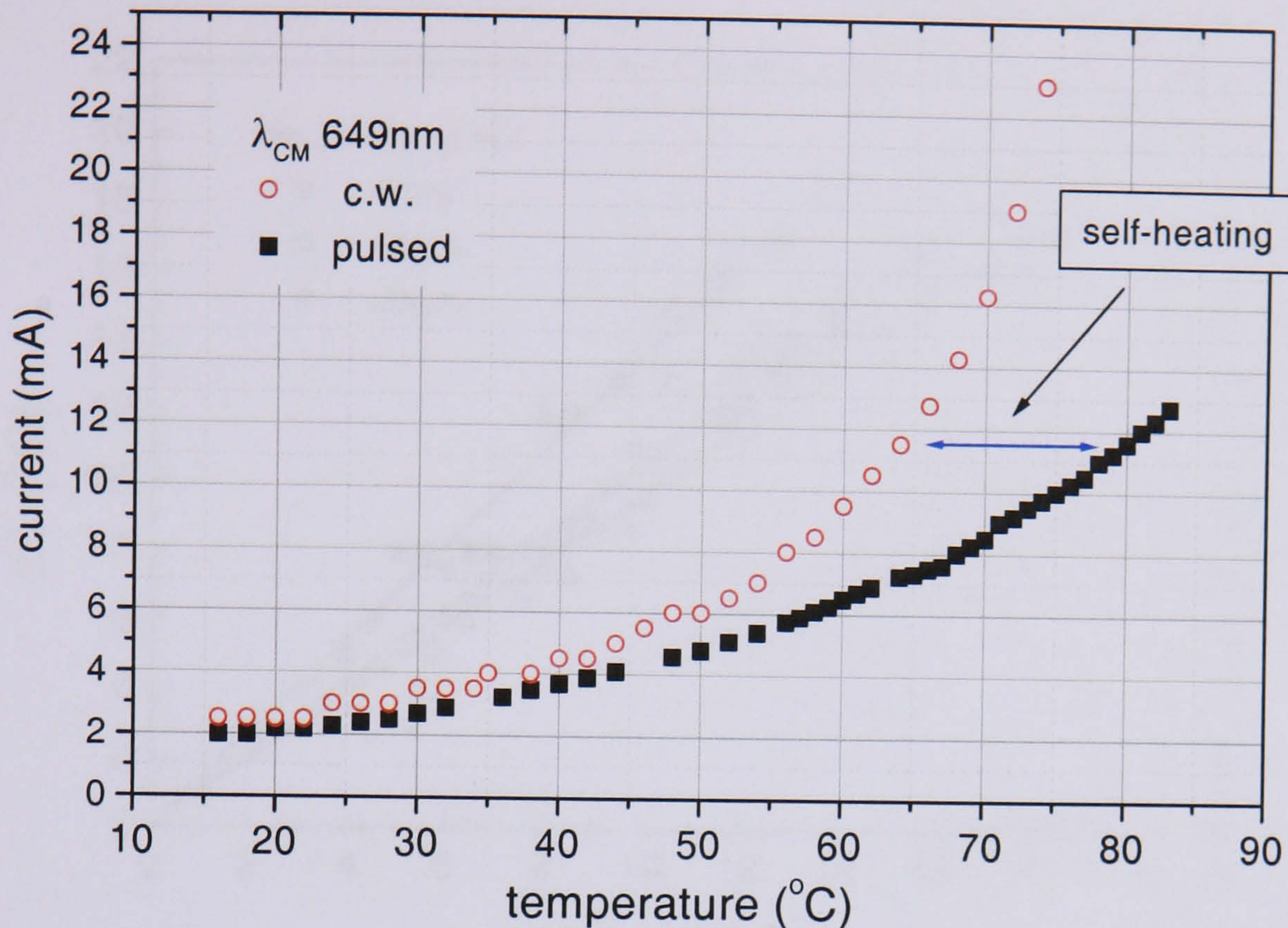

Figure 5.20: Current needed to achieve constant light output for pulsed and c.w. operation indicating the amount of self-heating.

for which the slightly longer wavelength means that leakage should play less of a role.

The difference in the temperature of the heat sink between the same c.w. and pulsed current required to achieve a constant light output can be used to determine the degree of self-heating, as indicated by the arrow in figure 5.20. With the help of the curves in figure 5.20 the actual temperature of the active region under c.w. operation can be estimated. The current of 11.5mA needed for a given light output at 64°C in c.w. operation is equal to that at 80°C in pulsed mode. Hence the actual temperature of the active region at a c.w. current of 11.5mA can reasonably be assumed to be 16°C higher than the ambient temperature and this difference is due to self-heating of the device. In figure 5.21 this temperature difference between c.w. and pulsed operation for three devices with different de-tuning (-1nm,+6nm and +9nm) is plotted as a function of current.

The slope of the three linear fits to the data decreases with increasing positive de-tuning. It is 1.37±0.03°C/mA for λ_{CM} = 649nm, 1.06±0.02°C/mA for

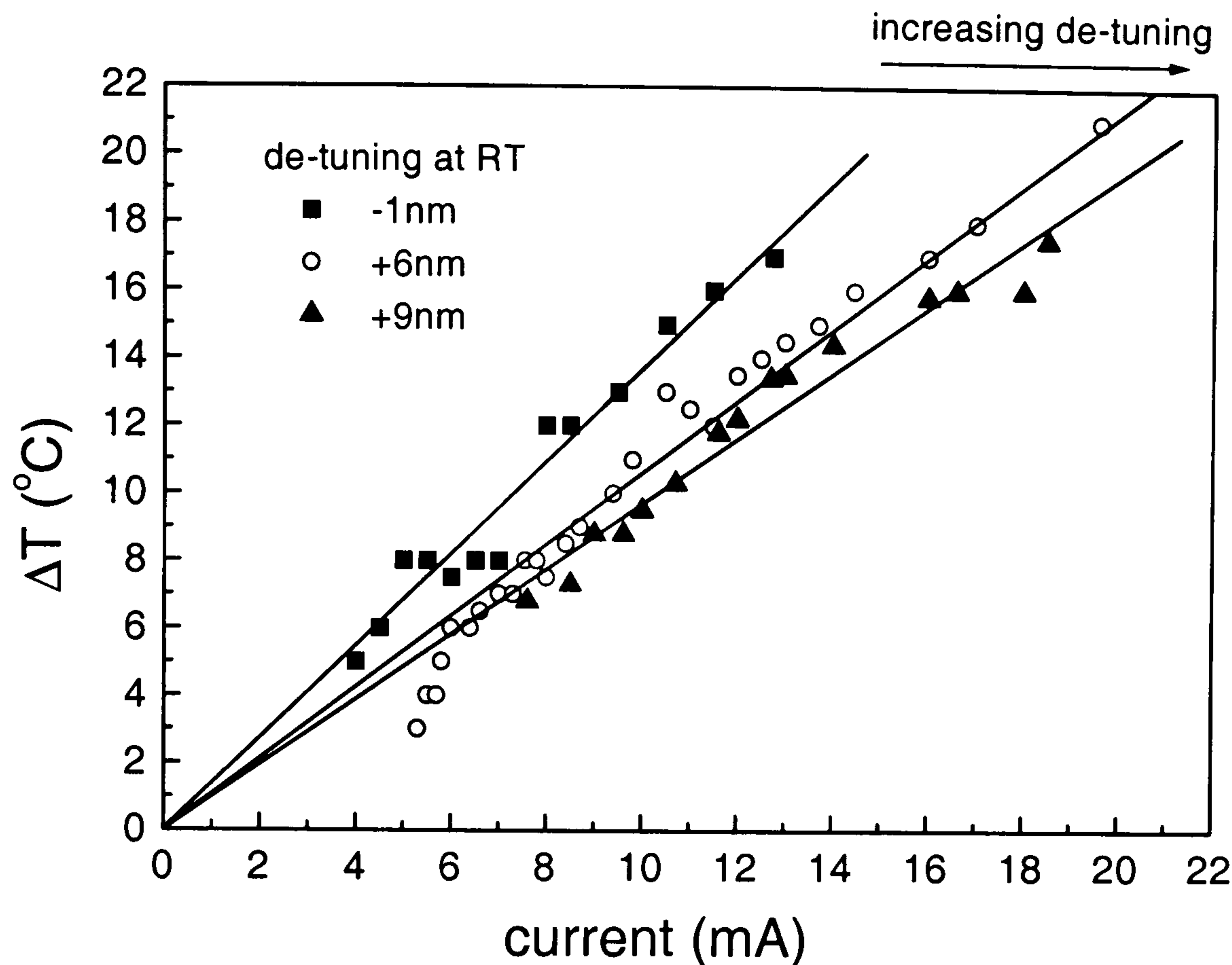

Figure 5.21: Internal temperature rise, ΔT, extracted from the difference between the device temperature for c.w. and pulsed operation for three devices with different de-tuning as indicated in the figure.

λ_{CM} = 656nm and 0.97±0.01°C/mA for the device with λ_{CM} = 659nm. This reconfirms the lower temperature sensitivity for the more positively de-tuned devices. The reason for the linear variation of ΔT with I is due to the fact that the heating of the device is proportional to the electrical power (P) input to the device. $P_{heat} = IV - P_{out}$ and P_{out} for all three devices is less than 1mW in that current range. This is equivalent to a power conversion efficiency of approximately 1-2% and hence the amount of P_{out} has negligible effect on P_{heat}. As V is approximately constant ($\sim 2V$), the power increases linearly with I and hence so does ΔT. The increase in ΔT is considerably less than in typical red VCSELs, where a value of 14.5°C /mA is reported [103]. This is mainly due to the much smaller device aperture ($\sim$ 14μm) of the VCSEL suggesting that ΔT, and the increase in it, decreases with device aperture diameter. The size dependence of self-heating will be discussed in the next chapter.

Self-heating also leads to a current dependence in the efficiency as be seen in figure 5.22 where the external quantum efficiency η_{eqe} is plotted for the three different devices at four temperatures. η_{eqe} is defined as the number of photons emitted from the device per electron injected i.e.:

$$\eta_{eqe} = \frac{light\ output \times e}{I \times photon\ energy}, \tag{5.2}$$

where I is the current passed through the device, e the electron charge and 1.907eV (equivalent to 650nm emission) is taken as the photon energy.

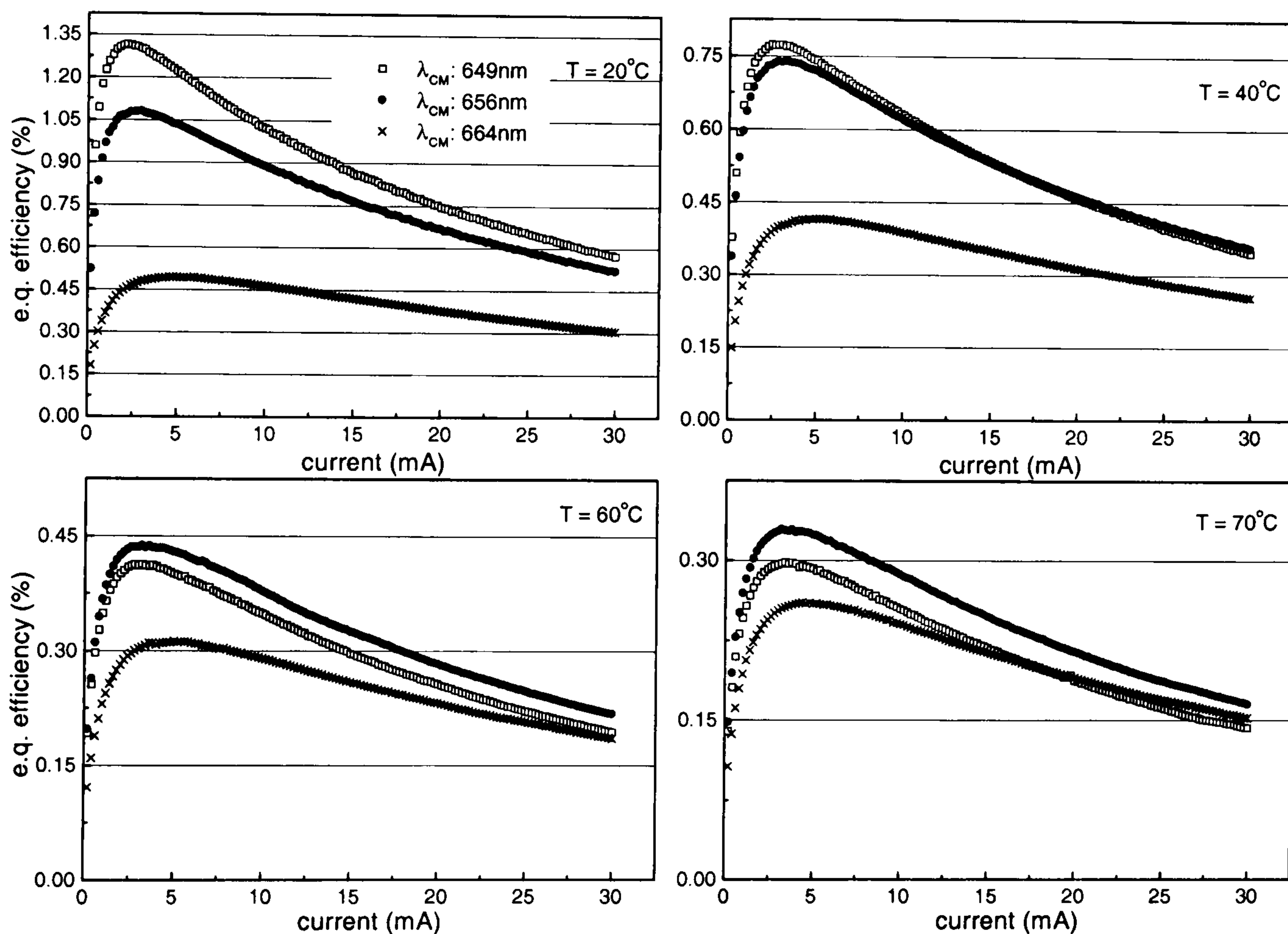

Figure 5.22: External quantum efficiency for three different devices at four different temperatures.

At 70°C the 664nm device is more efficient than the 649nm device only at currents higher than 16mA. In figure 5.22 it can also be observed that the current dependence is stronger for the initially tuned device (here the 649nm device). The maximum efficiency (at ~2mA) for the 649nm device is 2.3 times higher than the value at 30mA at 20°C. For the other devices this ratio is lower i.e. 2.1 for the 656nm and 1.6 for the 664nm device. This difference in the current dependence of the devices is

also due to self-heating. For the initially de-tuned devices, self-heating helps to tune them. The self-heating acts like an increase in the substrate temperature. Thus the light output decreases and the QW and CM shift to longer wavelength. If they are positively de-tuned at the ambient temperature, the self-heating brings them closer together. This is the reason why the efficiency of the de-tuned device decreases less strongly with increasing current compared to the tuned devices as seen in figure 5.22.

Ohmic self-heating is one of the factors that limits the device performance. The increase in the temperature of the active region enables other temperature induced losses to occur. Conversely self-heating helps de-tuned devices to tune in and thus makes them less temperature sensitive.

5.6.2 Leakage

Self-heating and the decrease of the spontaneous emission factor with temperature cannot account for all of the temperature induced decrease in efficiency. As will be discussed next, leakage plays a major role. The reason for carrier leakage in these devices can be seen in the bandstructure. Figure 5.23 shows a calculation of the conduction band alignment illustrating the Γ and one X conduction band minimum near the QW active region. The calculation is for the S1 RCLED structure (appendix A.1.) and is calculated for a current density of $520A/cm^2$, which corresponds to a bias of 20mA for a 70μm diameter device. The band structure and Fermi energy displayed in figure 5.23 have been calculated using a program by Dr A. Onischenko based on a drift diffusion model (DDM) [107].

A possible leakage path is indicated by the curved arrow marked e^-. This assumes that the carrier transfer to the X-minimum in the confining layers is the main contribution to leakage [102]. This is a particular problem as the effective mass of the X-minima are very large relative to the mass of the Γ-minimum leading to a large density of states. In addition to that there are 6 equivalent X minima compared to only one Γ minimum. Electrons moving from the n to the p side may

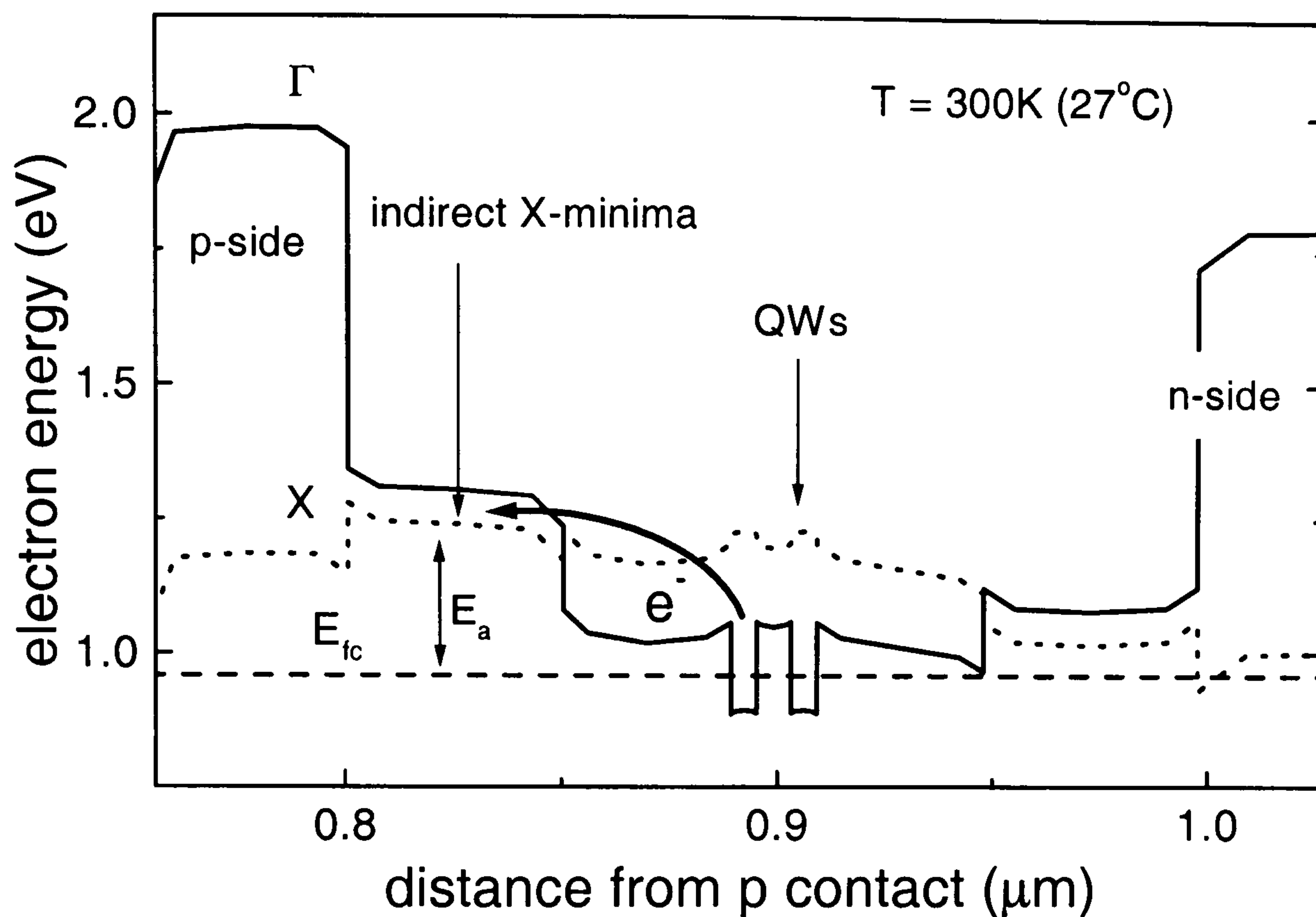

Figure 5.23: Detail of the conduction band alignment under forward bias, corresponding to 20mA for a 70μm device, showing the close proximity of the indirect X-minima which causes the carrier leakage. E_f is the Fermi energy and the difference between the energy of the X-minimum of the cladding and this Fermi energy is defined as the leakage activation energy E_a.

thermionically achieve enough energy to overcome the potential barrier from the Γ into the X minimum. The probability of this increases as $exp\frac{-E_a}{kT}$, where E_a describes an activation energy, which is also marked in the figure. The activation energy is defined as the difference between the conduction band quasi Fermi level and the X minima in the cladding. For a 70μm device under 20mA bias at 27°C the activation energy calculated by the program is E_a = 280meV. With increasing current i.e. increasing carrier density the Fermi level (E_{fc}) rises and thus the activation energy decreases. Therefore the density of carriers in the X-minima will increase not only with increasing temperature but also with increasing current density. As the X-minima are indirect, the probability of radiative X transitions is very low (and would also occur at a wavelength away from λ_{CM}). Thus most of the electrons will recombine non-radiatively via phonons, or recombine via defect states at the

contacts. Consequently, the higher the temperature, the more electrons have to be pumped into the active region in order to produce photons.

The effect of this can be seen in the LI curves. In figure 5.24 the current required to achieve a constant light output with increasing temperature is shown. The data points are extracted from full L-I curves measured at 2°C intervals.

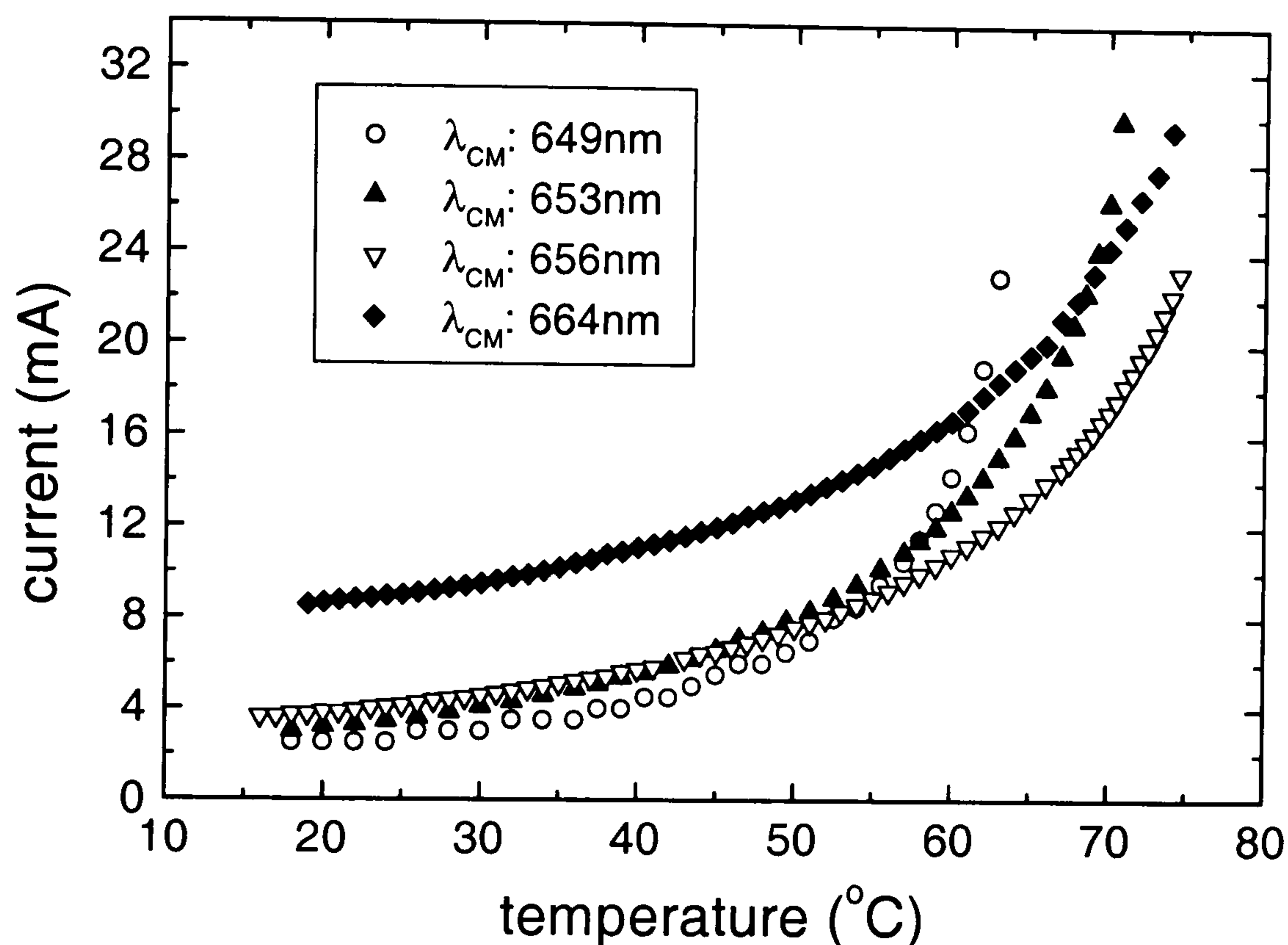

Figure 5.24: Current needed to achieve a constant light output for four different devices (λ_{CM} at 20°C is indicated) vs temperature.

Again, devices with different amounts of de-tuning (the λ_{CM} as it was measured for 20°C is indicated) are shown. The observation of a lower temperature sensitivity for the initially stronger positively de-tuned devices can be made here as well. For these devices more current is needed at lower temperatures, but as the temperature increases, less current is needed than for the initially tuned ones. In this temperature range, the 664nm device (filled diamonds in figure 5.24) requires less current than the 649nm device above 62°C, and as the 653nm device above 69°C and it will probably need less current than the 656nm device at temperatures above 80°C as well, but operating temperatures for most applications would be below 80°C. The influence of the de-tuning can be seen in the previously observed lower temperature

dependence of the de-tuned devices. This is mainly due to the fixed collection angle of $\sim 30^\circ$ and the difference in the far field spectra. With this collection angle, light up to 7nm - 8nm away from $\lambda_{CM}(0^\circ)$ is measured. For the 664nm device this means that the peak of the emission situated at λ_{QW} is not measured for low temperatures and thus more current is needed for this device than for the three others for which the QW emission falls within the collection angle. With increasing temperature more and more light is collected for the de-tuned devices making them less temperature sensitive. The overall influence of carrier leakage, which can be seen in the exponential increase of the current, is still prominent for all devices. To obtain a more quantitative description of the leakage, the data in figure 5.24 may be fitted with the following equation that describes the temperature dependence of the current.

$$I = bT + \frac{D}{exp(\frac{E_a}{kT})}, \tag{5.3}$$

where the first term is an approximation for the temperature dependence of the radiative recombination and the second term describes the temperature dependence of the leakage current. Figure 5.25 shows the pulsed data for the approximately tuned device at room temperature fitted according to equation 5.3. This pulsed data is used rather than the c.w. data in figure 5.24 to eliminate the self-heating effect.

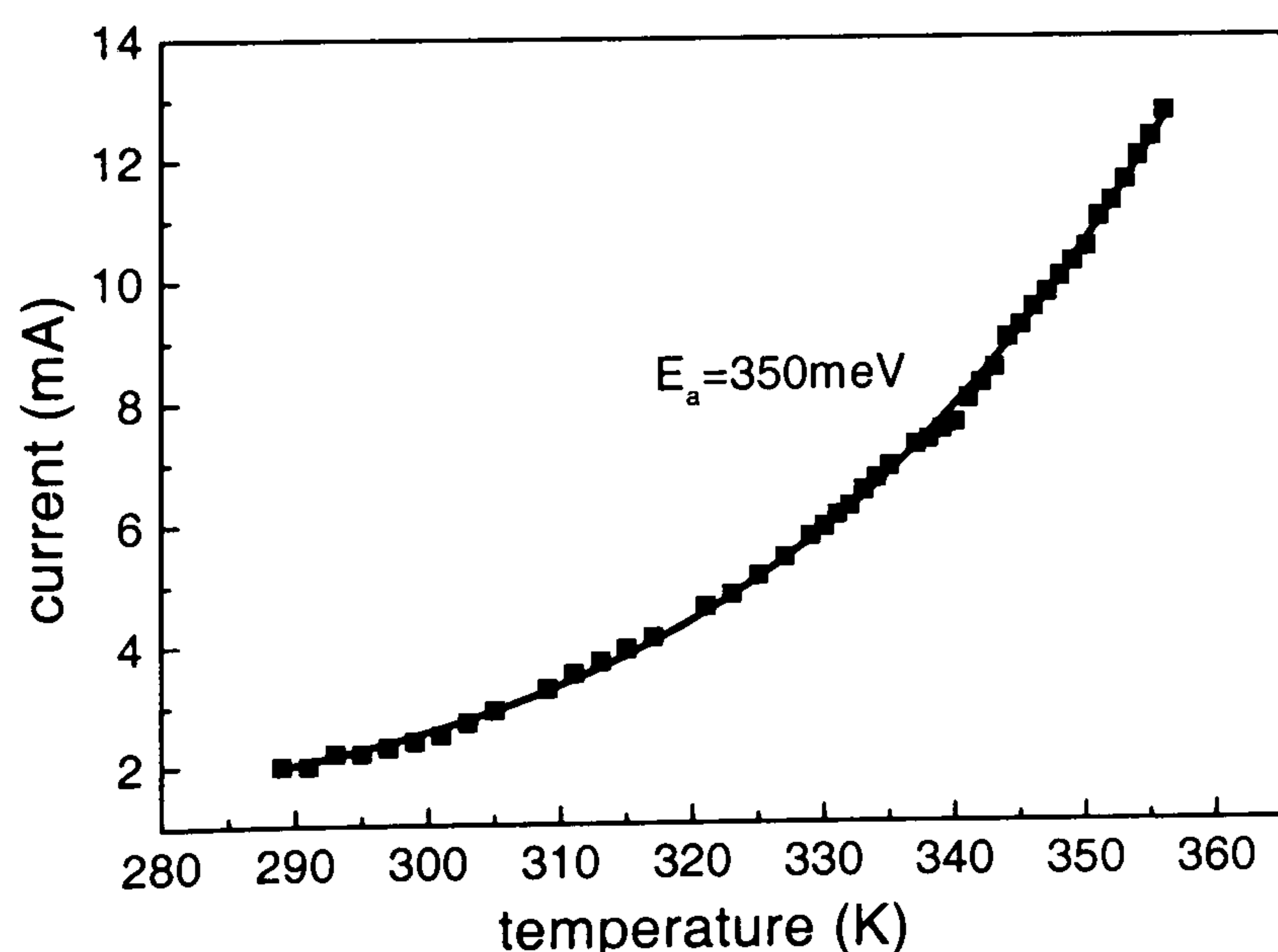

Figure 5.25: Fit according to equation 5.3 to the at room temperature tuned device.

The activation energy of 350±40meV determined from this fit is comparable with values in the range of 316 to 333meV that have been found by Smowton and Blood

for GaInP-based visible QW lasers [108]. From the DDM program, values between 250 and 380meV are extracted for the activation energy corresponding to current densities between 50 and $2500A/cm^2$, decreasing with increasing current density (as this increases the Fermi level). Hence the activation energy in figure 5.25 also depends on the current range and it will also be influenced by the initial and temperature-induced de-tuning.

The quantitative contribution that leakage plays in the increasing of the current required to maintain constant light output has to be investigated. To do this the variation of the current with temperature is simulated using the DDM program [107]. A schematic flow diagram of the operation of the DDM program can be seen in figure 5.26.

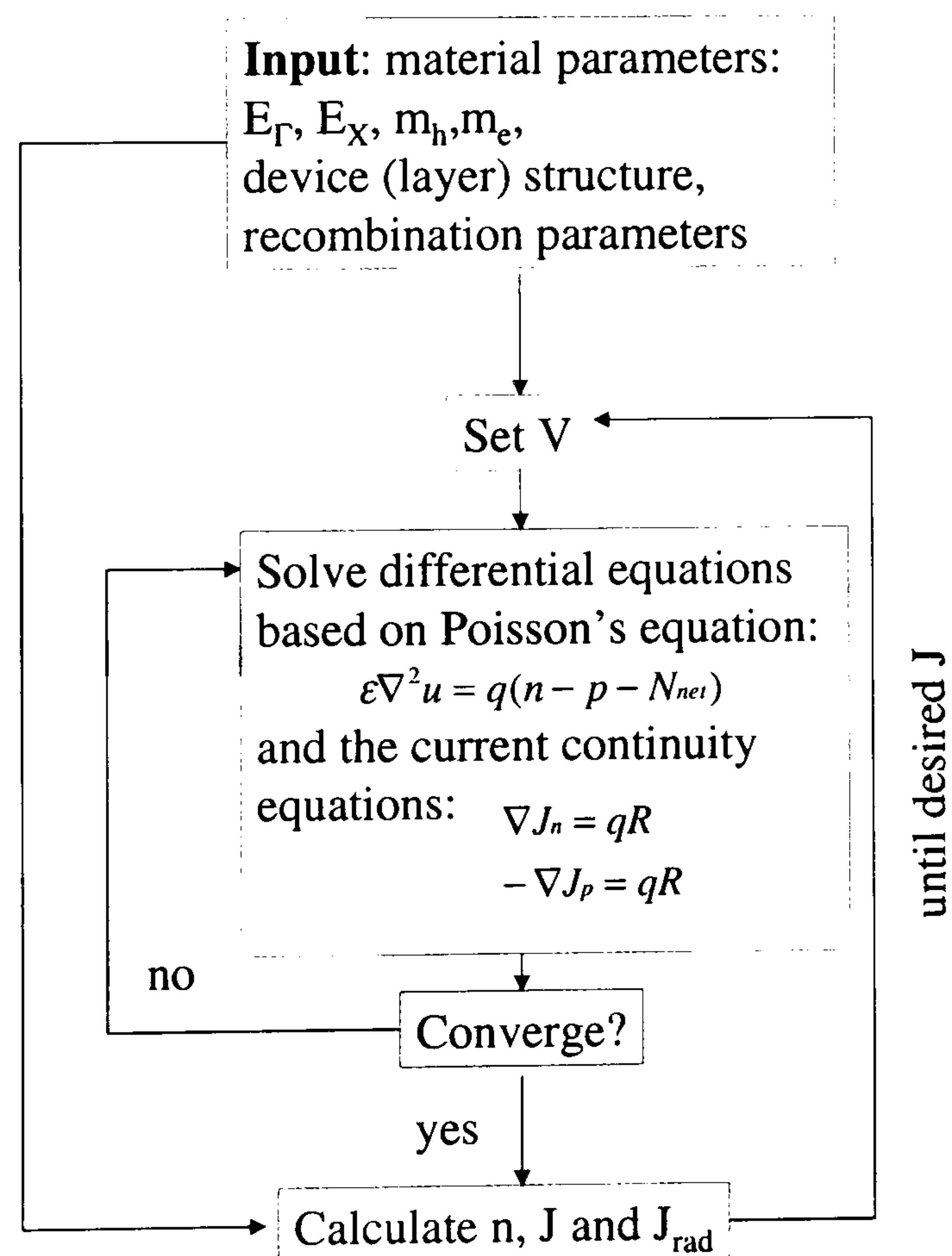

Figure 5.26: Diagram describing the program based on the drift diffusion model.

For all the devices, the theoretical proportion of the radiative current can be calculated and is compared with the measured results, as shown in figure 5.27. Here the

calculated radiative current together with the experimental results for pulsed and c.w. operation are plotted for the 664nm device.

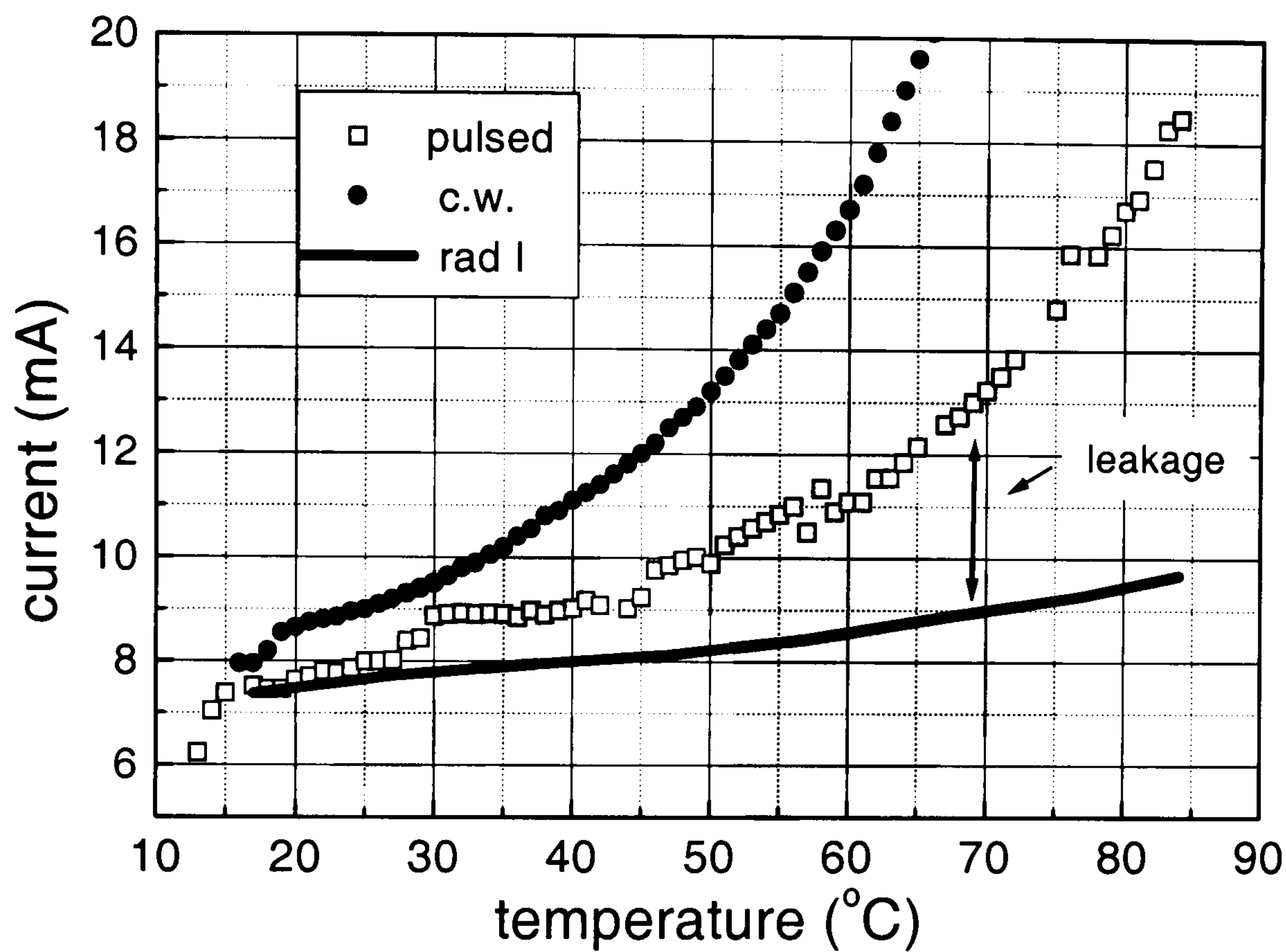

Figure 5.27: Calculated leakage current for achieving a constant light output together with the experimental currents measured under pulsed and for completion also the c.w. operation for the device with λ_{CM} (20°C)=664nm.

The radiative current required for a specific light output is calculated with the DDM program, by fitting to the measured pulsed current density to isolate the leakage from self-heating effects. The DDM model allows the various current paths and energy/carrier profiles to be calculated. The radiative current density calculated from the program increases approximately linearly with temperature confirming the assumptions made in equation 5.3. This ideal situation assumes no self-heating and no leakage. For all devices the percentage of the leakage current starts below 5% at 20°C but reaches almost 50% at 80°C.

Combining this with the previously calculated ratios of the self-heating to the total current, it can be concluded that the contribution of the radiative current is already less than 50% of the total injected current above 60°C. However it is im-

portant to note that these two factors cannot easily be separated, as particularly at higher temperatures, self-heating will lead to more leakage.

5.7 Conclusions

The effects of QW-CM de-tuning on the device spectra and on the light output characteristics have been investigated. The temperature dependent EL and LI measurements on devices with different amounts of de-tuning have shown that more strongly positively de-tuned devices are less temperature sensitive, when a collection angle of approximately 30° is assumed. This can be understood in terms of the QW tuning-in with increasing temperature and therefore weakening the effects of other temperature induced losses. The tuning-in is due to the different temperature dependencies of λ_{CM} and λ_{QW}. In positively de-tuned devices $\lambda_{QW} < \lambda_{CM}$. λ_{QW} increases 3 to 4 times faster than λ_{CM}, so the two wavelengths converge with increasing temperature.

Far field spectra reveal a cross-section through the angular dependence of the light output. Tuned devices have their maximum light output into the forward direction, whereas positively de-tuned ones show a two lobed output. The maximum light output is found at the angle where λ_{CM} and λ_{QW} are tuned. The angular dependence of the EL spectra shows that the spectral peak of the emission is determined by $\lambda_{CM}(\theta)$. If the total light output is calculated, the overall peak agrees with edge-EL spectra measured earlier and described in chapter 3.

With a collection angle of ~27°, that was chosen to simulate the coupling into a plastic fibre, the maximum light output at 20°C occurred for devices with a de-tuning between 0 and 3nm. The maximum light output and temperature sensitivity depend strongly on the collection angle. It has been confirmed that the maximum light output for a given temperature occurs for a device in which the QW emission peak falls in the middle of the escape (collection) angle. Assuming a collection angle of 27°, a compromise between high light output and low temperature sensitivity has

to be found. For the operating range of up to 80°C it can be calculated that a device positively de-tuned by 4.5nm (at 20°C) will have the highest light output at 80°C. Devices with stronger de-tuning will show less temperature sensitivity but will show lower light output for all operating temperatures.

The most important loss mechanism is carrier leakage into the indirect X-minima which accounts for almost 50% of the current at 80°C. An activation energy for leakage of 350meV has been found agreeing with other published values and theoretical calculations. The compactness of the active region of these devices leads to Ohmic self-heating. The combination of this with leakage in the devices is responsible for the strong temperature dependence that ultimately cannot be compensated for by de-tuning. Nevertheless, operation at temperatures of over 80°C have been observed which confirm the thermal performance advantages of RCLEDs over VCSELs at the same wavelength. Another advantage over VCSELs is the lower increase in self-heating $d\Delta T/dt = 1.4°\text{C/mA}$ for the initially tuned device. For an operating current of 20mA a light output of approximately 0.1mW is observed at 70°C for a collection angle of 27°. This corresponds to between 25-50% of the output at 20°C depending on the original de-tuning.

For tuned devices self-heating decreases the light output and thus increases the temperature sensitivity. For de-tuned devices, self-heating acts like an increase in the ambient temperature, thus helping the de-tuned devices to tune-in resulting in a lower temperature sensitivity.

Chapter 6

Influence of top DBRs and aperture size

6.1 Introduction

The top mirror reflectivity can be optimised to achieve the highest light output for coupling into an optical fibre [50]. If the top reflectivity is much lower than the bottom reflectivity the device acts like a conventional LED. Thus it would not have the high directionality of the light output that is needed for fibre coupling. Also, the enhancement of the spontaneous emission, that can be achieved by the bottom mirror alone, if the QW is very close to the mirror [35], will not be as high if the top mirror has a very low reflectivity. If the top and bottom reflectivity both equal unity, all the light gets reflected back and forth and no light can leave the device. In this chapter the general influence of the top DBR reflectivity on the light output shall be investigated.

In the previous chapter it was suggested that the size of the current/ output aperture could play a role particularly in the temperature dependence of the light output. This will also be investigated in this chapter. For a given current the current density is higher in a smaller device, which will thus behave differently from a larger

one. To find out about any intrinsic size dependencies the effect of the size of the devices at the same current density will also be investigated.

6.2 Dependence on number of top DBRs

To measure the influence of the top reflectivity, devices were processed from three different wafers with 8, 11 and 14 top DBR pairs. The number of bottom DBR pairs was 32 in all cases and the rest of the structure was also nominally identical for all three wafers which all had two QWs. The structural details for these wafers can be found in appendix A.4. For all these wafers the two QW positions were kept constant and were measured by edge-EL and PR to be at 651nm and 640nm respectively, as discussed in chapter 3. In figure 6.1 the reflectivity spectra for these three wafers as measured are shown.

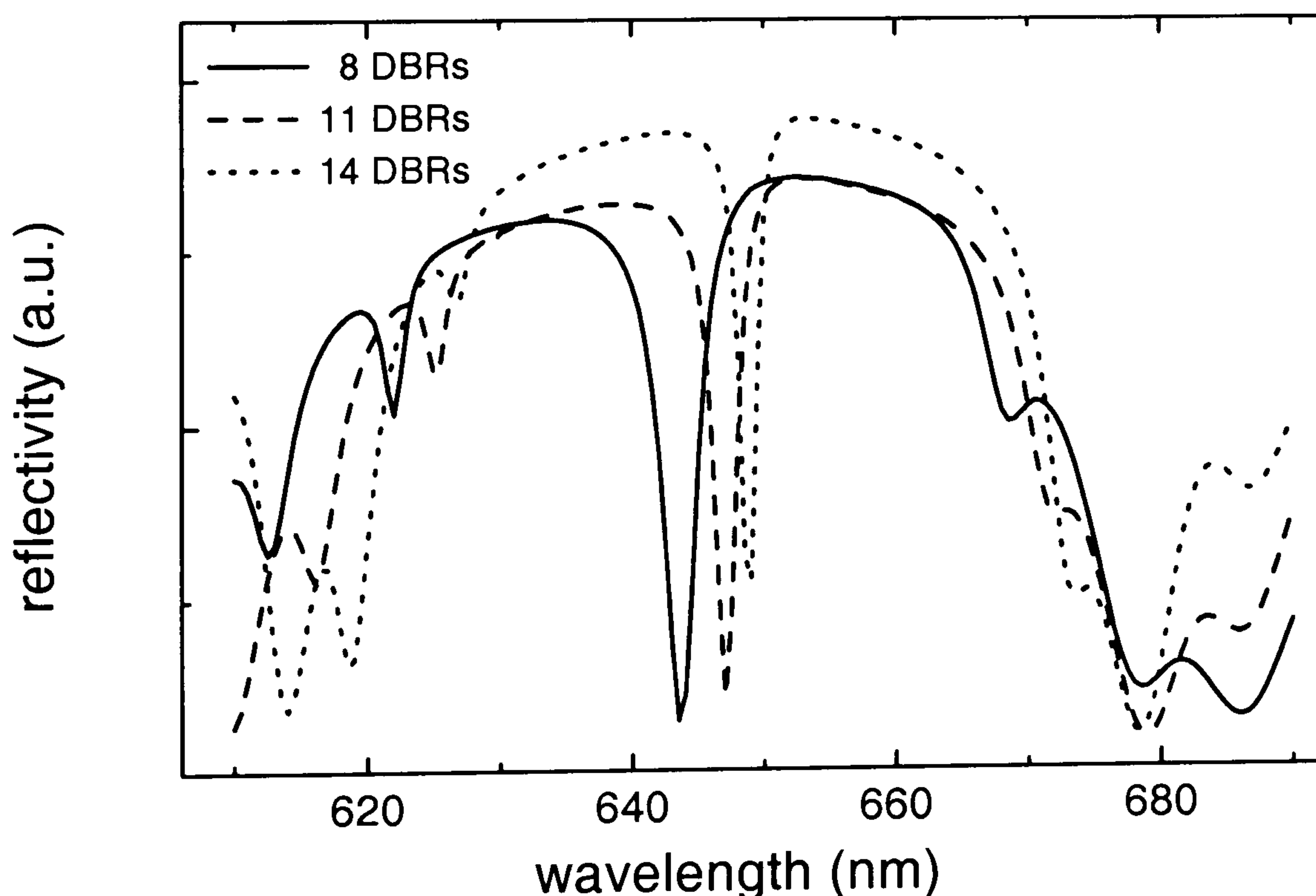

Figure 6.1: Measured normal incidence reflectivity spectra of three RCLED wafers with 8, 11 and 14 pairs of top DBRs. In all other respects the structures are nominally identical.

Three features can be seen. The total reflectivity is higher for the wafer with 14 top DBR pairs. The width at half the depth of the dip decreases from 2.9nm for the

wafer with only 8 pairs to 2nm for the one with 11 pairs and finally to 1.4nm for the one with 14 DBR pairs. The shift of the cavity mode (from 643.5nm and 647nm to 649nm) with increasing number of DBR pairs as already been observed in chapter 4 is due to non-intended changes between the growth of each wafer.

In order to avoid measuring again the effect of different QW-CM de-tuning, but only the influence of the top reflectivity, devices with the same cavity mode have to be found. The cavity mode varied slightly across the wafers. With the help of reflectivity measurements on the devices as described in chapter 4 devices from the three wafers with the same λ_{CM} could be chosen. As the variation of λ_{QW} is expected to negligible, devices with the same de-tuning but different number of top DBRs could be chosen for the comparison of their light output.

6.2.1 Electroluminescence spectra

In the electroluminescence spectra (figure 6.2) one can observe a difference in the FWHM for the devices with different numbers of top DBR pairs. The EL spectra were obtained at 20°C and 20mA for 70μm diameter devices. The observed FWHM of the spectra results from a combination of the effect of the width of the cavity dip and the collection angle.

The collection angle accounts for 6nm of the observed EL broadening as all the light up to an angle of 27°, corresponding to $\lambda_{CM}(27°)\sim$652nm, from normal incidence was collected. The initial width of the CM dip, which is different for the three structures, is responsible for the additional broadening and thus greater for the 8 DBR device. The width of the intrinsic QW emission is much broader than the CM dip for all currents and thus its broadening with current density has no influence on the FWHM of the EL spectrum. The spectra shown in figure 6.2 all have their λ_{CM} at 658nm but it can be seen that their emissions all peak somewhat below 654nm. The reason for this offset, as discussed in the previous chapter is due to the QW/CM de-tuning (here 7nm) and the large collection angle of the set-up.

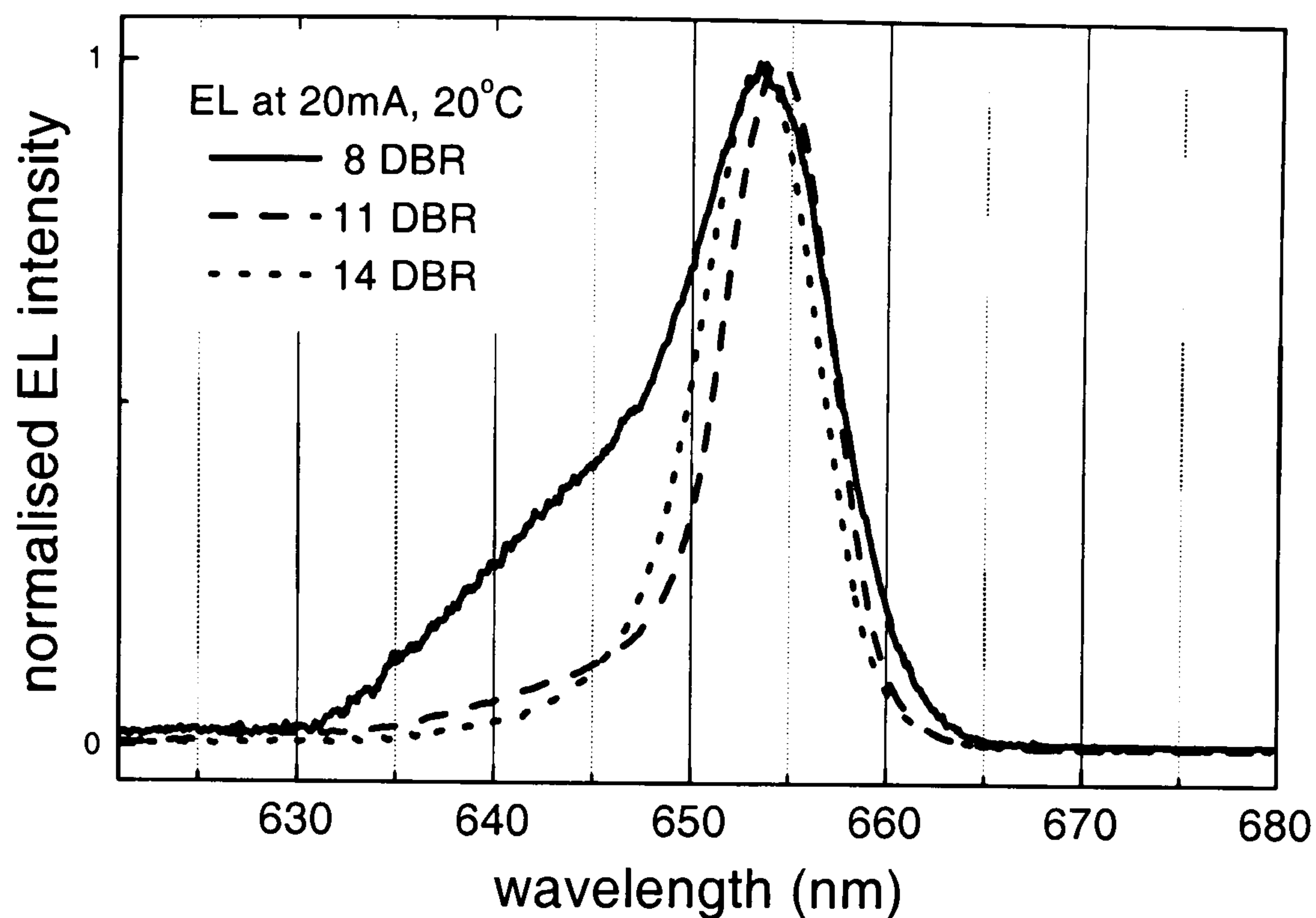

Figure 6.2: EL spectra for three devices with 8, 11 and 14 top DBRs at 20°C and 20mA. λ_{CM} = 658nm at 20°C for all devices determined by reflectivity measurements on the devices directly.

6.2.2 Light-current characteristics

The light current characteristics of three devices with 8, 11 and 14 top DBR pairs and a λ_{CM} of 658nm at 20°C have been investigated with the same collection angle. Thus at room temperature the devices are all positively de-tuned by 7nm with respect to the first and 18nm with respect to the second QW. Figure 6.3 shows the light output versus current measured with the probe station set-up for the three devices at four different temperatures.

There is little difference in the LI characteristics between the three devices. Benisty et al [35] suggested a way to calculate the critical number of pairs, p^{crit}, to gain most of the attainable extraction into a specific fraction of the solid angle defined by the $NA = sin\theta$:

$$p^{crit} \sim \frac{n}{2\Delta n} ln\left(\frac{4n\Delta n}{sin^2\theta}\right). \tag{6.1}$$

For this material system this suggests an minimum of 13 pairs for the optimal emission into a NA of 0.5. This is assuming $n = (n_1 + n_2)/2$ with $n_1 = 3.5$ (for

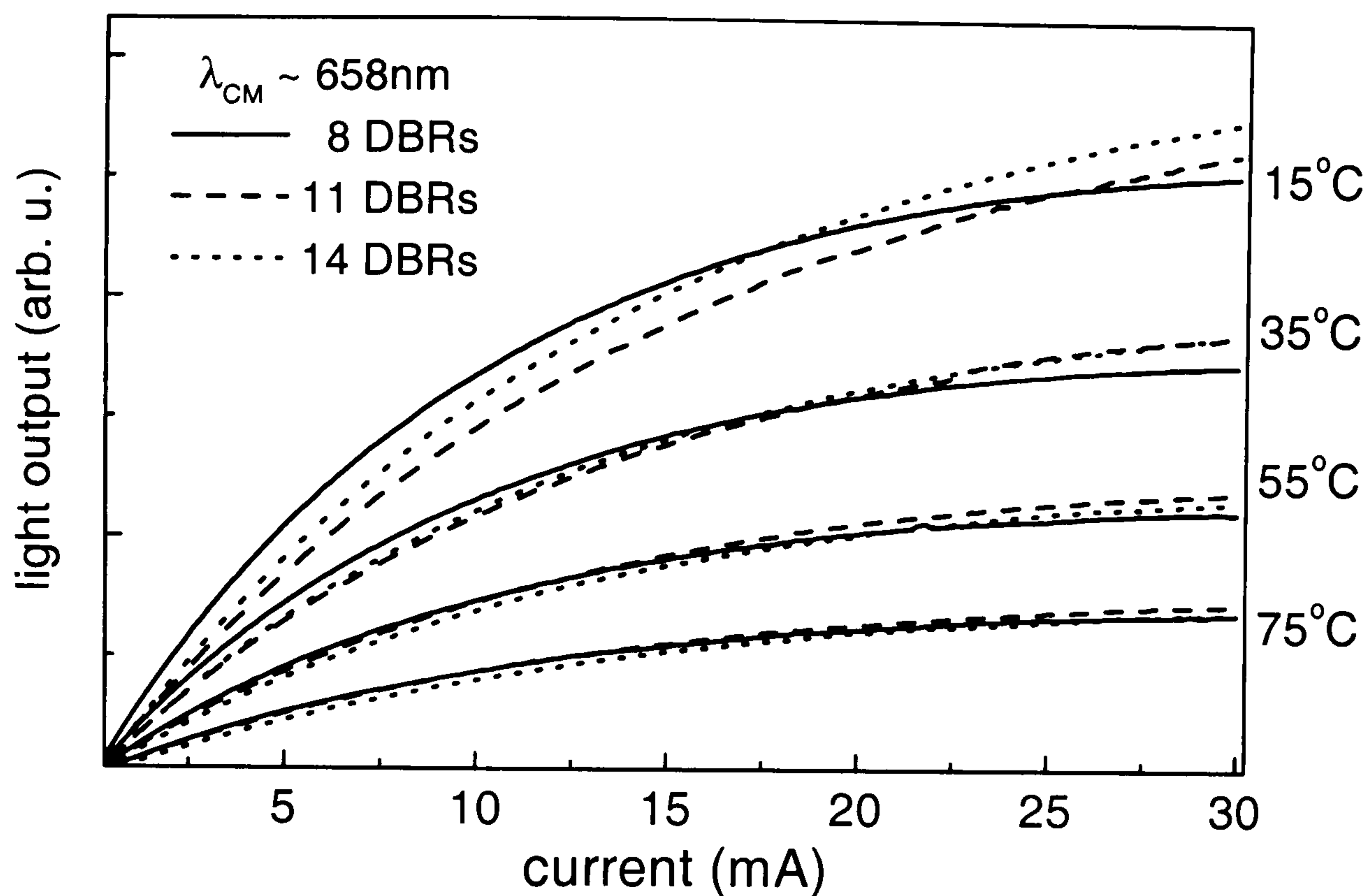

Figure 6.3: Light output versus current for three devices with different numbers of top DBRs but same amount of de-tuning for four different temperatures (λ_{CM} = 658nm, λ_{QW1} = 651nm, λ_{QW2} = 640nm).

the $Al_{0.5}Ga_{0.5}As$ layer) and $n_2 = 3.1$ (for the $AlAs$ layer) and $\Delta n = n_1 - n_2$. This would suggest that the 14 DBR device would be more suitable for coupling into a fibre with a NA of 0.5. This is confirmed by comparing figure 6.4 which shows the total light output (measured using a broad area detector) for the three in devices figure 6.3 at RT. The coupling, can be calculated as the ratio between the light output into the collection angle of 27° to the total light output. This is higher for the 14DBR device particular at higher currents. This confirms (from equation 6.1) the higher predicted coupling for the 14DBR device.

These measurements were performed at room temperature after the devices had been bonded onto TO-cans. As there is no effective heat-sinking or temperature control the roll over occurs at a lower current than for the bare devices shown in figure 6.3 (which were measured on the probe station with a heat-sink and temperature controller). However although showing the expected trend of the higher coupling for the 14DBR device the difference in the light output between the three devices is

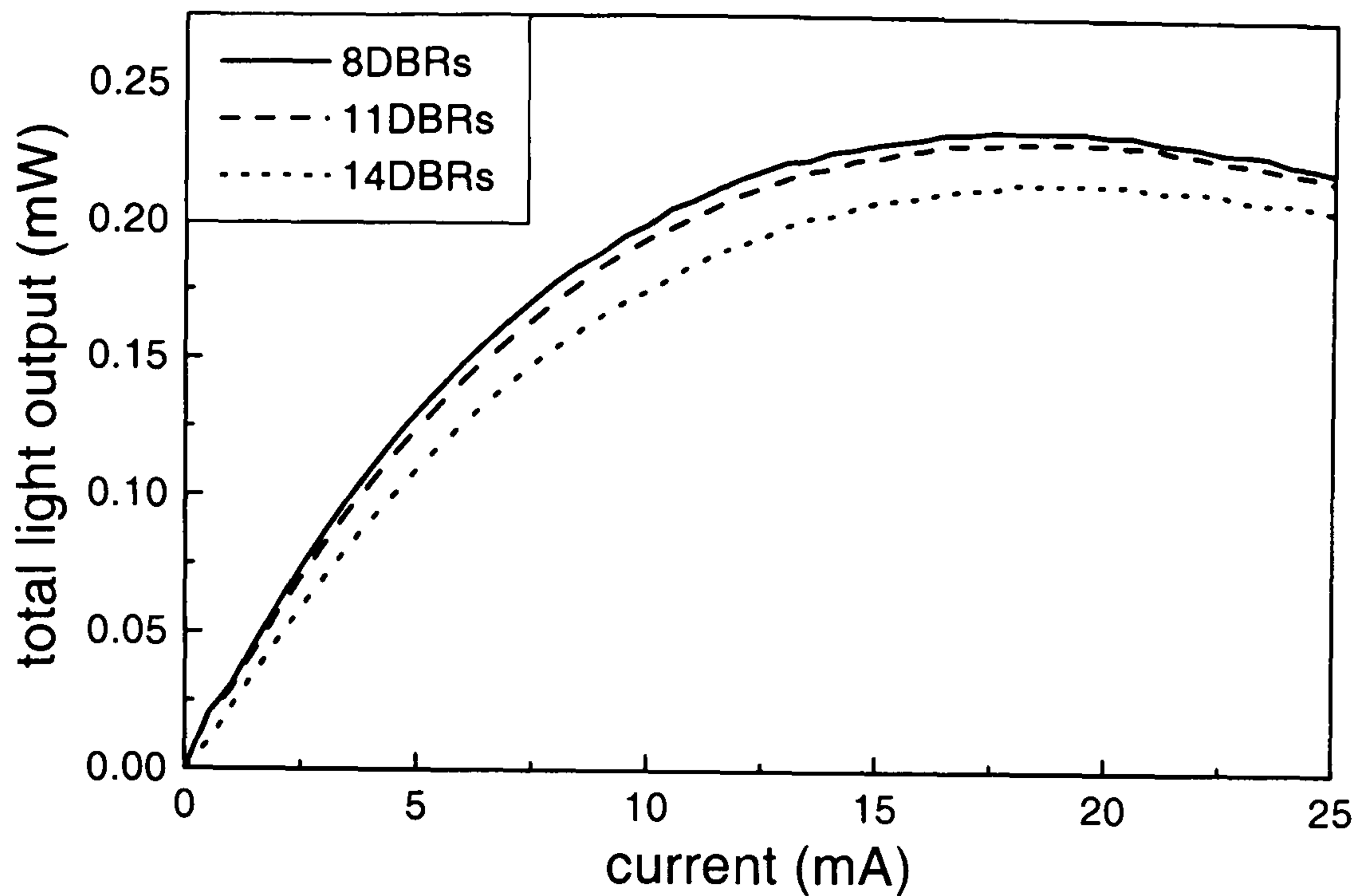

Figure 6.4: Total light output for the three de-tuned devices with different number of top DBRs shown in figure 6.3.

not very significant.

6.2.3 Temperature dependence

All of the devices studied here are for operation at 20mA, which is the standard current used by most LED manufactures to quantify devices and also the current at which LED data drivers are designed to run. A current of 20mA is a compromise between being low enough to minimise power consumption and high enough to allow stable operation. The variation of the light output with temperature into a NA of 0.5 at 20mA, can be extracted from the full L-I curves. This is shown in figure 6.5, which compares devices with different number of top DBRs and devices with different de-tuning.

In addition to the 3 devices with λ_{CM} = 658nm (shown in the last two graphs) two further devices, an 8 and an 11 DBR device with λ_{CM} = 652nm are shown. These two devices have therefore an almost negligible de-tuning, of about 1nm with respect to the first QW, and 12nm with respect to the second QW. Figure 6.5 shows

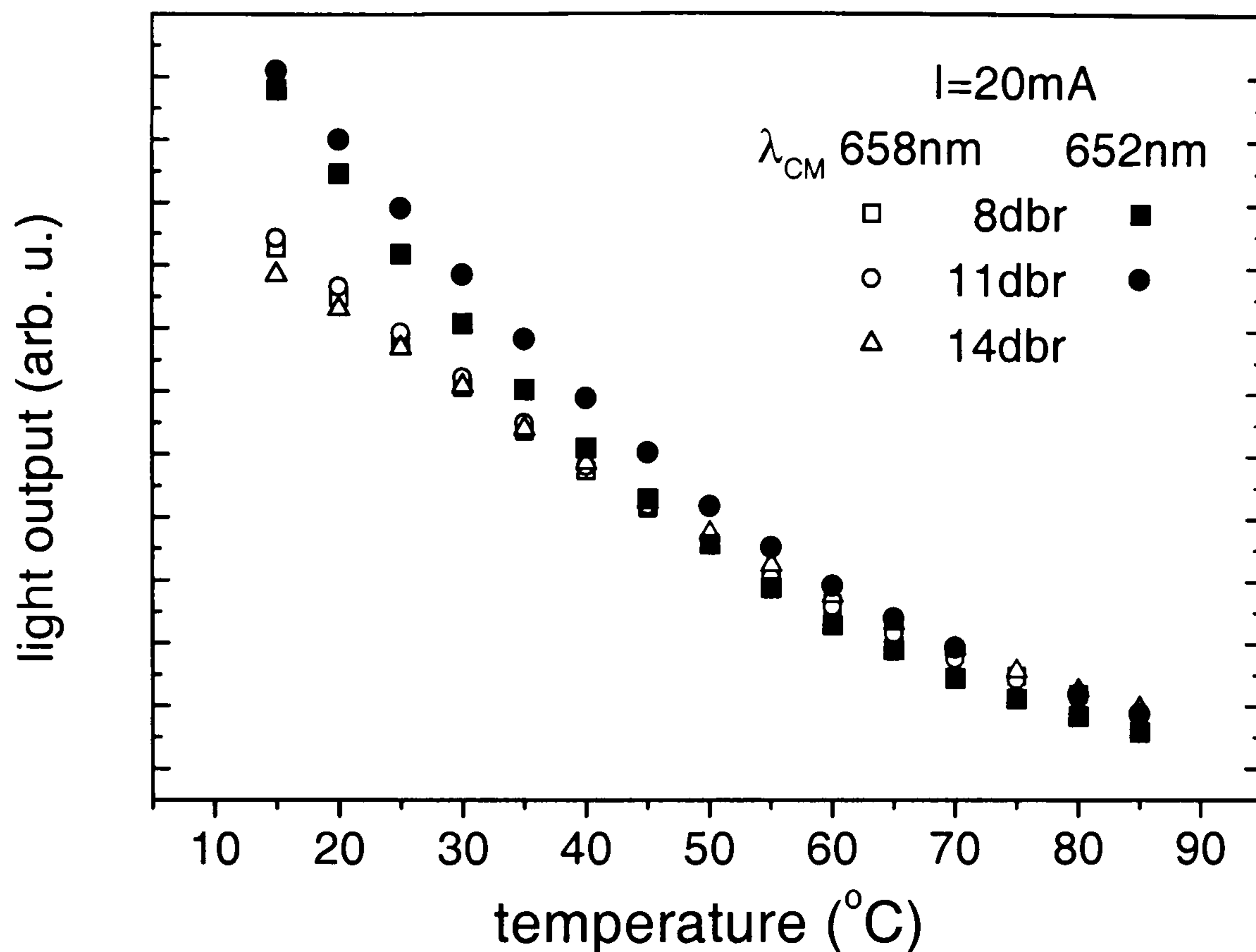

Figure 6.5: Temperature-dependent light output at 20mA for 5 different devices.

that the temperature dependence is almost exclusively determined by the amount of de-tuning and not by the number of DBR pairs. As seen in graph 6.3 the device with 14 DBR top pairs shows a stronger temperature dependence than the devices with less top DBR pairs. However, compared to the effect of the de-tuning this is almost negligible.

Overall it can be said that the variation in the top reflectivity between 8, 11 and 14 DBR pairs has only a small effect on the intensity and spectral form of the light output for a fibre-like collection angle of 27° as considered here. It was found that there is no difference in the temperature sensitivity for these otherwise identical devices.

6.3 Size dependence

To investigate the size dependence, devices were measured with different current and equivalent output apertures. The current apertures were defined by ion implantation and each device was fabricated with an output aperture according to the current aperture. The diameters that were available for investigations were 25μm, 50μm, 70μm, 100μm, 150μm and 200μm. Figure 6.6 shows images of the bare devices indicating the output diameter.

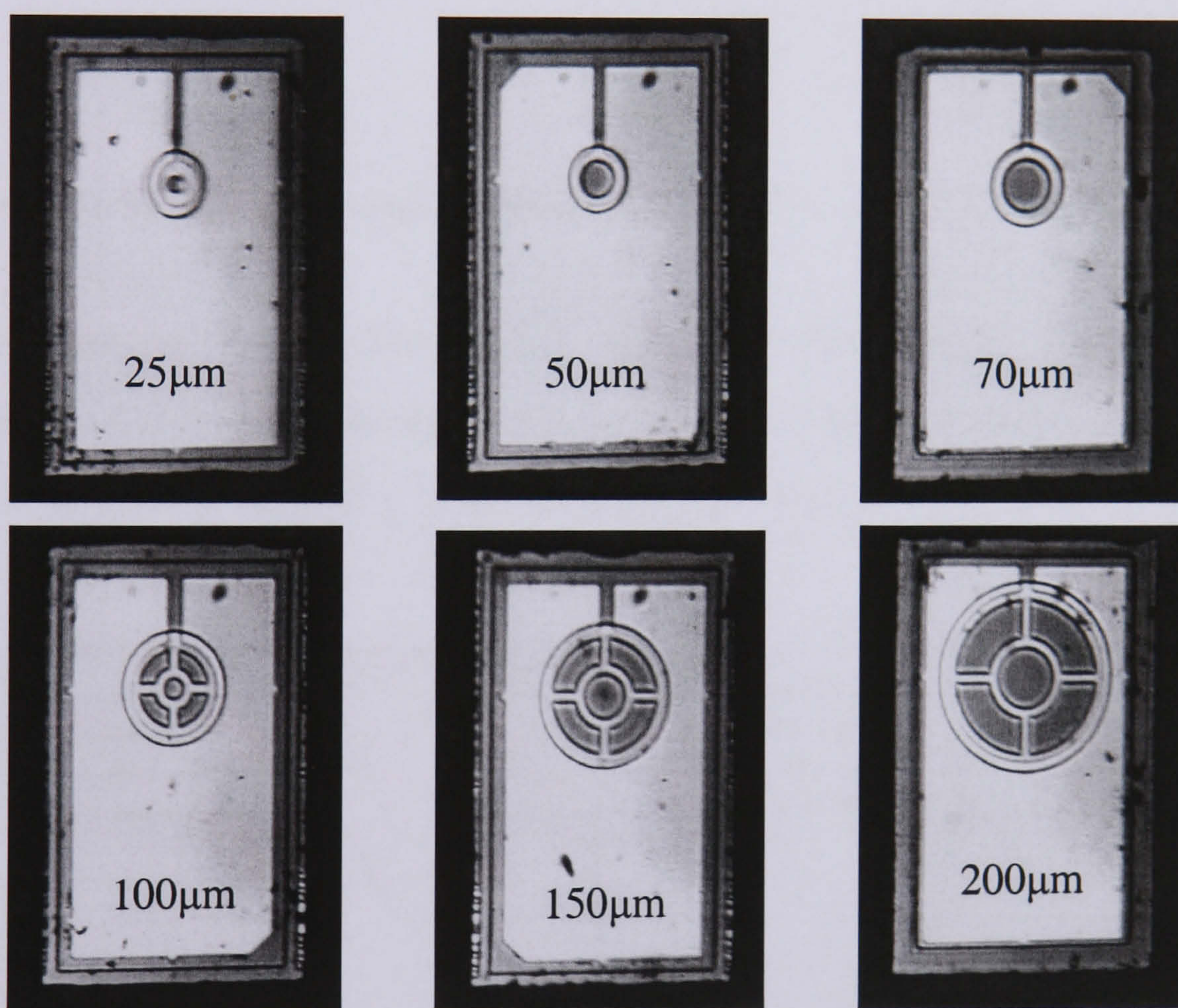

Figure 6.6: Pictures of the devices showing the different size apertures. All the devices are $600\mu m \times 420\mu m$.

This shows not only the different sizes but also the difference in the contact design between the three small and the three larger devices as will be discussed later. The devices were all processed from the S1 wafer which has a single QW emission at 650nm (structural details can be found in apppendix A.1.). The devices are therefore identical apart from the aperture size.

6.3.1 Electroluminescence spectra

The EL spectra were measured for all the different device sizes and at different current densities with the set-up described earlier in figure 5.3 at normal incidence without changing the angle as seen in figure 6.7.

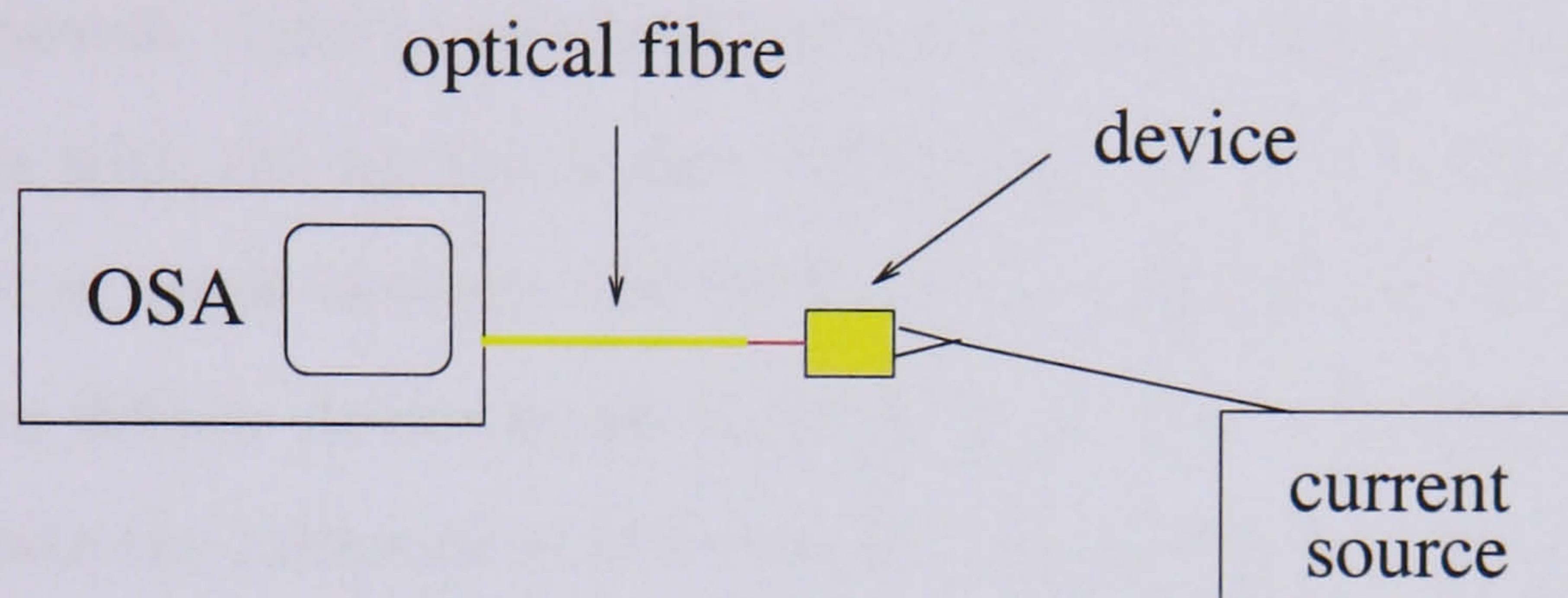

Figure 6.7: Set-up to measure normal incidence EL spectra of packaged devices.

Hence the measured EL spectra should only show the normal incidence contribution. However as the cavity finesse is not infinite the light at normal incidence is not purely determined by $\lambda_{CM}(0°)$. The resulting EL-spectra are shown in figure 6.8.

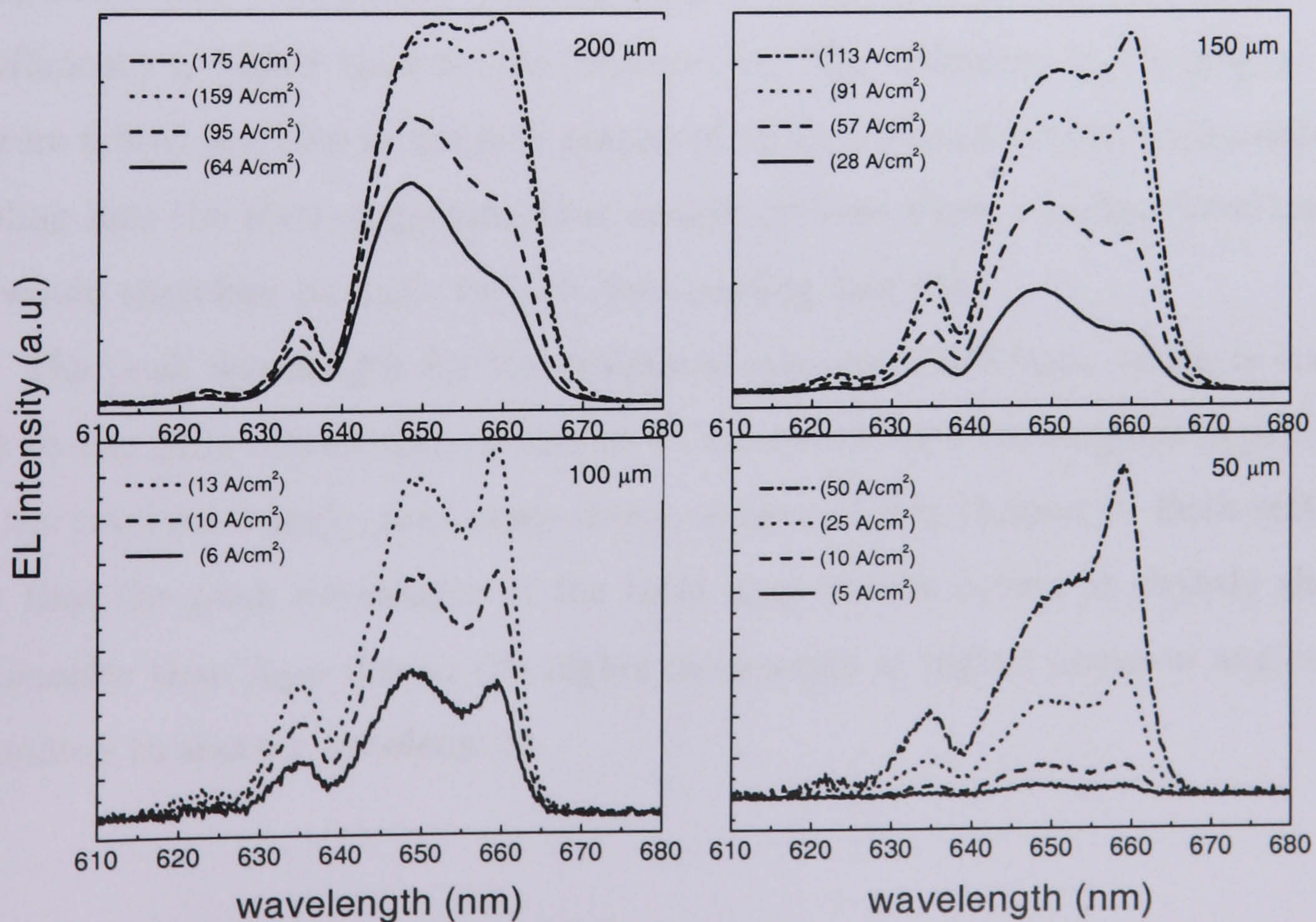

Figure 6.8: EL spectra for different device sizes for various indicated current densities.

For all devices there are two peaks in the spectra at 649nm and 659nm. These correspond to λ_{CM} at normal incidence (659nm) and the peak of the quantum well emission (650nm), respectively. At smaller currents and for the larger devices (smaller current densities), the quantum well peak at 650nm is more prominent than the peak corresponding to the normal incidence cavity mode wavelength at 659nm. The current density at which both peaks are at approximately the same height increases with the aperture size. One reason for this is the difference in the effective collection angle between the devices. At a distance of 2mm from the fibre light leaving the 200μm device at an angle of up to 6° is all collected by the fibre.

To eliminate the influence of this fibre coupling efficiency, measurements of the spectra were performed with all light collected into an integrating sphere before being passed into a spectrometer. Figure 6.9 shows a comparison of the front emission (coupled into a fibre) and the total emission collected with an integrating sphere at 20mA for two devices.

It is apparent from figure 6.9(b) and the inset, which shows the normalised spectra, that the shape, including the FWHM, of the total emitted spectra do not depend on the aperture size. The intensity for the larger device at the same current and thus the efficiency is higher than for the smaller one. The difference in the spectra seen in figure 6.9(a) and also in the four graphs of figure 6.8 must be due to the different coupling into the fibre suggesting that smaller devices show a higher directionality and would therefore be more suitable for coupling into fibre.

The peak wavelength for the integrated spectra is 648.5nm, which is comparable to the peak wavelength of 649nm as measured with the angular dependence into the total solid angle, previously shown in figure 5.8 in chapter 5. Both methods show that the peak wavelength of the total light output occurs at slightly shorter wavelengths than λ_{QW} due to the higher solid angle at higher emission angles corresponding to shorter wavelengths.

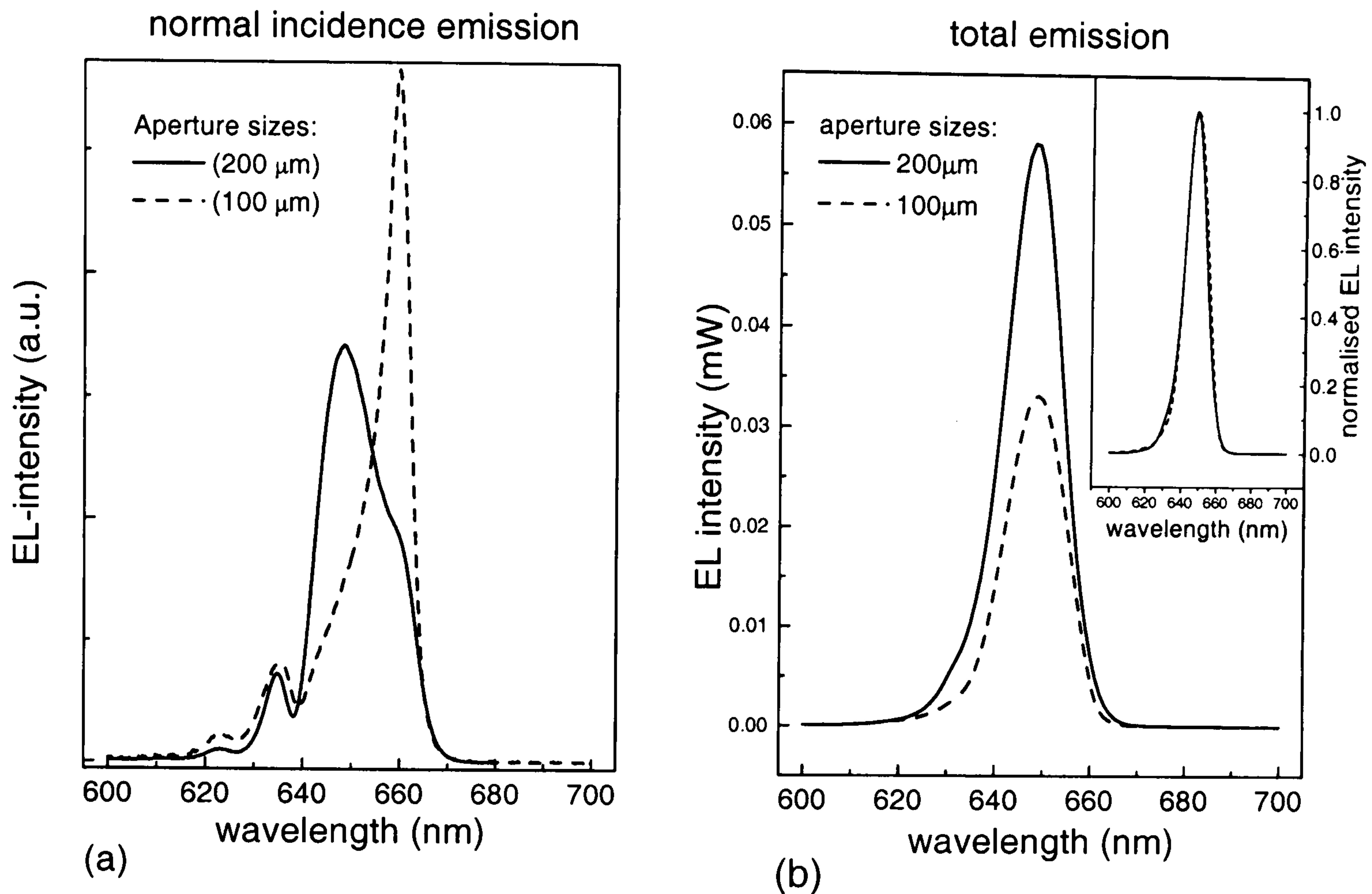

Figure 6.9: Comparison of the total spectral light output and the front emission at 20mA for a 100μm and a 200μm device.

6.3.2 Light-current characteristics

The light current characteristics (LI) were measured for all the available device sizes over a range of temperatures. Figure 6.10 shows the LIs at 25°C together with the external quantum efficiencies, η_{eqe}, (calculated from equation 5.2) over a current range of 0-20mA. The devices were packaged into TO-cans and the total light output, over the whole solid angle, was measured with a large area detector.

For a given current above 7mA it is clear that the light output and also the efficiencies are higher for the larger devices. Also there is a noticeable difference in the shape of the η_{eqe} versus current relations between the three small and the three larger devices: the maximum of the efficiency occurs at lower currents for the three smaller devices, and decreases more quickly with increasing current. The former effect is probably due to the difference in the contact design (as shown in figure 6.6). The faster

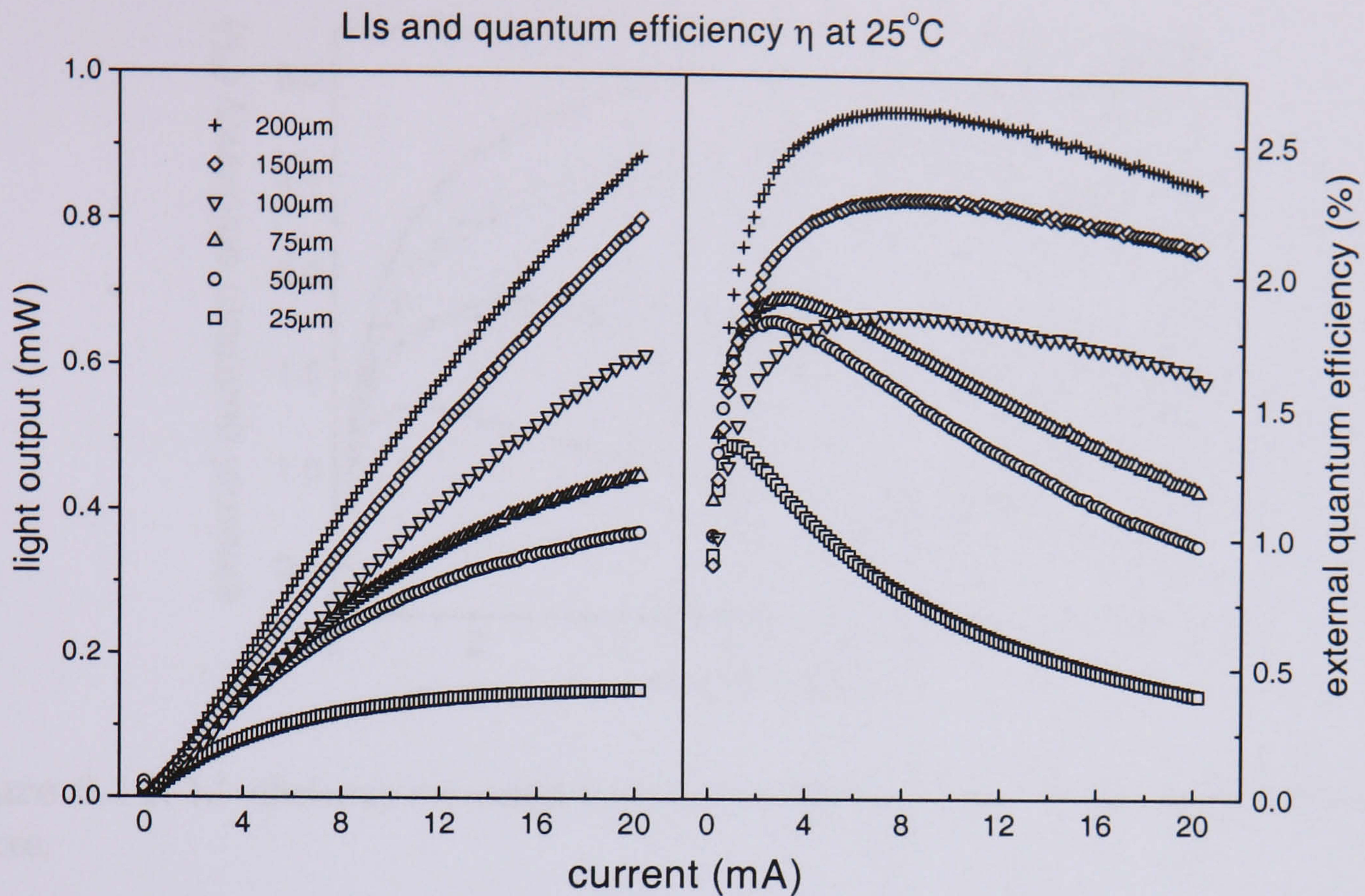

Figure 6.10: LI-curves and external quantum efficiencies for 6 different device sizes at 25°C.

decrease of η_{eqe} at higher currents for the smaller devices suggests that non-radiative and self-heating effects are more predominant in smaller devices. The spoked contact over the aperture for the three larger devices (as seen in figure 6.6) obscures some of the light. Hence at low currents, the efficiency appears to be higher for the smaller devices. In figure 6.11 the efficiency has been corrected for this effect.

The correction was made by assuming that the light is generated uniformly across the injected area but only that generated in the un-obstructed area is collected. This graph shows that larger devices are now more efficient for all currents.

To find out if there is an intrinsic size dependence, the external quantum efficiency for all the device sizes is plotted as a function of the current density as shown in figure 6.12. Here the data taken from pulsed measurements, which allow higher operating currents and thus more overlap between different device sizes, is plotted taking the obstruction of the contacts into account.

Figure 6.12 clarifies the reason for the different contact layouts for small and large

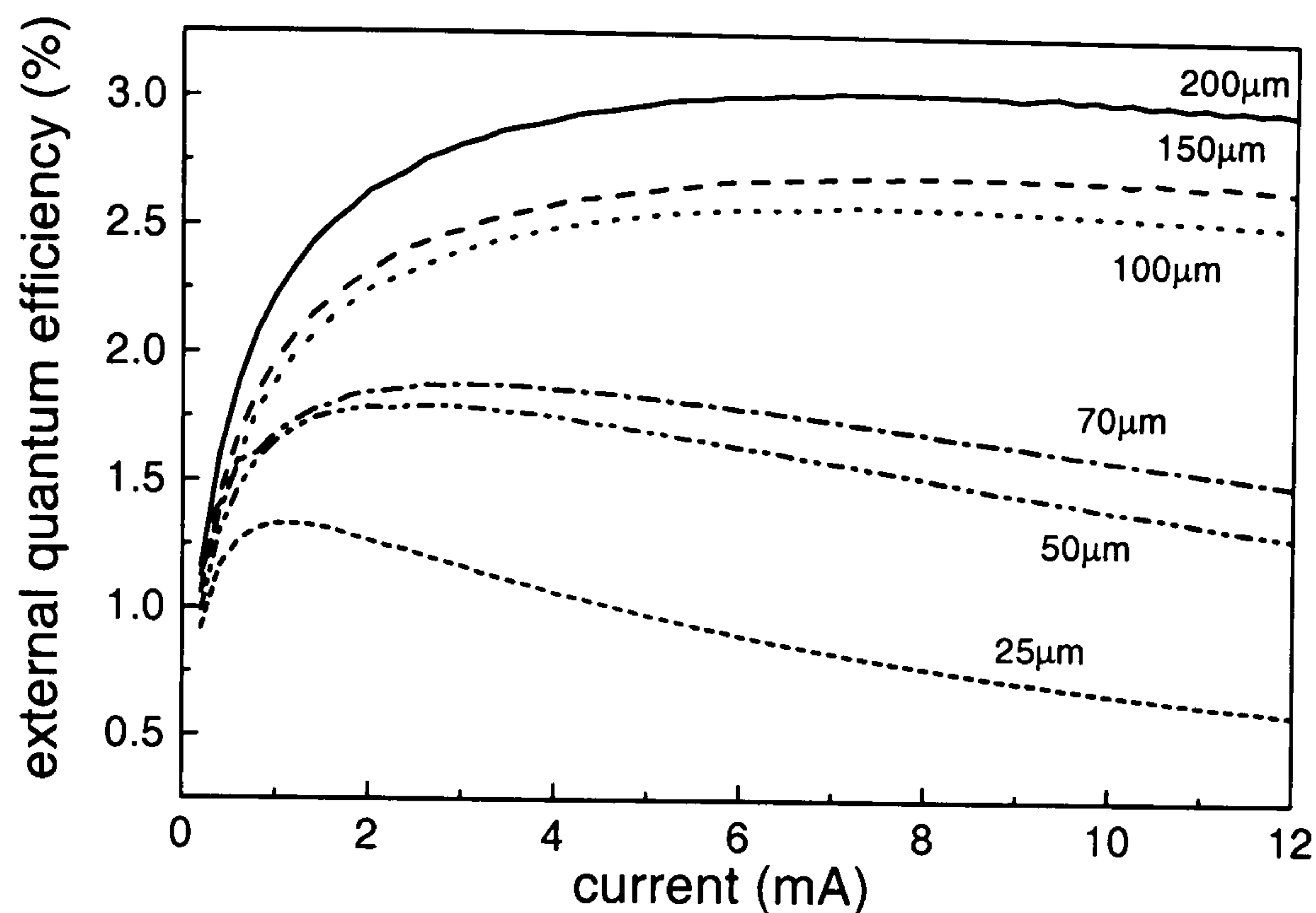

Figure 6.11: LI efficiency corrected for the obstruction due to the contacts in the larger devices.

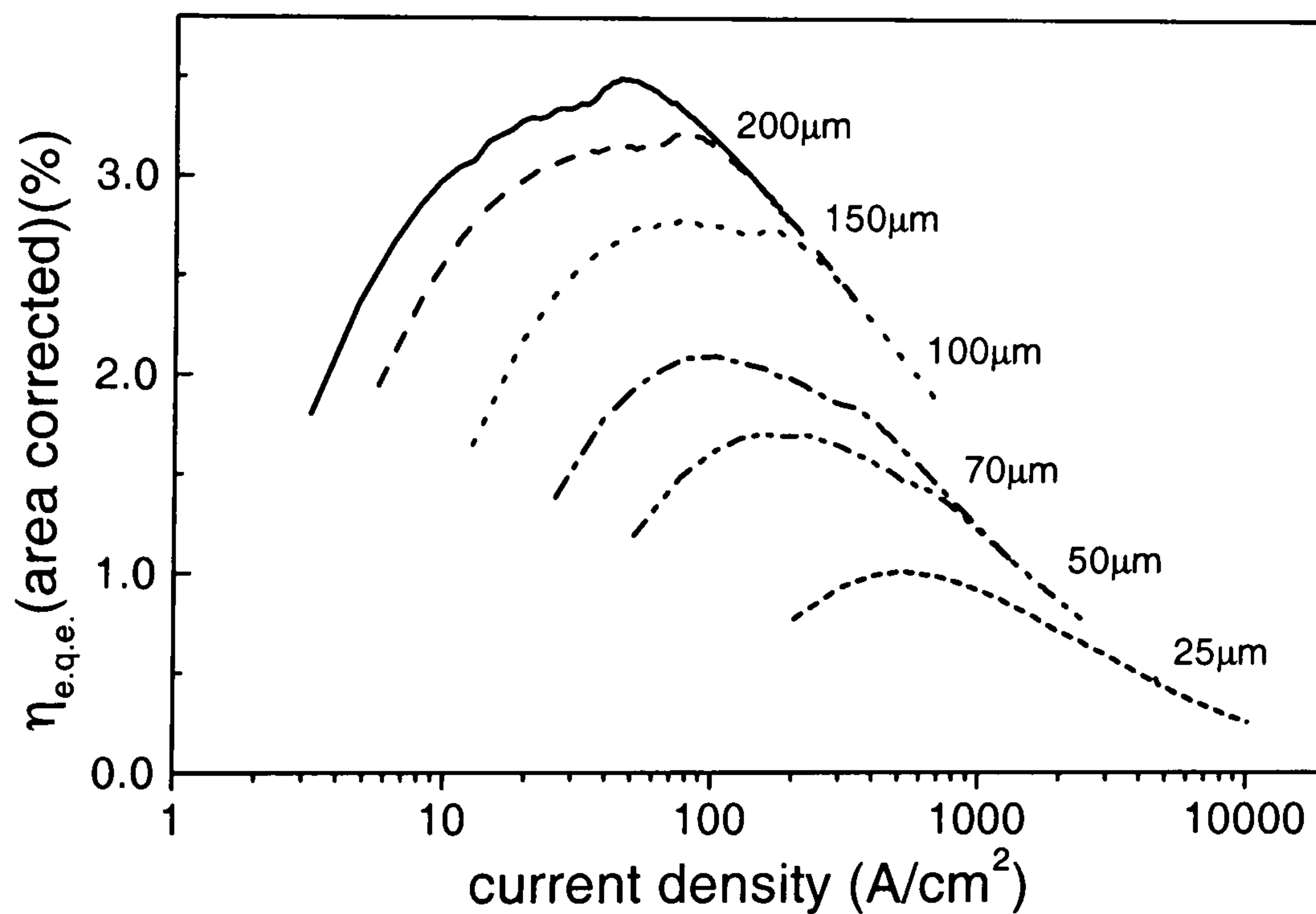

Figure 6.12: η_{eqe} (corrected for the contact geometry) for the same six devices under pulsed bias and versus current density.

devices: the extra contact ring on the larger devices has been added to improve the current spreading. Since the 70μm device does not have an extra ring the current does not spread uniformly and consequently the efficiency is not much above that of the 50μm device. In figure 6.12 it can be seen that apart from a quite long

"turn-on" region, the three larger devices lie along the same path. The smaller devices show slightly lower efficiencies than the larger ones. This may be due to two reasons. Firstly, the improved current spreading could make the larger devices more efficient. It could also suggest that there is some photon recycling [38] occurring in these large devices as has been reported by De Neve et al [109] for InGaAs-based RCLEDs. The reabsorption of photons and thus the photon recycling should become more prominent in larger devices as a larger lateral distance for photons to travel in the device increases the probability of reabsorption [110]. However as the efficiency is not increasing from the 100μm to the 200μm device it is concluded that there is no photon recycling. Finally any error in the alignment of the mask for the implant and for the output aperture will have a greater effect on the smaller devices thus leading to lower efficiencies. The overall decrease in efficiency with current density (after the initial rise for all devices) is due to two main causes. With increasing current density the initial emission spectrum broadens and so overlaps less with the cavity mode extraction window. At the same time, leakage currents and self-heating increase, making the devices less efficient at higher current densities.

For comparison the external quantum efficiency for devices processed from a different wafer (J02) are plotted in figure 6.13.

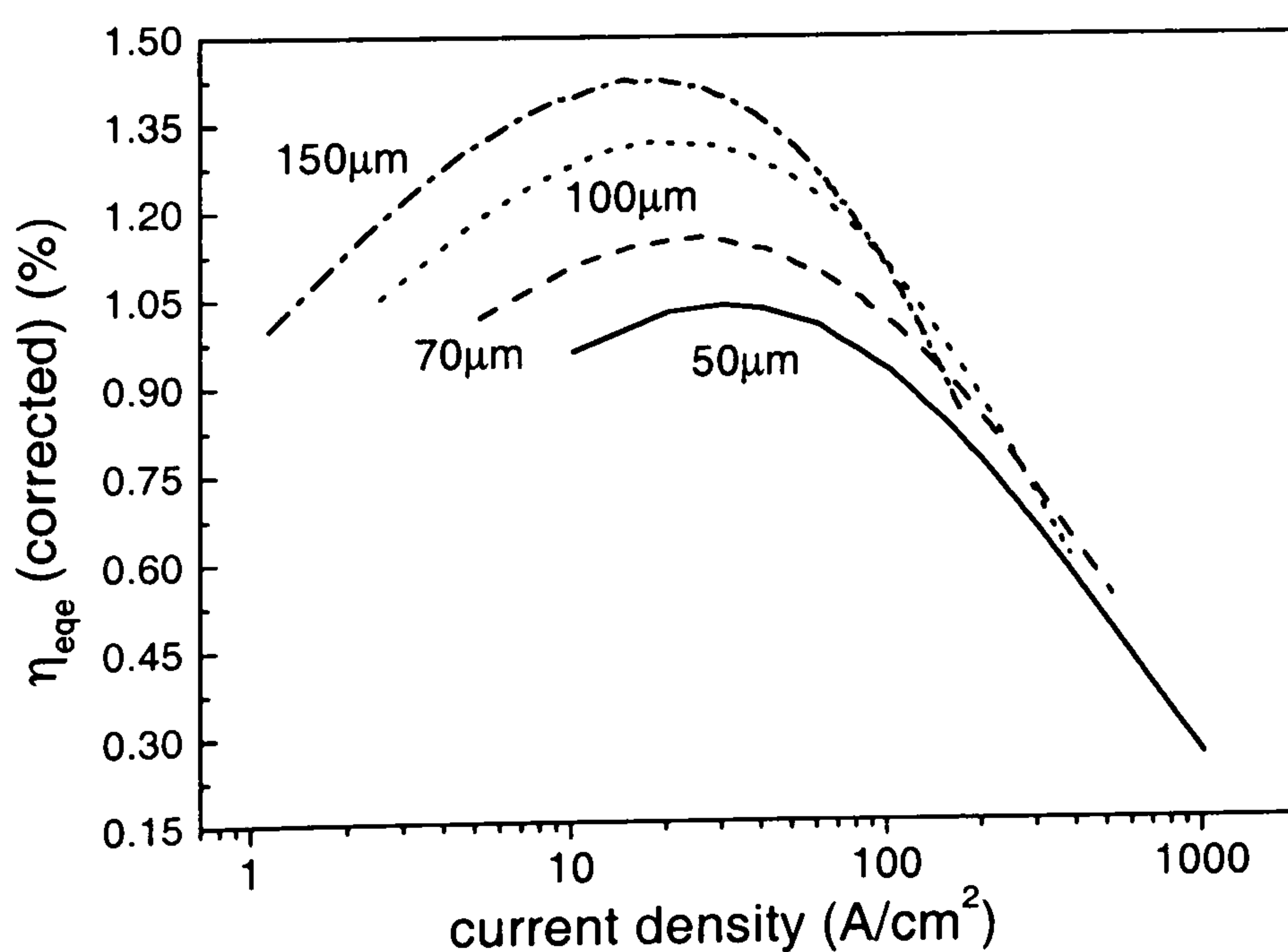

Figure 6.13: Normalised η_{eqe} versus current density for the four different device sizes processed from the J02 wafer.

The main difference between these two sets of devices lies in the contact structures, as seen in figure 6.14, where two 100μm devices are shown.

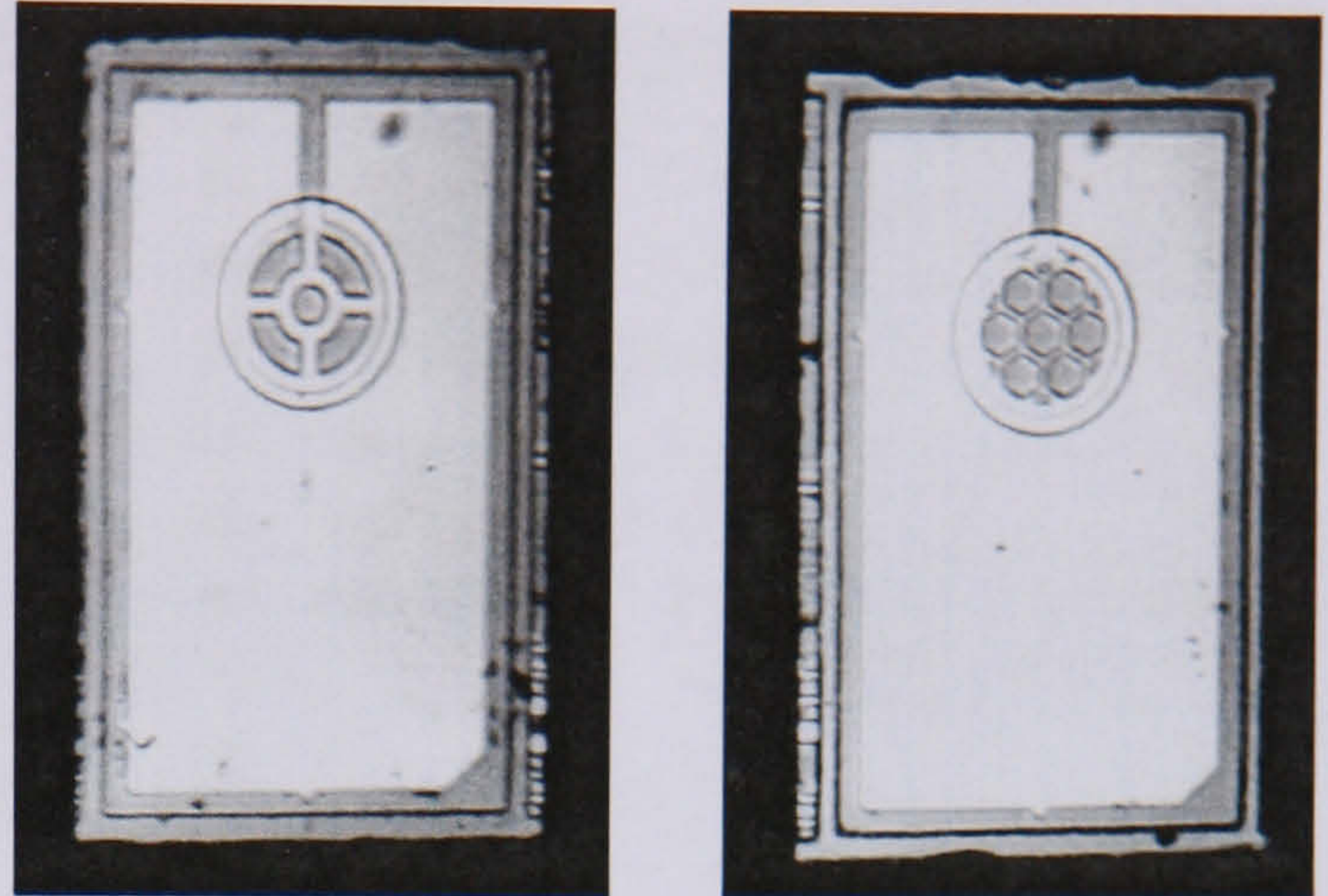

Figure 6.14: Difference of the contact design for the large devices of S1 and J02 design to improve the current spreading. Here shown for two $100\mu m$ devices. For the S1 devices there is only one contact ring, whereas the contact for the J02 devices consists of a honeycomb structure.

The J02 devices all have a honeycomb contact structure (apart from the two small aperture devices, 25 and $50\mu m$). In contrast, the three larger S1 devices have only one extra annular contact. The hexagons are the same size for all J02 devices and simply increase in number with device size. Hence there should be little difference in current spreading for the different device sizes as shown in figure 6.13. All device sizes have the same efficiency at high current density, so no evidence for photon recycling effects can be observed.

6.3.3 Temperature dependence

The maximum external quantum efficiency η_{max} for the different size devices as a function of temperature is shown in figure 6.15. The current at which this occurs, $I(\eta_{max})$, which is not varying significantly with temperature, rises for the larger devices and is also indicated. $I(\eta_{max})$ is approximately inversely proportional to the device diameter. This suggests that it is largely defined by self-heating as shall be discussed later.
The efficiency drops with increasing temperature (above 25°C) for all devices, but less for the smaller ones that have a lower efficiency at lower temperatures. The maximum efficiency for the 70μm device is higher than for the 100μm one. The reason for this seems to lie in the different contact design as indicated in figure 6.6.

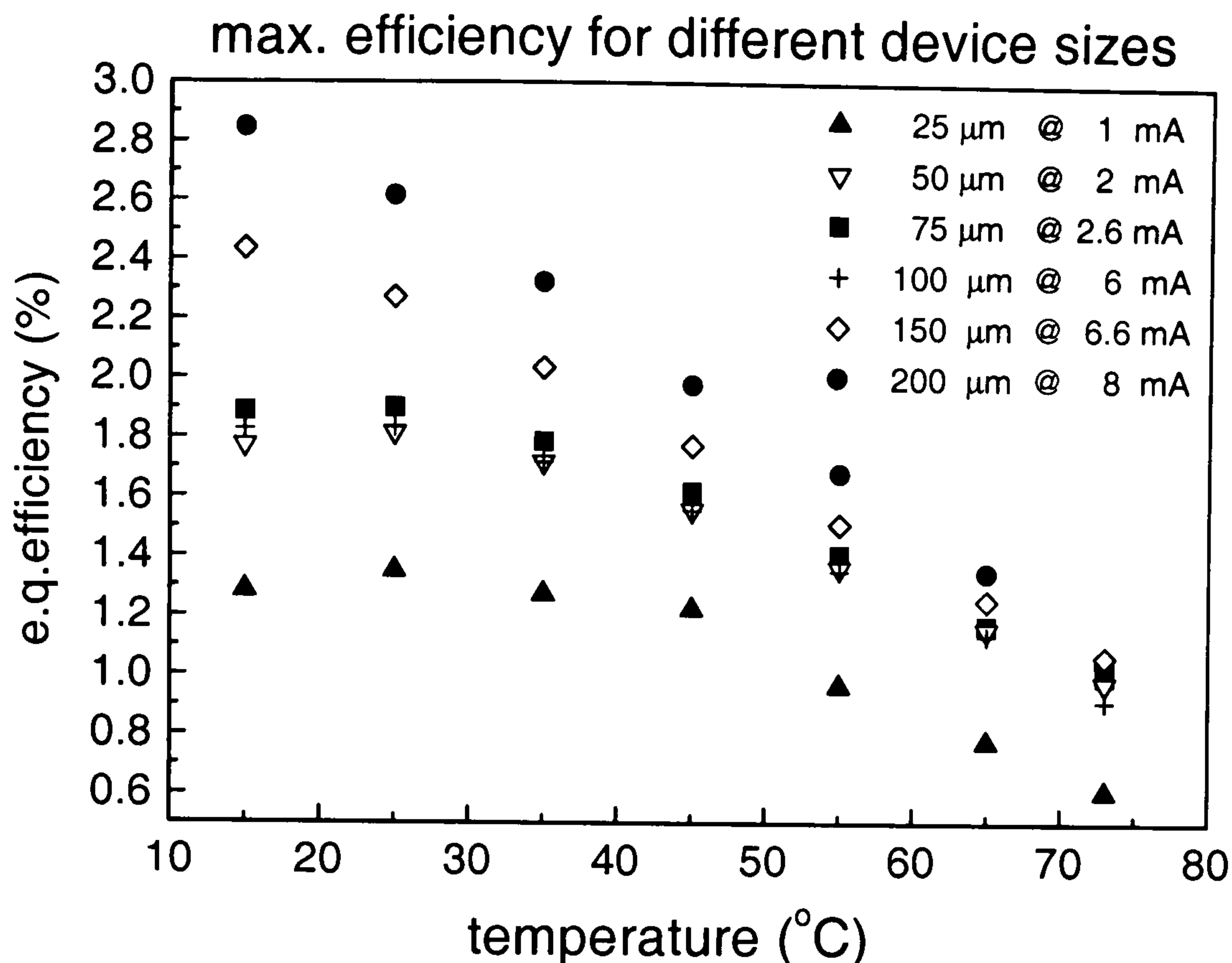

Figure 6.15: Maximum external quantum $_{max}$ efficiency for different device sizes as a function of temperature.

However for higher currents the efficiency is higher for the 100μm device as can be seen in figure 6.10.

To investigate the temperature dependence for the different device sizes, the light output density is plotted in figures 6.16 and 6.17 at a current density of $92A/cm^2$ for a range of temperatures and three different device sizes. In these figures devices from two different designs are compared. The devices in figure 6.17 are processed from wafer S1, while the devices in figure 6.16 are processed from a wafer with the J02 structure.

It can be seen in figure 6.16 that the light density for all four devices is nearly the same across the full temperature range irrespective of whether the correction is applied. For the set of S1 devices shown in figure 6.17 this is only true for temperatures above 40°C (without correction). The reason for this difference can be explained by comparing figures 6.12 and 6.13, where the efficiency versus current density is plotted. For the current density of $92A/cm^2$ as used in figures 6.16 and 6.17 the S1 devices have not all reached their highest efficiency and so differ more than the

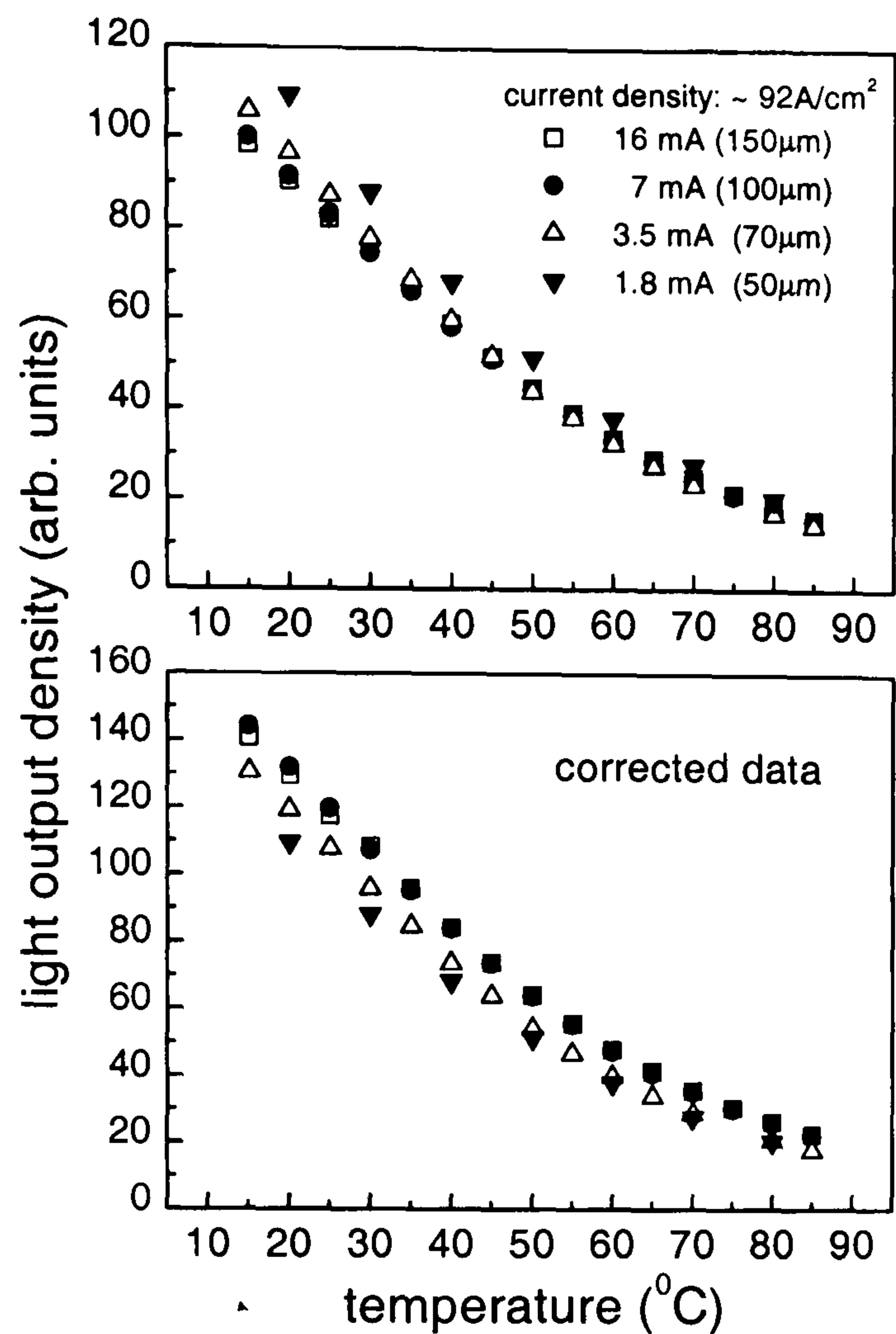

Figure 6.16: Light output density of three J02 devices with different aperture size at the same current density for temperatures between 15°C and 85°C.

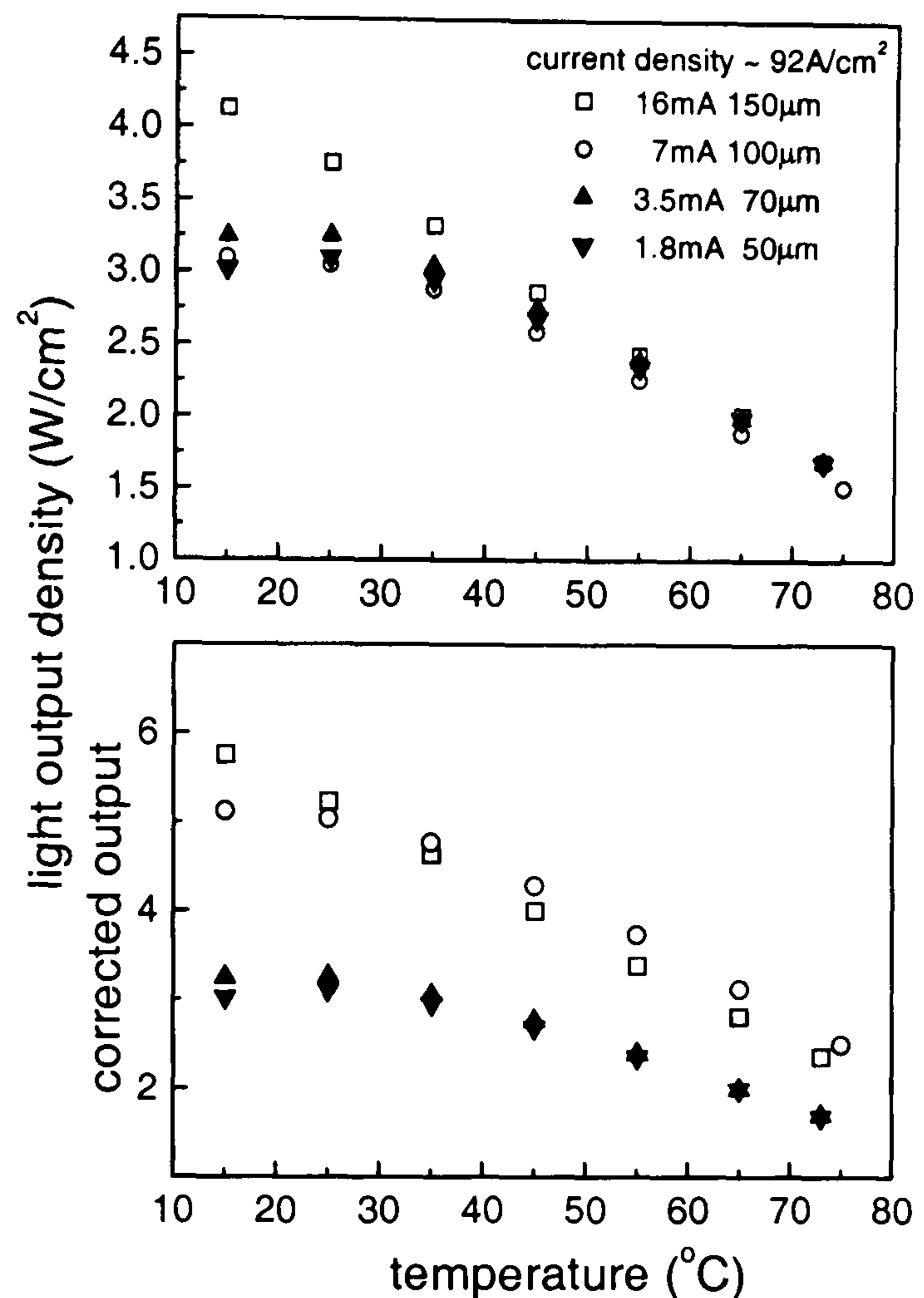

Figure 6.17: Light output density at the same current density for three S1 devices with different aperture size for temperatures between 15°C and 75°C.

ones shown in 6.16. The two wafers from which the devices were processed had two very different structures and were grown on different systems. The S1 devices had 8 top DBR pairs, and a de-tuning of +9nm for one QW transition. The J02 had 11 top DBR pairs and had two different QW transitions of which one was basically already tuned (+1nm de-tuned) and the other +12nm de-tuned. Finally, the devices also had two different contact designs, as can be seen in figure 6.14. Besides the devices themselves the measurements also differed. The S1 devices shown in figure 6.17 were bonded into TO-cans and so the total output (except for the limited can angle) was measured. The bare J02 devices were measured on the probe station with a collection angle of about 30°. This explains why the J02 devices deviate from the linear temperature dependence. At temperatures above 50°C the emission from

the second QW also reaches the collection window and so moderates the decrease with temperature. Figures 6.16 and 6.17 give no clear indication about any intrinsic size dependence. For the S1 devices with respect to the light output at 25°C the rate at which the light output decreases with temperature is $\sim$ 1%/°C over a temperature range from 25°C to 75°C independently of device size. The light output for the J02 devices decreases by $\sim$ 1.2%/°C with respect to the light output at 15°C over the range from 15°C to 85°C. In both cases this linear approximation are not strictly true but provide an indication of the temperature dependence that can then be compared with results from other devices. The measurements were made at the same current density to distinguish any intrinsic size dependence. The important temperature dependence however is how devices act for the same light output. To explore the temperature dependence further, self-heating for different device sizes is investigated.

6.3.4 Self-heating

As previously described in section 5.6.1, to investigate self-heating, the current required for a constant light output was measured for different temperatures under c.w. and pulsed mode. The temperature difference at a given current between the pulsed and the c.w. results is taken as the amount of self-heating of a device. In figure 6.18 the results for three different devices sizes are shown. Figures 6.18(a-c) show the current needed to obtain the same light output for the three different devices sizes under c.w. and pulsed operation. The temperature differences between pulsed c.w. mode for these three devices are shown in figure 6.18(d) together with linear fits to the data.

The self-heating is more prominent for the smaller devices, evident by the greater difference between c.w. and pulsed values seen in figures 6.18(a-c). The $d\Delta T/dI$ as plotted in figure 6.18(d) shows the same trend as it is increasing from 0.55°C/mA for the 200μm device to 2.3°C/mA for the 25μm device. How this exactly depends on the diameter depends on the heating effects present in these devices. The heating is

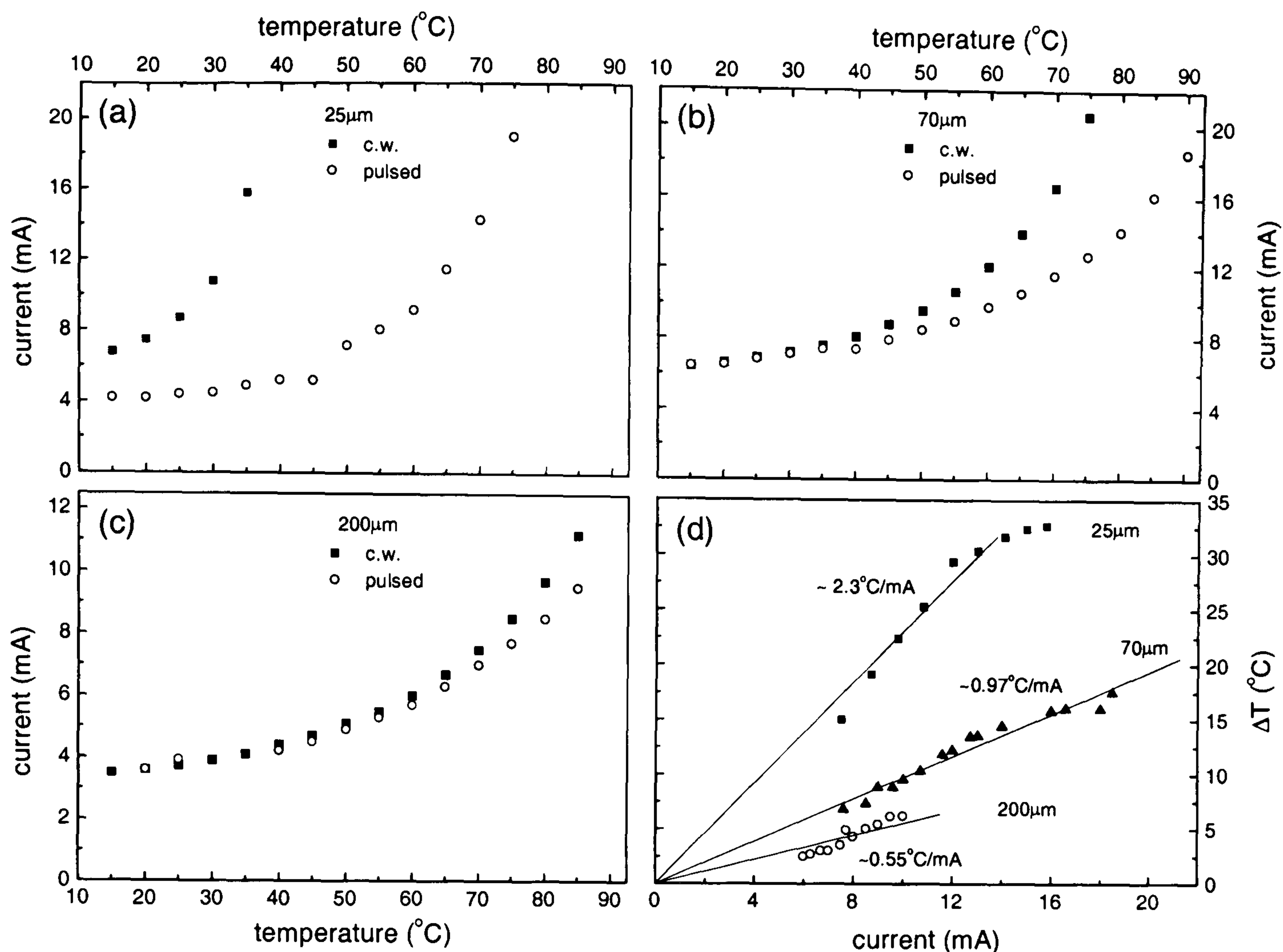

Figure 6.18: Current needed for a constant light output, $0.75\mu W$,(the same for all devices) under pulsed and c.w. operation for (a) $25\mu m$, (b) $70\mu m$ and (c) $200\mu m$ diameter devices. The extracted self-heating is plotted in graph (d).

caused by the current flow through the active region. The generated heat drops off radially to the perimeter and then towards the substrate which is held at a constant temperature. Hence, on average, the smaller devices see a higher temperature than the larger devices. If the device is considered to be a disc shaped heat source of diameter d dissipating into a semi-infinite substrate of thermal conductivity σ the rate the temperature rises with current may be found to be [111]

$$\frac{d\Delta T}{dI} = \frac{V}{2d\sigma}, \tag{6.2}$$

where V is the voltage across the device. IV is equal to the electrical power that is responsible for the heating. The voltage across the devices lies between 1.75V and 2.1V increasing with current and decreasing with device size. For the current ranges investigated here $dV/dI < 0.01V/mA$ and was thus neglected. The rate of change

$(d\Delta T/dI)$ for all the different devices is plotted in figure 6.19 versus $V/2d$.

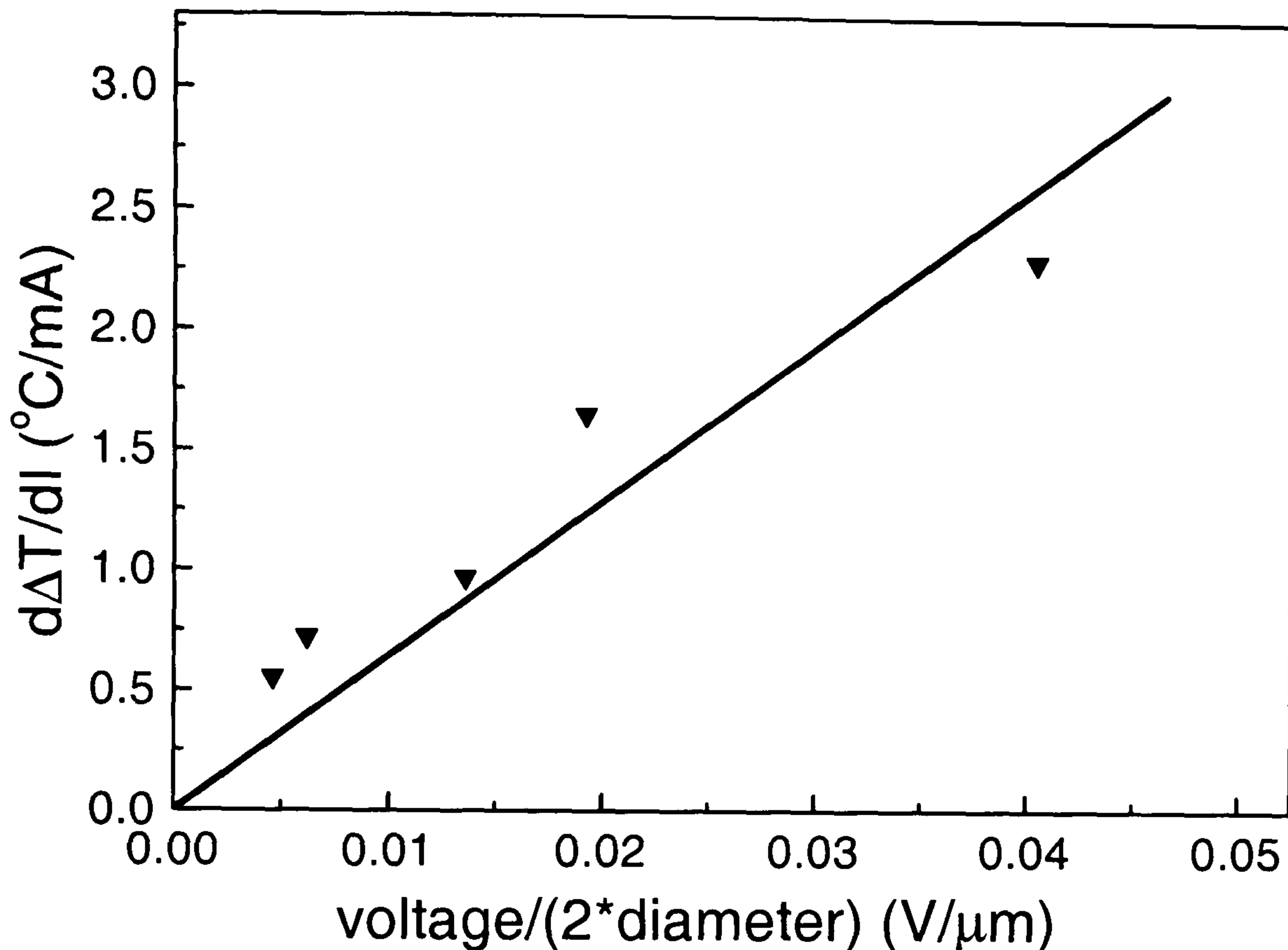

Figure 6.19: Rate of change of self-heating $(d\Delta T/dI)$ for different size devices versus $V/2d$ together with a linear fit to the data determining the thermal conductivity σ.

The thermal conductivity can be estimated from the inverse of the slope of a linear fit to the data. From this $\sigma = 0.15 \pm 0.02 W/cm°C$. In practice it is difficult to find the exact value for the thermal conductivity for the whole structure. For the QW material $Ga_{0.5}In_{0.5}P$ a value of $0.05 W/cm°C$ has been reported [112]. No value for AlGaInP could be found, but due to the higher anharmonicity caused by the difference in the size of the atoms, it is expected to be even lower than in GaInP as the phonon scattering is increased [113]. In [114] it has been shown that the thermal conductivity for AlAs/GaAs superlattices with a period of 50nm is higher $(0.25 W/cm°C)$ than for an $Al_{0.5}Ga_{0.5}As$ alloy $(0.11 W/cm°C)$. The same can be expected for the $AlAs/Al_{0.5}Ga_{0.5}As$ Bragg stacks with the same period. As the thermal conductivity of $Al_{0.75}Ga_{0.25}As$ is higher than for $Al_{0.5}Ga_{0.5}As$ $(0.14 W/cm°C)$ [112], the thermal conductivity of the Bragg stacks will also be higher than $0.25 W/cm°C$. This shows that the fitted value of $0.15 W/cm°C$ is well within the possible values

reported in the literature. This also confirms the 1/d dependence and adds credibility to the method used to determine the temperature rise. The increase of the self-heating with decreasing device size also confirms self-heating as the reason for the lower efficiencies and also the lower current at which the maximum efficiencies occur in smaller devices.

6.4 Conclusions

In this chapter the influence of the top DBR reflectivity (8, 11 and 14 DBR pairs) and the aperture size (25μm, 50μm, 70μm, 100μm, 150μm and 200μm diameters) on the light output in particular with increasing temperature have been investigated.

In conjunction with the results of the previous chapter it has been shown that the de-tuning has a greater influence on the light output than the number of top DBRs when a $\sim 30°$ collection angle is considered (typical collection angle for a POF). By comparing the total light output with the output coupled into a $60°$ cone, slightly higher coupling was observed for the device with 14 top DBRs. This confirms the theoretical predictions that devices with more than 13 DBR layers are more suitable for coupling into a fibre-like NA of 0.5.

The external quantum efficiency for larger aperture devices has been shown to be higher than for the smaller ones. Since the compactness of the active region is the main reason for the devices self-heating, this effect is more prominent for the smaller devices. Hence, there is an overall advantage to use larger devices if high light output is required. The maximum external efficiency at 25°C drops from 2.6% for the 200μm device to 1.4% for the 25μm device corresponding to a light output of 0.9mW and 0.15mW at 20mA, respectively. For lower current densities larger devices have the problem that the current is not spread uniformly enough. By introducing spoke or grid-like contacts this problem can be overcome but light is lost through the obstruction of the contacts. However, for the typical operating current of 20mA the larger devices investigated here show higher efficiencies. The lack of

good current spreading was seen for the 70μm device, for which the light output did not increase very much compared to the 50μm device as no extra contact improves the current spreading. In a second set of devices, the problem of current spreading was solved by using a contact grid of equally-sized hexagons and thus the current is spread equally in all device sizes. These devices had two different QW transitions. This decreased the temperature sensitivity at higher temperatures as the second QW tunes in at temperatures as the first QW is starting to de-tune negatively. Nevertheless, the light output decreased by $\sim 1.2\%$ compared to only $\sim 1\%$ for the other set of devices over a temperature range from 20°C and 80°C. There was no clear evidence of photon recycling being present in the larger devices, a phenomenon that may occur for devices larger than $\sim 100\mu$m.

Self-heating was found to increase inversely proportional to the diameter. As the heating is caused by the current flow through the active region and the generated heat drops off radially to the perimeter, a simple heating model could be applied and the thermal conductivity was determined to be $(0.15 \pm 0.02) W/cm°C$, which is within values found in the literature for the different layer materials forming the devices.

Chapter 7

Fibre coupling and modulation bandwidth

7.1 Introduction

In the two previous chapters the influence on the light output of the QW-CM detuning, the device aperture size and number of top DBR pairs have been investigated. In this chapter the influence of these results on some of the important factors for the application of RCLEDs shall be studied. RCLEDs emitting at around 650nm have been developed for use in short distance networks via plastic optical fibres (POFs). The three main factors of importance for these applications that will be investigated here are the fibre coupled power, the actual transmitted power to the end of the fibre and also the modulation bandwidth of the devices themselves.

The coupling into a PMMA step index (SI)-POF with 1mm core diameter, in particular comparing the coupling efficiency of tuned and de-tuned devices, will be discussed. The temperature dependence of this coupling efficiency and the resulting temperature stability of the system will also be shown. The modulation bandwidth of the devices determines how fast information can be transmitted using it as a source. The modulation bandwidth and its dependence on device size and QW-CM

de-tuning will be investigated in this chapter. From the size dependence of the modulation bandwidth, information about the carrier density and the main current paths will be discussed.

7.2 Fibre coupling

In the following section the actual coupling into a commercially available POF shall be considered. The coupling efficiency depends on the acceptance angle of the fibre and thus its numerical aperture. The numerical aperture (NA) for optical fibre depends on the refractive indices of the core and cladding of the fibre and has been expressed earlier in equation 1.1 and illustrated in figure 1.1. For PMMA plastic fibre this leads to NA=0.5, which corresponds to an acceptance angle of 30°. Therefore only light that leaves the device within a 60° cone will be accepted into the fibre. Not only is the numerical aperture, and thus the resulting coupling efficiency important but also the wavelength dependence of the transmitted signal. Two factors contribute to this. Firstly the attenuation of the fibre is strongly wavelength dependent as seen in figure 7.1.

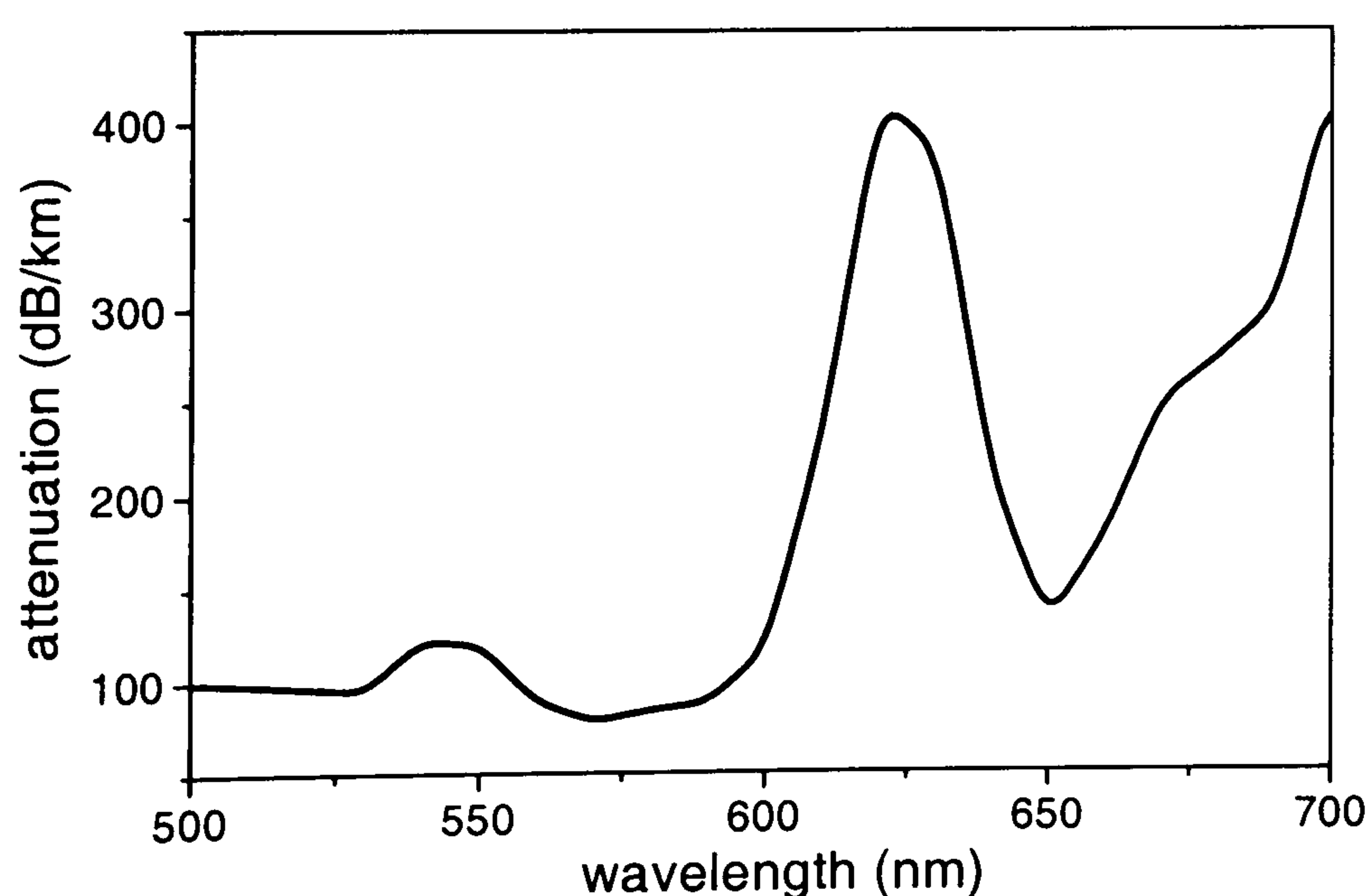

Figure 7.1: Attenuation of PMMA-POF from 500-700nm after [115].

Hence light at a wavelength of 650nm will be less absorbed by the fibre than light of a wavelength either side of this attenuation minimum. Secondly the fibre acceptance

angle also determines which wavelengths will be coupled into the fibre. As shorter wavelengths are emitted at higher angles from the RCLED they are less likely to be coupled into the fibre.

7.2.1 Influence of de-tuning

To investigate the fibre coupling, EL spectra of devices were recorded before and after passing through 30cm of POF. In figure 7.2 a comparison between an (a) tuned and a (b) strongly de-tuned device is made. The far field results indicating the amount of de-tuning of these devices were shown in figure 5.2. As λ_{QW} of these devices is ~650nm it coincides with the minimum attenuation loss of POF. Thus the de-tuning of the devices is with respect to the QW and also to the fibre loss.

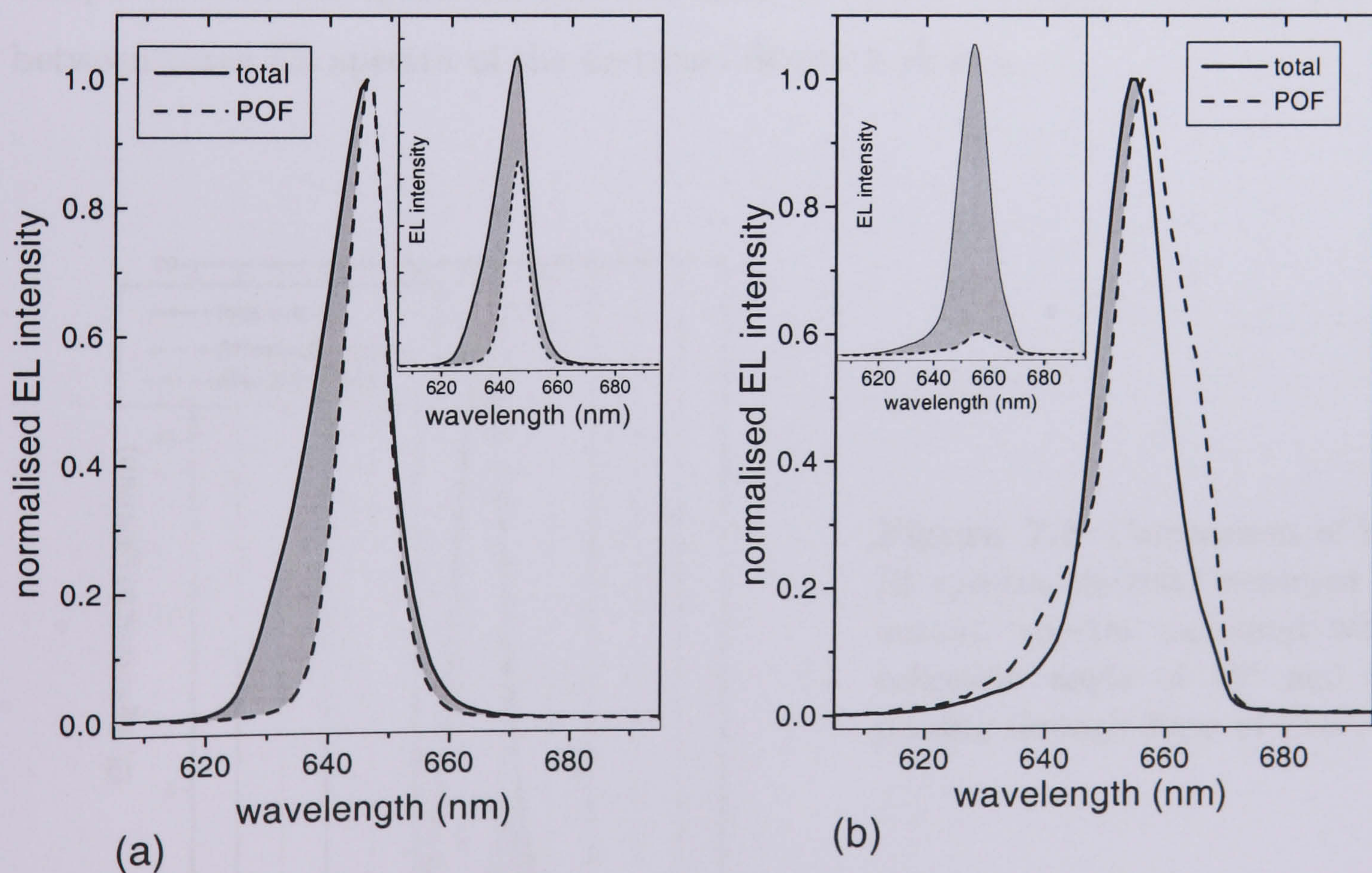

Figure 7.2: Normalised EL spectra for (a) a tuned (device O1) and (b) a strongly de-tuned device (O2) obtained with an integrating sphere and a spectrometer directly (solid line and grey area) and after passing through 30cm of 0.5 NA plastic optical fibre (dashed line and white area). The insets show the actual measured spectra.

The two graphs show the EL spectra at 10mA and room temperature, measured with a grating spectrometer, after collecting all the light in an integrating sphere. In the one case it was measured before (solid line) and in the other case after (dashed line) passing through 30cm of POF. To illustrate the change in the spectra they are normalised to the same peak value of 1. In the insets the actual EL intensity can be seen, and thus the decrease in intensity under the influence of the fibre.

The reduced intensity being transmitted at shorter wavelengths can be understood in the decreased coupling efficiency for these wavelengths, that are mainly emitted at higher angles by the RCLED, rather than in the attenuation of the fibre. The overall decrease in the intensity can be seen in the insets of figure 7.2, which show the measured spectra. It can be seen that the overall decrease in intensity for the de-tuned device is much higher than for the tuned device. The reason for this is due to the limited collection angle, which is of greater importance to de-tuned devices. This becomes clearer when spectra recorded at smaller collection angle are compared with the spectrum obtained after the fibre. In figure 7.3 a comparison between three EL spectra of the de-tuned device is shown.

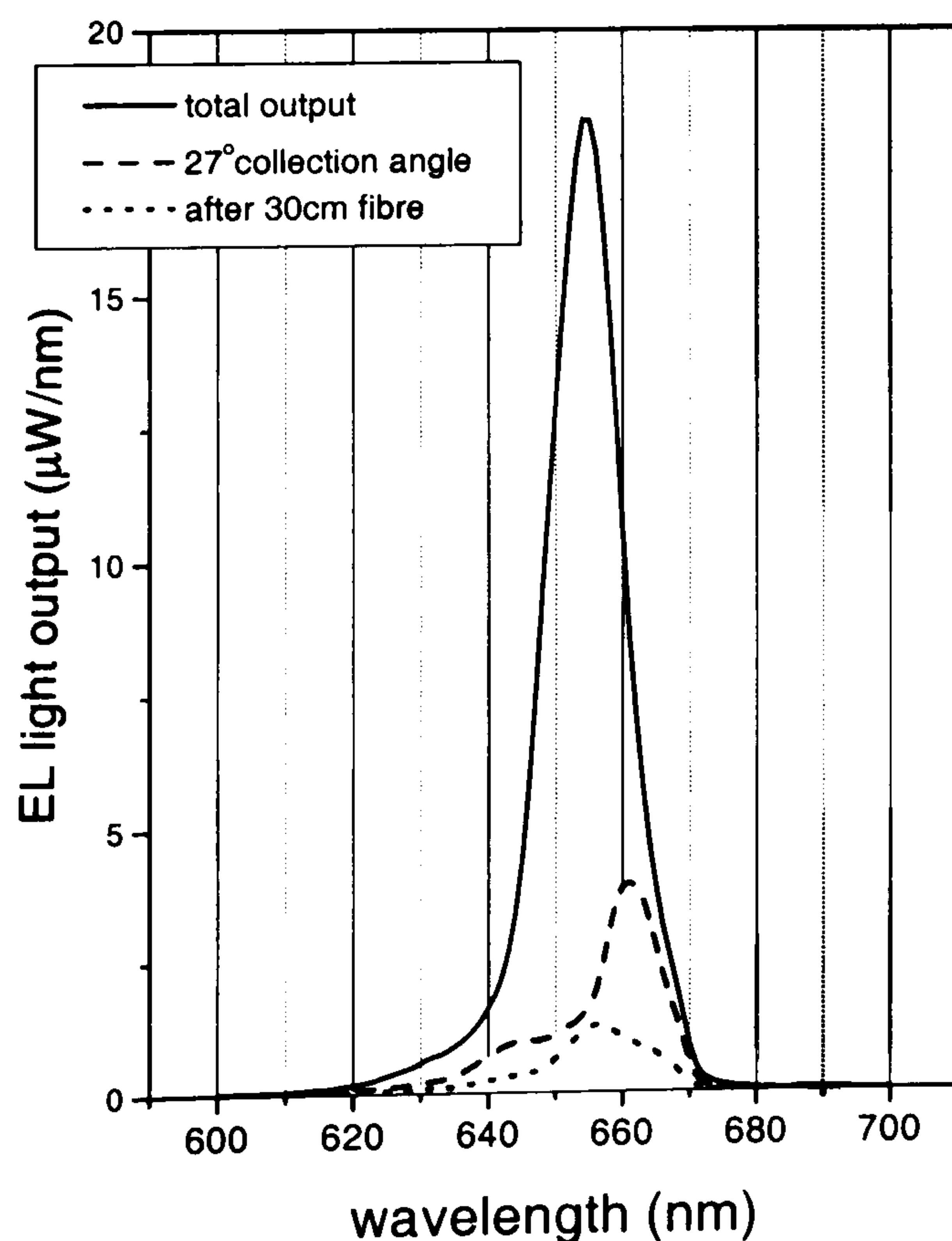

Figure 7.3: Comparison of three EL spectra, the total measured light output, spectra measured with a collection angle of 27° and after passing through 30cm of POF.

Here, together with the spectra already shown in figure 7.2 of the total light output and the light output after 30cm of fibre, the spectrum for a collection angle of 27° (similar to POF) is plotted. From this graph it becomes clear that most of the light is lost by not coupling into the fibre. In fact, of the total light output (calculated from the integral of the EL spectrum) only 22% of it is emitted into a cone of 27°and thus possibly coupled into the fibre. If all of this light was coupled into the fibre 35% of it reaches the other end of the fibre. This is similar to the 42% transmission that is observed for the tuned device assuming all of the light to be coupled into the fibre. Both values are smaller than expected for transmission through a 30cm piece of fibre. Assuming on average a constant attenuation of 200dB/km for the wavelength range of interest and allowing for 4% of reflection (according to Fresnel's equation 2.3 and a refractive index for the fibre of $\sim$1.5) at the interfaces, approximately 91% of the light should be transmitted over 30cm of fibre. The reason for the much higher observed attenuation could lie in a non-ideal fibre and in particular the cleave quality which would lead to both higher scattering loss and higher back-reflection.

7.2.2 Temperature dependence

As discussed in section 5.4.1 positive de-tuning is advantagous for temperature stability. With increasing temperature the de-tuning reduces. For initially positively de-tuned devices λ_{CM} and λ_{QW} move closer together with increasing temperature. This means that with increasing temperature a greater portion of light gets emitted into the 30° fibre acceptance cone. So while the overall light output decreases, the relative proportion of light coupled into the fibre increases, which could lead to an almost constant light output being coupled into the fibre over a given temperature range. Indeed even a small increase of the light coupled into the fibre with temperature (for low currents) has also been observed by Streubel et al [39].

For the far field pattern as seen in figure 7.4 this means that the two lobes (output peaks) come closer together i.e the far field narrows. Here far field spectra at four different temperatures for an initially positively de-tuned device are shown.

The arrow indicates the shift of the peak output.

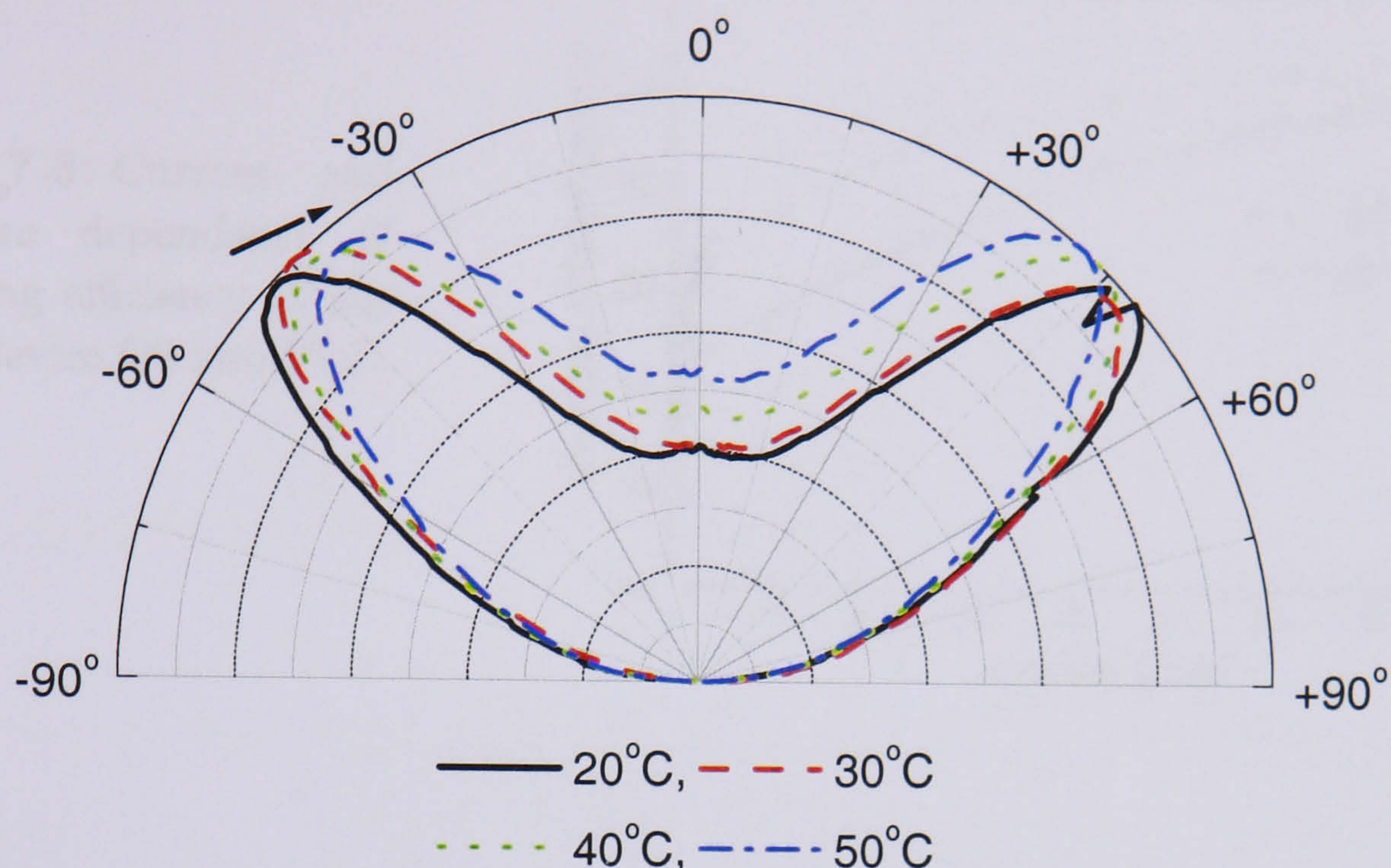

Figure 7.4: Temperature dependent normalised far field spectra of an initially de-tuned device, showing the narrowing of the spectra.

With increasing temperature a greater portion of light gets emitted into the forward direction and thus more light could possibly be coupled into the acceptance cone of a fibre. In figure 7.5 the coupling efficiency for a strongly de-tuned device (device O2 with maximum emission at 45°) is shown at two temperatures. This efficiency is calculated as the ratio of the LI measured after 30cm of fibre to the uncoupled LI. As expected the coupling efficiency at 50°C is higher than at 20°C as the de-tuning decreases with temperature. The efficiency also increases with current, which again is due to self-heating which would help to tune the device. In figure 7.6 a comparison of the coupling efficiency between the tuned and the de-tuned device can be seen at 20 and 50°C.

Firstly, it can be seen that the coupling efficiency is higher for the initially tuned device. It is around 40% compared to 20% for the de-tuned device. The efficiency increases with both current and temperature for the de-tuned device, whilst it decreases for the tuned device. An increase in the ambient temperature (or indirect heating of the active region through increasing current) will shift λ_{QW} to longer

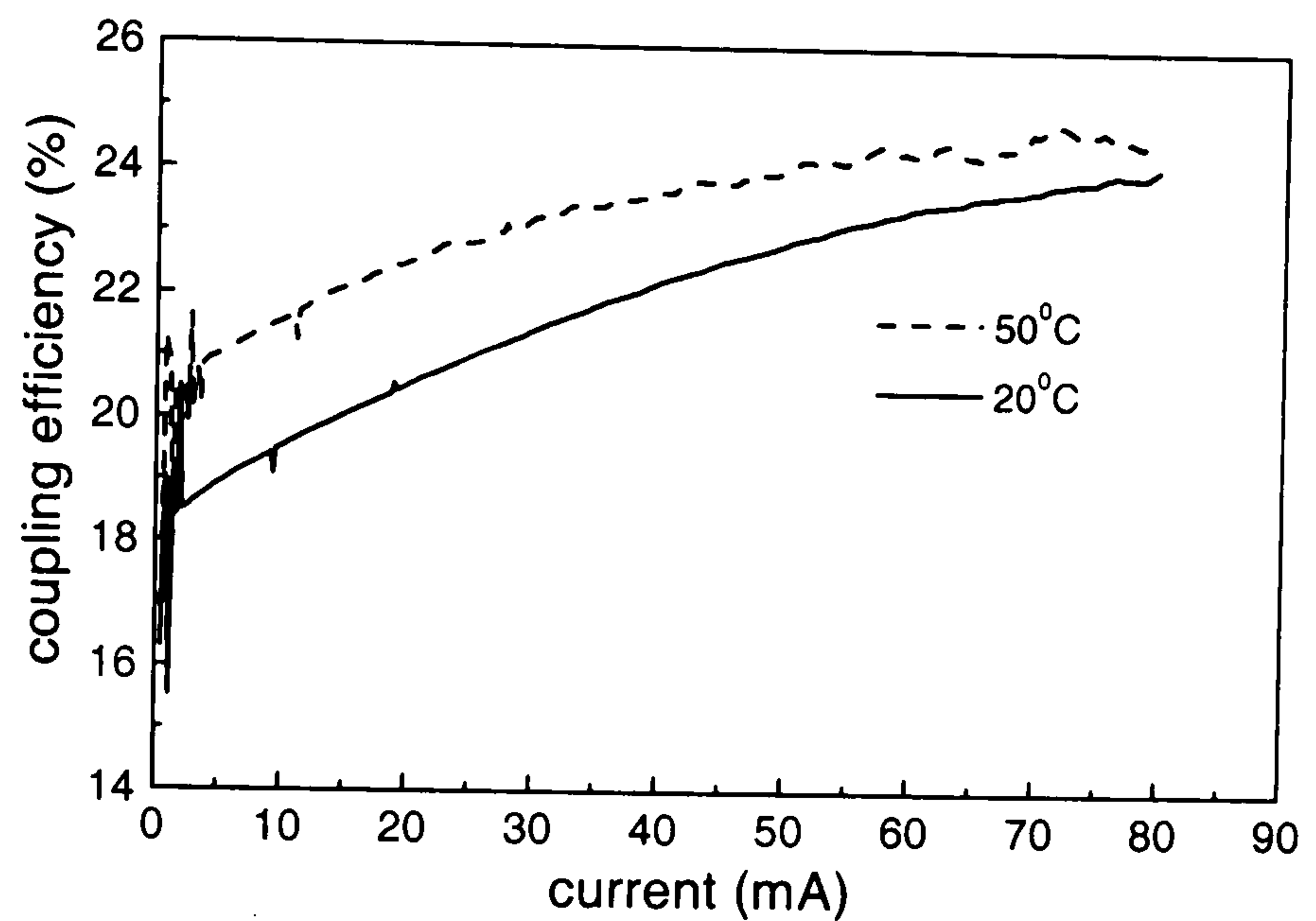

Figure 7.5: Current and temperature dependence of the coupling efficiency of the de-tuned device O2 into POF.

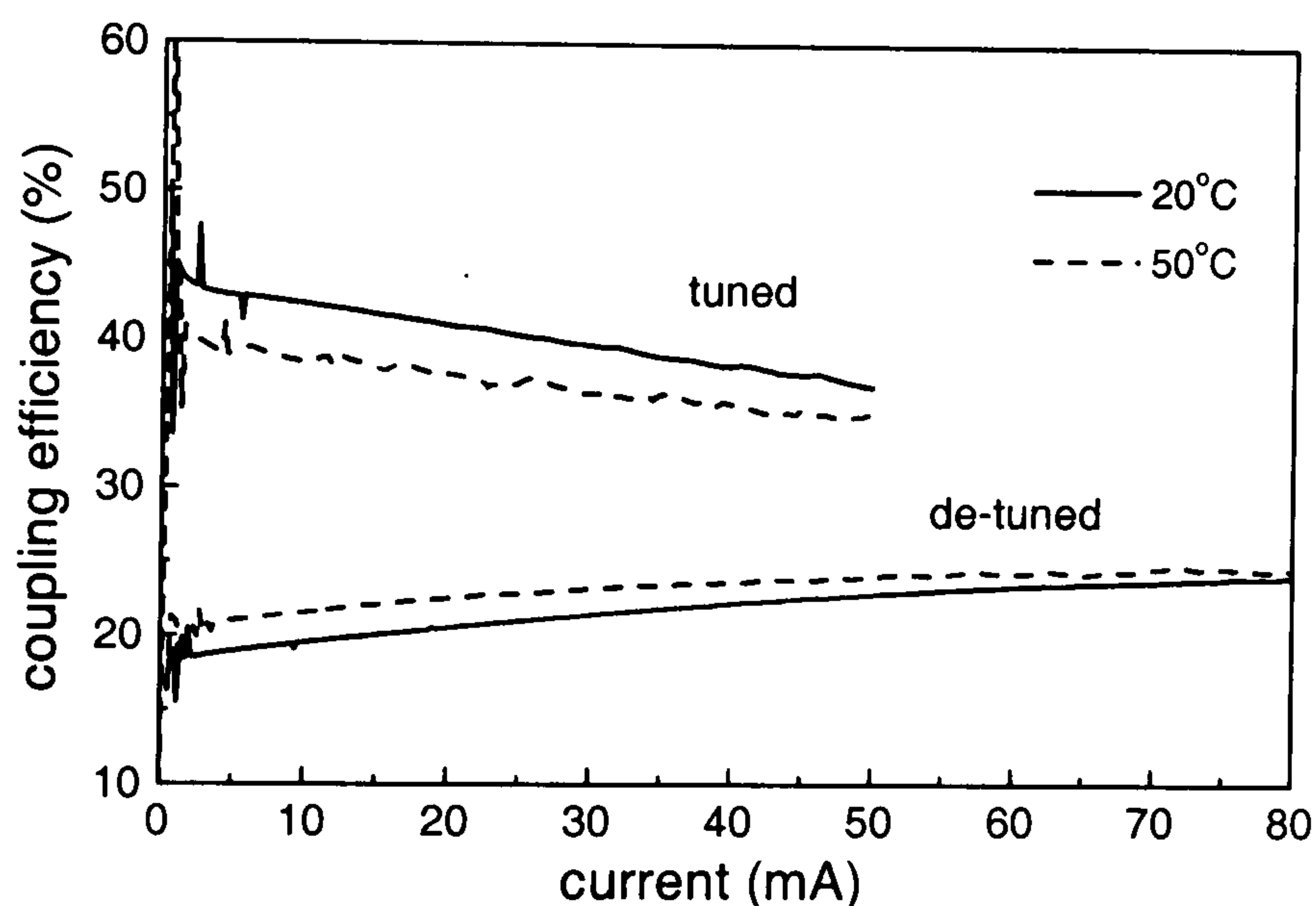

Figure 7.6: Comparison of POF-coupling efficiency for a tuned and a de-tuned device at two temperatures.

wavelengths. As the device was tuned at room temperature and thus $\lambda_{QW} = \lambda_{CM}$ (at RT) λ_{QW} will move to the longer wavelengths side of λ_{CM}, which leads to a decrease in the light output.

From the coupling experiments it becomes apparent that the best device depends on the particular application and the temperature conditions. The coupling and the transmission are at a maximum if the device is tuned at 650nm. However, for a tuned device the temperature sensitivity is higher. To achieve the most stable output over the desired temperature range it is advisable to use a device which is de-tuned at room temperature, as this will tune in with increasing temperature until

it is finally tuned at the highest operating temperature. Hence should not only λ_{CM} be away from 650nm but also λ_{QW}. If $\lambda_{QW} \sim 642nm$ at RT it will be approximately 650nm at 80°C. If the cavity is de-tuned so that it will also yield 650nm at 80°C (being ~648nm at RT) it will be possible to achieve the highest coupling and transmission at this temperature, thus compensating for other temperature induced losses.

7.3 Modulation bandwidth

An important characteristic of RCLED devices for data applications is their modulation bandwidth. The higher the bandwidth the faster they can be modulated and thus the more data can be transmitted. The modulation bandwidth is defined as the frequency at which the modulated power drops to one half of its low frequency value. This point is also called the -3dB point or the cut-off frequency (-3dB=10log(1/2)=10log(I/I_0)). In figure 7.7 the set-up used to measure the modulation bandwidth is shown.

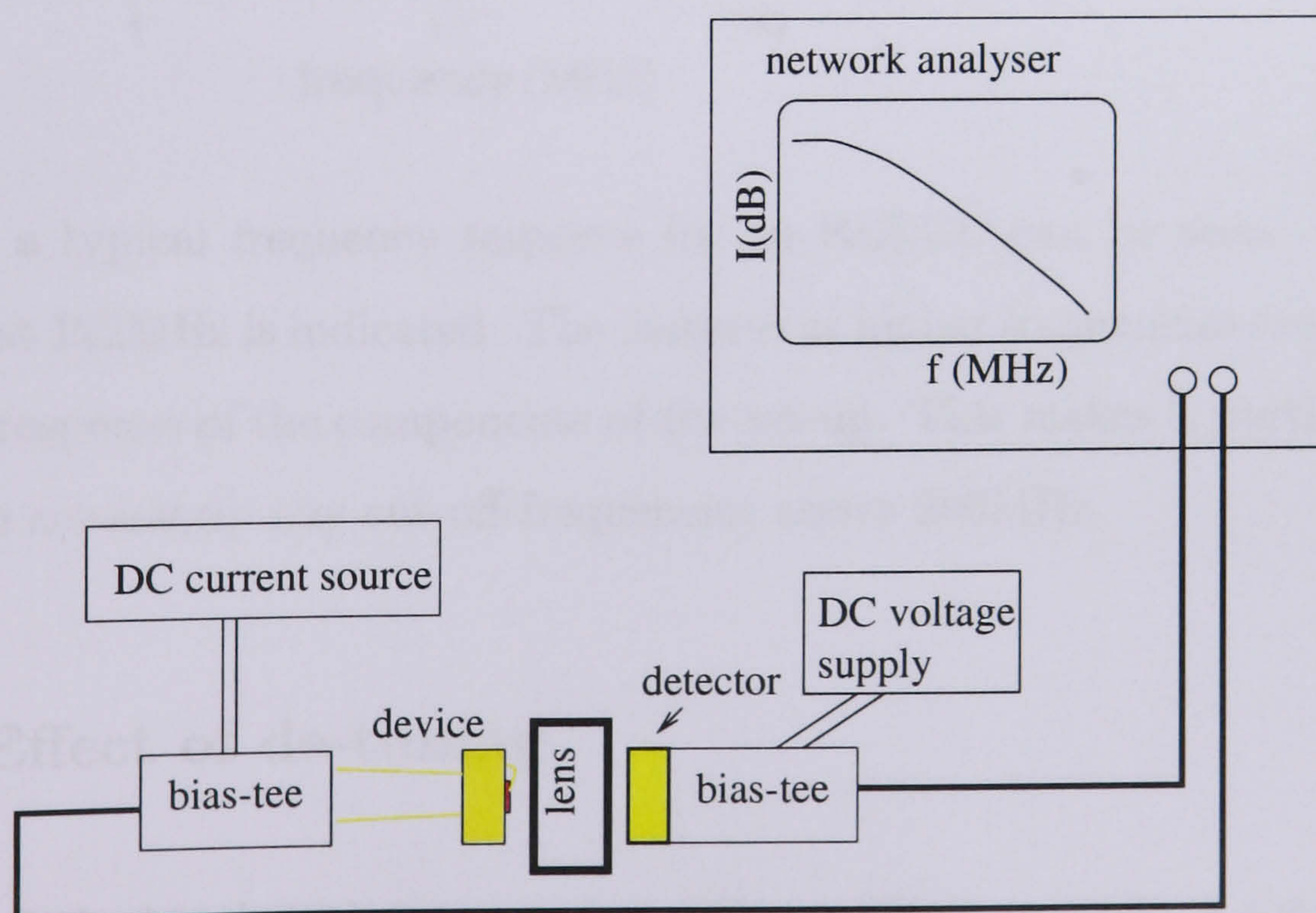

Figure 7.7: Set-Up to measure the modulation bandwidth.

In addition to the c.w. current supplied by the current source, the network ana-

lyzer provides an RF signal of -10dBm. This signal is swept through a frequency range of 0.3MHz to 500MHz and supplied through a bias tee to the device, together with the c.w. current. The light output is focused with a microscope objective with NA=0.65 onto a fast photodiode to detect the light. The diode is connected to a d.c. reverse bias power supply via a second bias tee which extracts the modulated signal for analysis on the network analyzer. The measured transmitted signal shows the frequency response of the device. The 3dB point can be read from the graph as seen in figure 7.8.

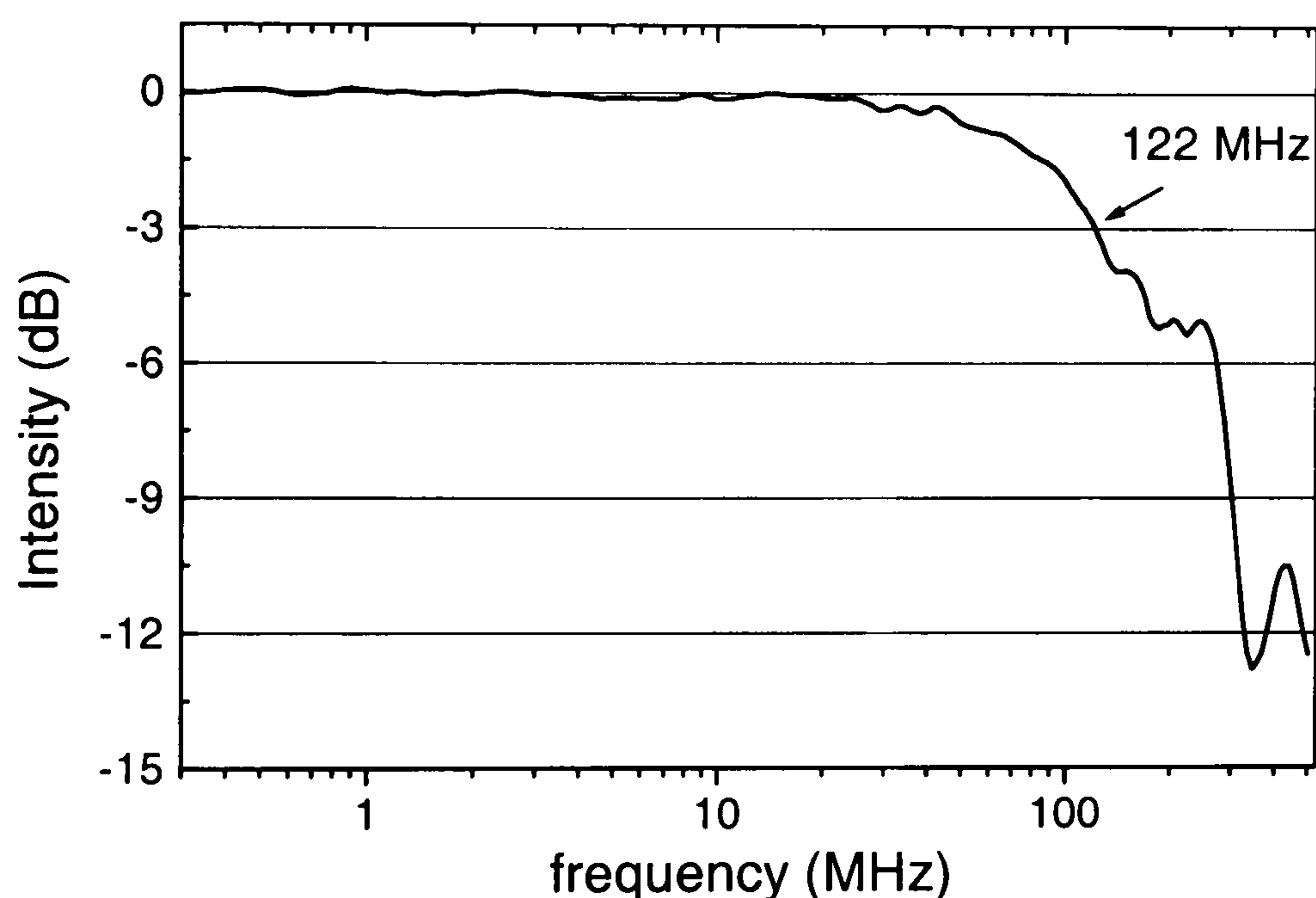

Figure 7.8: Typical frequency response from which the cut-off-frequency (bandwidth) can be extracted.

Here a typical frequency response for an RCLED can be seen. The cut-off-frequency at 122MHz is indicated. The features at higher frequencies are due to some frequency response of the components of the set-up. This makes it particularly hard to measure accurately any cut-off-frequencies above 200MHz.

7.3.1 Effect of de-tuning

In figure 7.9 the bandwidth measured at different (DC)-currents is shown for three 70μm devices with different de-tuning. Their λ_{CM} at 20°C are indicated in the graph and the QW peak emission peak lies at 650nm.

It can be seen that the bandwidth increases with increasing current for all

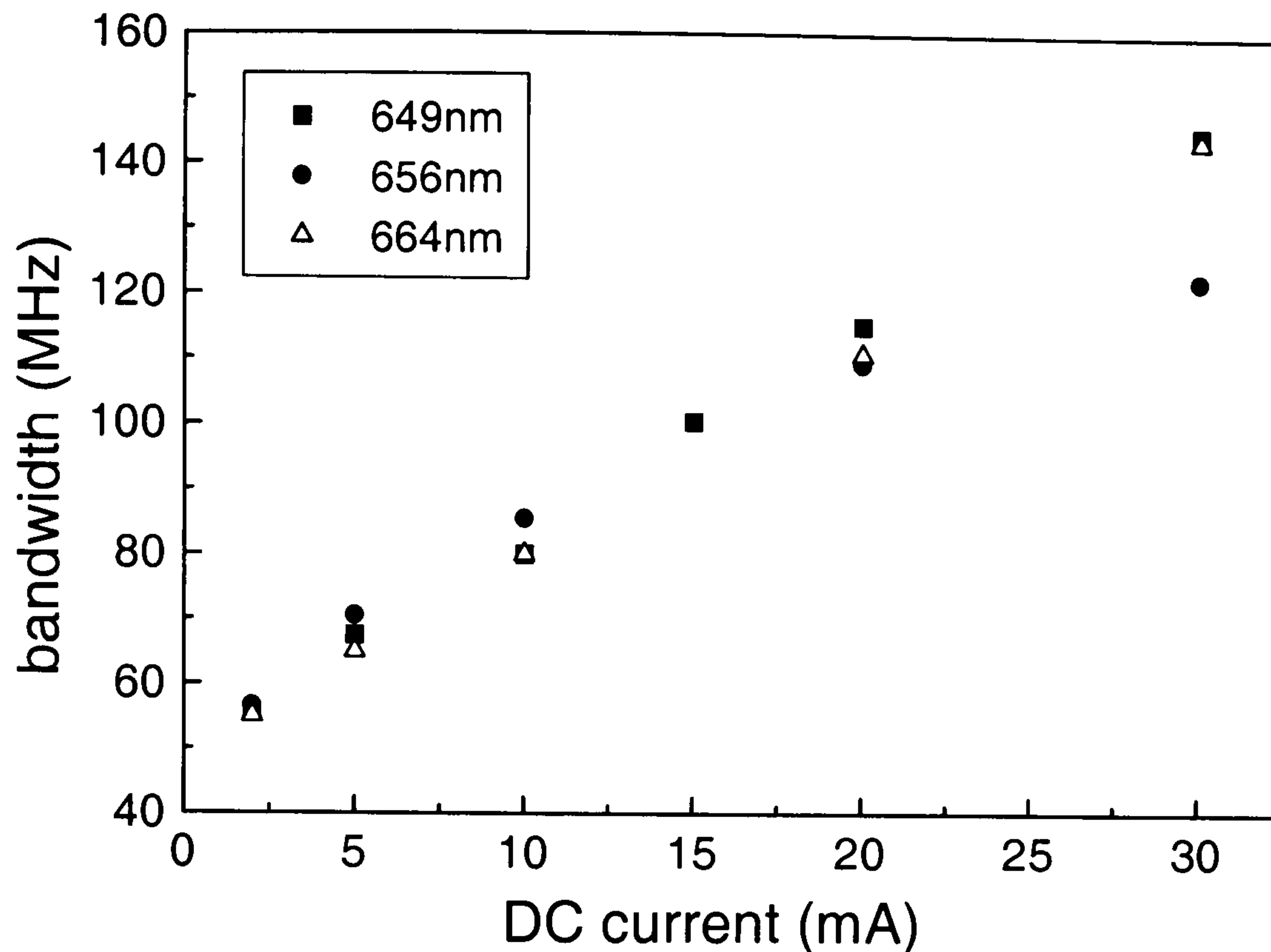

Figure 7.9: Bandwidth versus current for three 70μm devices with different de-tuning. Their λ_{CM} at 20°C are indicated in the graph.

devices. However, in contrast to what has been reported elsewhere [116] the tuned devices appear not to have a higher bandwidth than the de-tuned ones. The total light output for the de-tuned devices is higher, which might suggest a higher radiative current which would result in a higher bandwidth. The enhancement of the spontaneous emission is suggested to be higher in tuned devices as has been reported for microdisk lasers [117]. Along with the enhancement of the emission goes the reduction in the carrier lifetime. The photons get channelled into the cavity mode which reduces their lifetime. All this has less of an effect on RCLEDs as more than one mode is emitted.

7.3.2 Influence of aperture size

In this section the influence of the aperture size on the modulation bandwidth shall be discussed. In figure 7.10 the bandwidth for different DC currents and 6 different

device sizes (diameters as indicated in the graph) is plotted. These are the same devices investigated in the last chapter (processed from the S1 wafer).

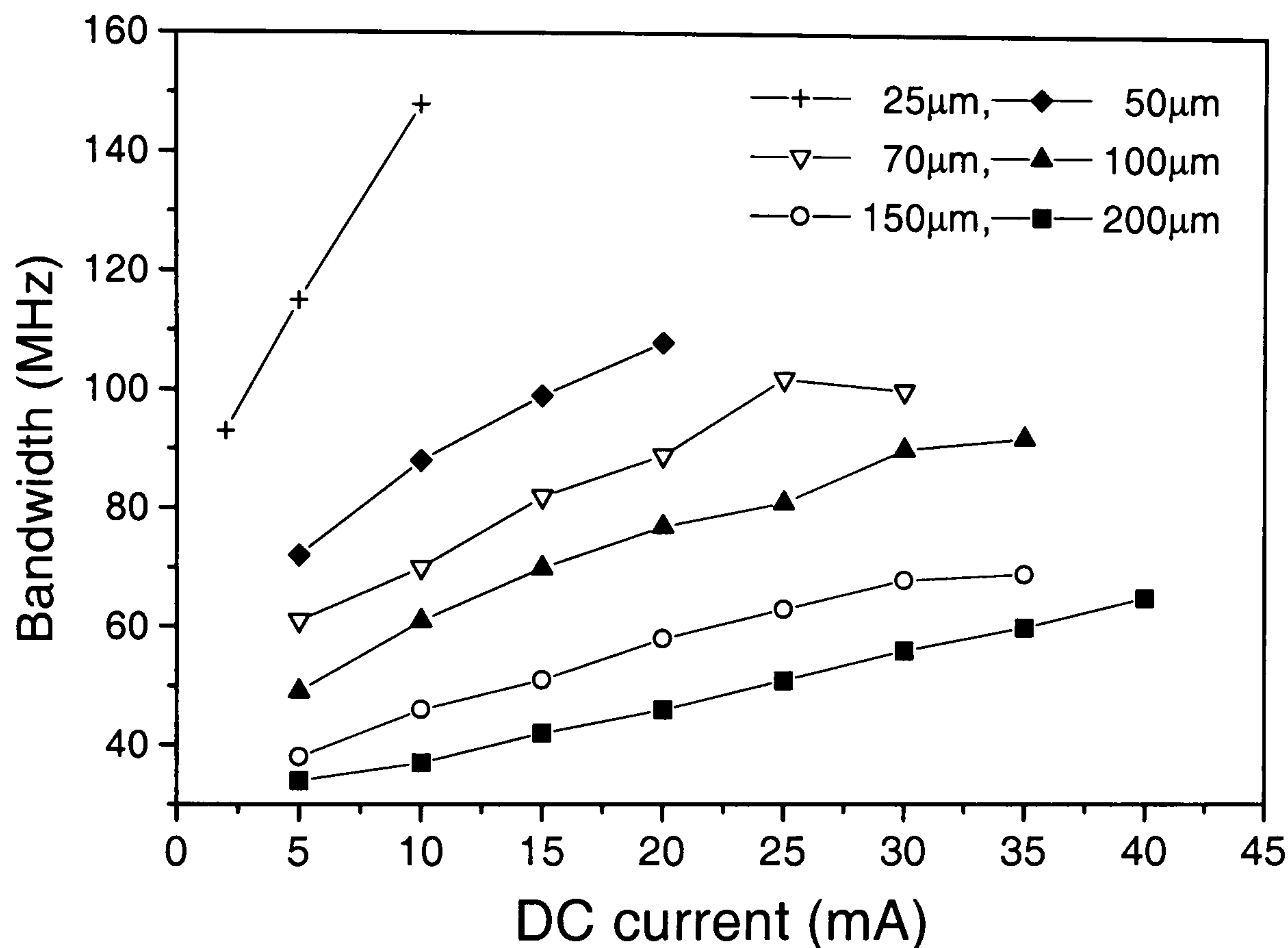

Figure 7.10: Bandwidth versus DC bias current for 6 different devices.

An increase of the bandwidth with increasing current density is observed (either by increasing current or decreasing device size). Therefore, for a given current smaller device sizes yield higher bandwidth, as has already been shown for RCLEDs [118]. At higher currents the frequencies roll off, which coincides with the thermal roll over for the different devices sizes [119]. To eliminate the effect of the size the results can be plotted against current density [120].

Theoretically the relation between the *radiative* current density and the modulation bandwidth can be calculated. The current density J can be expressed in three ways

$$\frac{J}{eL} = \frac{n}{\tau_s}, \quad \text{or in differential form} \quad \frac{dJ}{dn} = \frac{eL}{\tau}, \tag{7.1}$$

where n is the carrier density, L the thickness of the active region and τ_s the carrier lifetime and τ the differential carrier lifetime for all processes, respectively. These

equations are valid providing that all recombinations happen within L. The third way of representing J is by summing over the different current contributions

$$J = J_{nr} + J_{rad} + J_{leak} \tag{7.2}$$

$$J = eL(An + Bn^2) + D\,exp\left(\frac{-E_a(n)}{kT}\right), \tag{7.3}$$

Here An accounts for the non-radiative (J_{nr}), monomolecular contribution that is mostly defect related and hence A is called the monomolecular recombination coefficient. B is the bimolecular recombination coefficient that accounts for the spontaneous, radiative emission (J_{rad}). The last term represents the leakage current (J_{leak}), where the activation energy (E_a) is a function of the carrier density.

As the modulation bandwidth f is defined as $f = 1/(2\pi\tau))$ [121] it can be calculated by taking the derivative of J with respect to n and dividing by eL, where L is the total thickness of the active region. If the leakage current is assumed negligible this leads to

$$f = \frac{1}{2\pi\tau} = \frac{1}{2\pi}\left(\frac{1}{eL}\frac{dJ}{dn}\right) = \frac{1}{2\pi}(A + 2Bn). \tag{7.4}$$

In chapter 5 it was shown that the leakage is insignificant at room temperature, where these measurements are performed. The radiative current $J_{rad} = eLBn^2$. Re-arranging for n and substituting it into equation 7.4 leads to

$$f = \frac{1}{2\pi}\left(A + 2\frac{\sqrt{B}}{\sqrt{eL}}\sqrt{J_{rad}}\right). \tag{7.5}$$

and thus to a linear relation between f and $\sqrt{J_{rad}}$. In figure 7.11 the bandwidth is plotted with respect to the square root of the radiative current density. Here the radiative current density, J_{rad}, is calculated using the DDM model described in chapter 5 [107].

The predicted linear trend is confirmed for all devices irrespective of size in figure 7.11. Hence no intrinsic size dependence is observed that would have been expected if size dependent effects like photon recycling played a role [122]. This linear relationship is significant for the design of devices. If the bandwidth was solely determined by the radiative current density and thus by the carrier lifetime within the active region, only the radiative current would have to be increased to

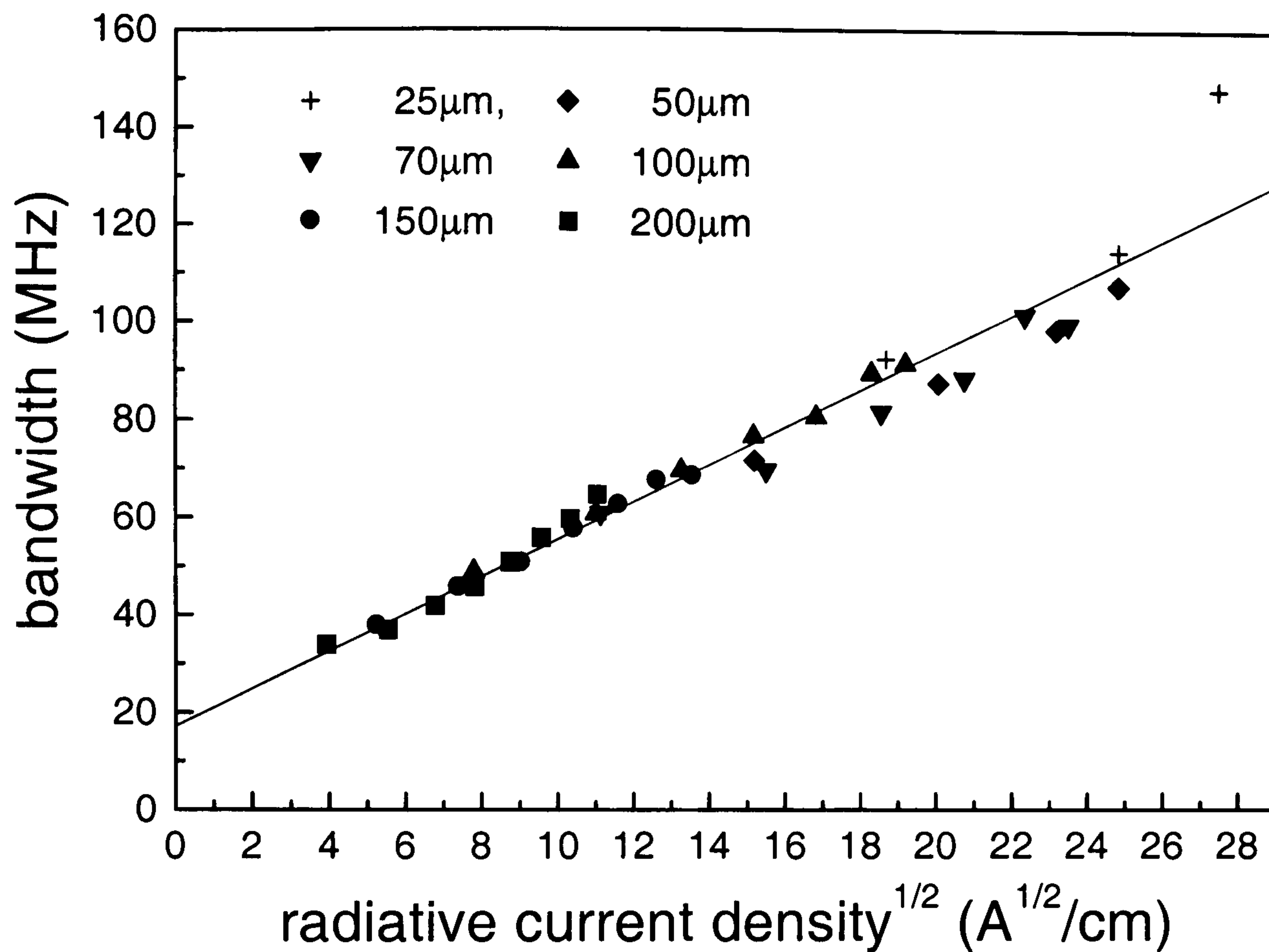

Figure 7.11: Bandwidth versus the square-root of radiative current density.

improve the modulation bandwidth. However, the non-radiative recombination also has a great influence as can be seen in bandwidth measurements that have been performed on devices that had been "burned-in" [118]. The burn-in (leaving the devices operating for several hours at temperatures of about 60°C to 70°C and a constant bias current) leads to migration of defects and thus to a possible increase in the light output (thus also the radiative current) and a decrease in the defect related recombination. Due to the latter a decrease in the bandwidth is observed.

From a linear fit of the data in figure 7.11, B can be extracted from the slope and A from the intercept. This also shows how both contributions affect the bandwidth. A high defect related current will lead to high bandwidth at low current, a high radiative current leads to higher bandwidth mainly at higher currents. Assuming that the width of the active region is given by the sum of the widths of the two quantum wells (and therefore $L = 2 \times 6nm = 1.2 \times 10^{-6}$cm) values for

$B = 3.0 \pm 0.5 \times 10^{-11} cm^3/s$ and $A = 1.1 \pm 0.2 \times 10^8 s^{-1}$ can be determined. This predicts that or carrier densities in the range of $n = 1 \times 10^{18}/cm^3$ to $n = 3 \times 10^{18}/cm^3$, the defect related monomolecular contribution An always exceeds the value for Bn^2. To make a more quantitative statement about the various current contributions, it is useful to know how the carrier density (n) varies with current, as shall be discussed next.

7.3.3 Calculation of the carrier density

The carrier density can be calculated using the bandwidth data. By plotting the differential carrier lifetime $\tau = 1/(2\pi f)$ against the total current density J, rearranging the differential form of equation 7.1 n can be deduced from

$$n = \int dn = \frac{1}{eL} \int \tau dJ. \tag{7.6}$$

The lifetime τ extracted from the measured bandwidth includes all the recombination effects. Equation 7.6 provides a way to calculate the carrier density by numerically integrating the graph of τ versus J as shown in figure 7.12 as suggested by Thompson [123]. The absolute value of n depends critically on the choice of the width of the active region, L. The result of the integral is shown in figure 7.13. The carrier density lies in the expected range between $10^{18}/cm^3$ and $10^{19}/cm^3$ over this current density range. This shows how with a relatively straightforward measurement of the frequency response of the device, the carrier density can be extracted.

Recalling that at room temperature and low current density region leakage is not important, equation 7.3 reduces to:

$$J = eL(An + Bn^2). \tag{7.7}$$

This leads to a way of determining A and B entirely experimentally, by plotting the current density J versus the carrier density n, as can be seen in figure 7.14. The

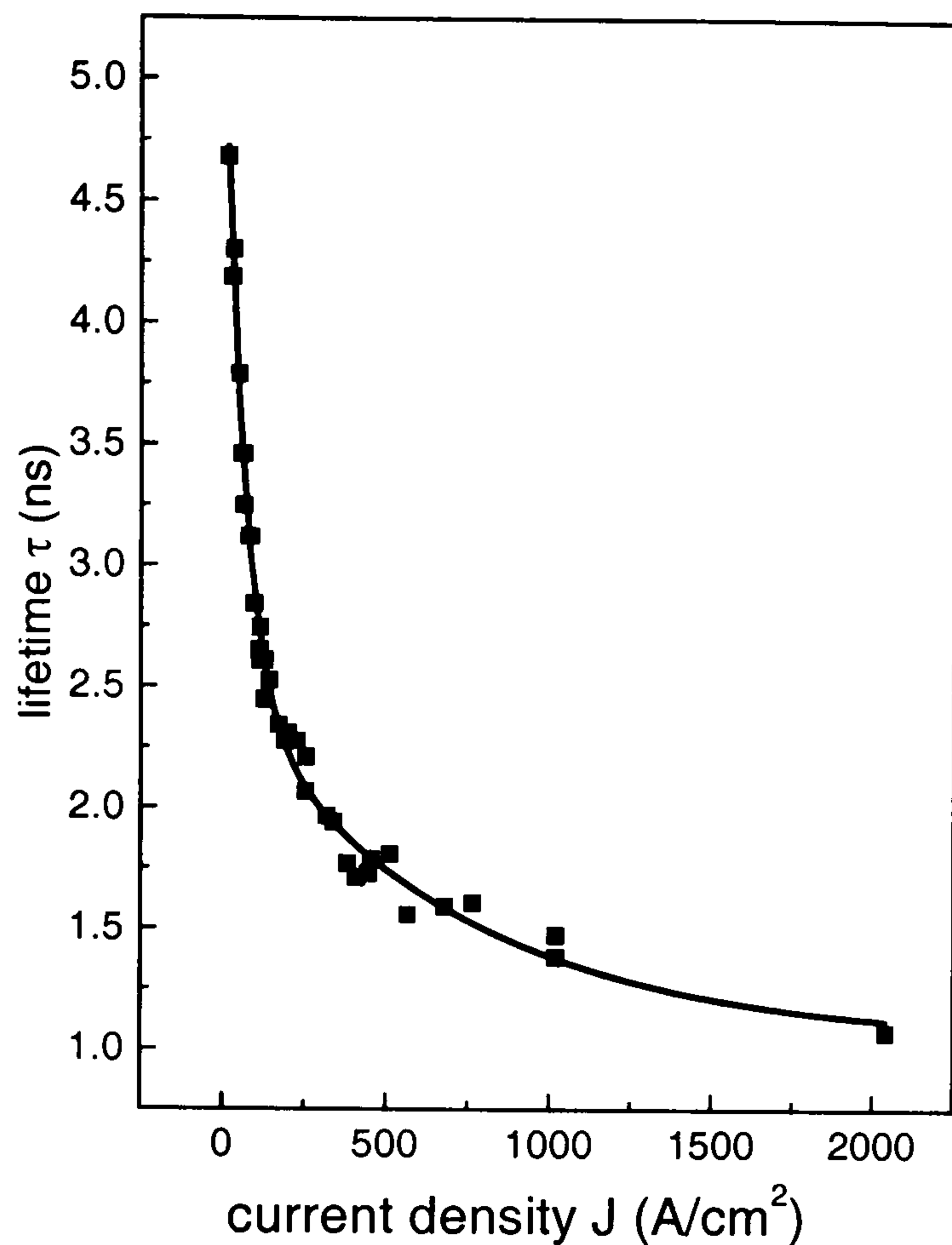

Figure 7.12: Differential carrier lifetime (τ) versus current density J for six devices.

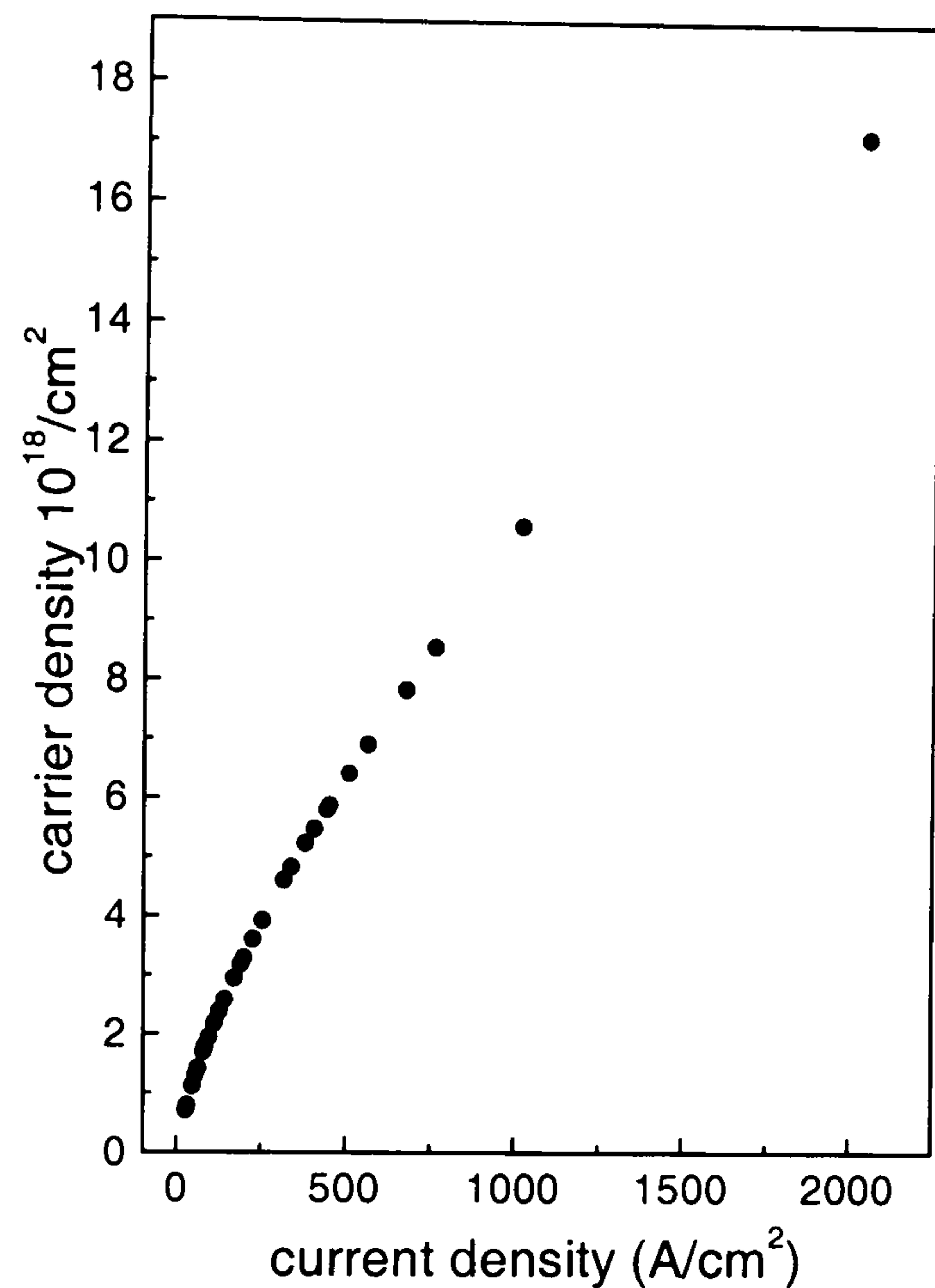

Figure 7.13: Carrier density n versus current density as calculated by integrating the data in figure 7.12.

data points can now be fitted with the quadratic equation 7.7. In the inset the mean square fitting error is plotted for fits over different number of points. The result for the best fit, in which only points up to $200A/cm^2$ were taken into account, is plotted in the graph as shown by the solid line.

Equation 7.7 is only true if leakage can be neglected. In chapter 5 it had been found that leakage was only important at higher temperatures and/ or high current densities. The data in figure 7.14 are extracted from room temperature measurements. The current density up to which equation 7.7 is applicable may be deduced from the inset of figure 7.14, which shows the mean square error for fits over different J ranges. This error remains approximately constant for fits made based upon the first 10 to 18 points. If more points, at higher J, are used for the fit, the error goes up quickly, as would be expected as equation 7.7 is not longer valid. If fewer points

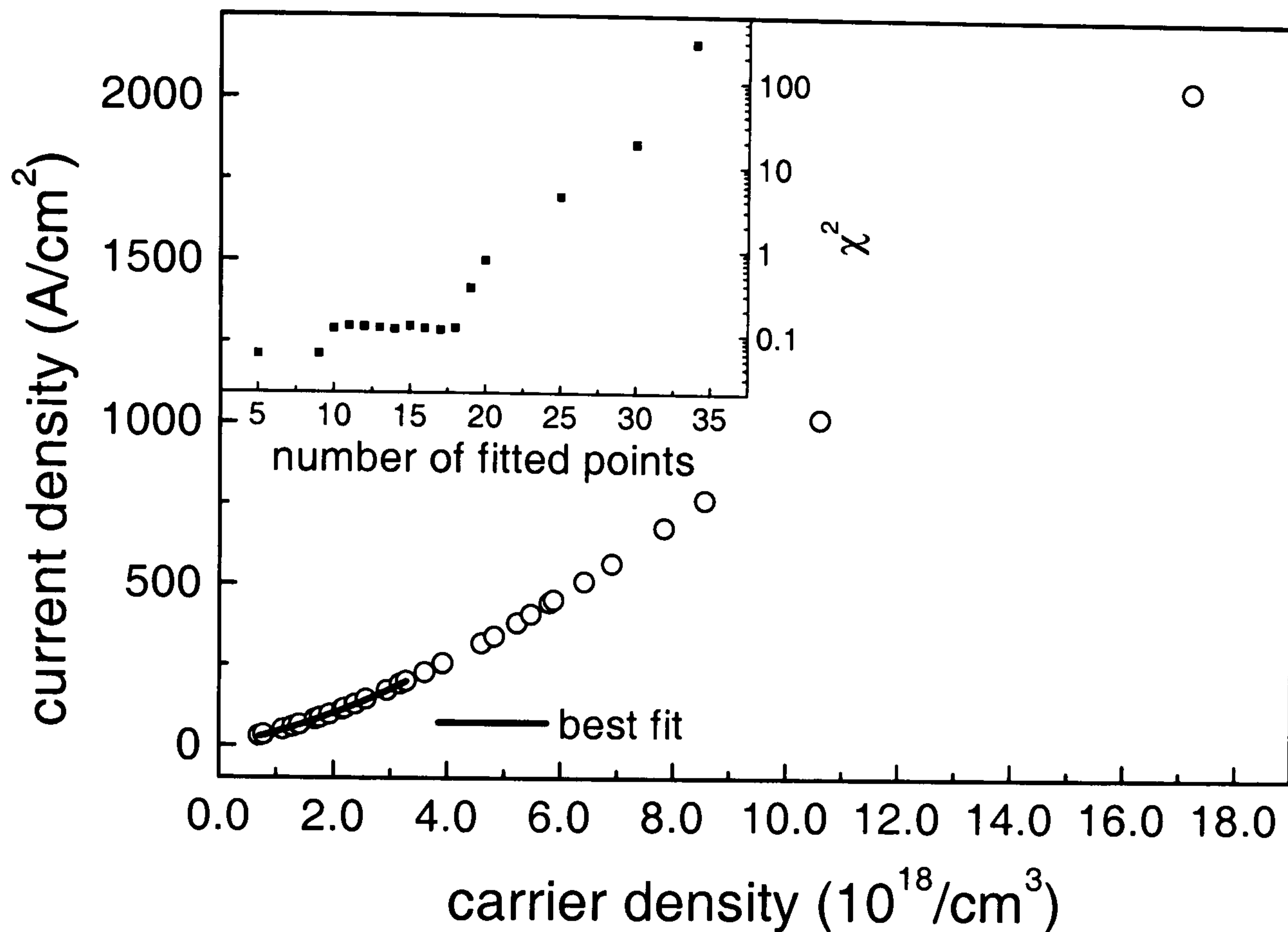

Figure 7.14: Current density versus carrier density together with a polynomial fit at low current densities. The inset shows the mean square error of the fit with respect to the number of fitted points corresponding to the current density.

are used, the error is naturally smaller but only because too few points are used. The effect on the A and B values for the different fits is plotted in figure 7.15 with respect to the number of fitted points. The equivalent values for the current and the carrier density are also indicated. The A and B values corresponding to the region with consistent fits are indicated by the open symbols in the graph and only these are used to determine A and B for the devices.

Taking the average of the values, as indicated by the horizontal lines on figure 7.15 gives $A = (1.75 \pm 0.02) \times 10^8/s$ (corresponding to a non-radiative recombination lifetime of $\tau_{nr} = 1/A = 5.7ns$) and $B = (4.3 \pm 0.1) \times 10^{-11} cm^3/s$. These values are both greater than the values extracted from the fit of figure 7.11, but still comparable. The main reason for the difference is that the two methods assume different values for n. Guina et al [118] reported a value of $B = 9.2 \times 10^{-11} cm^3/s$ and non-radiative

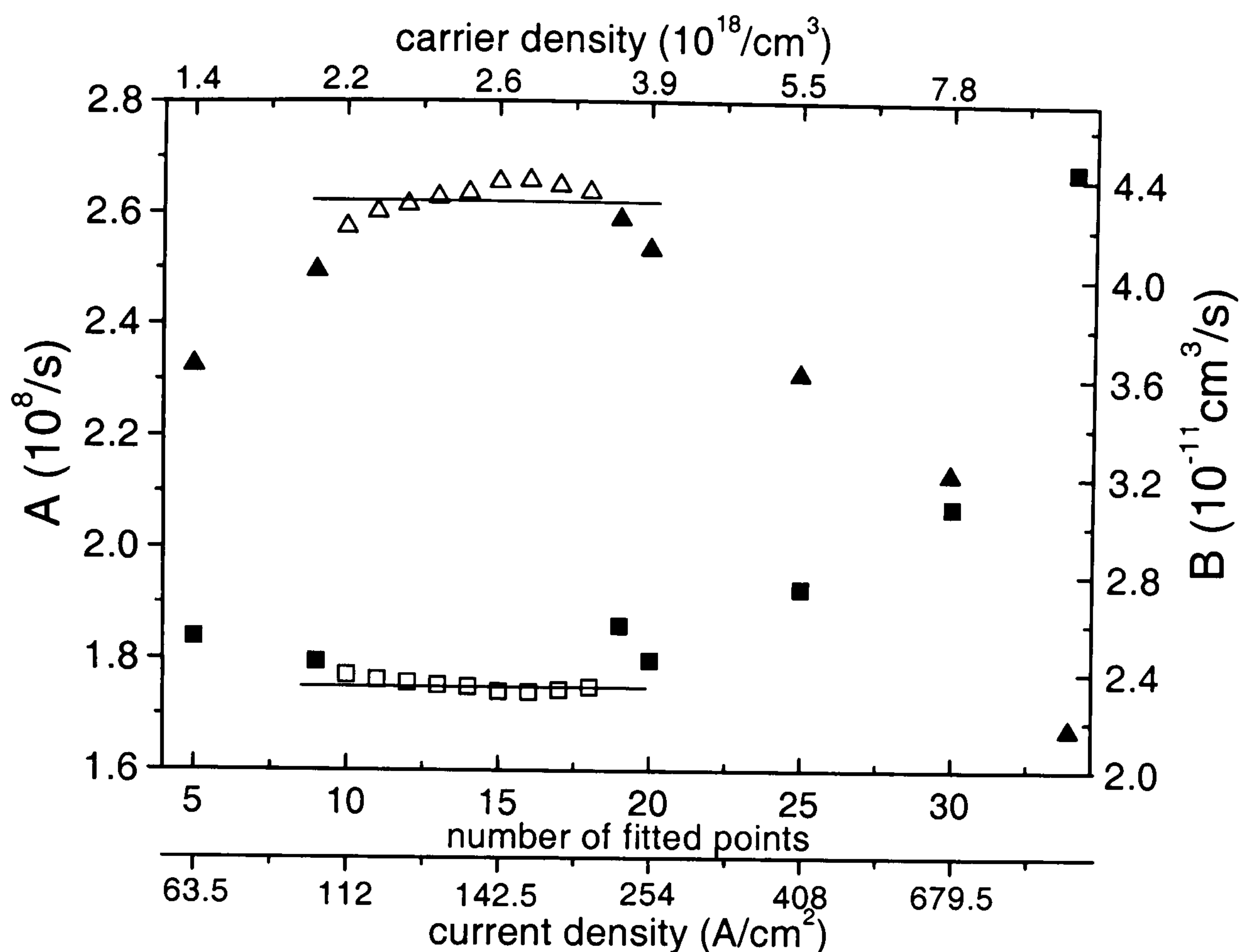

Figure 7.15: A and B as extracted from different fits to the J versus n data.

lifetimes between 1.63ns and 3.75ns, extracted from experimental bandwidth measurements and a rate equation model for similar InGaP-based devices. Their higher B value would suggest more efficient devices whereas the shorter non-radiative lifetime would lead to lower efficiency, in particular at low carrier densities. If similar device sizes to those of Guina et al are compared at 10 and 20mA with their measurements, the devices measured here show higher light output. However, as no values for the carrier density were available from [118] the reliability of both methods in determining A and B could not be compared.

With the experimentally deduced n, and the corresponding A and B values, the individual contribution of the different current paths can now be plotted. In figure 7.16 the An (dashed line) and Bn^2 term (dotted line) are plotted for current densities up to $200A/cm^2$, together with the total current density (solid squares) and the fit (solid line) that was used to determine A and B in figure 7.14.

Figure 7.16 also shows how good the fit is in figure 7.14, for the region of low current densities. Above $200A/cm^2$ the fit deviates from the experimental data. This is due

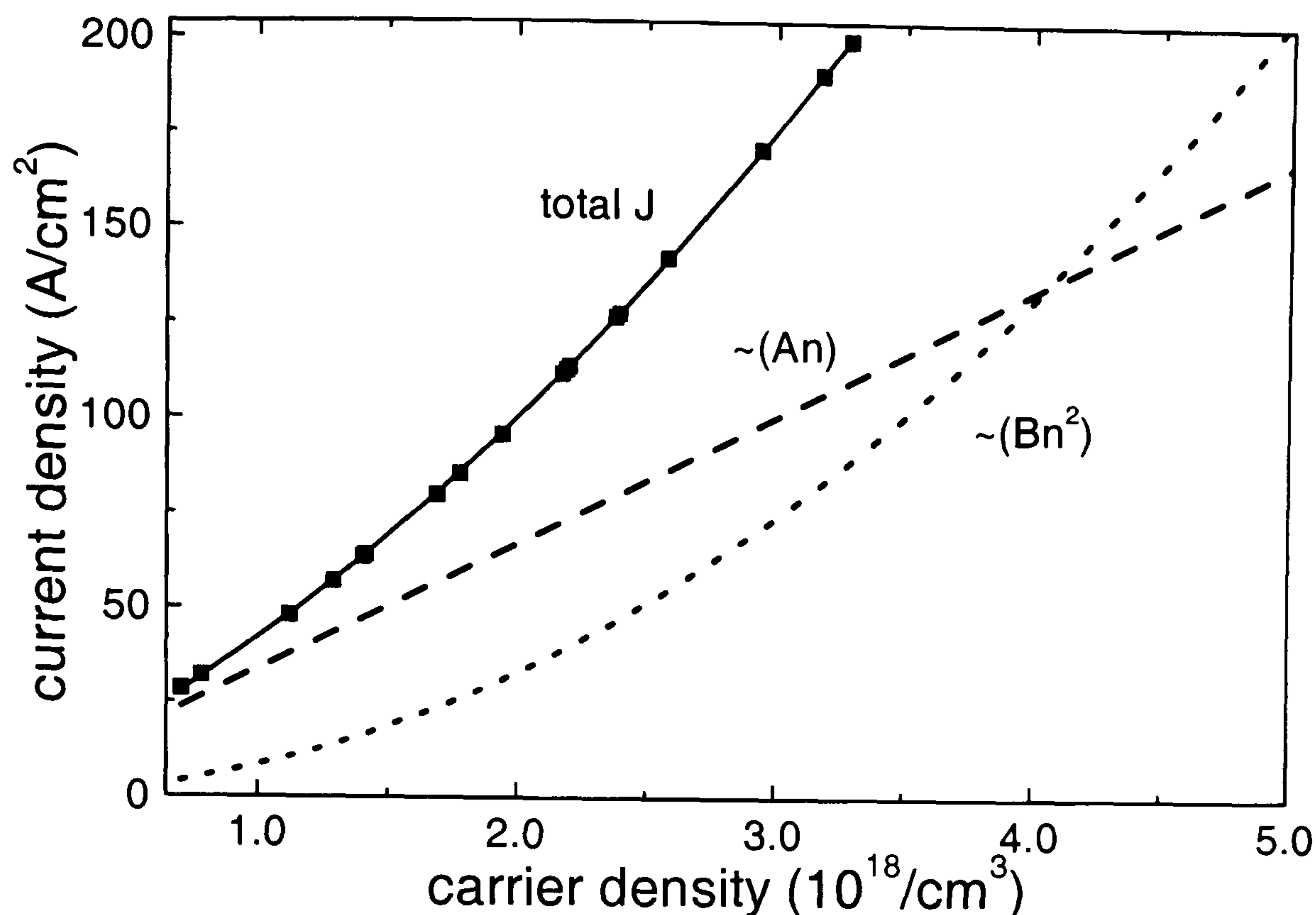

Figure 7.16: An (dashed line) and Bn^2 term (dotted line) together with the total current density (squares) and the fit with equation 7.7 (solid line) up to current densities of $200A/cm^2$.

to the effect of leakage. From the other two curves it can be seen that at carrier densities below $4 \times 10^{18}/cm^3$, the monomolecular current, dominates the total current flowing through the device. This may be due to defects in the active region of the devices or surface states on the aperture boundary caused by the implanted ions forming the current aperture.

With this knowledge of A, B, and n the different current contributions for different devices can be calculated. For the same input current, smaller devices will be at a higher current density. Thus the fraction of the radiative current (Bn^2) will be higher for these than for larger devices. However in chapter 6 it was observed that the external quantum efficiency is higher for larger devices. For higher current densities (that are present in smaller devices) the fraction of leakage current goes up. For smaller devices the self-heating is also more important, which again leads to more leakage. All of these factors limit the light output, particularly in the smaller devices, thus making them less efficient than the larger devices. However, the higher current density in the smaller devices leads to a higher operating bandwidth for a

given current. For the applications of these devices a compromise between high light output or high bandwidth will determine the optimum device size.

7.3.3.1 Power dependence of J versus n

The n dependence of the current density J is given by

$$\frac{J}{eL} = An + Bn^2 + \frac{J_{leak}(n)}{eL}. \quad (7.8)$$

Over a limited range of n, $J \propto n^z$, where z is the carrier density dependence of J. The slope of a plot of log(J) versus log(n), as it is shown in figure 7.17 gives the value of z indicating the main current contribution.

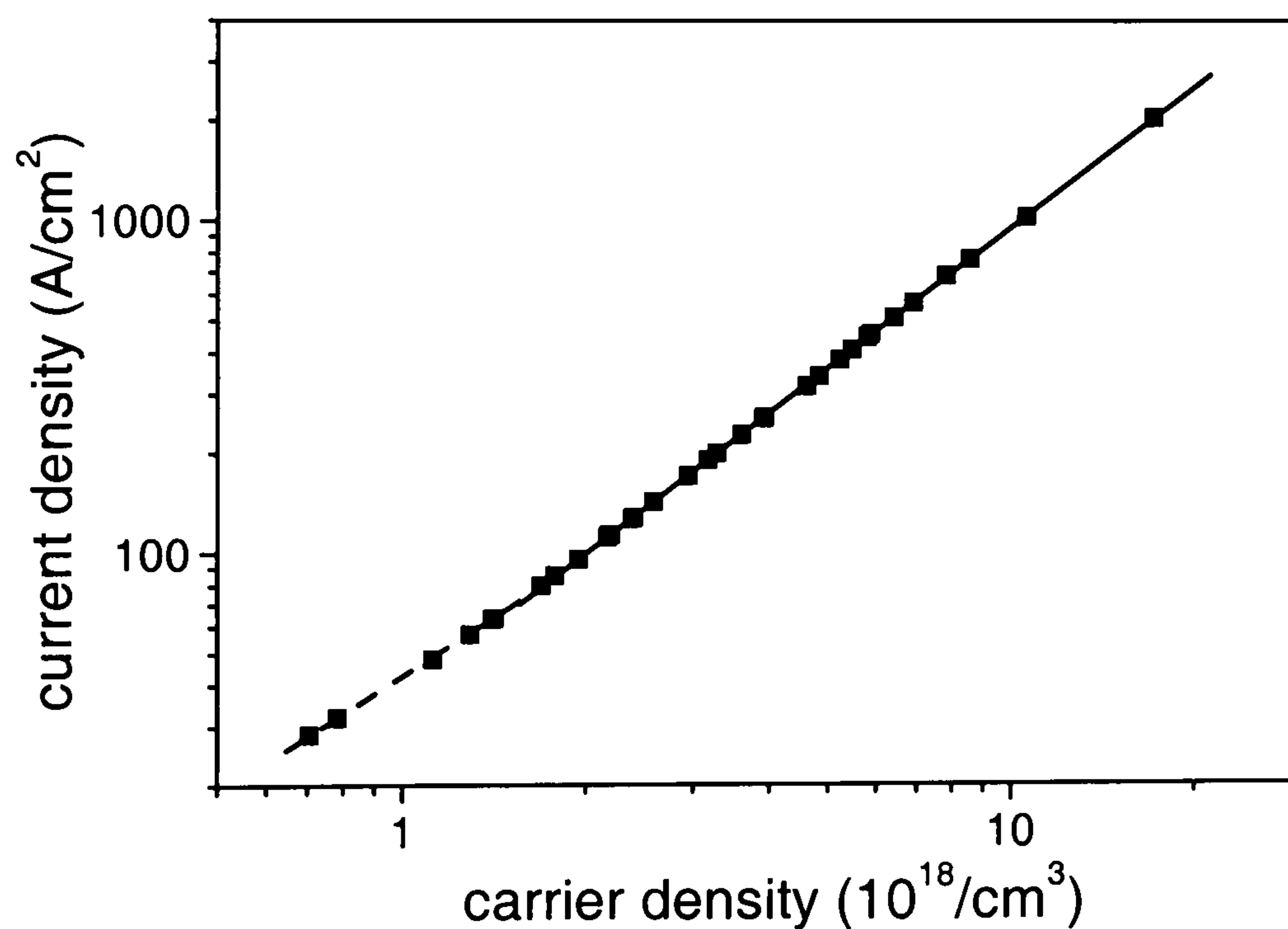

Figure 7.17: Current density versus carrier density to find the main current contribution.

As the slope increases over this range two linear fits are performed. From the first fit up to a carrier density of 1.7×10^{18} $z = 1.18\pm0.02$ and thus indicating that the defect related current (the monomolecular contribution) dominates in these devices. This confirms the high An contribution to the total injected current over this range of carrier density. From the second linear fit for the higher current densities $z = 1.40\pm 0.01$. This confirms the higher radiative contribution at higher current densities.

7.3.4 Temperature dependence

At RT and low current densities neither leakage nor self-heating are affecting the devices. To see the influence of temperature on the recombination the bandwidth (f) is measured for a series of currents at varying temperatures. In figure 7.18 the lifetime $\tau = 1/(2\pi f)$ is plotted versus temperature for two devices: one 200μm device at an DC current of 10mA (current density $J = 64A/cm^2$) and one 70μm device at 20mA ($J = 520A/cm^2$).

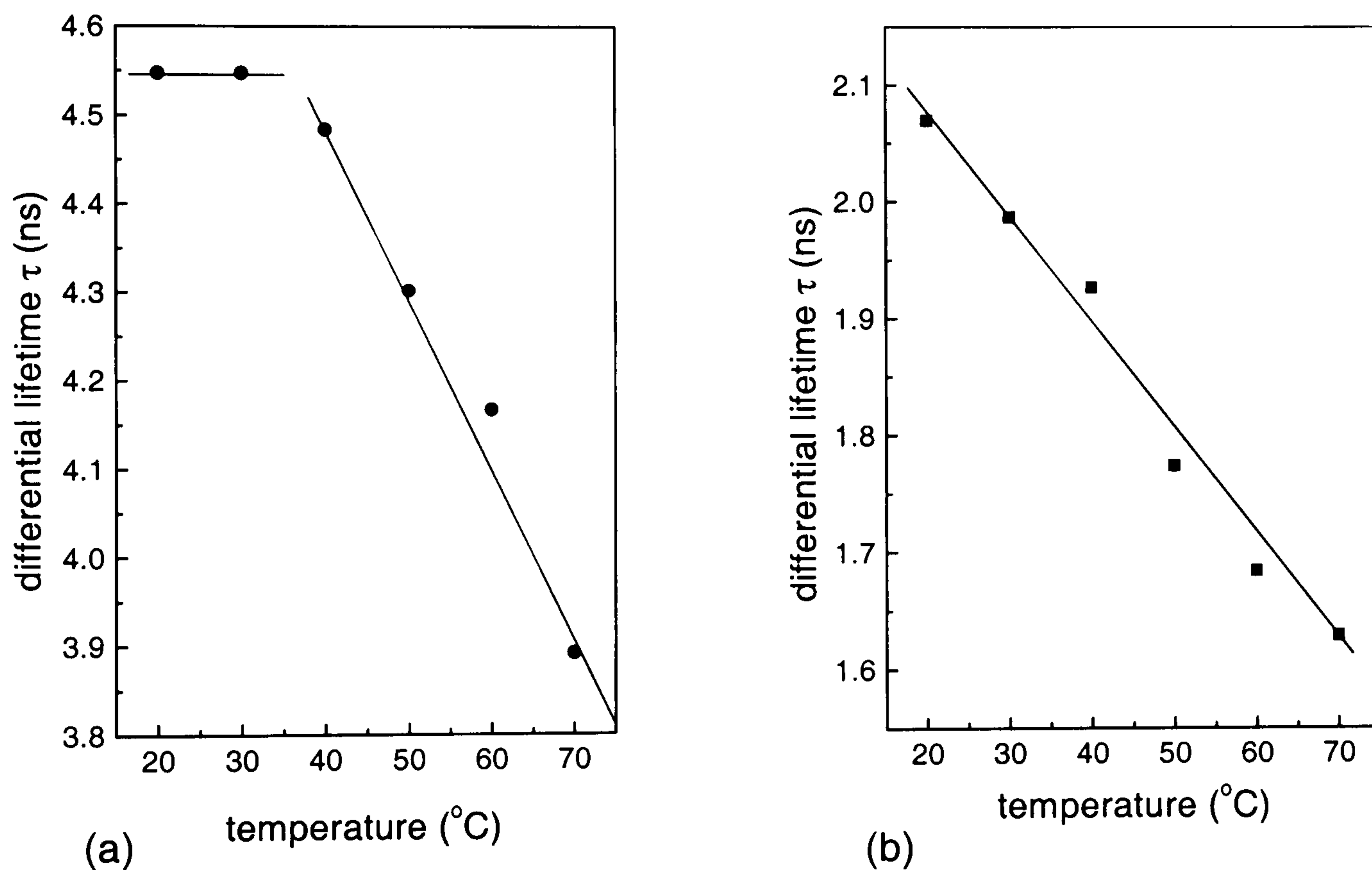

Figure 7.18: Total carrier lifetime (τ) measured for an (a) 200μm device at 10mA ($J = 64A/cm^2$) and (b) for a 70μm device at 20mA ($J = 520A/cm^2$) for a range of temperatures between 20°C and 70°C. The lines are just guides to the eye.

It can be seen in figure 7.18(a) that the lifetime is constant up to 30°C after which it starts to decrease. The total differential lifetime is given by

$$\frac{1}{\tau} = \frac{1}{\tau_{nr}} + \frac{1}{\tau_{rad}} + \frac{1}{\tau_{leak}} = A + 2Bn + \frac{1}{\tau_{leak}} \quad (7.9)$$

In the low temperature region, where leakage is negligible, τ_{leak} is very large

and so the total lifetime is determined mainly by the radiative and defect recombination lifetimes. At higher temperatures an additional recombination path becomes available which reduces the overall lifetime. This confirms that for temperatures starting at 40°C leakage starts to play a significant role. The effect of the higher current density can be seen in figure 7.18(b). The total lifetime is significantly shorter than for the device at lower current density and decreases for all temperatures. The current density at which these devices were measured was $520A/cm^2$. As this is higher than $200A/cm^2$ it confirms that leakage plays a role even at RT at this current density.

To quantify the leakage lifetime, the bandwidth and thus the total lifetime is measured for constant light output. The results for the differential lifetime can be seen in the inset of figure 7.19. The lifetime associated with leakage is calculated using equation 7.9 and assuming the following for the temperature dependence of $1/\tau_{nr}$ and $1/\tau_{rad}$ or A and B respectively: $A(T) \propto T^{0.5}$ [124] and $B(T) \propto 1/T$ [125]. Due to the change in extraction efficiency with temperature it is found in chapter 5 that the radiative current $\propto Bn^2$ increases linearly with T if the light output is held constant as is here. Therefore it can be assumed that $Bn = const$ and thus $1/\tau_{rad} = const$.

A linear fit of the inverse lifetime gives an activation energy for the leakage of 313±7meV, which is comparable with the results of 350meV obtained in chapter 5. The two points at lower temperature do not lie on this linear fit. Any error in A and B and their assumed temperature dependence will have a higher effect on these low temperature values. At higher current densities the total lifetime is more determined by leakage and thus this region is used to determine the activation energy associated with leakage.

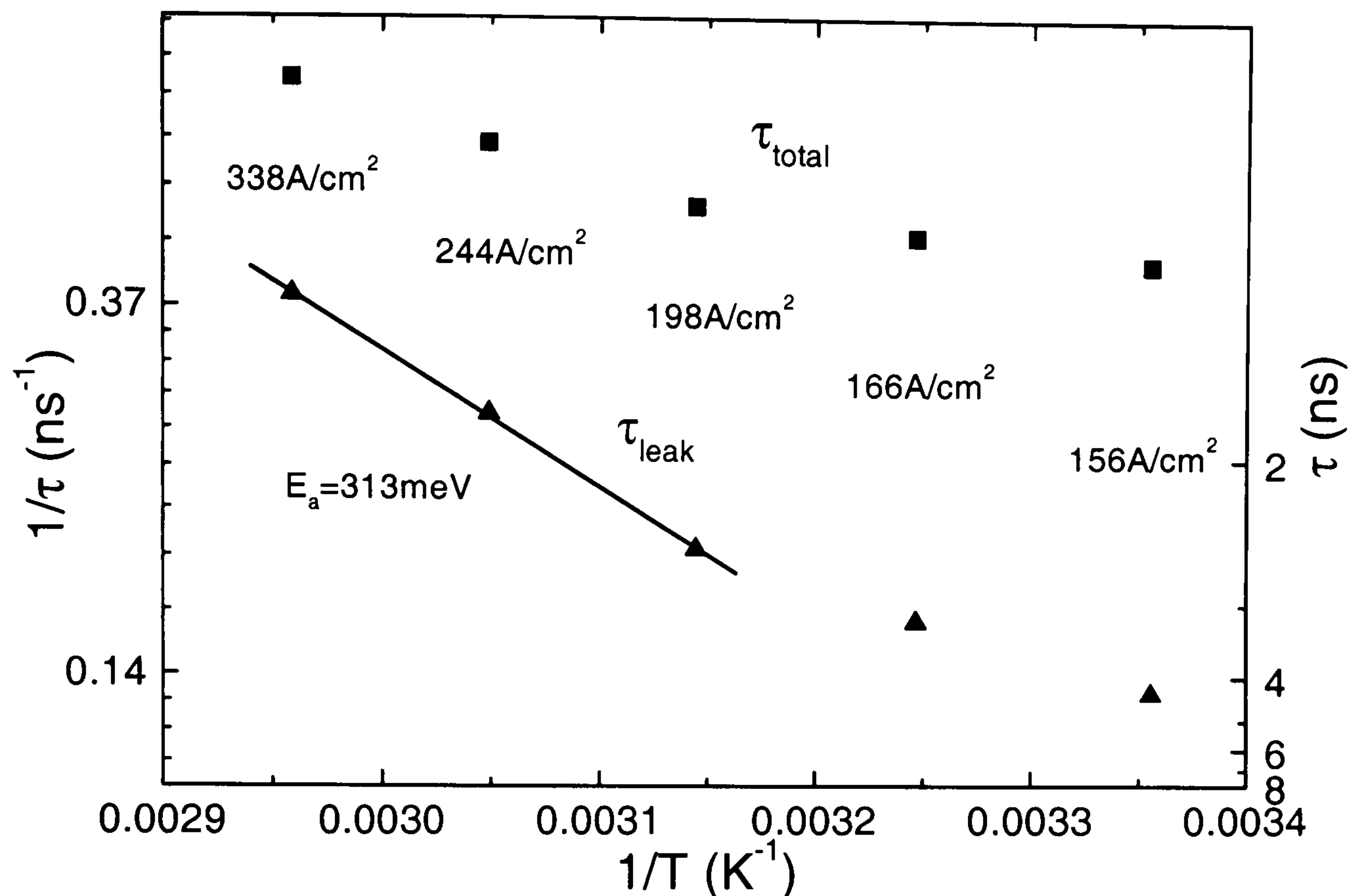

Figure 7.19: Inverse leakage lifetime versus inverse temperature on a semilogarithmic scale. τ_{leak} is calculated from total lifetime measurements for constant light output using equation 7.9 and the in the text described temperature dependencies of A and B. The total measured lifetimes together with the current densities for each point is also shown.

7.4 Conclusions

In this chapter measurements important for the application of RCLEDs for local area network communications based upon POF were discussed. The coupling into POF is more efficient for devices where λ_{QW} is tuned with respect to λ_{CM} and to the minimum of the fibre attenuation at 650nm. The main disadvantage for de-tuned devices is not so much the attenuation of the fibre but rather the restricted collection angle. If the coupling efficiency is measured for increasing temperature it increases for the de-tuned devices, confirming the lower temperature sensitivity for de-tuned devices as discussed in chapter 5.

From the modulation bandwidth measurements modulation speeds of between 30 and 150MHz are observed depending on device size and bias current. This would be sufficient for use in in-car networks, where data rates of up to 24Mbps are used.

No difference in the bandwidth for differently de-tuned devices could be observed. The bandwidth scales linearly with the square-root of the radiative current density. Hence there is no intrinsic size dependence which would have been expected if effects like photon recycling played a role. From the bandwidth measurements over a range of current densities, the carrier density could be calculated. This could then be used to determine the monomolecular and radiative recombination parameters, $A = 1.75 \times 10^8/s$ and $B = 4.3 \times 10^{-11} cm^3/s$, respectively. The relative size of these parameters determines the amount of radiative recombination to the total injected current. Together with the experimentally determined carrier density these results show that at room temperature non-radiative recombination dominates the devices up to a carrier density of $4 \times 10^{18}/cm^3$ corresponding to a current density of $130A/cm^2$. This is confirmed by the power dependence of the current on carrier density, $J \propto n^z$ yielding $z = 1.36$ as the exponent. It was shown that at RT from a current density of $200A/cm^2$ leakage becomes more important for these devices. The decrease in the differential carrier lifetime with temperature shows that above 40°C leakage in these devices becomes significant at relatively low J values. An activation energy for the leakage of 313meV was determined from the extraction of the leakage lifetime. This value agreed well with an activation energy of 350meV found earlier in chapter 5 and similar values reported in the literature.

Chapter 8

Thesis conclusions

8.1 Summary

The main aim of this thesis was to investigate the parameters affecting the performance of GaInP-based resonant-cavity LEDs emitting at 650nm. These devices are produced to work in short distance networks using PMMA plastic optical fibre (POF), which has an attenuation minimum at 650nm. For several applications temperature stability over a large range (typical 0°C to 80°C) is crucial for these devices as temperature control is un-economical for the intended low cost applications. In this thesis it was shown that the temperature sensitivity decreases with increasing device size and was also improved for positive QW-CM de-tuning ($\Delta\lambda = \lambda_{CM} - \lambda_{QW}$) when a POF-like collection angle (NA$\sim$0.5) was reproduced.

The emission of an RCLED is determined by the QW emission peak wavelength (λ_{QW}) and line width (Γ_{QW}), the cavity mode wavelength (λ_{CM}) and, in particular, the relative position of these two wavelengths. Hence it is very important to know λ_{CM} and λ_{QW} accurately. To obtain λ_{QW} from the supplied wafers, photo-modulated reflectance (PR) and edge electroluminescence (EL) were used. λ_{CM} was found from reflectivity measurements on wafers and devices. The performance of the devices was characterised by light-current (LI) and spectrally

resolved EL measurements while varying device parameters such as the de-tuning between λ_{CM} and λ_{QW}, the aperture size and the number of top DBR pairs. The following paragraphs give a review of the main outcomes of the thesis.

After a short introduction to the subject in chapter 1, chapter 2 explained the basic concepts of RCLEDs, the underlying physical background and introduced the basic measurement principles for the characterisation of devices.

In chapter 3 the measurements that were performed on the RCLED wafers to find λ_{QW} were discussed. The theory and the experimental techniques of photo-modulated reflectance and edge electroluminescence were considered. With various analysing techniques, the values of λ_{QW} for different wafers were confirmed to be near the required 650nm.

In chapter 4 the theory of reflectivity for a multilayer structure was discussed and used to calculate and to fit experimentally measured reflectivity spectra. For one of the wafers the fitting predicted thinner top than bottom DBR pairs suggesting an error in the growth. This was confirmed using SEM imaging. Along with conventionally measured R-spectra of wafers, reflectivity measurements performed directly on devices were introduced and examined. This proved a valuable tool not only to determine differences between wafers and devices but also to pick devices with a particular λ_{CM} for further investigation.

In chapter 5 the influence of the λ_{CM}-λ_{QW} de-tuning on the device performance was investigated. The amount of de-tuning has a strong influence on the far field pattern. The maximum light output for a device occurs when the QW maximum emission intensity is situated in the middle of the spectral escape window confirming the predictions of Ochoa et al [96] in 1999. If all the light is collected, this corresponds to a de-tuning of 45°, and thus 15nm. Since devices tune-in with increasing temperature (i.e. λ_{QW} red shifts towards λ_{CM}), the light

output of more strongly de-tuned devices is less temperature sensitive than for those initially tuned. The focus with these measurements was on the application of coupling the light into POF. For a POF acceptance angle of 30° the optimum de-tuning is much lower and only 2nm. Therefore for each measured temperature a device that is positively de-tuned by 2nm at that temperature shows the maximum light output. The light output decreases by between 0.9% - 1.6% from 20°C to 70°C. The optimum device provides a compromise between high light output and low temperature sensitivity for a collection angle of 30° (as for POF).

The high temperature sensitivity was attributed to two main effects; electron leakage into the X-minima of the p-cladding and Ohmic self-heating of the device due to resistance in the DBRs. It was observed that the percentage of leakage current goes up with the total current and with increasing temperature and reaches almost 50% at 80°C. It was also shown that self-heating accounts for 50% of the current at a device temperature of 70°C. However, self-heating increases with current and therefore leads to more leakage so both effects can not be described independently of each other.

The size dependence and influence of the top reflectivity were discussed in chapter 6. In comparison with the de-tuning, the influence of the different numbers of top DBR pairs (8, 11 and 14 pairs) has a negligible effect on the light output and its temperature dependence. The coupling efficiency into the fibre-like collection angle was slightly higher for the device with 14 DBRs in agreement with theoretical predictions by Benisty et al [35].

The external efficiency for larger aperture devices was found to be higher than for the smaller ones. In addition, it was found that the compactness of the active region is the main reason for the device self-heating. Therefore, this effect is more pronounced in smaller devices. Hence, if high light output and temperature stability are required, there is an advantage in using larger devices. The insufficient current spreading encountered in larger devices was overcome by using a grid contact. However, this grid obstructs some of the light, which makes the larger devices less

efficient at currents below 7mA. No clear evidence for photon recycling, which would lead to even higher efficiencies for the larger devices was found. The increased self-heating for smaller devices could be fitted with a simple heating model using a reasonable value of the thermal conductivity $\sigma = 0.15 \pm 0.02 W/cm^{\circ}C$ for the devices.

In chapter 7 the coupling efficiency into POF and the modulation bandwidth were measured. These are both important parameters in determining how successful RCLEDs can be for applications in local area networks. It was shown that the coupling into POF was more efficient for a device with zero de-tuning at 650nm mainly because of the acceptance angle allowing only light emitted within a cone of $\sim 54^{\circ}$ to be collected by the fibre and because for a tuned device most of the light is directed into the forward direction. However, the advantage of the de-tuning was seen in the temperature and current dependence of the coupling. Due to self- or external heating the initially de-tuned devices tune-in leading to a lower temperature sensitivity.

The modulation bandwidths of these devices varied between 30MHz and 150MHz increasing with increasing current density. The higher bandwidth for smaller devices that was observed here was also observed in devices reported by Dumitrescu et al [28] in 2001. The bandwidth values confirmed that the devices investigated here could be used in local area networks (e.g. for in-car entertainment). The upper limit of the bandwidth was given by the measurement conditions and was achieved with the $25\mu m$ device at an operating current of 10mA. However as small devices show the highest bandwidth the maximum modulation will ultimately be determined by the highest operation current for the smaller devices. Increased self-heating will however cause smaller devices to thermally roll-over at relatively low currents $\sim$20mA.

It was also shown that the bandwidth measurements could be used to calculated the carrier density, which then was used to extract the recombination parameters $A = 1.75 \times 10^8/s$ and $B = 4.3 \times 10^{-11} cm^3/s$. In the temperature dependence of the differential lifetime it was observed that leakage becomes

important at temperatures greater than 40°C.

In summary, it was shown that the optimum visible RCLED device depends strongly on the desired application. If high light output at a given operating temperature is the main concern, it will depend on the NA aperture of the light collection, as has also been reported by Oulton et al [99] in 2001. If the total light output is collected, strongly de-tuned devices (~14nm) will show the highest light output. For the application of POF with a NA=0.5 the maximum light output was obtained for devices tuned or up to 3nm de-tuned. If high light output and stable temperature operation is the main concern, large devices should be used. The advantages of smaller devices include the higher directionality for fibre coupling, better current spreading, and the higher bandwidth for a given operating current.

8.2 Outlook

In answering many questions about the performance of 650nm RCLEDs various further aspects of device operation have been found that would be interesting for further investigations.

The difference of the temperature dependencies of devices with one and two QW emission wavelengths is a particularly interesting aspect. The results presented in this thesis indicate that a better temperature sensitivity could be achieved for two dissimilar QWs.

Additional experiments on fibre coupling, data transmission and how the fibre influences the overall bandwidth of the system would give a clearer picture about the most suitable device. It could be investigated if the device proposed in chapter 7 with λ_{QW} = 642nm and λ_{CM} = 648nm showed the best temperature performance if coupled into POF.

The bandwidth measurements have proved to be a useful tool not only in terms of device characterisation but also in discovering important intrinsic parame-

ters of the material. By investigating the temperature dependence of the modulation bandwidth further it should be possible to find the temperature dependence of the monomolecular (A) and radiative (B) recombination parameters. The temperature dependence of the lifetime would also lead to more information about the temperature variation of the carrier density. This could then be used to quantify the amount of leakage at higher temperatures and compare this with values obtained using the drift diffusion model program.

As the reflectivity fitting showed good initial results, other R spectra could be fitted and compared.

Many of the techniques used in this thesis, could also be applied to devices at other wavelengths, in particular for other LEDs or RCLEDs at 570nm or 1310nm which are of interest for both POF and silica fibre based applications.

Bibliography

[1] Aeschylus. *The Oresteia.* Penguin Classics, 1979.

[2] M.J. Howes and D.V. Morgan, editors. *Optical Fibre Communications.* John Wiley & Sons, 1980.

[3] M.D. Fagen, editor. *A History of Engineering and Science in the Bell System: The early years (1875-1925).* Bell Telephone Laboratories, Incorporated, 1975.

[4] J. Hecht. *Fiber Optics Technician's Handbook*, chapter 1: *The origins of Fiber Optics communications.* Delmar Learning, 2nd edition, 2000.

[5] S. Ungar. *Fibre Optics: Theory and Applications.* John Wiley & Sons, 1990.

[6] H.H. Hopkins and N.S. Kapany. A Flexible Fibrescope, using Static Scanning. *Nature*, **172**:39–41, (1954).

[7] T.H. Maiman. Stimulated Optical Radiation in Ruby. *Nature*, **187**:493–4, (1960).

[8] C.C. Eaglesfield. Optical Pipeline: A Tentative Assessment. *Proc. IEE*, **109B**:26–32, (1962).

[9] K.C. Kao and G.A. Hockham. Dielectric-fibre surface waveguides for optical frequencies. *Proc. IEE*, **113**(7):1151–58, (1966).

[10] A. Neyer, B. Wittmann, and M. Jöhnck. Plastic-Optical-Fiber-Based Parallel Optical Interconnects. *IEEE J. Select. Topics Quantum Electronics*, **5**(2):193–200, (1999).

[11] COMMSPLACE.COM. http://www.commsplace.com/Knowledge/ITcs/html/tutorials/fibre-optics/introduction-fibre-optics.htm. *www.* 09-04-03.

[12] D. McGRAW. LEDs light up medical diagnostics. *Comp. Semi.*, April (2001).

[13] H.P.A. VAN DEN BOOM, W. LI, P.K. BENNEKOM, I. TAFUR MONROY, AND G.-D. KHOE. High-Capacity Transmission Over Polymer Optical Fibre. *IEEE J. Select. Top. Quant. Elec.*, **7**(3):461–70, (2001).

[14] TORAY INDUSTRIES. http: //ap1.toray.co.jp/opf/e/raytela/whatspof/ carnet.html. *www*, (2001).

[15] N. ANSCOMBE. Europe puts plastic optical fibre to work. *Opto & Laser Europe*, (9):38–9, (2001).

[16] S. MORIKURA, K. KINOSHITA, K. NUMATA, AND S. FURUSAWA. High Speed POF Transmission Technology and its Standarization. *Proc. 27th Eur. Conf. on Opt. Comm.*, pages 20–21, (2001).

[17] J. HEWETT. Gradual progress for high-brightness LEDs. *Opto & Laser Europe*, May (2002).

[18] S. NAKAMURA AND S.F. CHICHIBU, EDITORS. *Introduction to Nitride Semiconductor Blue Lasers and Light Emitting Diodes.* Taylor Francis, London and New York, 2000.

[19] M.G. CRAFORD, N. HOLONYAK, AND F.A. KISH. In Persuit of the ultimate lamp. *Scient. American.*, pages 49–53, February (2001).

[20] H. SODA, K. IGA, C. KITAHARA, AND Y. SUEMATSU. GaInAsP/InP surface emitting injection lasers. *Jpn. J. Appl. Phys.*, **18**:2329, (1979).

[21] K. IGA. Vertical-Cavity Surface-Emitting Laser - Progress and Prospects. *IEICE Trans. Electron.*, **E85**:10–20, (2002).

[22] T. WHITAKER. Surface Emitters Have The Edge. *Comp. Semi.*, 4(2):18–29, (1998).

[23] E.F. SCHUBERT, Y.H. WANG, A.Y.CHO, L.-W. TU, AND G.J. ZYDZIK. Resonant cavity light-emitting diode. *Appl. Phys. Lett*, **60**(8):921–3, (1992).

[24] H. Yokoyama, K. Nishi, T. Anan, H. Yamada, S.D. Broson, and E.P Ippen. Enhanced spontaneous emission from GaAs quantum wells in monolithic microcavities. *Appl. Phys. Lett.*, **57**(26):2814–6, (1990).

[25] F. De Martini, G. Innocenti, G.R. Jocobovitz, and P. Mataloni. Anomalous Spontaneous Emission Time in a Microscopic Optical Cavity. *Phys. Rev. Lett.*, **59**(26):2955–58, (1987).

[26] A.T. Meney, A.D. Prins, A.F. Phillips, J.L. Sly, E.P. O'Reilly, D.J. Dunstan, A.R. Adams, and A. Valster. Determination of the Band Structure of Disordered AlGaInP and its Influence on Visible-Laser Characteristics. *IEEE J. Select. Topics Quantum Electronics*, **1**(2):697–705, (1995).

[27] M. Guina, S. Orsila, M. Dumitrescu, M. Saarinen, P. Sipilä, V. Vilokkinen, B. Roycroft, P. Uusimaa, M. Toivonen, and M.Pessa. Light-Emitting Diode Emitting at 650 nm with 200-MHz Small-Signal Modulation Bandwith. *IEEE Phot. Tech. Lett.*, **12**(7):786–88, (2000).

[28] M. Dumitrescu, M. Saarinen, N. Xiang, M. Guina, V. Vilokkinen, and M. Pessa. Red Wavelength Range Microcavity Emitters. *phys. stat. sol. (a)*, **188**(3):943–954, (2001).

[29] Firecomms. http: //66.129.71.182/docs/whitepapers/ ReviewofPOF.pdf. *www*, (2001). 16-01-03.

[30] M.S. Ünlü and S. Strite. Resonant cavity enhanced photonic devices. *J. Appl. Phys.*, **78**(2):607–37, (1995).

[31] J.A. Lott, R.P. Schneider, J.C. Zolper, and K.J. Malloy. AlGaInP Visible Resonant Cavity Light-Emitting Diodes. *IEEE Phot. Techno. Lett.*, **5**:631, (1993).

[32] M. Jalonen, M. Toivonen, J. Köngäs, A. Salokatve, and M. Pessa. Oxide-confined resonant cavity red light-emitting diode grown by solid source molecular beam epitaxy. *Elec. Lett*, **33**:1989, (1997).

[33] J. Blondelle, H. De Neve, P. Demeester, P. Van Daele, G. Borghts, and R. Baets. 16 % external quantum efficiency from planar microcavity LEDs at 940nm by precise matching of cavity wavelength. *Elec. Lett.*, **31**(15):1286–8, (1995).

[34] J.J. WIERER AND D.A. KELLOGG AND N. HOLONYAK JR.L. Tunnel contact junction native-oxide aperture and mirror vertical-cavity surface-emitting lasers and resonant-cavity light-emittting diodes. *Appl. Phys. Lett.*, **74**(7):926–8, (1999).

[35] H. BENISTY, H. DE NEVE, AND C. WEISBUCH. Impact of Planar Microcavity Effects on Light Extraction - Part I: Basic Concepts and Analytical Trends. *IEEE J. Quantum Elec.*, **34**(9):1612–31, (1998).

[36] R. BOCKSTAELE, J. DERLUYN, C. SYS, S. VERSTUYFT, I. MOERMAN, P. VAN DAELE, AND R. BAETS. Realisation of higly efficient 850nm top emitting resonant cavity light emitting diodes. *Elec. Lett*, **35**(18), (1999).

[37] V. VILOKKINEN, P. SIPILÄ, M. SAARINEN, S. ORSILA, M. DUMITRESCU, P. SAVOLAINEN, M. TOIVONEN, AND M. PESSA. Resonant cavity light-emitting diodes at 660 and 880 nm. *Mat. Sci. Eng. B*, **74**:165–7, (2000).

[38] B. DEPRETER, I. MOERMAN, R. BAETS, P. VAN DAELE, AND P. DEMEESTER. InP-based 1300 nm microcavity LEDs with 9 % quantum effciency. *Elec. Lett.*, **36**(15), (2000).

[39] K. STREUBEL, U. HELIN, V. OSKARSSON, E. BÄCKLIN, AND Å. JOHANSSON. High Brightness Vissible (660nm) Resonant-Cavity Light-Emitting Diode. *IEEE Phot. Tech. Lett.*, **10**(12):1685–87, (1998).

[40] K. STREUBEL AND R. STEVENS. 250Mbit/s plastic fibre transmission using 660nm resonant cavity light emitting diode. *Elec. Lett.*, **34**(19), (1998).

[41] J.W. GRAY, Y.S. JALILI, P.N. STAVRINOU, M. WHITEHEADAND G. PARRY, A. JOEL, R. ROBJOHN, R. PETRIE, S. HUNJAN, P. GONG, AND G. DUGGAN. High-efficiency, low voltage resonant-cavity light-emitting diodes operating around 650nm. *Elec. Lett.*, **36**(20):1730–31, (2000).

[42] R. WIRTH AND CH. KARNUTSCH AND S. KUGLER AND K. STREUBEL. High-Efficiency Resonant-Cavity LEDs Emitting at 650 nm. *IEEE Phot. Tech. Lett.*, **13**(5):421–3, (2001).

[43] P. MODAK, M. D'HONDT, I. MOERMAN, P. VAN DAELE, P. MIJLEMANS, AND P. DEMEESTER. 5.2 % efficiency InAlGaP microcavity LEDs at 640nm on Ge substrate. *Elec. Lett.*, **37**(6), (2001).

[44] P. Modak, D. Delbeke, I. Moerman, R. Baets, P. Van Daele, and P. Demeester. InAlGaP microcavity LEDs on Ge-substrates. *J. Cryst. Growth*, **221**:668–73, (2000).

[45] P. Sipilä, M. Saarinen, M. Guina, V.Vilokinen, M. Toivonen, and M. Pessa. Temperature behaviour of resonant cavity light-emitting diodes at 650 nm. *Semicond. Sci. Technol.*, **15**:418, (2000).

[46] Zarlink. ZL60003 Plastic Optical Fiber Communications - 125 to 250Mbps Data Sheet, June (2002).

[47] H. Kroemer. A Proposed Class of Heterojunction Injection Lasers. *Proc. IEEE*, :1782–3, (1963).

[48] E. Dupont, H.C. Liu, M. Buchanan, S. Chiu, and M. Gao. Efficient GaAs light-emitting diodes by photon recycling. *Appl. Phys. Lett.*, **76**(1):4–6, (2000).

[49] I. Schnitzer, E. Yablonovitch, C. Caneau, T.J. Gmitter, and A. Scherer. 30% external quantum efficiency from surface textured, thin-film light-emitting diodes. *Appl. Phys. Lett*, **63**(16):2174–6, (1992).

[50] R.Royo, R.P. Stanley, and M. Ilegems. Planar dielectric microcavity light-emitting diodes: Analytical analysis of the extraction efficiency. *J. Appl. Phys.*, **90**(1):283, (2001).

[51] G. Björk, S. Machida, Y. Yamamoto, and K. Igeta. Modification of spontaneous emission rate in planar dielectric microcavity structures. *Phys. Rev. A*, **44**(1):669–81, (1991).

[52] D.B. Deppe and C. Lei. Spontaneous emission from a dipole in a semiconductor microcavity. *J. Appl. Phys.*, **70**(7):3443–8, (1991).

[53] E.M. Purcell. Spontaneous Emission Probabilities at Radio Frequencies. *Phys. Rev.*, **69**:681 B10, (1946).

[54] R.J. Rogers, D.B. Deppe, and B.G. Streetman. Effect of an AlAs/GaAs mirror on the spontaneous emission of an InGaAs-GaAs quantum well. *Appl. Phys. Lett.*, **57**(1):1858–60, (1990).

[55] H. Yokoyama and K. Ujihara, editors. *Spontaneous Emission and Laser Oscillation in Microcavities.* CRC Press, 1995.

[56] C.Wilmsen, H. Temkin, and L.A. Coldren, editors. *Vertical-Cavity Surface-Emitting Lasers.* Cambridge University Press, 1999.

[57] H. Yokoyama. Physics and Device Applications of Optical Microcavities. *Science*, **256**:66–70, (1992).

[58] S.D. Broson, H.Yokoyama, and E.P. Ippen. Spontanoeus Emission Rate Alteration in Optical Waveguide Structures. *IEEE J. Quant. Elec.*, **26**(9):1492–99, (1990).

[59] R. Wirth, W. Huber, Ch. Karnutsch, and K. Streubel. Resonators provide LEDs with laser-like performance. *Comp. Semi.*, (1):49–53, (2002).

[60] T. Takamori, A.R. Pratt, and T. Kamijoh. Temperature dependence of InGAAs/GaAs quantum well microcavity light-emitting diodes. *Appl. Phys. Lett.*, **74**(24):3598–3600, (1999).

[61] M. Dumitrescu, L. Toikkanen, P. Sipilä, V. Vilokkinen, P. Melanen, M. Saarinen, S. Orsila, P. Savolainen, M. Toivonen, and M. Pessa. Modeling and optimization of resonant cavity light-emitting diodes grown by solid source molecular epitaxy. *Microelec. Engineering*, **51-52**:449–460, (2000).

[62] C. Dill, R.P. Stanley, U. Oesterle, D. Ochoa, and M. Ilegems. Effect of detuning on angular emission pattern of high-efficiency microcavity light-emitting diodes. *Appl. Phys. Lett.*, **73**(26):3812–14, (1998).

[63] H.A. Macleod. *Thin-Film Optical Filters.* Adam Hilger Ltd, 2nd edition, 1986.

[64] S. Ghosh, S. Constant, T.J.C. Hosea, and T.E. Sale. Edge-emission electroluminescence study of as-grown vertical-cavity surface-emitting laser structures. *J. Appl. Phys.*, **88**(3):1432–38, (2000).

[65] P.D. Berger, C. Bru, T. Benyattou, G. Guillot, A. Chenevas-Paule, L. Couturier, and P. Grosse. Investigations of vertical cavity

surface emitting laser by photoreflectance spectroscopy. *Appl. Phys. Lett.*, **68**(9):4–6, (1996).

[66] T.E. Sale, T.J.C. Hosea, and P.J.S. Thomas. Photomodulated Reflectance as a Valuable Nondestructive Process Tool for VCSELs. *IEEE Phot. Technol. Lett.*, **12**:1328, (2000).

[67] S.B. Constant, S. Ghosh, T.E. Sale, and T.J.C. Hosea. Nondestructive spectroscopic characterisation of visible resonant cavity light emitting diode structures. *IEE Proc.-Optoelectron.*, **148**(1):69–73, (2001).

[68] F.H. Pollak and H.Shen. Modulation spectroscopy of semiconductors. *Mat. Sci. Eng.*, R10:275–374, (1993).

[69] B.O. Seraphin and R.B. Hess. Franz-Keldysh effect above the fundamental edge in Germanium. *Phys. Rev. Lett.*, **14**(5):138–40, (1965).

[70] E. Matatagui A.G. Thompson and M. Cardona. Thermoreflectance in Semiconductors. *Phys. Rev.*, **176**(3):950–60, (1968).

[71] A. Gavini and M. Cardona. Modulated Piezoreflectance in Semiconductors. *Phys. Rev. B*, **1**(2):672–82, (1970).

[72] J.L. Shay. Photoreflectance Line Shape at the Fundamental Edge in Ultrapure GaAs. *Phys. Rev. B*, **2**(4):803–7, (1970).

[73] B.O. Seraphin and N. Bottka. Band-Structure Analysis from Electro-Reflectance Studies. *Phys. Rev.*, **145**(2):628, (1966).

[74] P.J. Klar, G. Rowland, P.J.S. Thomas, A. Onischenko, T.E. Sale, T.J.C. Hosea, and R.Grey. Photomodulated reflectance study of $In_xGa_{1-x}As/GaAs/AlAs$ microcavity vertical-cavity surface emitting laser structures in the weak-coupling regime: The cavity/ground-state-exciton resonance. *Phys. Rev. B*, **59**(4):2894–901, (1999).

[75] P.J. Klar, C.M. Townsley, D. Wolverson, J.J. Davies, D.E. Ashenford, and B. Lunn. Photomodulated reflectivity of $Zn_{1-x}Mn_xTe/ZnTe$ multiple-quantum wells with below-bandgap excitation. *Semicond. Sci. Technol.*, **10**:1568–77, (1995).

[76] B.V. SHANABROOK, O.J. GLEMBOCKI, AND W.T. BEARD. Photoreflectance modulation mechanismus in GaAs-Al_xGa_{1-x} multiple quantum wells. *Phys. Rev. B*, **35**(5):1506–08, (1987).

[77] D.E. ASPNES. Third-derivative Modulation spectroscopy with low-field Electroreflectance. *Surf. Science*, **37**:418–42, (1973).

[78] C. VAZQUEZ-LOPEZ AND H. NAVARRO AND R. ACEVES AND M.C. VARGAS AND C.A. MENEZES. Electroreflectance, photoreflectance, and photoabsorption properties of polycrystalline CdTe thin films prepared by the gradient recrystallization and growth technique. *J. Appl. Phys.*, **58**:2066–9, (1985).

[79] Y.P.VARSHNI. Temperature dependence of the energy gap in semiconductor. *Physica*, **34**:149–54, (1967).

[80] J. TALGHADER AND J.S. SMITH. Thermal dependence of the refractive index of GaAs and AlAs measured using semiconductor multilayer optical cavities. *Appl. Phys. Lett.*, **66**(3):335–37, (1995).

[81] G. KNOWLES, S.J. SWEENEY, T.E. SALE, AND A.R. ADAMS. Assessing the Performance of visible (665 nm) Vertical Cavity Surface Emitting Lasers Using High Pressure and Low Temperature Techniques. *phys. stat. sol. (b)*, **223**:581–85, (2001).

[82] S.A. CHOULIS, S. TOMIC, E.P. O'REILLY, AND T.J.C. HOSEA. Determining the band-structure of an InGaNAs/GaAs semiconductor laser structure using non-destructive photomodulated reflectance measurements and $\mathbf{k}\cdot\mathbf{p}$ studies. *Solid State Comm*, 125:155–59, (2003).

[83] S.A. CHOULIS, S. GHOSH, AND T.J.C. HOSEA. Resonances between the cavity mode and five excitonic transitions in an InGaAs/GaAs/AlAs vertical-cavity surface-emitting laser structure using photomodulated reflectance. *J. Appl. Phys.*, 99(10):5547–53, (2000).

[84] J.S. TOLL. Causality and the Dispersion Relation: Logical Foundations. *Phys. Rev.*, **104**(6):1760–70, (1956).

[85] T.J.C. HOSEA. Estimating Critical-Point Parameters from Kramers-Kronig Transformations of Modulated Reflectance Spectra. *phys. stat. sol. (b)*, **182**:K43–47, (1994).

[86] S. Ghosh, T.J.C. Hosea, and S.B. Constant. Photoreflectance line shape symmetry and quantum-well ground-state exciton energy in vertical-cavity surface-emitting laser structures. *Appl. Phys. Lett.*, **78**(21):3250–52, (2001).

[87] T.J.C. Hosea. PR fitting program, 1999-2001. University of Surrey, GU2 7XH.

[88] Y. Yu and M. Cardona. *Fundamentals of Semiconductors.* Springer-Verlag, 2nd edition, 1999.

[89] E. Yablonovitch, T.J. Gmitter, R.D. Meade, A.M. Rappe, K.D. Brommer, and J.D. Joannopoulos. Donor and Acceptor Modes in Photonic Band Structure. *Phys. Rev. Lett.*, **67**(24):3380–3, (1991).

[90] T.E. Sale. Cavity and reflector design for vertical cavity surface emitting lasers. *IEE Proc.-Optoelectron.*, **142**:37–43, (1995).

[91] M.V Klein and T.E. Furtak. *Optics.* Wiley Sons, New York, 1986.

[92] T.J.C. Hosea. Jones program to calculate reflectivity, 1999-2003. University of Surrey, GU2 7XH.

[93] P.J. Klar, G. Rowland, T.E. Sale, T.J.C. Hosea, and R. Grey. Reflectance and Photomodulated Reflectance Studies of Cavity Mode and Excitonic Transitions in an InGaAs/GaAs/AlAs/AlGaAs VCSEL Structure. *phys. stat. sol. (a)*, **170**:145–58, (1998.

[94] D.C. Yin and Y.Inatomi. Measurement of Refractive Index of GaP Crystal over a Large Temperature Range Using Interferometry. *Cryst. Res. Technol.*, **35**(2):221–28, (2000).

[95] I. Vurgaftman and J.R. Meayer and L.R. Ram-Mohan. Band Parameters for III-V compound semiconductors and their alloys. *Appl. Phys. Rev.*, **89**:5815, (2001).

[96] D. Ochoa, R. Houdre, R.P. Stanley anc C. Dill, U. Oesterle, and M. Ilegems. Device simultaneous determination of the source and cavity parameters of a microcavity light-emitting diode. *J. Appl. Phys.*, **85**(5):2994–6, (1999).

[97] P.N. STAVRINOU, M. WHITEHEAD, G. PARRY, AND C.C. BUTTON. Angular spectrum of visible resonant cavity light-emitting diodes. *J. Appl. Phys.*, **86**(6):3475–77, (1999).

[98] R.ROYO, R.P. STANLEY, M. ILEGEMS, K. STREUBEL, AND K.H. GULDEN. On-wafer determination of intrinsic spontaneous spectrum of vertical cavity surface-emitting devices. *Elec. Lett.*, **36**(25), (2000).

[99] R.F. OULTON, J.W. GRAY, P.N. STAVRINOU, AND G. PARRY. Insight into planar microcavity emission as a function of numerical aperture. *Optics Comm.*, **195**:327–338, (2001).

[100] T. CALVERT, B. CORBETT, AND J.D. LAMBKIN. 80°C continuous wave operation of AlGaInP based visible VCSEL. *Elec. Lett.*, **38**(5), (2002).

[101] S.J. SWEENEY, G. KNOWLES, T.E. SALE, AND A.R. ADAMS. Quantifying the Effect of Indirect Carrier Leakage on Visible Al(GaInP) Lasers Using High Pressure and Low Temperature. *phys. stat. sol. (b)*, **223**:567–72, (2001).

[102] D. PATEL, J.M. PIKAL, C.S. MENONI, K.J. THOMAS, F.A. KISH, AND M.R. HUESCHEN. Effect of indirect minima carrier population on the output characteristics of AlGaInP light-emitting diodes. *Appl. Phys. Lett.*, **75**(20):3201–03, (1999).

[103] G. KNOWLES, S.J. SWEENEY, T.E. SALE, AND A.R. ADAMS. Self-heating effects in red (665 nm) VCSELs. *IEE Proc.-Optoelectron.*, **148**(5/6):256–60, (2001).

[104] K.D. CHOQUETTE, R.P. SCHNEIDER, M. HAGEROTT CRAWFORD, K.M. GEIB, AND J.J. FIGIEL. Continous wave operation of 640-660 nm selectively oxidised AlGaInP vertical-cavity lasers. *Elec. Lett*, **3**(14):1145–46, (1995).

[105] M. SAARINEN, M. TOIVONEN, N. XIANG, V. VILOKKINEN, AND M. PESSA. Room-temperature CW operation of red vertical-cavity surface-emitting lasers grown by solid-source molecular beam epitaxy. *Elec. Lett.*, **36**(14), (2000).

[106] A. KNIGGE, M. ZORN, H. WENZEL, M. WEYERS, AND G. TRÄNKLE. High efficiency AlGaInP-based 650nm vertical-cavity surface emitting lasers. *ELec. Lett*, **37**(20), (2001).

[107] A.I. Onischenko, T.E. Sale, E.P.O'Reilly, A.R. Adams, S.M. Pinches, J.E.F. Frost, and J. Woodhead. Progress in the design and development of AlGaInP visible VCSELs. *IEE Proc. Optoelectron.*, **147**:15, (2000).

[108] P.M. Smowton and P. Blood. Threshold current temperature dependence of $GaInP/(Al_yGa_{1-y})InP$ 670nm quantum well lasers. *Appl. Phys. Lett.*, **67**(9):1265–7, (1995).

[109] H. De Neve, J. Blondelle, P. Van Daele, P. Demeester, R. Beats, and G. Borghs. Recycling of guided mode light emission in planar microcavity light emitting diodes. *Appl. Phys. Lett.*, **70**(7):799–801, (1997).

[110] H. Benisty, H. De Neve, and C. Weisbuch. Impact of Planar Microcavity Effects on Light Extraction - Part II: Selected Exact Simulations and Role of Photon Recycling. *IEEE J. Quantum Elec.*, **34**(9):1632–43, (1998).

[111] L.A. Coldren and S.W. Corzine. *Diode Lasers and Photonic Integrated Circuits*. Wiley, New York, 1995.

[112] S. Adachi. Lattice thermal resistivity of III-V compound alloys. *J. Appl. Phys.*, **54**(4):1844–8, (1983).

[113] P.S. Zory Jr. *Quantum Well Lasers*. Acadmic Press, Inc., 1993.

[114] T. Yao. Thermal properties of AlAs/GaAs superlattices. *Appl. Phys. Lett.*, **51**(22):1798–1800, (1987).

[115] Hewlett Packard. DC to 10 MBd Versatile Link with Plastic Optical Fibre or Hard Clad Silica Fiber (HCS) for Factory Automation and Idustrial Control Applications, Application Note 1080, (1995).

[116] M. Pessa, M. Toivonen, P. Savolainen, S. Orsila, P. Sipilä, M. Saarinen, P. Melanen, V. Vilokinen, P. Uusimaa, and J. Haapamaa. Growth of resonant cavity quantum well light emitting diodes and two-junction solar cells by solid source molecular beam epitaxy. *Thin solid Films*, **367**:260–66, (2000).

[117] M. FUJITA, R. USHIGOME, AND T. BABA. Large Spontaneous Emission Factor of 0.1 in a Microdisk Injection Laser. *IEEE Phot. Tech. Lett.*, **13**(5):403–5, (2001).

[118] M. GUINA, J. DEKKER, A. TUIKAINEN, S. ORSILA, M. SAARINEN, M. DUMITRESCU, P. SIPILÄ, P. SAVOLAINEN, AND M.PESSA. Influence of deep level impurities on modulation response of InGaP light emitting diodes. *J. Appl. Phys.*, **89**(2):1151–55, (2001).

[119] J.A. LEHMANN, R.A. MORGAN, D. CARSLON, M. HAGEROT CRAWFORD, AND K.D. CHOQUETTE. High-frequency modulation characteristics of red VCSELs. *Elec. lett.*, **33**(4), (1997).

[120] P. LANDAIS, B. ROYCROFT, A. SHAW, B. DEPRETER, I. MOERMAN, AND J. HEGARTY. Small-Signal Analysis of 1.3-μm Microcavity Light-Emitting Diodes. *IEEE Phot. Techno. Lett.*, **11**(11):1342–44, (1999).

[121] G.E. SHTENGEL, D.A. ACKERMAN, P.A. MORTON, E.J. FLYNN, AND M.S. HYBERTSEN. Impedance-corrected carrier lifetime measurements in semiconductor lasers. *Appl. Phys. Lett.*, **67**(11):1506–08, (1995).

[122] D. DELBEKE, R. BOCKSTAELE, P. DIENSTMAN, R. BAETS, AND H. BENISTY. High-Efficiency Semiconductor Resonant-Cavity Light-Emitting Diodes: A Review. *IEEE J. Select. Top. Quant. Elec.*, **8**(2):189–206, (2002).

[123] G.H.B THOMPSON. Analysis of Radiative and nonradiative recombination law in lightly doped InGaAsP Lasers. *Elec. Lett.*, **19**(5):154–5, (1983.

[124] S.M. SZE. *Physics of Semiconductor Devices.* John Wiley Sons Inc., 2nd edition, 1981.

[125] E.P. O'REILLY AND M. SILVER. Temperature sensitivity and high temperature operation of long wavelength semiconductor lasers. *Appl. Phys. Lett.*, 63:3318, (1993).

[126] J.A. WOOLAM CO. INC. Guide to Using WVASE32. J.A. Woolam Co. inc., (1996) and references therein.

Appendix

Here the structural details of the investigated structures and devices can be found.

A.1 Structure S1

Layer	Repeats	Material	x	Thickness (nm)	Doping
1 cap	1	GaAs		88.6	Zn
2	1	$Al_xGa_{1-x}As$	0.5	30.9	C
3	1	$Al_xGa_{1-x}As$	1-0.5	10	C
4	7	$AlAs$		41.4	C
5	7	$Al_xGa_{1-x}As$	0.5-1	10	C
6	7	$Al_xGa_{1-x}As$	0.5	37.6	C
7	7	$Al_xGa_{1-x}As$	1-0.5	10	C
8	1	$AlAs$		46.8	C
9	1	Al_xGaInP	0.7	49.8	Zn
10	1	Al_xGaInP	0.3	38.8	
11 QW	1	$InGaP$		6	
12	1	Al_xGaInP	0.3	8	
13 QW	1	$InGaP$		6	
14	1	Al_xGaInP	0.3	38.8	
15	1	Al_xGaInP	0.7	49.8	Si
16	1	$AlAs$		46.8	Si
17	30	$Al_xGa_{1-x}As$	0.5-1	10	Si
18	30	$Al_xGa_{1-x}As$	0.5	37.6	Si
19	30	$Al_xGa_{1-x}As$	1-0.5	10	Si
20	30	$AlAs$		41.4	Si
21	1	$Al_xGa_{1-x}As$	0.5-1	10	Si
22	1	$Al_xGa_{1-x}As$	0.5	37.6	Si
23	1	$Al_xGa_{1-x}As$	1-0.5	10	Si
24	1	$AlAs$		38.3	Si
25	1	$Al_xGa_{1-x}As$	0-1	10	Si
26 buffer	1	GaAs		200	Si

Table 8.1: Structure S1

A.2 Structure S2

Layer	Repeats	Material	x	Thickness (nm)	Doping
1 cap	1	GaAs		88.6	Zn
2	1	$Al_xGa_{1-x}As$	0.5	30.9	C
3	1	$Al_xGa_{1-x}As$	1-0.5	10	C
4	7	$AlAs$		41.4	C
5	7	$Al_xGa_{1-x}As$	0.5-1	10	C
6	7	$Al_xGa_{1-x}As$	0.5	37.6	C
7	7	$Al_xGa_{1-x}As$	1-0.5	10	C
8	1	$AlAs$		46.8	C
9	1	Al_xGaInP	0.7	49.8	Zn
10	1	Al_xGaInP	0.3	38.3	
11 QW_1	1	$InGaP$		7	
12	1	Al_xGaInP	0.3	8.25	
13 QW_2	1	$InGaP$		4.5	
14	1	Al_xGaInP	0.3	39.55	
15	1	Al_xGaInP	0.7	49.8	Si
16	1	$AlAs$		46.8	Si
17	30	$Al_xGa_{1-x}As$	0.5-1	10	Si
18	30	$Al_xGa_{1-x}As$	0.5	37.6	Si
19	30	$Al_xGa_{1-x}As$	1-0.5	10	Si
20	30	$AlAs$		41.4	Si
21	1	$Al_xGa_{1-x}As$	0.5-1	10	Si
22	1	$Al_xGa_{1-x}As$	0.5	37.6	Si
23	1	$Al_xGa_{1-x}As$	1-0.5	10	Si
24	1	$AlAs$		38.3	Si
25	1	$Al_xGa_{1-x}As$	0-1	10	Si
26 buffer	1	GaAs		200	Si

Table 8.2: Structure S2

A.3 Structure J01

Layer	Repeats	Material	x	Thickness (nm)	Doping
1 cap	1	GaAs		10	Mg
2 DBR	8	$Al_xGa_{1-x}As$	0.5	46.1	Mg
3 DBR	8	AlAs		52.2	Mg
4 barrier	1	$(Al_xGa_{1-x})_{0.51}In_{0.49}P$	0.5	95.5 varied	
5 QW	1	InGaP		4	
6 barrier	1	$(Al_xGa_{1-x})_{0.51}In_{0.49}P$	0.5	95.5 varied	
7 DBR	32	AlAs		52.2	Si
8 DBR	32	$Al_xGa_{1-x}As$	0.5	46.1	Si
9 buffer	1	GaAs		200	Si

Table 8.3: Structures with varying cavity thicknesses.

A.4 Structure J02

Layer	Repeats	Material	x	Thickness (nm)	Doping
1 cap	1	GaAs		88.6	Mg, Zn, C
2 DBR	8, 11, 14	$Al_xGa_{1-x}As$	0.5	46.1	Mg, Zn, C
3 DBR	8, 11, 14	AlAs		52.2	Mg, Zn, C
4 barrier	1	$(Al_xGa_{1-x})_{0.51}In_{0.49}P$	0.5	93.7	
5 QW_1	1	InGaP (for PL: 652nm)		7.5	
6 barrier	1	$(Al_xGa_{1-x})_{0.51}In_{0.49}P$	0.5	89.8	
7 QW_2	1	InGaP(for PL: 642nm)		7.5	
8 barrier	1	$(Al_xGa_{1-x})_{0.51}In_{0.49}P$	0.5	93.7	
9 DBR	1	AlAs		52.2	Si
10 DBR	32	$Al_xGa_{1-x}As$	0.5	46.1	Si
11 DBR	32	AlAs		52.2	Si
12	1	$Al_xGa_{1-x}As$	0-1	10	Si
13 buffer	1	GaAs		200	Si

Table 8.4: Structures with different numbers of top DBR pairs.